



An Experimental Study of the nvPM Emissions Produced by Alternative Aviation Fuels in a Newly-Developed RQL Research Combustor

By

Joseph Harper

Thesis submitted to Cardiff University for the degree of Doctor of Philosophy

School of Engineering

Cardiff University

2022

Acknowledgements

I would like to sincerely thank the following people:

My supervisor Andrew Crayford for offering me this opportunity, and for the consistent guidance and encouragement that has been instrumental in enabling me to complete this thesis.

My secondary supervisor Phil Bowen.

My industrial supervisor Mark Johnson at Rolls Royce.

Eliot Durand for advising me on the EUR reference system and loss correction.

Tony Giles for assisting me at the Gas Turbine Research Centre (GTRC) with the spray measurements.

Steve Morris, Jack Thomas, and the rest of the GTRC staff for facilitating my experiments.

Paul Malpas for all of his help with the atomisers.

Franck Lacan for the use of the SLM machine.

EPSRC and to Rolls Royce for funding this research.

And finally, all my family and friends for the constant support.

Abstract

Emissions from aircraft are known to impact both the local and global environment, and are expected to increase with the predicted rise in air travel in future years. Of these emissions, non-volatile Particulate Matter (nvPM) is known to negatively affect both the local and global environment. The use of Sustainable Aviation Fuels (SAF) has been shown to greatly reduce nvPM emissions due to reductions in aromatic compounds, and can also allow for offsetting of CO₂. With the introduction of increasingly stringent regulations concerning nvPM following the CAEP/11 meeting, it is anticipated that SAF will see increased use in the commercial aviation sector in upcoming years. As such, there is a need to understand their behaviour in representative aero combustion environments.

This thesis describes the development of a non-proprietary RQL combustion rig used for experimentation concerning the emissions produced by SAF, manufactured using a combination of Additive Manufacturing (AM) and conventional machining. Combustion emissions tests were undertaken using multiple iterations of the combustor, with a range of conventional fuels, SAF, and fuel blends. Emissions were sampled using ICAO compliant instrumentation, and corrected for system losses using size-dependant loss corrections. The effects of fuel properties and combustor operating conditions on loss corrected nvPM were explored, yielding a new proposed hydrogen content trend for correlating fuel properties to nvPM emissions. A systematic assessment of sample system loss correction procedures indicated that, without system loss corrections, reductions in nvPM number achievable through the use of a high hydrogen content SAF (as currently reported in literature) are overreported by 6-9%.

Droplet sizing and spray imaging were used to characterise the atomisers developed for the combustor. Suitable correlations from the literature were subsequently optimised using a linear regression code for best quality of fit with experimental data. Spray experimentation showed that small variations in average droplet sizes may be expected across alternative fuels due to physical fuel properties (7-12% at the conditions tested). Using the correlation developed, small predicted increases in SMD of ~5% were found to reduce combustion stability and consistently exacerbate nvPM emissions, leading to relative increases of 5-72% for E_{mass} , 11-89% for E_{number} , and 1-7% for GMD.

Published and Presented Work

- Fuel, published 2022

Journal Publication - Influence of alternative fuel properties and combustor operating conditions on the nvPM and gaseous emissions produced by a small-scale RQL combustor (Joseph Harper, Eliot Durand, Philip Bowen, Daniel Pugh, Mark Johnson, Andrew Crayford) [1]

- Annual Aerosol Science Conference (AASC), November 2021

Presentation - Development of Additive Manufactured Atomisers for the Study of nvPM Emissions from Sustainable Aviation Fuels (Joseph Harper, Andrew Crayford, Franck Lacan, Phil Bowen, Mark Johnson, Anthony Giles)

- 3rd ECATS Aviation and Climate Conference, October 2020

Presentation - Effect of Fuel Composition on nvPM Emissions Produced by an RQL Combustion Rig using Conventional and Alternative Fuels (Joseph Harper, Andrew Crayford, Franck Lacan, Phil Bowen, Mark Johnson, Anthony Giles)

- Proceedings of ASME Turbo Expo, published 2019

Conference Proceedings - Manufacture, Characterisation and Stability Limits of an AM Prefilming Air-Blast Atomiser (Andrew Crayford, Franck Lacan, Jon Runyon, Philip Bowen, Shrinivas Balwadkar, Joseph Harper, Daniel Pugh) [2]

Contents

1.	Introduction	1
1.1.	Emissions from Aircraft	1
1.1.1.	Overview	1
1.1.2.	CO ₂ Emissions.....	3
1.1.3.	Non-CO ₂ Gaseous Emissions.....	4
1.1.4.	Particulate Matter	5
1.2.	Regulations Concerning Aircraft Emissions.....	8
1.3.	Reducing Emissions through Developments in Aircraft Gas Turbine Technologies	11
1.3.1.	Gas Turbine Design	11
1.3.2.	The RQL Methodology	14
1.3.3.	Concerns with nvPM Emissions from RQL Combustors.....	18
1.4.	Reducing Aircraft Emissions using Drop-in Fuels and SAF.....	20
1.5.	Research Motivations and Thesis Structure	26
2.	Factors Impacting nvPM Formation in Aircraft Combustors	29
2.1.	Aviation Fuel Key Chemical Components	29
2.2.	SAF Conversion Processes	32
2.2.1.	Fischer-Tropsch (F-T) Fuels	32
2.2.2.	Hydroprocessed Esters and Fatty Acids (HEFA) Fuel.....	33
2.2.3.	Alcohol-to-Jet (ATJ) Fuels.....	35
2.2.4.	Catalytic Hydrothermal Conversion Jet (CHCJ) Fuel	35
2.3.	Chemical Effects on nvPM Emissions.....	37
2.3.1.	Chemical Mechanism of nvPM Formation.....	37
2.3.2.	Emissions Reductions through the use of Low-Aromatic Fuels	40
2.3.3.	Linking Chemical Properties to nvPM	43
2.4.	Atomisation in Gas Turbines	46
2.4.1.	Atomisation Mechanisms.....	47
2.4.2.	Characterising Atomisation Quality	51
2.4.3.	The Impact of Atomisation Quality on Emissions.....	53
2.4.4.	Factors Affecting Atomisation for Airblast Atomisers	56
2.4.5.	Prefilming Airblast Atomiser Empirical Correlations	58
2.5.	Cone Angles.....	64
2.6.	Summary and Gap Analysis	67
3.	Experimental Facilities and Apparatus	69
3.1.	Fuel Analysis Techniques	69
3.1.1.	Nuclear Magnetic Resonance (NMR) Spectroscopy	69
3.1.2.	Gas Chromatography (GC)	71

3.2.	GTRC Generic RQL Combustor	73
3.2.1.	AM Atomiser Design	73
3.2.2.	Combustion Liner	77
3.3.	NvPM Emissions Sampling and Measurement.....	78
3.3.1.	HPOC	78
3.3.2.	European Mobile Reference Sampling and Measurement System	81
3.4.	nvPM Loss Corrections	85
3.4.1.	Particle Loss Mechanisms.....	85
3.4.2.	Size Dependant System Loss Correction Methodology.....	87
3.4.3.	Specific Energy Corrections	90
3.5.	Gaseous Measurements	91
3.5.1.	Measurement System.....	91
3.5.2.	Gaseous Corrections.....	92
3.6.	Malvern Spraytec97 Laser Diffraction Experimentation.....	95
3.6.1.	Measurement Principle	95
3.6.2.	Calibration.....	97
3.6.3.	Experimental Setup	99
3.7.	High Speed Imaging (HSI)	101
3.7.1.	Overview	101
3.7.2.	Image Processing Method.....	102
3.8.	Phase Doppler Anemometry (PDA)	107
4.	Assessment of Additive Manufacturing (AM) in the Development of Prefilming Airblast Atomisers	112
4.1.	Overview	112
4.2.	Design Considerations.....	113
4.2.1.	Atomiser Features	113
4.2.2.	Static Pressure Loss Calculations.....	119
4.3.	Phase I Atomisers	128
4.3.1.	Design	128
4.3.2.	Assessment of Flow Behaviour	131
4.4.	Phase II Designs	133
4.5.	Assessment of Manufacturing Quality.....	137
4.6.	Chapter Summary.....	142
5.	Characterisation of nvPM Emissions from Alternative Fuels (Mk. I Combustor)	143
5.1.	Operating Conditions.....	144
5.2.	Fuel Properties.....	146
5.2.1.	Chemical Properties.....	146

5.2.2.	Physical Properties	150
5.2.3.	Energy Content.....	153
5.3.	Results.....	154
5.3.1.	nvPM Emissions.....	154
5.3.2.	Gaseous Emissions	157
5.3.3.	Rig Operating Conditions	161
5.4.	Empirical Analysis of Fuel Compositional Effects	163
5.4.1.	Hydrogen Content Trends	163
5.4.2.	Consideration of the Effects of Other Fuel Properties on nvPM Emissions.....	167
5.5.	Assessment of Correction Procedures	171
5.5.1.	System Loss Corrections	171
5.5.2.	Assessment of Specific Energy Corrections	173
5.6.	Assessment of the Effects of Combustor Conditions on nvPM..	176
5.6.1.	Power/Thrust.....	176
5.6.2.	Primary Air.....	177
5.6.3.	Fuel Flowrate.....	178
5.6.4.	Secondary Air.....	181
5.7.	Chapter Summary.....	182
6.	Refinement of the RQL Design (Mk. II Combustor).....	185
6.1.	Overview	185
6.2.	Laser Diffraction Experimentation	185
6.2.1.	Ambient Temperature Atomiser Characterisation	185
6.2.2.	Elevated Temperature Atomisation Characterisation	191
6.2.3.	Sum Squared-Error Regression Analysis.....	194
6.3.	Mk. II Combustion Liner.....	200
6.3.1.	Design Considerations.....	200
6.3.2.	Flow Partitioning.....	202
6.4.	Mk. II Combustor Emissions Testing	205
6.4.1.	Overview	205
6.4.2.	Emissions Results	208
6.5.	Chapter Summary.....	212
7.	Further Investigation of Airblast Atomiser Sprays (Mk. II-A Combustor)	214
7.1.	Overview	214
7.2.	HSI Experimentation	215
7.2.1.	Water Results	215
7.2.2.	Jet A-1 Results	220
7.3.	PDA Atomiser Characterisation	225

7.3.1.	Comparison of Droplet Sizes across Atomisers	225
7.3.2.	Investigation of Spray Variability across Drop-in Fuels.....	230
7.4.	Emissions Experimentation	238
7.4.1.	Overview	238
7.4.2.	Emissions Results	240
7.4.3.	Comparisons Across Datasets	245
7.5.	Chapter Summary.....	247
8.	Conclusions	250
8.1.	Discussion	250
8.2.	Conclusions	252
8.3.	Future work.....	253
9.	References.....	255
10.	Appendices	266
10.1.	HSI Image Processing Macros	266
10.2.	Linear Regression MATLAB Code (El-Shanawany et al. Example)	

List of Figures

Figure 1-1 - World energy trilemma index [12]	2
Figure 1-2 - Emissions production from a typical two engine aircraft (representative 150 passengers) over a 1 hour flight [3]	3
Figure 1-3 - Transmission Electron Microscopy (TEM) imaging of typical aircraft nvPM agglomerate structures [22]	5
Figure 1-4 - Visualisation of PM sizes [3].....	7
Figure 1-5 - Research aircraft producing cirrus cloud contrails [34]	7
Figure 1-6 - Impact of various emissions on radiative forcing up to 2018 [35]	8
Figure 1-7 - ICAO compliant measurement setup [24]	10
Figure 1-8 - Rolls Royce Trent 1000 turbofan engine [47].....	12
Figure 1-9 - A typical gas turbine combustor.....	13
Figure 1-10 - Emissions dependence on engine operating conditions [16]	15
Figure 1-11 - Variability of NO _x and CO production with flame temperature [16]	16
Figure 1-12 - Representation of an RQL Combustor with typical equivalence ratios [53]	17
Figure 1-13 - NO _x emissions profile vs equivalence ratio - [16]	18
Figure 1-14 - nvPM mass and number emissions produced by real-world engines (by manufacturer) as percentages of the CAEP/11 regulatory limits [54].....	20
Figure 1-15 - Proposed design modification necessary for modern aircraft powered by liquid hydrogen (left) and ethanol (right) [59]	22
Figure 1-16 - Net CO ₂ Emissions from international aviation forecast 2005-2050 [11]	24
Figure 2-1 - From left to right: n-heptane (n-C ₇ H ₁₆), and 2,3 di-methylpentane (i-C ₇ H ₁₆).....	30
Figure 2-2 - From left to right: Cyclopentane (C ₇ H ₁₄ , a mono-cycloparaffin), and decalin (C ₁₀ H ₁₈ , a di-cycloparaffin)	30
Figure 2-3 - From left to right: Benzene (C ₆ H ₆ , base molecule), Toluene (C ₇ H ₈ , an alkyl-benzene), Tetralin (C ₁₀ H ₁₂ , a cycloaromatic) and Dialin (C ₁₀ H ₁₀ , a cycloaromatic)	31
Figure 2-4 - From left to right: Naphthalene (C ₁₀ H ₈ , base molecule) and 1,2,3,4-Tetrahydroanthracene (C ₁₄ H ₁₄ , a naphtheno-diaromatic)	31
Figure 2-5 - HEFA conversion process [63]	33
Figure 2-6 - Predicted lifecycle CO ₂ emissions for various aviation fuels [5]	34
Figure 2-7 - CHCJ conversion process [63].....	36
Figure 2-8 - Soot particle formation during fuel combustion [91].....	38
Figure 2-9 - Comparison of nvPM formation for a Jet-A fuel compared to a camelina-derived CH biofuel [94].....	41

Figure 2-10 - Correlating nvPM number and mass emissions to hydrogen content [106].....	44
Figure 2-11 - Examples of liquid jet breakup mechanisms [112]	49
Figure 2-12 - Wavy jet breakup [112]	50
Figure 2-13 - Typical Particle Size Distribution (PSD) for a spray	51
Figure 2-14 - Airblast spray droplet frequency distribution with several mean diameter locations, recreated from [112]	53
Figure 2-15 - Droplet burning [116].....	54
Figure 2-16 - Variation in modelled soot formation in a model combustor for sprays of differing droplet sizes [118]	56
Figure 2-17 - Pintle type prefilming airblast atomiser [16]	59
Figure 2-18 - A and B regression coefficients [117]	64
Figure 2-19 - Example of the differences across Jet A-1 and water sprays for a prefilming airblast atomiser [117]	66
Figure 2-20 - Airblast atomiser sprays at increasing ambient pressures at a fuel flowrate of 35 g/s, and dP/P of 0.05 [131].....	67
Figure 3-1 - NMR principles showing nuclear spin precession movement for an atom in an external magnetic field (left) and the effect of an applied radio pulse (right), [134].....	70
Figure 3-2 - Typical jet fuel hydrocarbon compositional data determined using 2D GCxGC.....	72
Figure 3-3 - Parker-Hannifin atomiser design (left) and interaction between air and fuel flows at the atomiser exit (right) [127]	74
Figure 3-4 - RQL atomiser prototype design.....	75
Figure 3-5 - Typical powder bed fusion process [152] (left) and General Electric LEAP engine atomiser (right)	76
Figure 3-6 - Mk. I RQL combustor with atomiser placement	78
Figure 3-7 - GTRC HPOC Setup	79
Figure 3-8 - Piccolo sampling probe	79
Figure 3-9 - HPOC setup with RQL combustor placement	80
Figure 3-10 - EASA measurement system	82
Figure 3-11 - Particle system loss mechanisms [160]	85
Figure 3-12 - Particle penetration (transport) efficiency vs. particle diameter for a typical ICAO compliant sampling system [161]	87
Figure 3-13 - Impact of system loss corrections on nvPM emissions	90
Figure 3-14 - Malvern Spraytec97 measurement principle	96
Figure 3-15 - Malvern Spraytec97 system outputs.....	97
Figure 3-16 - Malvern Spraytec97 optics receiver module.....	98
Figure 3-17 - Recommended background calibration signal.....	98
Figure 3-18 - Malvern Spraytec97 measurement setup diagram and photograph	99

Figure 3-19 - Schematic and photograph of manufactured pressure tap.....	101
Figure 3-20 - GTRC spray booth with HSI setup	102
Figure 3-21 - Uncorrected intensity signal across all 2000 images of a typical image stack (intensities inverted)	103
Figure 3-22 - Corrected intensity signal.....	104
Figure 3-23 - Effect of correcting for residual background illumination	105
Figure 3-24 - Images before (a) and after (b) thresholding	106
Figure 3-25 - STD plot following thresholding	106
Figure 3-26 - Spray cone angle measurement	107
Figure 3-27 - Refraction of coherent light through a liquid particle (reproduced from Dantec homepage [173]).....	108
Figure 3-28 - PDA measurement principle [173]	110
Figure 4-1 - Representation of a straight bladed swirler assembly [16], and trigonometry for a helix.....	113
Figure 4-2 - Inner (left) and outer (right) air swirlers	114
Figure 4-3 -Swirler assembly effective flow area calculations	115
Figure 4-4 - Curved bladed swirler assembly.....	117
Figure 4-5 - Additional air flow path dimensions	118
Figure 4-6 - Atomiser prefilmer dimensions	119
Figure 4-7 - Static pressure profile across a simple orifice [184]	122
Figure 4-8 - Flow entering a contraction [185]	124
Figure 4-9 - Representation of pressure losses across atomiser air channels....	126
Figure 4-10 - Swagelok ¼” to 3/8” connector	127
Figure 4-11 - CAD Render of Atomiser I-D	129
Figure 4-12 - Phase I atomiser manufacturing CAD file with supports (left) and printed atomisers (right)	131
Figure 4-13 - Measured pressure loss values vs. predicted trends (left) and swirler gaps visible in the original atomiser (right)	132
Figure 4-14 - Calculated Cd values across phase I atomisers	133
Figure 4-15 - CAD Images of straight blades (left) vs. curved blades (right)	135
Figure 4-16 - Phase II atomiser manufacturing technique (failed atomiser highlighted)	137
Figure 4-17 - Unprocessed image (top) and binarized image used for dimensional analysis (bottom).....	139
Figure 5-1 - Hydrogen contents and total aromatics contents of the fuels tested.	147
Figure 5-2 - Compositions of fuels by main hydrocarbon families (GCxGC).....	148
Figure 5-3 (a-d) - Fuel chemical content of paraffins (a), cycloparaffins (b), mono-aromatics (c) and di-aromatics (d) plotted against the fuel hydrogen content.	149

Figure 5-4 - Measured MW values of the test fuels using the weighted method and GCxGC data	150
Figure 5-5 (a-c): Fuel physical properties of surface tension, kinematic viscosity and liquid density respectively plotted against hydrogen content. Dashed red lines indicate permissible ASTM specifications for commercial jet fuels where applicable	151
Figure 5-6 - Predicted variability in SMD (with respect to J-REF) for the tested fuels using simple correlation [124]	153
Figure 5-7 - Specific energy content (left) and volumetric energy content (right) as measured by ASTM D3338, plotted against hydrogen content.....	154
Figure 5-8 - Typical measured PSD across fuels (left) and measured vs. EEP GMD (right)	155
Figure 5-9 - Combustor-exit nvPM EI mass (a), number (b) and measured GMD (c) against fuel hydrogen content at different combustor pressures and rig operating conditions.....	156
Figure 5-10 - Measured gaseous emissions at condition C at varying pressure for different fuels	159
Figure 5-11 - Calculated combustor efficiency across range of pressures for tested fuels	160
Figure 5-12 - Deviation between AFR calculated from mass flow controllers and calculated from gaseous data	161
Figure 5-13 (a and b) - Measured combustor liner ambient pressures and atomiser pressure drop across different test cases and fuels.	162
Figure 5-14 - Measured combustor exit temperatures for different test conditions	163
Figure 5-15 - Normalised correlations indicating the impact of fuel hydrogen content (polynomial trend) on nvPM emissions relative to a reference fuel. ...	164
Figure 5-16 - Normalised correlations indicating the impact of fuel hydrogen content (inverse power) on nvPM emissions relative to a reference fuel.	165
Figure 5-17 - Normalised correlations indicating the impact of fuel hydrogen content (constrained power) on nvPM emissions relative to a reference fuel. .	166
Figure 5-18 - Normalised correlations indicating the impact of fuel total aromatic content on nvPM emissions relative to a reference fuel.....	168
Figure 5-19 - Normalised correlations indicating the impact of paraffin, cyclo-paraffin, and mono-aromatic content respectively on nvPM emissions relative to a reference fuel.....	169
Figure 5-20 - Normalised correlation using a compound parameter of fuel hydrogen and di-aromatic content [108] on nvPM emissions relative to a reference fuel	171
Figure 5-21 - k_{thermo} and k_{sl} factors across fuels determined for 1.9 bar, condition C	172
Figure 5-22 - Calculated overpredictions in EI _{number} emissions savings (normalised to J-REF) by the exclusion of size-dependant system loss corrections.	173
Figure 5-23 - Combustor exhaust temperature plotted against fuel hydrogen content (left) and specific energy (right).....	174

Figure 5-24 - Specific energy normalised nvPM emissions	174
Figure 5-25 - Predicted equivalent fuel consumptions across fuels, relative to J-REF, normalised for fuel specific energy content (left) and volumetric energy content (right)	176
Figure 5-26 - Impact of pressure vs. loss corrected emissions	177
Figure 5-27: Impact of primary air flow rate on nvPM formation across different fuels tests.....	178
Figure 5-28: Effect of varying the primary air on combustor-exit nvPM EI mass (a), number (b) and measured GMD (c)	178
Figure 5-29 - Effect of varying the fuel flow rate on combustor-exit nvPM EI mass (a), number (b) and measured GMD (c), conditions A vs. C	179
Figure 5-30 - Effect of varying the fuel flow rate on combustor-exit nvPM EI mass (a), number (b) and GMD (c), conditions B vs. D	179
Figure 5-31 - Calculated combustion efficiency across operating conditions ...	180
Figure 5-32 - Combustor-exit nvPM EI mass (a), number (b) and GMD (c), conditions A vs. D.....	181
Figure 5-33: Effect of varying the secondary air on combustor-exit nvPM EI mass (a), number (b) and measured GMD (c)	182
Figure 6-1 - Atomiser I-C operating with water flowrates of a) 10 g/s, b) 20 g/s, c) 30 g/s	186
Figure 6-2 - Atomiser operation during laser diffraction experimentation	187
Figure 6-3 - Measured SMD values vs. air mass flowrate.....	188
Figure 6-4 - Measured SMD values against U_a and measured dP/P	189
Figure 6-5 - Impact of increasing fuel flowrate on SMD	190
Figure 6-6 - PSD Profiles for atomiser I-C operating with 1.6 g/s water and a) 3.0 g/s of air b) 6.0 g/s of air c) 9.0 g/s of air	191
Figure 6-7 - Measured background signal across varying air temperatures	192
Figure 6-8 - Variation in measured SMD across different air preheat temperatures	193
Figure 6-9 - SMD vs. air velocity across different air preheat temperatures	193
Figure 6-10 - Measured SMD values across atomisers vs. values predicted using correlations from the available literature	194
Figure 6-11 - MATLAB linear regression output	195
Figure 6-12 - Measured SMD values vs. derived correlation for all phase I atomisers	197
Figure 6-13 - (Left) variation in predicted SMD values across test fuels for 1.62 g/s liquid flowrate and unheated air using derived correlation. (Right) predicted SMD values across fuels at for the Mk. I combustor at condition C.	198
Figure 6-14 - Transply cooling dome.....	200
Figure 6-15 - The “magic circles” design concept [49]	202
Figure 6-16 - RQL air partitioning.....	203

Figure 6-17 - Render of the Mk. II combustor with atomiser placement	205
Figure 6-18 - GCxGC compositional data for additional test fuels	207
Figure 6-19 - Predicted SMD values for Mk. II combustor operating conditions (B-HE2)	208
Figure 6-20 - Mk. II loss corrected nvPM emissions	209
Figure 6-21 - Predicted combustion efficiency across fuels.....	210
Figure 6-22 - Primary zone nvPM buildup (left) and thermal damage to the liner (right)	212
Figure 7-1 - Measured pressure drops for the phase II atomisers.....	216
Figure 7-2 - Atomiser II-B exhibiting the collapse in spray cone	219
Figure 7-3 - Atomiser I-D operating at 1.6 g/s water with 3.30 g/s air (left) and 3.60 g/s air (right). The instability is resolved at 3.60 g/s air.	220
Figure 7-4 - Measured spray cone angles.....	224
Figure 7-5 - Single frame (above) and thresholded images (below) of atomiser II-E operating with a) water and b) Jet A-1	225
Figure 7-6 - Measured AMD (above) and SMD (below) for water sprays	227
Figure 7-7 - Measured data rates (above) across water spray profiles for atomiser I-C (left) and II-E (right), compared to HSI images from Section 7.2.1	228
Figure 7-8 - WMSMD values vs. mass flowrate across the atomisers	229
Figure 7-9 - WMSMD values across atomisers vs. predicted U_a (left) and dP/P (right)	229
Figure 7-10 - Comparison between average SMD values for atomiser I-C measured using laser diffraction and PDA.....	230
Figure 7-11 - SMD profiles across both atomisers operating with different aviation fuels	231
Figure 7-12 - Measured data rates and validation rates for atomiser I-C operating with Flites Jet A-1 (left) vs. A-HA.....	232
Figure 7-13 - SMD plot across aviation fuels with regions affected by low validation rates.....	233
Figure 7-14 - Averaged WMSMD plots for atomiser I-C (left) and II-E (right) operating with water and aviation fuels	233
Figure 7-15 - Malvern correlation predictions vs. measured PDA values	234
Figure 7-16 - Measured PDA data and correlations derived from linear regression using Equation 2-16. a) atomiser I-C with water, b) atomiser II-E with water, c) atomiser I-C with aviation fuels, d) atomiser II-E with aviation fuels	236
Figure 7-17 - Comparisons of sprays across atomiser I-C (left) and II-E (right) within the combustor confinement space.....	239
Figure 7-18 - Variations in nvPM emissions for reduced atomisation conditions	241
Figure 7-19 - Comparison of nvPM emissions across Mk. II and Mk. II-A experimentation	242
Figure 7-20 - Calculated combustion efficiencies for the Mk. II-A combustor...	243

Figure 7-21 - NvPM deposit and thermal damage observed for the Mk. II-A combustor	244
Figure 7-22 - Normalised emissions datasets across the Mk. I, Mk. II and Mk. II-A experimentation	245
Figure 7-23 - Overprediction of achievable nvPM number reductions for non-loss corrected emissions data vs. fuel hydrogen content	247

List of Tables

Table 3-1 - Gas Analysis Uncertainties	92
Table 3-2 - ARP 1533C Gas Analysis Tool Instrument Coefficients	94
Table 4-1 - Phase I Atomiser Modifications	130
Table 4-2 - Predicted Airflow Partitioning	131
Table 4-3 - Phase II Atomiser Dimensions	136
Table 4-4 - Phase I Atomiser Measurements	140
Table 4-5 - Phase II Atomiser Measurements	141
Table 5-1 - Fuel, air and atmospheric conditions of test matrix	145
Table 5-2 - Fuel Physical Properties	152
Table 5-3 - Coefficients and Quality of Fit for Polynomial Law	164
Table 5-4 - Coefficients and Quality of Fit for Inverse Power Law	166
Table 5-5 - Coefficients and Quality of Fit for Constrained Power Law	166
Table 6-1 - Linear Regression Derived Coefficients for Empirical Atomisation Equations	196
Table 6-2 - Mk. II Combustor Operating Conditions	206
Table 6-3 - General Fuel Properties of Mk. II Test Fuels	207
Table 7-1 - Variability in spray structure across atomisers (all atomisers operating with 1.62 g/s water flowrate)	217
Table 7-2 - Atomiser I-C (Mk. II Combustor) operating at A3.00 F1.37 rotated in 45-degree increments	218
Table 7-3 - Variability across atomisers operating with Flites Jet A-1 at 1.62 g/s fuel flowrate	222
Table 7-4 - Measured Spray Cone Angles	223
Table 7-5 - Regression Coefficients derived for Equation 2-11	237
Table 7-6 - Operating Conditions during Mk II-A Testing	240

List of Equations

Equation 1-1 - ICAO Mass Emission Index	10
Equation 1-2 - ICAO Number Emission Index	10
Equation 2-1 - Chemical Equation for Incomplete Combustion	37
Equation 2-2 - Flame Radiation vs. Hydrogen Content.....	45
Equation 2-3 - Flame Radiation vs. Hydrogen Content and Di-aromatics	45
Equation 2-4 - Reynolds Number (Re)	47
Equation 2-5 - Weber Number (We)	48
Equation 2-6 - Ohnesorge Number (Oh)	49
Equation 2-7 - Arithmetic Mean Diameter (AMD)	51
Equation 2-8 - Sauter Mean Diameter (SMD).....	52
Equation 2-9 - Simple Correlation for Impact of Fuel Physical Properties vs. SMD	58
Equation 2-10 - Generic SMD Correlation (Simplified)	60
Equation 2-11 - Generic SMD Correlation	60
Equation 2-12 - Generic SMD Correlation + Density Corrections.....	60
Equation 2-13 - Rizkhalla et al. Generic SMD Correlation	61
Equation 2-14 - Rizkhalla et al. SMD Correlation	61
Equation 2-15 - Jasuja et al. SMD Correlation	61
Equation 2-16 - El-Shanawany and Lefebvre Generic SMD Correlation	62
Equation 2-17 - El-Shanawany and Lefebvre SMD Correlation	62
Equation 2-18 - El-Shanawany and Lefebvre SMD Correlation (using D_h)	62
Equation 2-19 - Prompt Generic SMD Correlation	63
Equation 2-20 - Prompt SMD Correlation.....	63
Equation 2-21 - Tareq et al. SMD Correlation (Water)	64
Equation 2-22 - Tareq et al. SMD Correlation (Jet A1).....	64
Equation 3-1 - Hydrocarbon Chemical Formula	72
Equation 3-2 - Weighted Hydrogen Content Method (Part 1)	72
Equation 3-3 - Weighted Hydrogen Content Method (Part 2)	73
Equation 3-4 - Weighted MW Method (Part 1)	73
Equation 3-5 - Weighted MW Method (Part 2)	73
Equation 3-6 - Standard Deviation Calculation.....	82
Equation 3-7 - Propagation of Uncertainties (Addition/Subtraction)	83
Equation 3-8 - Propagation of Uncertainties (Multiplication/Division)	83
Equation 3-9 - Thermophoresis Loss Factor Calculation	86
Equation 3-10 - Thermophoretic Loss Corrected EI_{number} Calculation	86

Equation 3-11 - Thermophoretic Loss Corrected EI_{mass} Calculation	86
Equation 3-12 - System Loss Correction Method	88
Equation 3-13 - ENERGY-EI Calculation	91
Equation 3-14 - Specific Energy Corrected Fuel Flowrate Calculation	91
Equation 3-15 - ARP 1533C Gaseous Correction Combustion Equation	93
Equation 3-16 - Carbon Monoxide Emission Index	94
Equation 3-17 - NO _x Emission Index	94
Equation 3-18 - Unburned Hydrocarbons Emission Index	94
Equation 3-19 - Fuel/Air Ratio Calculation	95
Equation 3-20 - Combustion Efficiency Calculation	95
Equation 3-21 - PDA Droplet Velocity Calculation	108
Equation 3-22 - PDA Droplet Size Calculation	109
Equation 3-23 - PDA Relative Refractive Index Calculation	109
Equation 3-24 - Weighted Mean Sauter Mean Diameter (WMSMD).....	110
Equation 4-1 - Calculation of Blockage due to Blade Thickness in Direction of Incident Air	115
Equation 4-2 - Calculation of Swirler Assembly Inlet Area (Accounting for Blade Blockage)	115
Equation 4-3 - Calculation of Turned Swirler Area	115
Equation 4-4 - Air Velocity Estimation	115
Equation 4-5 - Swirl Number (S_n).....	115
Equation 4-6 - Calculation of Total Pressure	120
Equation 4-7 - Benoullis Equation (No Height Change)	120
Equation 4-8 - Effective Area Calculation	121
Equation 4-9 - Pressure Loss Basic Equation.....	123
Equation 4-10 - Propagation of Pressure Loss (Series Elements)	123
Equation 4-11 - Propagation of Pressure Loss (Parallel Elements)	123
Equation 4-12 - Pressure Loss Resistivity Factor (Expansion)	123
Equation 4-13 - Pressure Loss Resistivity Factor (Contraction)	124
Equation 4-14 - Pressure Loss Resistivity Factor (Swirler).....	124
Equation 4-15 - Pressure Loss Resistivity Factor (Swirler).....	125
Equation 4-16 - Partitioned Mass Flowrate Calculation.....	125
Equation 4-17 - Total Pressure Loss Resistivity Factor.....	126
Equation 4-18 - Total Pressure Loss Resistivity Factor (Simplified).....	127
Equation 4-19 - Coefficient of Discharge (C_d)	133
Equation 5-1 - Dynamic Viscosity (ν)	151
Equation 5-2 - COD R^2 Calculation	164

Equation 5-3 - Adjusted R^2 Calculation.....	164
Equation 5-4 - Polynomial Hydrogen Content Trend	164
Equation 5-5 - Inverse Power Hydrogen Content Trend.....	165
Equation 5-6 - Constrained Power Hydrogen Content Trend	166
Equation 6-1 - SMD Correlation Developed using Linear Regression	197
Equation 6-2 - Optimal Ignitor Location Calculation	201
Equation 6-3 - Recirculation Zone Length Calculation	201
Equation 6-4 - Combustor Mass Flow Partitioning Calculation	203

List of Notations

<u>Symbol</u>	<u>Units</u>	<u>Description</u>
A_x	mm ²	Area
AMD, D_{10}	μm	Arithmetic Mean Diameter
AFR	-	Air-to-Fuel Ratio
ALR	-	Air-to-Liquid Ratio
α	-	Atomic H/C Ratio
C_d	-	Coefficient of Discharge
D, d	mm	Diameter
DA	% wt.	Diaromatic Content
DF	-	Dilution Factor
dP/P	%	Pressure Drop
e	MJ/kg	Specific Energy
EI_{mass}	mg/kg	Emissions Index (mass)
EI_{number}	#/kg	Emissions Index (number)
ϕ	-	Equivalence Ratio
ϕ_x	-	Pressure Resistivity Factor
GMD	nm	Geometric Mean Diameter
H_x , %H	% wt.	Hydrogen Content
k_{thermo}	Dimensionless	Thermophoretic loss correction factor
k_{sl}	Dimensionless	Line loss correction factor
K_{sw}	Dimensionless	Blade loss factor
L, L_c	mm	Characteristic Length
λ	m	Wavelength
m, \dot{m}	Kg/s	Mass flowrate
μ	-	Mean value
μ_x	Pa.s	Dynamic Viscosity
M_x	u	Atomic Mass
MW	Kg/mol.	Molecular weight
n	-	Number of data points
n_x	-	Refractive Index
ρ	-	Number of Variables
P	Pa	Pressure
P_T	Pa	Total Pressure

θ, ψ	$^{\circ}$	Angle
θ_c	$^{\circ}$	Cone Angle
q	N/m^2	Dynamic Pressure
q''_{rad}	W/m^2	Flame Radiation Heat Flux
ρ	Kg/m^3	Density
Re	Dimensionless	Reynold Number
σ	-	Standard Deviation
σ_x	N/m	Surface Tension
SMD, D_{32}	μm	Sauter Mean Diameter
S_n	Dimensionless	Swirl Number
t	mm	Film thickness
t_b	mm	Blade thickness
T_x	$^{\circ}C, ^{\circ}K$	Temperature
Oh	Dimensionless	Ohnesorge Number
ν	mm^2/s	Kinematic viscosity
U	m/s	Velocity
We	Dimensionless	Weber Number
WMSMD	μm	Weighted Mean Sauter Mean Diameter
W_t	%wt	Mass Composition

Subscripts

a	Air
C	Carbon
H	Hydrogen
i	Inner
L	Liquid
o	Outer
p	Prefilmer
R	Relative

List of Abbreviations

AM	Additive Manufacture	FID	Flame Ionisation Detection
AMD	Arithmetic Mean Diameter	GC	Gas Chromatography
APC	Advance Particle Counter	GHG	Greenhouse Gas
AFR	Air-to-Fuel Ratio	GMD	Geometric Mean Diameter
ALR	Air-to-Liquid Ratio	GTL	Gas-to-Liquid
ATJ	Alcohol-to-Jet	H₂O	Water
BC	Black Carbon	HEFA	Hydro processed Esters and Fatty Acids
BTL	Biomass-to-Liquid	HSI	High Speed Imaging
CHCJ	Catalytic Hydrothermal Conversion Jet	ICAO	International Civil Aviation Organisation
CO	Carbon Monoxide	LAQ	Local Air Quality
CO₂	Carbon Dioxide	MW	Molecular Weight
CORSIA	Carbon Offsetting and Reduction Scheme for International Aviation	NMR	Nuclear Magnetic Resonance
CPC	Condensation Particle Counter	NO_x	Nitrous Oxides
CTL	Coal-to-Liquid	nvPM	Non-volatile Particulate Matter
DZ	Dilution Zone	PDA	Phase Doppler Anemometry
EC	Elemental Carbon	PSD	Particle Size Distribution
EEP	Engine Exit Plane	QZ	Quench Zone
EI	Emissions Index	RMS	Root Mean Square
RQL	Rich Quench Lean	SAF	Sustainable Aviation Fuel
RZ	Rich Zone		

SLM	Selective Laser Melting	TC	Total Carbon
SMD	Sauter Mean Diameter	UHC	Unburned HydroCarbons
SN	Smoke Number	WMSMD	Weighted Mean Sauter Mean Diameter
SO_x	Sulphur Oxides	VUV	Vacuum UltraViolet

1. Introduction

1.1. Emissions from Aircraft

1.1.1. Overview

Over recent decades, steady growth of the commercial aviation sector has made modern air travel more accessible and widespread than ever. In 2017, 9.56 million European flights (EU-28+EFTA countries) were recorded [3], with passenger air traffic expected to increase at a steady rate of 3.7-5% per annum as a result of population and economic growth [4]-[7]. Most modern aircraft are powered by gas turbine engines, which utilise the thermal energy produced by combustion of aviation kerosene fuels refined from crude oil. Currently, the most widely consumed fuels in commercial aviation are Jet A-1 and Jet-A; Jet A-1 being the most used fuel in European flights and Jet-A the most used in US flights [8]. Jet A-1 and Jet A are very similar in composition and manufacturing origins, with the only significant differences being a slightly lower freezing point for Jet A-1 (-47°C for Jet A-1 compared to -40°C for Jet A), as well as the inclusion of an anti-static agent. These similarities mean that both fuels are regulated under the ASTM D1655 standard [9]. Other aviation fuels used on a large scale globally include JP-8 and JP-5 used by the US military, TS-1 and RT fuels used primarily in Russia, and RP-3 used in China [10].

In 2016, global aviation was found to be responsible for approximately 5.8% of the world's oil consumption, consuming the equivalent of 5 million barrels a day [10]. Pre-COVID predictions suggested that the increase in flights would lead to an increase in fuel consumption for international flights (making up approximately 65% of global aviation) to 2.4-3.8 times that of 2015 levels by 2050 [11]. Unfortunately, conventional aviation fuels present significant drawbacks which limit their suitability for continued use in the long-term. Healthy energy systems are expected to perform highly in all three categories of the energy trilemma index (*Figure 1-1*), which considers energy equity (reliability, affordability, and abundance), security of supply, and environmental sustainability of an energy system [12]. Conventional aviation fuels perform poorly in terms of security of supply and environmental sustainability. Global crude oil reserves are finite, with many developed countries heavily reliant on importation

from other countries to maintain security of supply. Also, emissions from aircraft have a number of negative CO₂ and non-CO₂ effects, affecting the Local Air Quality (LAQ) and human health in areas of high air traffic (e.g., near airports), as well as the global environment.

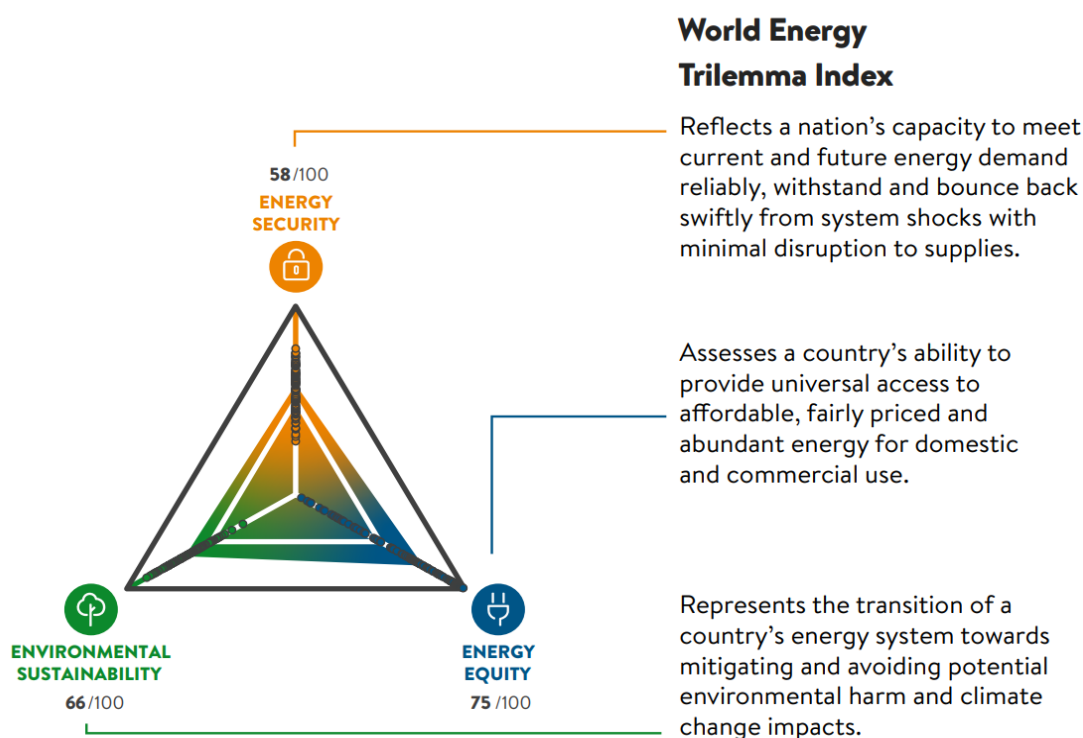


Figure 1-1 - World energy trilemma index [12]

Harmful emissions are invariably produced by the combustion of conventional hydrocarbon fuels refined from crude oil. During the ideal combustion of jet fuel, only Carbon Dioxide (CO₂) and water vapour (H₂O) are produced. In real world engines however, additional pollutants are formed, namely Carbon Monoxide (CO), Nitrous Oxides (NO_x), Sulphur Oxides (SO_x), Unburnt Hydro-Carbons (UHC), and Particulate Matter (PM) [3]. A representation of typical quantities of aircraft emissions produced by an aircraft engine is shown in **Figure 1-2**. These emissions are harmful to human health and result in a number of effects to the atmosphere at high altitudes (near the stratosphere), including the formation of cloud cirrus contrails and ozone [7], [10]. When including non-CO₂ effects, global aviation is believed to account for ~5% of total anthropogenic climate change [7].

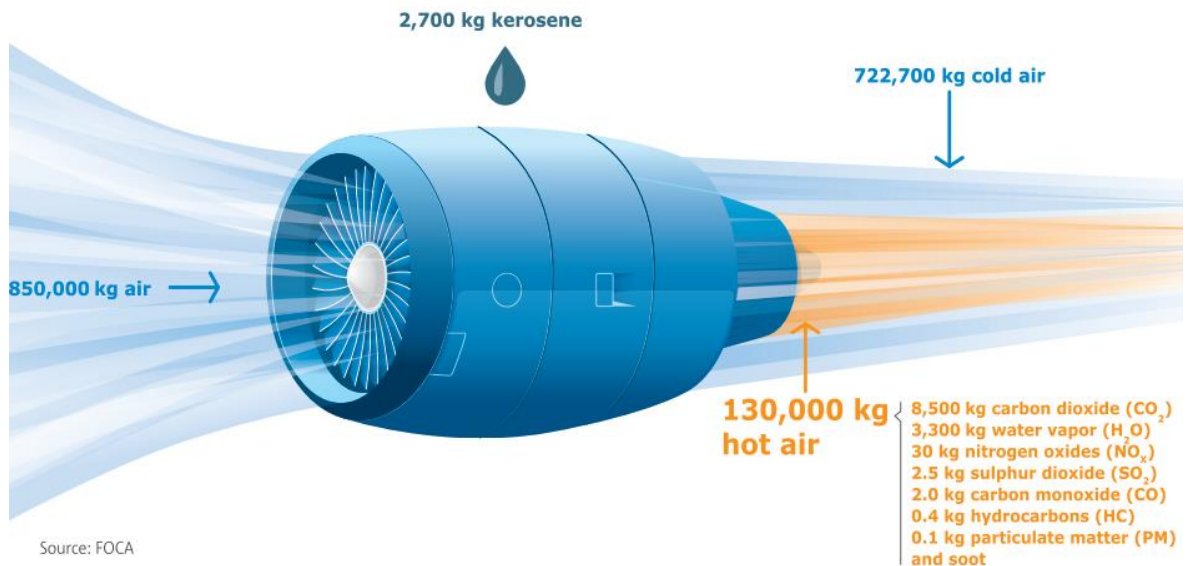


Figure 1-2 - Emissions production from a typical two engine aircraft (representative 150 passengers) over a 1 hour flight [3]

1.1.2. CO₂ Emissions

Undoubtedly the most widely documented harmful emission from human activity is CO₂. CO₂ is a Greenhouse Gas (GHG) with a well understood impact on the environment and is known to be the primary pollutant responsible for the post-industrial global warming effect. The civil aviation sector is currently responsible for approximately 2-3% of CO₂ emissions, and this value is expected to rise with the predicted growth of aviation in upcoming decades, as well as making up a greater proportion of total emissions as other sectors decarbonise [7]. In 2017, CO₂ emissions from global aviation were recorded at 973 Mt, further increasing to a peak of 1027 Mt by 2019 [13]. European data suggests that flights in EU28 and EFTA countries alone were responsible for approximately 160 Mt of CO₂ in 2017, representing 3.8% of total EU CO₂ emissions and 13.9% of those from transport [3], [14].

Although the recent COVID-19 pandemic significantly reduced air travel, subsequently reducing global CO₂ emissions from aviation by approximately a third, this effect is anticipated to only be temporary and emissions trends will most likely normalise to those witnessed prior to the pandemic without suitable reduction measures [7]. Pre-COVID, net CO₂ emissions from aviation were anticipated to steadily rise at around 3-4% per year with the expected increase in aviation [15]. As a direct product of combustion, CO₂ emissions from aircraft burning conventional fuels are inevitable and can only be mitigated by reducing

fuel consumption, achieved either by reducing the total number of flights or by incorporating more fuel-efficient aircraft burning less fuel per passenger km (increased fuel efficiency).

1.1.3. Non-CO₂ Gaseous Emissions

The combustion of aviation fuels also leads to the production of Nitrous Oxides (NO and NO₂, referred to as NO_x) and Sulphur Oxides (SO_x). Of the two, NO_x emissions present a much greater concern in the context of the climate impacts from aviation, and are formed in much higher quantities than SO_x emissions, which are produced in small quantities due to the oxidation of fuel bound sulphur as a carryover from crude oil refinement. NO_x emissions can form via several mechanisms, but the majority of aircraft NO_x forms in high temperature regions of combustion (above 1800 K) via the thermal (Zeldovich) mechanism [16]. International aviation was found to be responsible for 2.50 Mt of NO_x emissions in 2015, and is expected to grow to 2.2-3.3 times this value by 2040 [3].

Both NO_x and SO_x can mix with the water held by clouds to produce acid rain which has damaging effects on wildlife and vegetation, and corrodes building materials. In addition, NO_x emissions emitted at low altitudes act as a catalyst for the generation of ground-level ozone which can cause respiratory problems and act as a precursor to photochemical smog. Meanwhile, NO_x emissions generated at higher altitudes near the stratosphere have been linked to the depletion of the upper ozone layer, which plays a critical role in blocking harmful UV radiation responsible for causing skin cancers [17].

Generally, aircraft gas turbines exhibit very high combustion efficiencies (conversion of fuel chemical energy into thermal energy) at above 99.9% for most engine conditions, with slightly lower efficiencies of 98-99.5% at low power conditions [18]. Reduced combustion efficiency leads to the production of both CO and UHC, as products of the incomplete combustion. In aircraft combustors, CO formation can occur in fuel rich zones of poor mixing where lack of oxygen and inadequate burning rates prevent the complete oxidation of carbon atoms to CO₂. CO has the effect of inhibiting red blood cells from transporting oxygen around the body, which is lethal to humans in high enough concentrations. Similarly, UHC is witnessed at low combustion efficiencies where fuel does not fully combust

before being emitted to the atmosphere. Rink and Lefebvre [19] state that UHC fractions are composed of unburned fuel droplets and products of fuel thermal degradation, and are typically an indication of inadequate spray quality. UHC compounds can combine with ground-level NO_x to form photochemical smog, and are also toxic in themselves [16].

1.1.4. Particulate Matter

Alongside gaseous emissions, aircraft engines are sources of Particulate Matter (PM). These are predominantly solid, non-volatile particles composed of mostly carbon, with small amounts of other compounds such as hydrogen, oxygen, and trace elements [16]. In addition to non-volatiles, volatile constituents from condensed gaseous emissions are also witnessed, either forming separate particulates or coating the non-volatile, purely carbonaceous particles [20]. Aircraft particulates are ultrafine (<100 nm diameter), with a typical range of Geometric Mean Diameters (GMD) between 20-45 nm having been previously observed [21]. Example images of aircraft particulates emitted from a modern gas turbine engine are presented below in *Figure 1-3*.

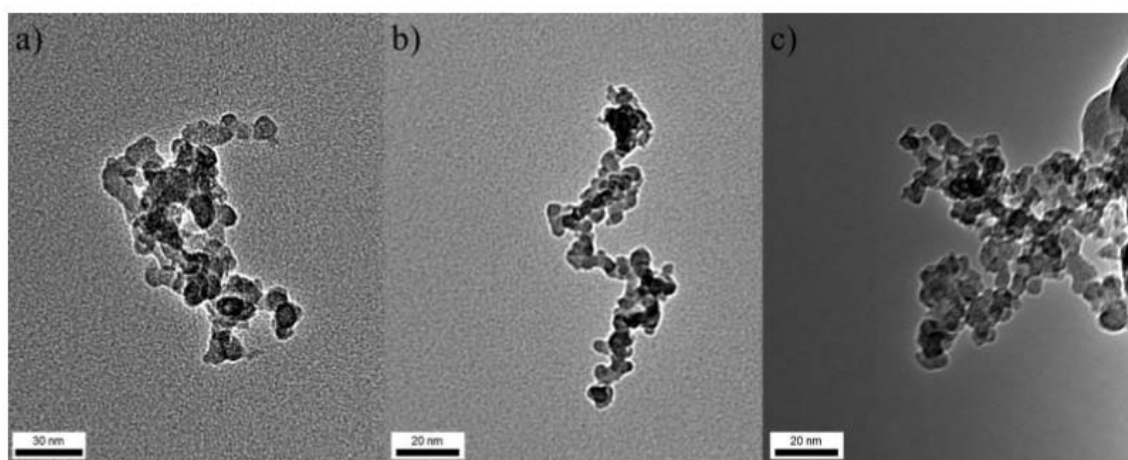


Figure 1-3 - Transmission Electron Microscopy (TEM) imaging of typical aircraft nvPM agglomerate structures [22]

The definition and naming conventions used in PM characterisation may vary depending on the field of study and primary concern in which the research aims to address, as well as the instrumentation used. Unfortunately, this can lead to confusion for those unfamiliar with the terminology and/or intercomparison of studies. Additionally, it is important to note that differences between the classification of carbon and measurable quantities can also introduce uncertainty

across studies. In many combustion studies, non-volatile aircraft particulates are referred to as soot, though this is perhaps a somewhat loose term referring to carbon particles produced during combustion of fuels. Meanwhile, air quality aerosol studies typically use metrics for quantities of measurable carbon from thermo-optical analyses, which separate Total Carbon (TC) emissions into Elemental/Black Carbon (EC/BC) and Organic Carbon (OC). In this classification, EC is considered as the non-volatile fraction composed of black, graphitic carbon structures, while OC refers to any other carbon present found usually as compounds with other elements such as condensed hydrocarbon vapours, and which volatilise in an inert high temperature environment [23]. The term now preferred in aircraft aviation standards is non-volatile Particulate Matter (nvPM), defined in by the International Civil Aviation Organisation (ICAO) Annex 16 standard as solid, non-volatile carbon components of aircraft PM which do not volatilise above temperatures of 350°C [24].

NvPM has numerous harmful effects making it an undesirable emission from aircraft. Within combustors themselves, nvPM particles transfer thermal radiation which can damage combustor components and reduce engine operational lifespans [16], [25]. NvPM also reduces the Local Air Quality (LAQ) of areas with high air traffic such as near airports, and negatively affects the global environment [6], [10]. The small size of aircraft particulates places them within the PM_{2.5} category, referring to particles with diameters less than 2.5 µm, which pose the greatest concern to human health (*Figure 1-4*). Particles of this size are small enough to be absorbed through the natural barriers of the lung linings and into the bloodstream, and are linked to increased hospital admissions and mortality rates [26]. Short term exposure to aircraft particulates can cause breathing difficulties in those with pre-existing respiratory conditions (e.g. asthma), the very young, or the elderly [26]. Long term exposure is linked to an increase in cardiovascular and respiratory diseases, including lung cancer [26]-[29]. Of the 16,000 premature deaths attributed to aviation, nearly 14,000 (87%) are estimated to be caused by aircraft PM emissions [30].

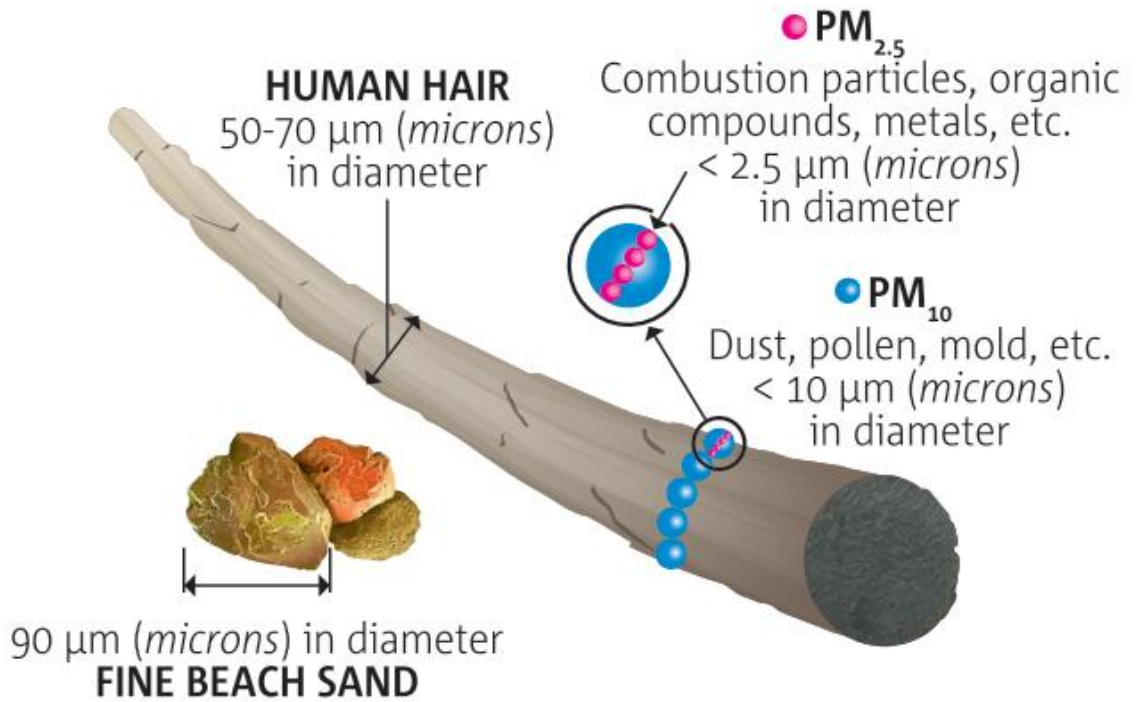


Figure 1-4 - Visualisation of PM sizes [3]

Aircraft nvPM emissions also exhibit both local and global warming effects. The absorption of thermal radiation by airborne nvPM causes a regional warming of the air. NvPM deposited onto polar ice caps increases heat absorption of ice caps and diminishes their ability to reflect sunlight through a phenomenon called the albedo effect, leading to increased heat absorption and melting rates [31], [32]. NvPM emitted at high altitudes acts as sites for water absorption and the nucleation of cirrus cloud contrails [33], shown in **Figure 1-5**.



Figure 1-5 - Research aircraft producing cirrus cloud contrails [34]

Contrails form in the wake of aircraft as visible plumes, which reflect sunlight and infrared radiation. The formation mechanisms of contrails and their exact impact on the environment is currently not well understood and subject to ongoing research. Depending on humidity conditions and time of day, they may

have either a cooling or warming effect on the local climate of an area, but are believed to have a net positive effect on global radiative forcing, leading to an overall warming effect [35]. Recent evidence suggests that the total radiative forcing impact of aircraft contrails may be equal to or greater than that of CO₂ [33], [36], [37], and could account for 3% of the total anthropogenic radiative forcing [15]. The contributions of various emissions from aviation to radiative forcing are shown in **Figure 1-6**.

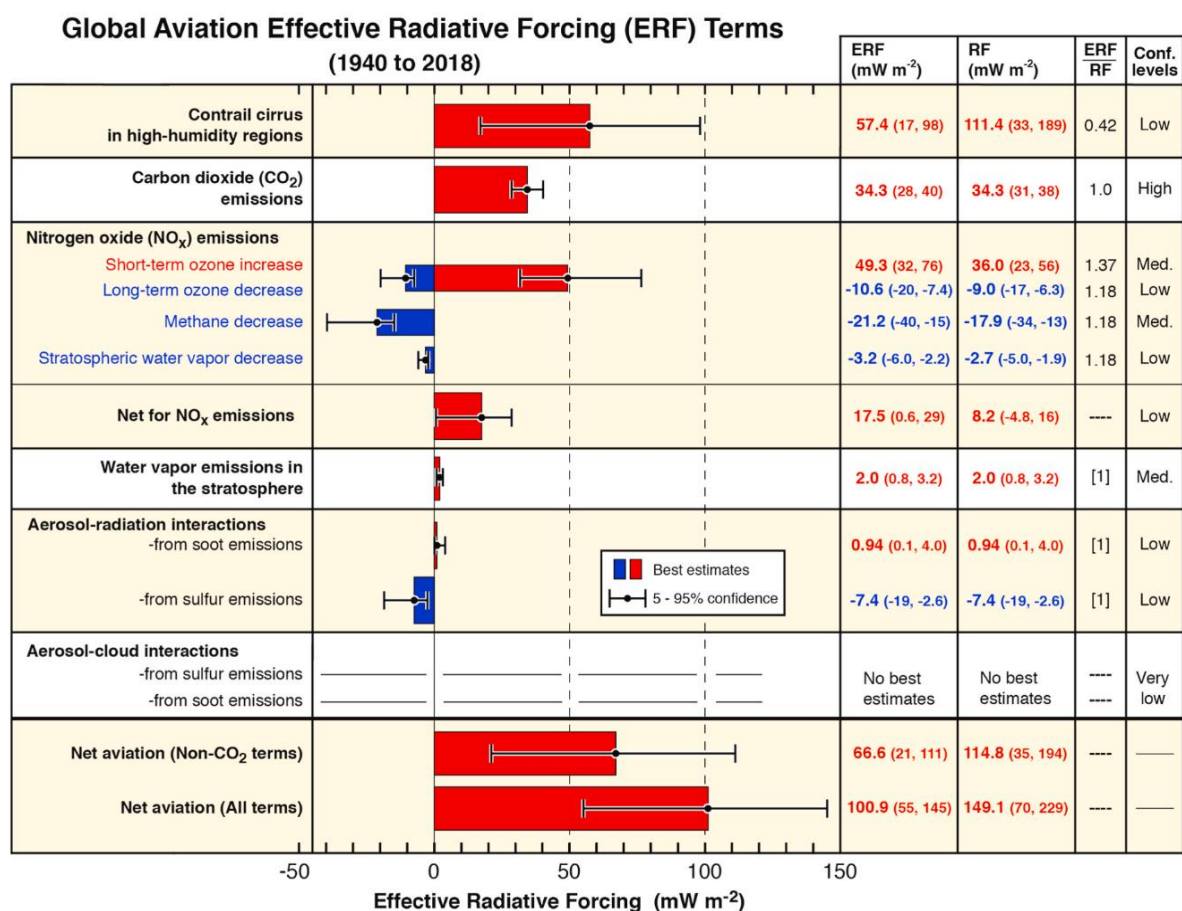


Figure 1-6 - Impact of various emissions on radiative forcing up to 2018 [35]

1.2. Regulations Concerning Aircraft Emissions

The consequences of harmful emissions from aircraft will prove a continually prevalent issue unless suitable measures and developments to the aviation sector are implemented. The reduction of greenhouse gas emissions and radiative forcing is critical in reducing the warming of the planet in accordance with the primary aim of the Paris Agreement and COP26 Glasgow Climate Pact in keeping global temperature increases below 1.5°C compared to pre-industrial levels [38]. Current goals for European aviation are outlined in the European

Commission Flightpath 2050 document, which specifies emissions reductions of 75% for CO₂ and 90% for NO_x compared to 2000 levels [39].

Although operation of local air traffic is controlled nationally, there are currently 193 national governments (including the UK and much of the developed world) committed to the regulatory standards outlined by the ICAO, a funded agency of the United Nations [40]. In order to tackle CO₂ emissions from aviation, the ICAO devised the Carbon Offsetting and Reduction Scheme for International Aviation (CORSIA), setting a series of targets to ensure carbon neutral growth of international aviation post-2020 [11]. This includes the development of more efficient aircraft and the adoption of Sustainable Aviation Fuel (SAF). An aspirational goal of 2% per annum improvement to aircraft fuel efficiencies up to 2050 has been highlighted, determined through efficiency improvements to both aircraft technologies and operations [11]. The UK government has also proposed its own targets in 2021 towards decarbonising the aviation sector under the Jet zero strategy, including carbon neutral growth up to 2050 and a 78% reduction in CO₂ emissions by 2035 compared to 1990 levels [41].

Regarding non-CO₂ emissions from aviation, the standardised reporting of fuel venting, smoke and gaseous (UHC, CO and NO_x) emissions produced by commercial aircraft has been outlined by the ICAO Annex 16 Volume II document for environmental protection since 1981, and amended following the meetings of the Committee of Aviation Environmental Protection (CAEP) [24]. The latest update (4th edition) was undertaken in 2018 following the 10th meeting (CAEP/10) held in February 2016, and has introduced more stringent regulations towards aircraft emissions. Historically, regulation of PM from aircraft by the ICAO was achieved using smoke number (SN) measurements, as outlined in the ARP1179 protocol [42]. SN measurements were introduced in 1981 as optical measurements of exhaust plume visibility, but are not representative of nvPM [43]. More recently, aircraft regulations concerning particulates are based around a standardised nvPM measurement protocol, introduced following the CAEP/10 meeting [20], [44], [45]. The subsequent CAEP/11 meeting agreed on the removal of smoke number as regulatory parameter for aircraft, and will see the standardised reporting of nvPM mass and number emissions taking effect for aircraft >26.7 kN from the 1st of January 2023 [20], [45].

ICAO standards now prescribe a sampling and measurement system for the collection and measurement of aircraft nvPM emissions, outlined by the Annex 16 Volume II document [24] and ARP 6320 [46]. This consists of a suitable sampling probe for the collection of engine exhaust, which is transferred to the relevant measurement instrumentation through a series of flowlines, all of which are maintained at specified ambient conditions by careful monitoring at various points. The measurement section includes instrumentation for the measurement of nvPM mass and number, and CO₂ for subsequent data processing. Further details will be provided on the sampling system used during this project in **Section 3.3.2**. A diagram of the necessary components used in a suitable sampling system is shown in **Figure 1-7**.

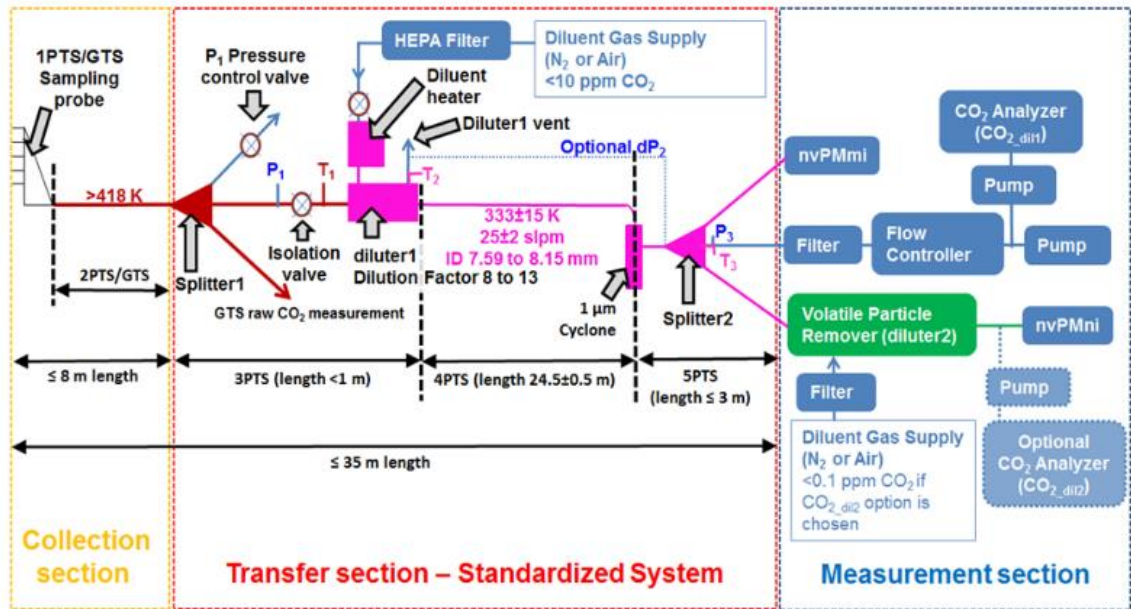


Figure 1-7 - ICAO compliant measurement setup [24]

Standard metrics for the presentation of nvPM emissions data from aircraft, as outlined by the ICAO, are Emissions Indices (EI), determined either by mass (EI_{mass}) or number (EI_{number}) [24]. Measured nvPM concentration values output by measurement instrumentation are converted into normalised values of nvPM produced per kg of fuel burned, as shown in **Equations 1-1 and 1-2**.

$$EI_{\text{mass}} [g/kg_{\text{fuel}}] = \frac{\text{nvPM}_{\text{mass-STP}} \times 22.4 \times 10^{-6}}{CO_{2\text{dil}} \times (M_C + \alpha \times M_H)} \quad 1-1$$

$$EI_{\text{number}} [\#/kg_{\text{fuel}}] = \frac{\text{nvPM}_{\text{num-STP}} \times DF_2 \times 22.4 \times 10^6}{CO_{2\text{dil}} \times (M_C + \alpha \times M_H)} \quad 1-2$$

1.3. Reducing Emissions through Developments in Aircraft Gas Turbine Technologies

1.3.1. Gas Turbine Design

Aircraft fuel efficiencies (fuel burn per passenger km) have benefited from gradually improving technologies since the beginning of international aviation. In the near term (circa 2035), reductions in aircraft fuel efficiency are expected from “*evolutionary technology*” improvements to existing aircraft designs, as highlighted by the IATA Aircraft Technology Roadmap to 2050 [4]. These are anticipated to yield a further 25-30% improvement to fuel efficiencies, before the introduction of longer-term “*revolutionary technologies*” and radically different aircraft designs move aviation beyond the limits of traditional tube-and-wing aircraft. Evolutionary technologies include improved airframe aerodynamics, reduction of mechanical losses, increased implementation of electronic system components, and improvement of engine designs. This last area has been continually undertaken by engine manufacturers over the many years since the introduction of the first jet airliners through a process of iterative refinement.

Simplistically, an aircraft gas turbine engine can be separated into four main sections: 1) a compressor section, 2) a combustion chamber section, 3) a turbine section, and 4) an outlet nozzle. Inlet air used for combustion is pressurised in the compressor section and fed into one or more combustion chambers, within which fuel is mixed in and combustion is initiated. The resultant expanding gases are used to drive a series of turbines before exhausting into the atmosphere at accelerated speeds. Most large commercial aircraft are operated using high-bypass turbofan engines, which generate additional thrust from cold bypass air driven by a large, powered fan and partitioned away from the combustion itself. These engines exhibit very good fuel efficiencies and low noise [6]. A Rolls Royce Trent 1000 high bypass (10:1) turbofan engine, widely used in commercial aviation, is shown in **Figure 1-8**.

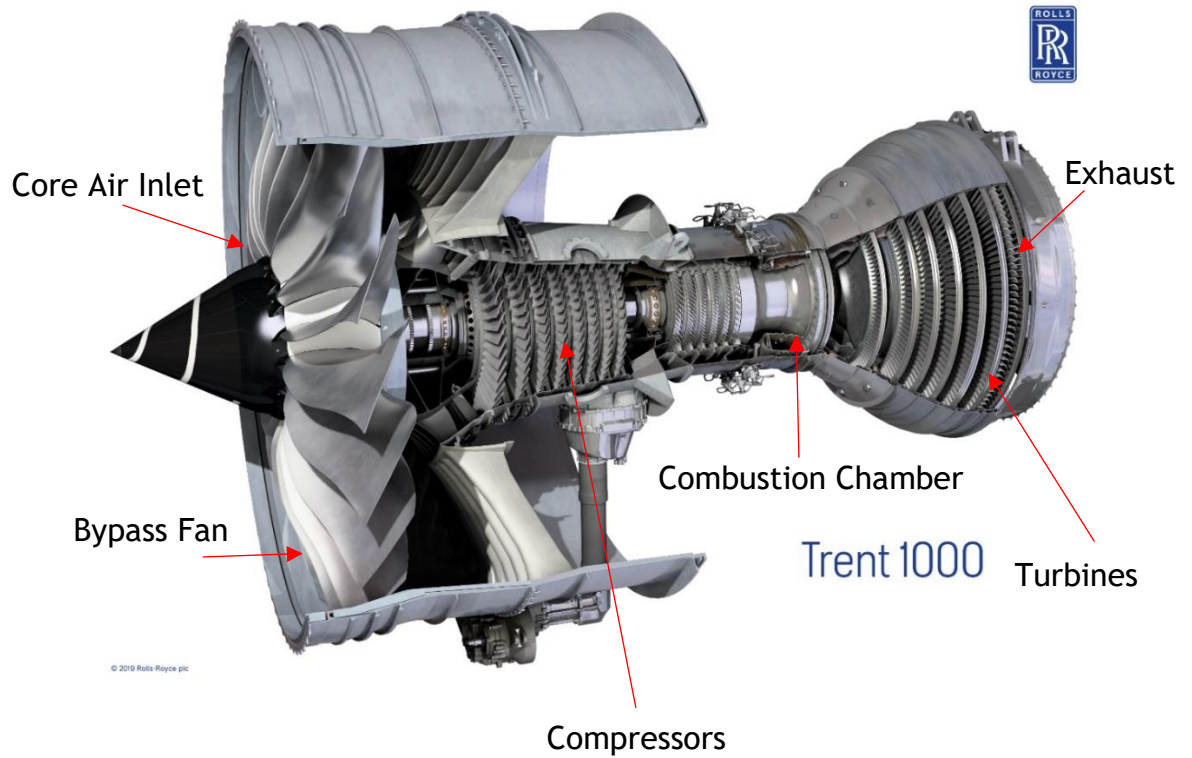


Figure 1-8 - Rolls Royce Trent 1000 turbofan engine [47]

The combustion reactions necessary for operation of the engine occur within the combustor section, which acts as an enclosed space in which liquid fuel and air is mixed and ignited at elevated temperatures and pressures. Evolving engine designs since the earliest jet engines adopted steadily increasing operating pressures and inlet temperatures in order to maximise their combustion efficiencies [16]. It is known that a maximum threshold to which combustion efficiencies can be improved by increased temperatures and pressures exists, and given that aircraft engine efficiencies are so high already, any improvements would not yield the aforementioned target 2% annual reductions in aircraft fuel consumption. As such, manufactures employ other methods of improving engine fuel efficiencies, such as incorporation of lighter materials, improved aerodynamics through the engine, and higher bypass ratios [4]. For example, the Rolls Royce *UltraFan* engine achieves a very high bypass ratio using lightweight composite fan blade materials and a 64 MW power gearbox, alongside a highly efficient lean burn combustor and compression section operating at a 70:1 pressure ratio, allowing for 25% improvements to overall fuel efficiency compared to first-generation Trent engines, as well as, reduced NOx emissions, nvPM emissions, and noise. [4], [48].

Most modern aircraft engines utilise annular arrangements, although tubular (“can”) or tuboannular arrangements may also be found in small engines or older large engines [16]. A schematic representation of a typical can-type gas turbine combustor is shown in **Figure 1-9**.

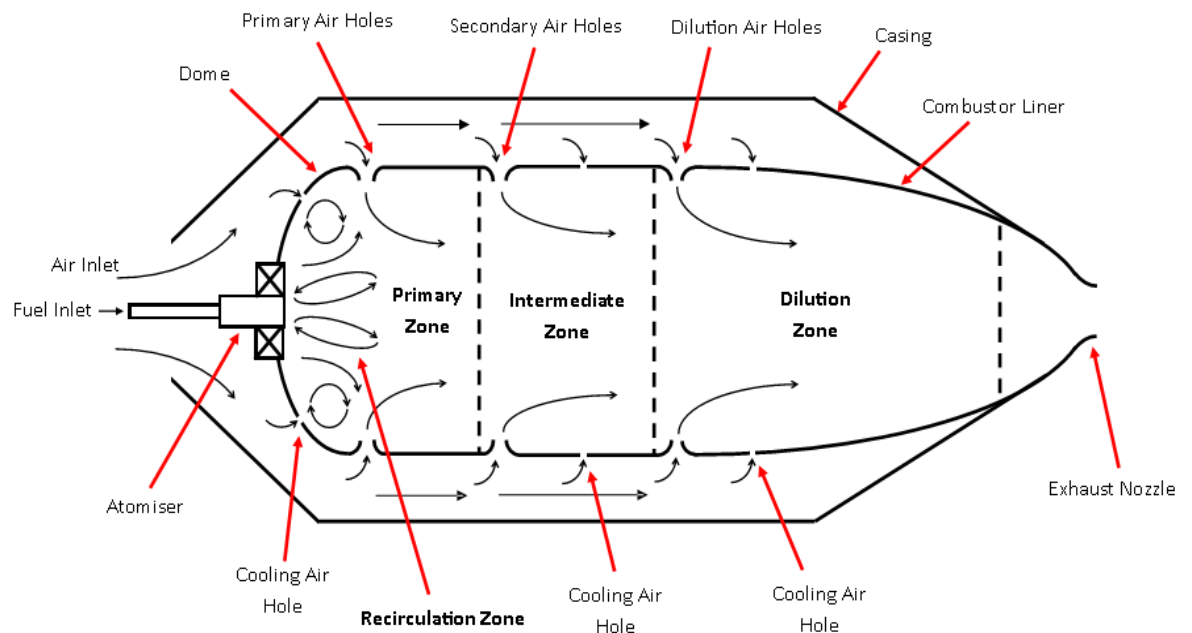


Figure 1-9 - A typical gas turbine combustor

In combustors of this type, liquid fuel is introduced into a combustion liner by a fuel atomiser, which serves to break up bulk fuel into smaller droplets. This is followed by a period of evaporation, which is enhanced by elevated fuel preheat temperatures. Meanwhile, pressurised air from the compressor is fed to the liner from a single source and partitioned at various points. The majority of air first passes into an outer annulus between the casing and combustor liner, and is then driven by the resultant pressure differential through a series of air holes and into the liner. The evaporated fuel is mixed with combustion air fed through the quench holes and ignited. This region is normally referred to as the primary combustion zone. Within this region, a recirculation zone is established imparting a degree of swirl onto the air, achieved using swirlers within the atomiser itself or additional air swirlers placed circumferentially on the outside of the atomiser.

The recirculation zone promotes the mixing of hot burned gases with unburned reactants and helps to provide the necessary residence time for complete combustion of the reactants in the flame. This ensures continued combustion and high combustion efficiencies, while also anchoring the resultant

flame to an established region within the combustor [16], [49]. A curved dome is often employed to allow for a smooth increase in cross sectional area and to reduce pockets in which additional recirculation zones can form, which have been known to cause soot deposits [25]. The primary zone is then followed by the intermediate and dilution zones in which additional air is provided through the liner, ensuring complete combustion of the fuel by the engine exit. Cooling air holes or slots may also be employed at different points in the combustion liner to reduce surface temperatures through convective film cooling. This helps to decrease thermal stresses on the liner and increase combustor lifespans. The burned gases are finally released through an exhaust nozzle, typically with a reduced cross-sectional area to accelerate the gases. The expansion of the exhaust gases as a result of fuel thermal energy release during combustion provides the aircraft thrust, and is also used to drive the turbines in turbofan engines.

1.3.2. The RQL Methodology

Aircraft emissions are primarily dependent on the flame characteristics within combustors, and vary with combustor operating conditions such flame temperature, pressure, local equivalence ratios, and power output. Increasing engine power normally correlates to an increase in flame temperature due to the additional heat release from higher fuel flows, and increases in operating pressure as the compressor stage spins faster. Low power conditions (e.g. idle) are associated with increased CO and UHC emissions, while higher power conditions are associated with higher NO_x and nvPM, as is shown in *Figure 1-11*.

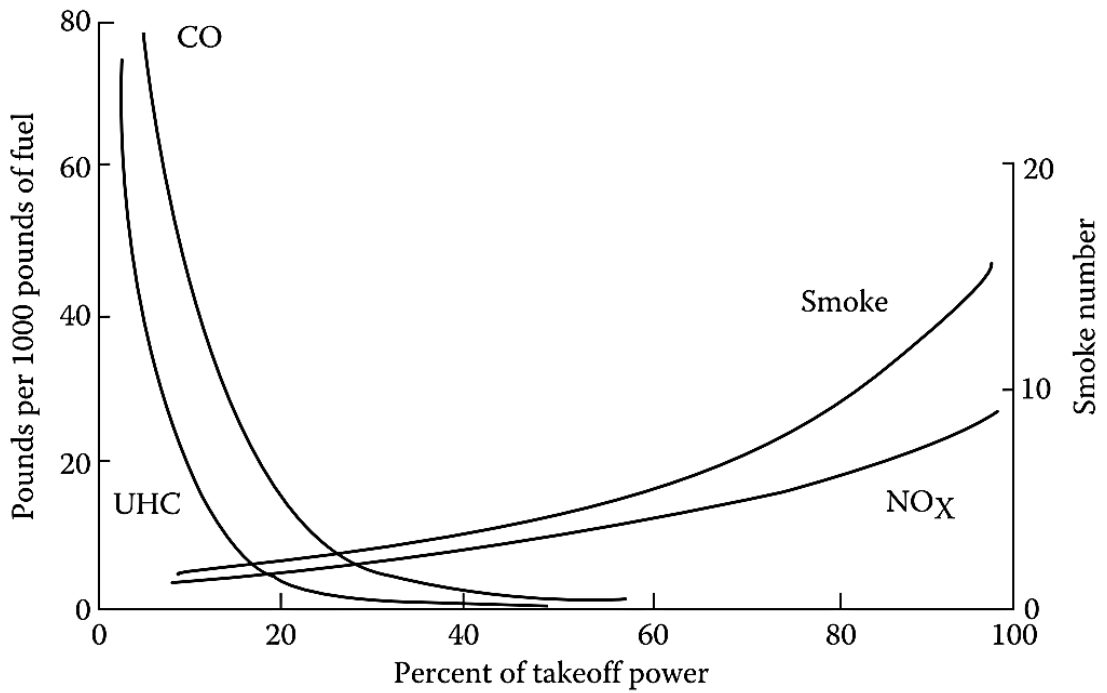


Figure 1-10 - Emissions dependence on engine operating conditions [16]

CO and UHC emissions form at low power conditions as a result of reduced flame temperatures (<1670 K) leading to slower fuel evaporation and reduced chemical kinetic reaction rates, which prevent the conversion of fuel and air into CO₂ and result in lower combustion efficiencies (as mentioned in **Section 1.1.2**). Meanwhile NO_x production is encouraged by higher flame temperatures (>1900 K) through the thermal NO_x mechanism. As such, low gaseous emissions may be achieved by maintaining flame temperatures within the 1670-1900 K range, as is represented in **Figure 1-11**.

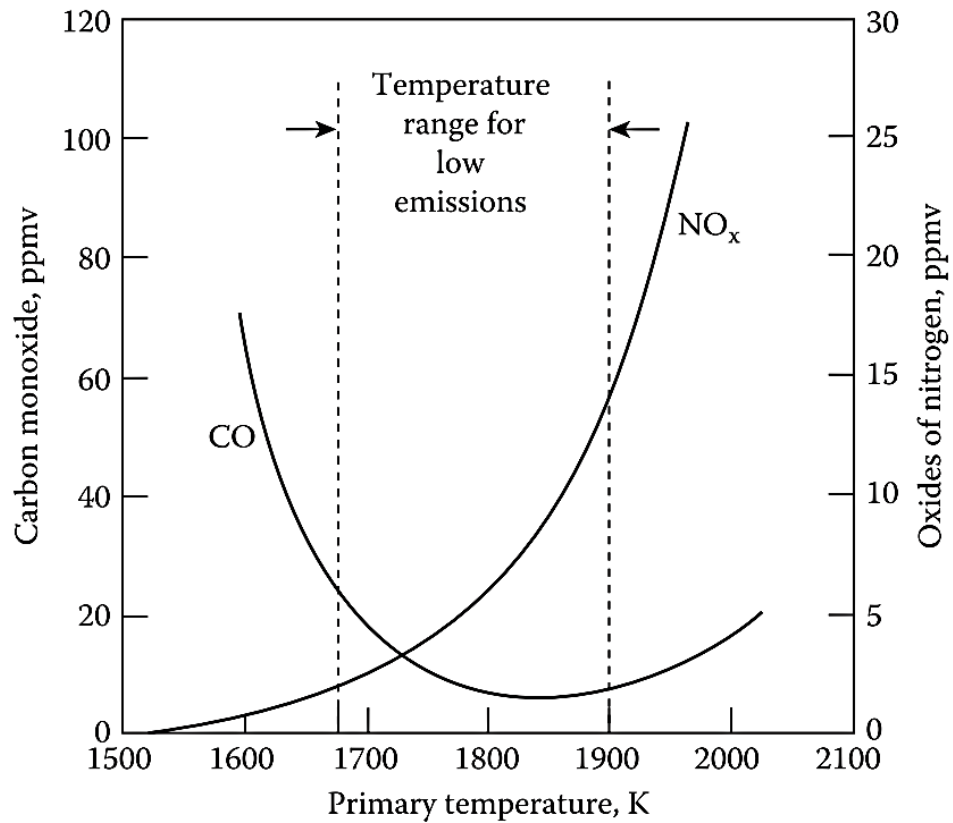


Figure 1-11 - Variability of NO_x and CO production with flame temperature [16]

Historically, early combustors operated with flame equivalence ratios in a narrow range near stoichiometry, which was beneficial for combustion efficiency but also led to high operating temperatures and NO_x formation. In order to mitigate concerns surrounding NO_x, a number of low-emission combustion chamber technologies have been developed and are employed in most modern aircraft engines. These include the Rich-Burn, Quick-Quench, Lean-Burn concept (RQL), and lean burn concepts [16], [50], [51]. Most in-production engines utilise the well-established RQL concept, including the Rolls Royce Phase 5 combustor for the Trent series engines, the TALON series combustor in Pratt and Whitney engines, and in GE Low Emissions Combustor (LEC) used in CF34 engines [52]. The key operating principle of the RQL methodology is to utilise staged combustion from careful partitioning of airflows, so as to separate the combustion process into three distinct regions: Rich-Burn, Quick-Quench and Lean-Burn, analogous to the primary, secondary and dilution zones outlined in *Section 1.3.1*. An example of the equivalence ratios used in an RQL combustor is shown in *Figure 1-12*.

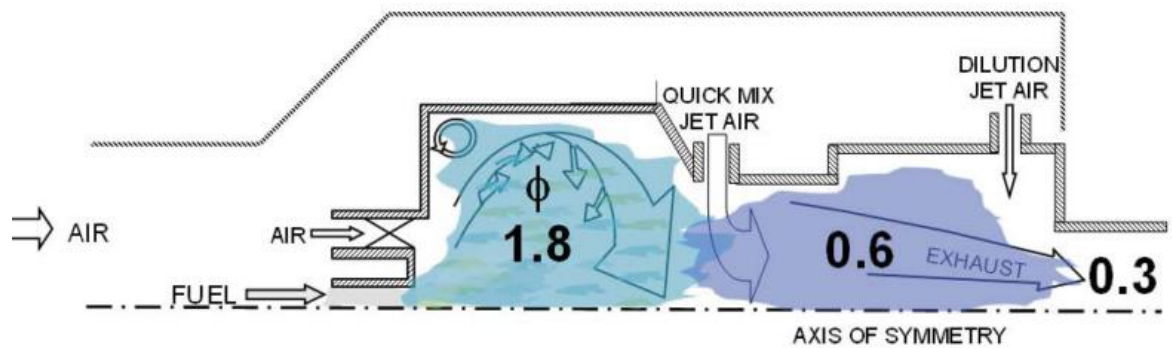


Figure 1-12 - Representation of an RQL Combustor with typical equivalence ratios [53]

RQL combustors achieve low NO_x emissions by limiting the residence time of combustion at equivalence ratios near stoichiometry, where the highest rates of heat release occur. Fuel and air enter the primary zone at a high equivalence ratios (typically between 1.2-1.8) [16], [53]. This results in a cooler flame with reduced rates of thermal NO_x formation, while also providing good combustion stability due to high rates of hydrogen and hydrocarbon radicals produced by the rich combustion, which is desirable in aviation [52]. However, because rich primary combustion typically leads to higher formation rates of nvPM and other incomplete combustion products, the resultant combustion gases exiting the primary zone must be treated in the subsequent Quick-Quench and Lean-Burn combustion zones, in which the combustion equivalence ratio is rapidly lowered to well below stoichiometry (~0.3) using large volumes of additional air. By rapidly reducing the equivalence ratio between these two extremes of equivalence ratio, the residence time of the combustion near stoichiometry where flame temperature (and thus thermal NO_x generation) is minimised. This is represented graphically in **Figure 1-13** as a “low NO_x route” from high to low equivalence ratio across the combustor length, contrasted against a “high NO_x route” formed by allowing a longer residence time of the combustion near stoichiometry.

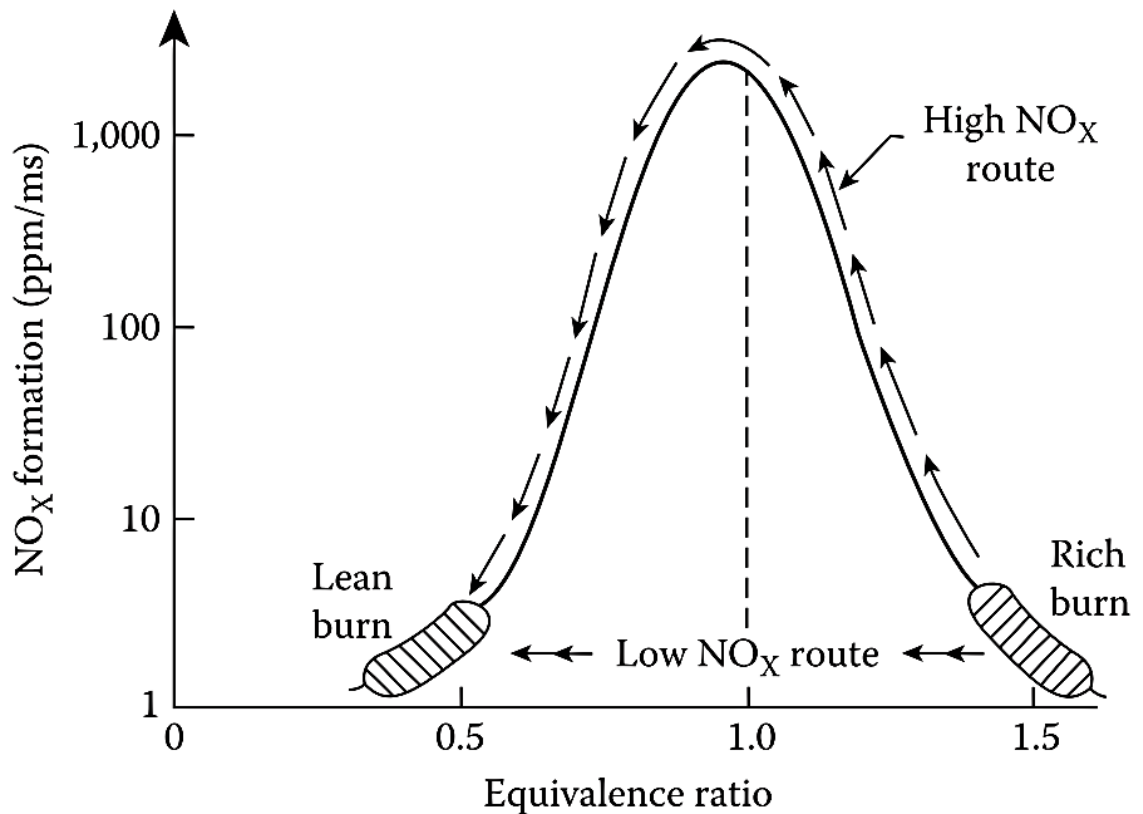


Figure 1-13 - NO_x emissions profile vs equivalence ratio - [16]

1.3.3. Concerns with nvPM Emissions from RQL Combustors

Controlling nvPM emissions is somewhat more complicated than gaseous emissions. Local equivalence ratios are an essential factor in nvPM emissions produced by aircraft combustors. The majority of nvPM formation occurs in the combustor primary zone near the atomiser fuel spray, where the recirculation of fuel and oxygen deficient burned gases leads to local pockets of high temperature, fuel-rich combustion [16], [25]. These pockets of fuel rich combustion greatly accelerate nvPM formation reactions, such that a simplistic model considers all nvPM formation to be isolated to the primary zone. The addition of air and lowering of the local equivalence ratio in later region cause a portion of the nvPM to be consumed through oxidation reactions. Additional detail on the mechanisms of nvPM formation and oxidation are detailed further in subsequent sections (**Section 2.3.1**). Alongside dependencies on equivalence ratio, nvPM emissions are always worsened by increased operating pressures, which is why worsened nvPM emissions are typically observed at higher engine power conditions [16]. Also, higher temperatures in the primary zone can speed up the chemical reactions

responsible for nvPM formation, while higher temperatures in later regions can promote particle oxidation and burnout.

While RQL designs have helped to drastically reduce NO_x emissions, they tend to be prone to nvPM formation due to the especially rich combustion found in their primary zones [52]. Increasing concern surrounding the negative effects of nvPM has led to the development of alternative combustor technologies for low NO_x and nvPM, most notably lean burn technologies. Lean burn combustors, such as Lean Premixed Prevaporised (LPP) and Lean Direct Injection (LDI) combustors, utilise overall lean combustion in their primary zones to maintain a cool (<1900 K) flame temperature for low NO_x production, while also inhibiting nvPM formation due to the absence of rich combustion. A successful lean burn combustor design, currently used in both the General Electric LEAP and GenX engines, is the CFM International Twin Annular Premixing Swirler (TAPS) combustor concept, which utilises partially premixed lean combustion. The absence of rich combustion affords typical reductions in nvPM emissions an order of magnitude lower for lean burn technologies than most RQL designs [52]. This is especially favourable with recent updates in the regulation of nvPM emissions (*Section 1.2*) and it is likely that these technologies will see continued implementation in upcoming years.

However, lean burn technologies are not without their drawbacks. Compared to RQL combustors, lean burn technologies typically exhibit reduced combustion stability and relight characteristics since combustion occurs near flame Lean BlowOut (LBO) limits, while autoignition and flashback risks are raised as a result of the premixing generally employed [52]. While lean burn and other low-NO_x technologies being introduced typically also reduce nvPM it is anticipated that early development issues and difficulty introducing these technologies into the existing fleet, while ensuring stable operation and engine longevity, would not reduce nvPM emissions by an order of magnitude as is initially apparent, although reductions would still be significant [11]. As such, regulatory emissions testing of in-service aircraft engines currently displays a wide variability in engine nvPM emissions. This is demonstrated in *Figure 1-14*, which shows the nvPM emissions produced by in-production engines (including both RQL and lean burn technologies) across manufacturers against the CAEP/11 nvPM regulatory limits with respect to engine thrust, calculated using up-to-date and openly available emissions data from the ICAO aircraft engine emissions databank [54].

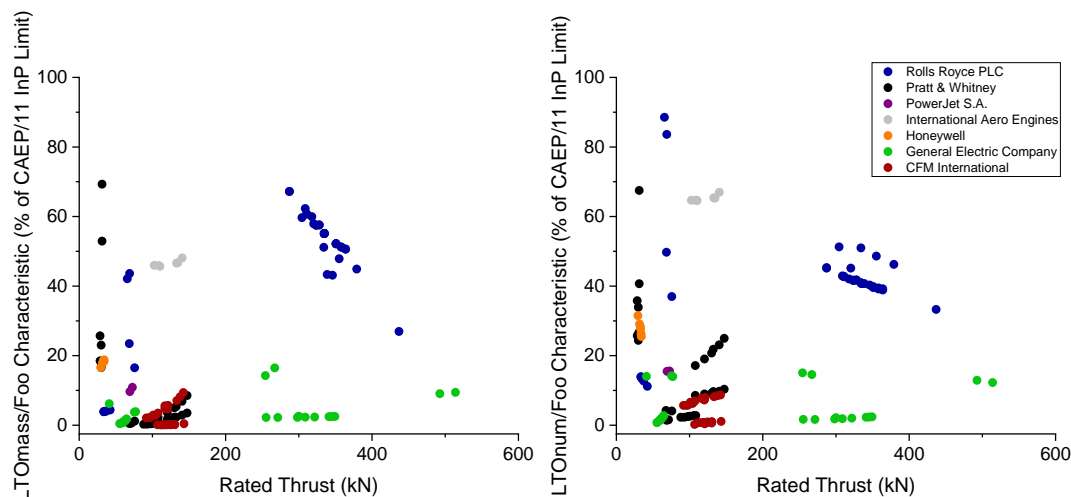


Figure 1-14 - nvPM mass and number emissions produced by real-world engines (by manufacturer) as percentages of the CAEP/11 regulatory limits [54]

1.4. Reducing Aircraft Emissions using Drop-in Fuels and SAF

In the EU, improvements to engine combustor technologies and fuel efficiencies reduced the fuel burned per passenger km flown by 24% between 2005 and 2017, but were countered by the increase in flights over the same time, resulting in overall increases to CO₂ and NO_x emissions by 22 million tonnes (+16%) and 170 million tonnes (+25%), respectively [3]. Pre-COVID projections showed that, even under the most optimistic scenarios, the current rate of improvements to aircraft technologies and operations could only yield an annual improvement to aircraft fuel efficiency of 1.3-1.4% up to 2050, well below the aspirational goal of 2% per annum highlighted by the ICAO [7], [11]. It appears evident that developments in engine technologies alone are too slow to achieve current emissions reduction goals within specified time frames when factoring in the rapid growth of commercial aviation. Therefore, other technological advancements will be necessary.

A key area of development which may aid in this is that of low-emission alternative fuel sources for aircraft, to replace the existing conventional jet fuels. It has been suggested that future aviation may be hybrid-electric or fully electric, as have been proposed by Airbus [55], or powered by alternative liquid fuels including alcohols, cryogenic hydrogen or methane, and ammonia. [56]-[58]. However, the suitability of these fuels is currently limited by underdeveloped manufacturing infrastructures and, in particular, the state of the commercial aviation sector. Modern aircraft are the evolution of technologies introduced many

decades ago, centred around the continued availability of crude oil fuels. Converting the current fleet of commercial aircraft to accommodate radically different fuels sources to modern Jet A-1 and Jet A fuels would likely require complete overhauls of existing aircraft or entirely new aircraft designs. This would be expensive and time consuming, since aviation fuels must meet a very stringent set of safety and operating requirements for use in commercial aviation. Blakey *et al.* [5] highlights two main factors limiting the viability of widespread use of a given alternative fuel introduced as a replacement to current conventional fuels:

1. Extreme conditions under which combustion must reliably and safely occur, such as the low temperatures and pressures experienced at high altitudes, which can present lubricity or freezing issues, especially in colder climates.
2. Logistical issues associated with the potential handling of multiple fuels at airports.

In addition, the viability of an alternative fuel is affected by latent energy contents, measured on a mass or gravimetric basis (specific energy, MJ/kg), and volumetric basis (energy density, MJ/L). These are key fuel properties associated with aviation fuels (especially during long-haul flights) dictating the maximum operating ranges of aircraft, where specific energy relates to aircraft take-off weights, while energy density relates to fuel tank sizing requirements. For example, along with storage concerns, liquid hydrogen exhibits a much higher specific energy than Jet A-1 fuels, but a much lower energy density, which would require considerable modification and resizing of aircraft fuel tanks, and consideration of different operating range behaviour between short and long-haul flights. **Figure 1-15** demonstrates some potential design considerations for the use of alternative fuels.

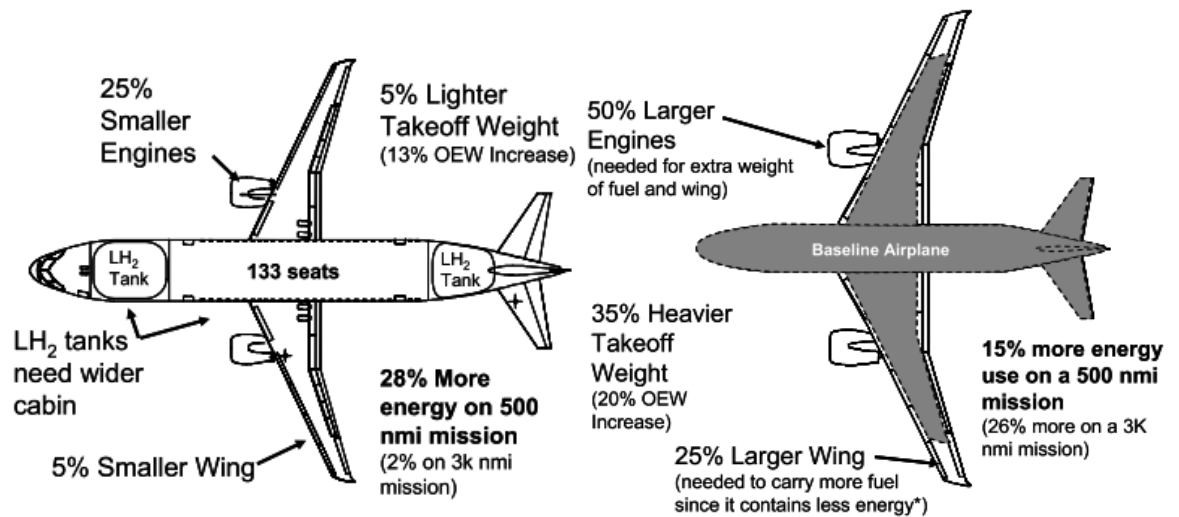


Figure 1-15 - Proposed design modification necessary for modern aircraft powered by liquid hydrogen (left) and ethanol (right) [59]

Because of the above concerns, many of the fuels outlined in the previous section are viewed as long-term alternatives to current fuels, and which still require significant development time. In the near term, the most promising alternatives to conventional Jet A-1 fuels are “drop-in” fuels, which have received a good deal of attention and development in recent years. Drop-in fuels are kerosene fuels derived from non-crude oil feedstocks, which resemble conventional aviation fuels closely enough for a smooth integration into the existing fleet with minimal changes to aircraft design [60]. As such, drop-in fuels contain many of the same compounds as conventional aviation fuels, helping them to retain key Fit-For-Purpose (FFP) properties necessary to satisfy operating requirements of current aircraft engines. New candidate fuels for international aviation are approved following the ASTM D4054 process [61].

To date, alternative aviation fuels able to satisfy the drop-in criteria have been successfully manufactured from a number of feedstocks, including natural gas, coal, waste products, and biological feedstocks. Fuels derived from natural gas and coal are advantageous in that their global deposits are more numerous and show better security of supply than crude oil [62]. However, a continued reliance on fossil fuels is socially unfavourable, and the issue of CO₂ emissions still remains since emissions correlate directly to fuel burn quantities. Being liquid hydrocarbon fuels of relatively similar compositions to conventional aviation kerosene, drop-in fuels produce similar gaseous emissions to conventional fuels. However, alternative aviation fuels derived from biological feedstocks (aka. bio-jet fuels) allow for an offsetting of direct CO₂ emissions from aircraft operation

through carbon capture at their feedstocks, resulting in significant reductions to total life-cycle CO₂ emissions, including those produced during manufacturing, transportation, combustion etc. [5].

Suitable feedstocks used in the production of bio-jet fuels include starchy, sugary, and oily crops, lignocellulosic (wood-based) matter, microalgae, residues from agricultural or forestry sources, and biological waste matter such as waste fats, oils and greases, and municipal solid waste [63], [64]. Fuels offering the most significant reductions to lifecycle CO₂ emissions from the aviation sector are termed Sustainable Aviation Fuel (SAF) by the ICAO [65]. The requirements an aviation fuel must meet to be considered “sustainable” are somewhat ill-defined, and a potential point of controversy depending on the feedstock used for production (additional detail outlined in **Section 2.2.2**). For example, the recast-to-2030 Renewable Energy Directive (RED II [66], [67]) concerning increased usage of renewable biofuels in the EU transport sector, makes distinction between biological feedstocks of high and low Indirect Land Use Change (ILUC). It is explained that the repurposing of key agricultural food production sites towards biofuel production, may incite pressure to extend agricultural land into areas of high carbon stock such as primary forests, wetlands, and peatlands, or else risk food supply shortage (although some argue this could be partially mitigated by measures such as farming rotation cycles alongside other crops [68]). High-ILUC fuels are those produced in areas where the release of stored carbon from the necessary land conversion risks negating any achievable greenhouse gas reductions. This is undesirable and these fuels should not be classified as sustainable.

For the purposes of this project, a general definition of SAF would be a kerosene-like fuel capable of significant reductions in lifecycle CO₂ emissions refined from feedstocks without requiring detrimental repurposing of land space. For example, to be eligible under CORSIA sustainability criteria the ICAO specifies greenhouse gas reductions of at least 10% and manufacturing feedstocks from biomass not grown in high carbon stock land areas [69]. A best case scenario predicts that the complete replacement of Jet A-1 fuels with SAF could allow for up to 63% achievable reductions in net CO₂ emissions from commercial aviation by 2050 [11], [70] (See *Figure 1-16*).

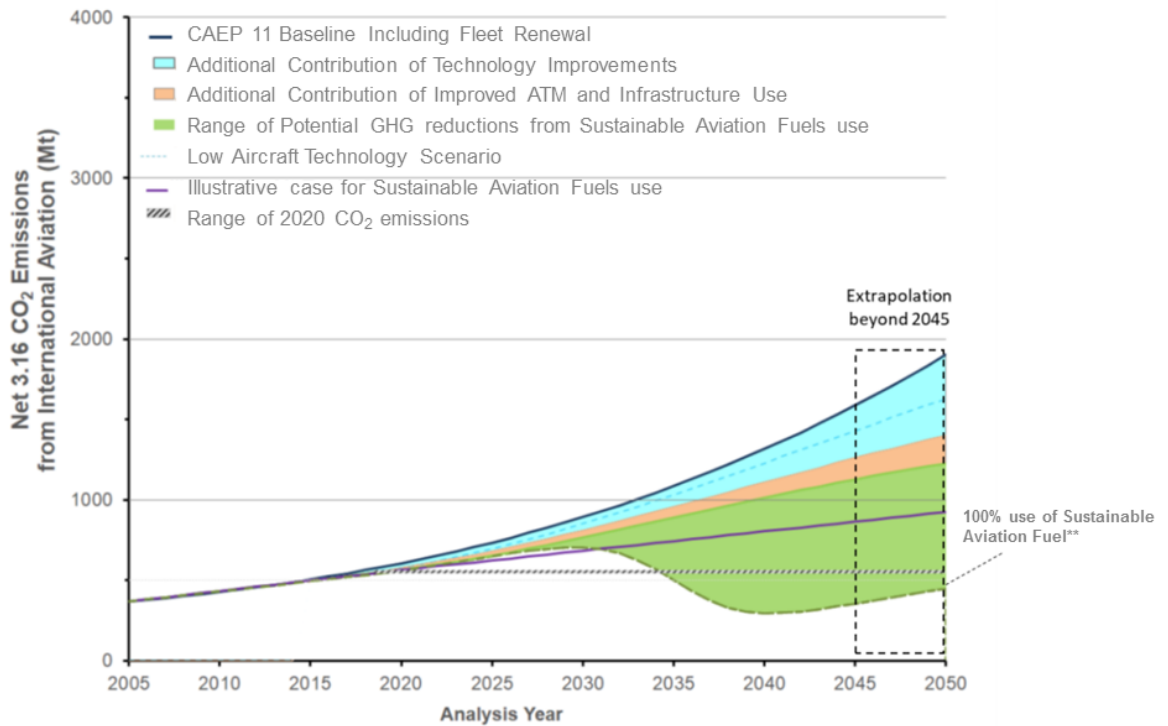


Figure 1-16 - Net CO₂ Emissions from international aviation forecast 2005-2050 [11]

Additionally, many candidate SAF exhibit drastically reduced aromatic contents compared to conventional Jet A-1 fuels. Aromatic compounds are known to be the primary cause of nvPM formation from aviation fuel combustion, and are normally found in relatively high quantities in jet fuels as by-products (along with sulphur) of the crude-oil distillation process. Although there are processes that exist to completely remove aromatics from jet fuels, they are typically not implemented by manufacturers due to high associated costs, and aromatic contents are instead only reduced as much is necessary to fall within regulations [16]. ASTM D1655 specifications currently allow a total aromatic volume content of 25% [9]. Many neat (pure form) SAF inherently contain few to no aromatic compounds, although this has been seen to result in fuel leakage issues, since aromatics induce an advantageous seal swell effect on elastomer O-rings of aircraft fuel tanks upon contact [60], [71], [72]. Most SAF classify as “near drop-in”, and are currently unsuitable for use in 100% SAF powered commercial flights. Instead, drop-in status can be achieved when using SAF as blends with conventional aviation fuels. For example, the aforementioned fuel leakage issues associated with low aromatic SAF may be circumvented by blending SAF with conventional aviation fuel to achieve a minimum of ~8% aromatic compounds.

The infrastructure of SAF is rapidly evolving with the heightened consideration of the consequences of human activity on the environment. New

approved conversion processes, test flights, and plans for increased utilisation of SAF in commercial aviation have all been seen in the past few years alone. Approved conversion processes for the production of aviation ready SAF and the maximum allowable blending ratios with conventional fuels (by volume) are highlighted by the ASTM D7566 standard [64], [73], and in the ASTM D1655 standard. At the time of writing, ICAO approved SAF are as follows:

ASTM D7566 [73]

- FT-SPK - Synthetic Paraffinic Kerosene (SPK) manufactured using the Fischer-Tropsch conversion process, allowed up to 50% volume.
- FT-SPK/A - FT-SPK with increased aromatics, allowed up to 50%.
- HEFA-SPK - Synthetic Paraffinic Kerosene derived from Hydroprocessed Esters and Fatty Acids, also called Hydrotreated Renewable Jet (HRJ) fuel or plant-based Hydrotreated Vegetable Oils (HVO), up to 50%.
- HFS-SIP - Synthesised Iso-Paraffins derived from Hydroprocessed Fermented Sugars, up to 10%.
- ATJ-SPK - Alcohol-to-Jet fuels, allowed up to 50%.
- CHCJ - Catalytic Hydrothermal Conversion Jet fuels, allowed up to 50%.
- HC-HEFA-SPK - Synthesised Paraffinic Kerosene derived from algae, allowed up to 10%.

ASTM D1655 [9]

- Co-processing of fats, oils, and greases during petroleum refining.
- Co-processing of the F-T process.

The potential for emissions reductions achievable from increased implementation of low-aromatic SAF is apparent, and it has been suggested that the use of low aromatic fuels coupled with RQL methodology could be utilised to significantly control both NO_x and nvPM emissions [74]. Authors have stated recently that, while the physiochemical fuel properties of conventional fuels are well understood, a knowledge gap exists in understanding those of alternative fuels, including SAF, and their relation to emissions behaviour, especially soot emissions [5], [75], [76]. A number of factors are thought to influence engine emissions, which can be generally separated into two categories: 1) Chemical effects affecting the flame reaction chemistry, and 2) Physical effects including fuel atomisation quality prior to combustion and flow behaviours [16]. Quantifying

the emissions produced by aircraft gas turbine engines is currently a highly empirical process requiring extensive and costly engine ground tests prior to fuel certification. However, the complex nature of aircraft engines and the many different influences affecting emissions make quantifying the impacts of individual fuel properties difficult, and there appears to be no universally accepted index for predicting of nvPM formation in aircraft operating with alternative fuels.

1.5. Research Motivations and Thesis Structure

Commercial aircraft are a known source of harmful emissions affecting both the local and global environment. This has led to the introduction of more stringent emissions standards for civil aviation, and targets for emissions reductions into the future. However, it appears that advancements in aircraft technology, while still capable of offering improvements to aircraft fuel efficiencies and emissions reductions, do not appear to be advancing at the rates required to achieve highlighted emissions targets. Of the emissions produced by aircraft, nvPM emissions have been found to degrade local air quality and present health concerns for many years, and may also have a greater impact on the wider global environment than previously thought. This is concerning, since existing RQL combustors, while offering excellent operational stability and acting as established methods of reducing NO_x emissions, are known to be prone to nvPM formation due to high equivalence ratios found in their primary zones.

Aircraft nvPM emissions can be significantly reduced by the use of low-aromatic drop-in fuels and SAF, the latter of which can also facilitate reduced lifecycle CO₂ emissions. The increased adoption of SAF with drop-in capabilities into the commercial aviation section could prove as an effective method of cutting nvPM and CO₂ emissions in the near term, alongside gradual improvements to aircraft engine technologies. Because of this, SAF have received increased attention in recent years, and new goals are being set for their use in the civil aviation section. However, it has been highlighted that the physiochemical properties of alternative fuels, and the mechanisms by which they influence emissions from combustion, are less well understood compared to conventional fuels. As such, there is a need to understand the causes of nvPM emissions

produced by SAF, including understanding of the effects of various alternative fuel physiochemical properties.

Detailed fundamental emissions studies using generic research combustors, such as those recently undertaken [25], [76], [77], can provide a greater insight into formation of emissions during liquid fuel combustion. These can be coupled with detailed modelling studies available today due to modern advancements in computational power, which act as validation tools for measured data and provide insight into the chemical processes resulting in the formation of emissions from combustion. To facilitate studies of this nature, there is a need for accurate and comprehensive emission datasets collected from representative aircraft engines, using up-to-date measurement protocols, and with detailed reporting of various fuel properties and engine operating conditions. These can be used to act as a testbed for newly developed modelling strategies, and to explore the effects of physiochemical properties on nvPM formation. Overall, this will help to provide a better understanding of the emissions produced by SAF and help towards the development of new SAF emission standards.

With this in mind, the aim of this study is to undertake a detailed investigation of the emissions performances of drop-in fuels and ICAO approved SAF, in a generic RQL-type combustor manufactured through low-cost manufacturing techniques. The RQL combustor would be developed to afford greater control and monitoring of the various flow processes used for combustion than other similar combustors. In doing so, variations in fuel physiochemical properties across conventional and drop-in fuels could be explored. In the process of benchmarking the combustor, a detailed investigation of atomisation behaviour, including variability across conventional aviation fuels and drop-in fuels could also be explored, with emphasis on the significance of various fuel physical properties.

Chapter 4 details the design process and development of atomisers produced through Additive Manufacturing (AM), towards the refinement of an existing RQL research combustor.

Chapter 5 outlines the emissions trends observed during the Horizon 2020 JetSCREEN campaign, in which the generic RQL combustor was operated using a range of conventional fuels, SAF, and fuel blends.

Chapter 6 details steps taken towards refinement of the combustor design, including modifications for greater control of the flow processes and droplet sizing characterisation using water spray experiments. The refined combustor was then used in the consolidation of observed emissions trends.

Chapter 7 explores more closely the spatial characteristics of the atomisers, for both water sprays and jet fuels. The variability across conventional fuels and blended fuels are examined. Emissions experimentation was used to explore the impact of atomisation spatial characteristics on nvPM, and isolate the impacts of atomisation droplet sizes on nvPM emissions. A final comparison of the collected nvPM emissions datasets is included with analysis of common trends.

2. Factors Impacting nvPM Formation in Aircraft Combustors

This chapter aims to act as a review of the current body of literature relating to the production of nvPM from SAF. In order to better understand the factors influencing nvPM formation, it is necessary to describe the typical chemical compositions of conventional aviation fuels, with emphasis on how different hydrocarbons affect the promotion of nvPM and overall combustion. This facilitates a comparison with the typical compositions of SAF, and an investigation of recent experimental studies demonstrating the achievable emissions reductions associated with them.

Following this, a further investigation into the previously witnessed effects of physiochemical fuel properties on nvPM can be undertaken. Because an objective of this work is to explore the impact of both chemical and physical fuel properties on nvPM emissions, it is also necessary to explore studies relating multiple fuel properties to nvPM formation in combustion. A review of the effects of fuel physical properties will be mostly concerned with their subsequent impacts on atomisation, which also warrants description with regards to its relevance in gas turbines, the mechanisms and factors influencing droplet breakup, and previously observed impacts of varying atomisation quality on nvPM formation.

2.1. Aviation Fuel Key Chemical Components

Conventional aviation fuels are a mixture of many hundreds, if not thousands of hydrocarbons typically ranging between C₈-C₁₆, whose compositions often vary across individual batches [78]. The main hydrocarbon families found in aviation fuels may be separated into aliphatic and aromatic groupings, with aliphatic compounds being preferable over aromatic compounds from both a combustion and emissions perspective. The main aliphatic groupings found in aviation fuels are:

- **Paraffins/Alkanes** - Hydrogen-saturated hydrocarbon molecules with the most favourable combustion characteristics in fuels, burning with comparatively clean flames which produce very little soot [16]. Isomers of paraffins exist as straight chained (n-paraffins) or branched molecules (iso-paraffins/i-paraffins), examples of which are shown in *Figure 2-1*. Both

groups of paraffins are described by the chemical formula C_nH_{n+2} . However, n-paraffins are typically associated with higher specific energies than i-paraffins, which by contrast have low reactivity, but better low temperature lubricity properties [10].

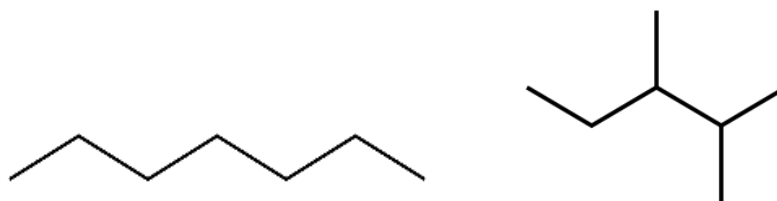


Figure 2-1 - From left to right: n-heptane ($n-C_7H_{16}$), and 2,3 di-methylpentane ($i-C_7H_{16}$)

- **Cycloparaffins/Naphthenes** - Saturated cyclic hydrocarbons formed by the replacement of two hydrogen branched atoms with internal C-C bonds to form a central ringed structure of carbon atoms. The reduced hydrogen saturation makes these compounds slightly less effective from a combustion standpoint than paraffins. As such, these compounds are viewed as the second most desirable components in jet fuels [16]. Components typically found in Jet A-1 fuels are single-ringed mono-cycloparaffins, and double ringed di-cycloparaffins, examples of which are shown in **Figure 2-2**.

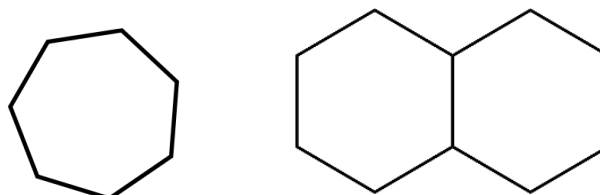


Figure 2-2 - From left to right: Cyclopentane (C_5H_{10} , a mono-cycloparaffin), and decalin ($C_{10}H_{18}$, a di-cycloparaffin)

- **Alkenes/Olefins (C_nH_{2n})** - Unsaturated chained hydrocarbons with overall good combustion properties, but their tendencies to form resinous gums and other deposits make them undesirable within jet fuels. Typically limited to under 1% of a fuel's composition ASTM D1655 [9].

Aromatic molecules are unsaturated hydrocarbons with one or more Benzene rings (C_6H_6) in their molecular structure. Each ring contains three double Carbon-Carbon bonds in its molecular structure, resulting in fewer hydrogen atoms and an overall decreased hydrogen content compared to aliphatic compounds of

like carbon number. As such, aromatics generally exhibit poorer combustion characteristics [16], and as previously mentioned, are widely regarded as the primary components in aviation fuels responsible for nvPM emissions. Aromatic compounds often exhibit higher volumetric energy contents compared to paraffins, and so liquid fuels containing high aromatic content can actually possess a slight energy advantage for a fixed fuel tank compared to paraffinic fuels, while the opposite is true when considering energy content on a gravimetric (mass) basis [5]. The typical subgroupings for aromatic compounds are as follows:

- **Mono-Aromatics** - Compounds built around the base element Benzene i.e. containing a single benzene ring in their molecular structure, are classed as monoaromatics, and are the most common aromatic family found within in aviation fuels. The mono-aromatic classification encompasses alkyl-benzenes (e.g. toluene) which consist of benzene rings with alkyl branches, and cyclo-aromatics (e.g. tetralin and dialin) which contain a ringed structures as a functional groups.

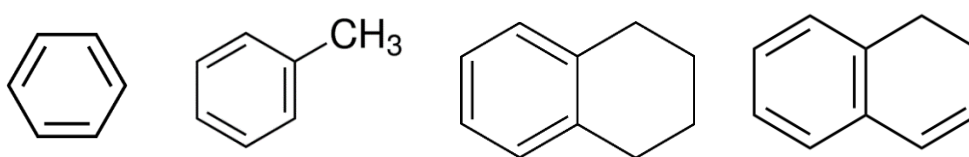


Figure 2-3 - From left to right: Benzene (C₆H₆, base molecule), Toluene (C₇H₈, an alkyl-benzene), Tetralin (C₁₀H₁₂, a cycloaromatic) and Dialin (C₁₀H₁₀, a cycloaromatic)

- **Di-aromatics/Naphthalenes** - Aromatic compounds containing two benzene rings are subsequently classed as di-aromatics or naphthalenes, and built around the base molecule Naphthalene (C₁₀H₈). These compounds possess an even greater hydrogen unsaturation than mono-aromatics, and are therefore even less desirable in combustion. Within the 25% vol. maximum for total aromatics outlined by ASTM D1655 [9], up to 3% vol. di-aromatics is permitted.

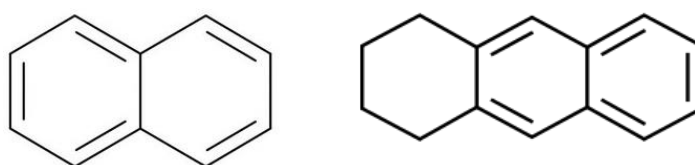


Figure 2-4 - From left to right: Naphthalene (C₁₀H₈, base molecule) and 1,2,3,4-Tetrahydroanthracene (C₁₄H₁₄, a naphtheno-diaromatic)

- **Polyaromatics** - Aromatic compounds containing three or more benzene rings. They are not typically found in Jet fuels.

2.2. SAF Conversion Processes

2.2.1. Fischer-Tropsch (F-T) Fuels

The Fischer-Tropsch conversion process was developed in 1925 by Franz Fischer and Hans Tropsch as a method of converting synthesis gas, commonly referred to as syngas ($H_2 + CO$), into a Synthesised Paraffinic Kerosene (SPK) fuel resembling aviation kerosene. The choice of feedstock used to derive the syngas defines the naming of each resultant F-T fuel, following the X-to-Liquid labelling system, with Gas-to-Liquid (GTL) fuels derived from natural gas, Coal-To-Liquid (CTL) from coal feedstocks, Biomass-to-Liquid (BTL) from biomass, and Power-to-Liquid (PTL) using hydrogen derived from the electrolysis of water using renewable energy coupled with CO derived from CO_2 from carbon capture technologies.

Liu *et al.* [79], and Wang and Tao [63] describe the basic steps involved in the F-T conversion process. Syngas is first extracted from a suitable feedstock through gasification, and cleaned to remove CO_2 and other undesirable compounds. The resultant gases are then converted into a wide variety of liquid hydrocarbon products through carbon chain building reactions at elevated temperatures and pressures, utilising an appropriate catalyst such as iron or cobalt [73]. Conventional refinery processes (hydrocracking, isomerization, hydrogenation, and fractionation) are then employed to isolate the desired hydrocarbons of carbon chain lengths suitable for aviation. The resultant F-T fuel is typically a mixture of straight chain paraffins and olefins, with very low aromatic contents and sulphur contents, allowing for significant reductions in both nvPM and sulphurous emissions. The typically higher specific energies of paraffinic components can also allow for small reductions in fuel consumption, and thus, CO_2 generated during operation in aircraft per kg fuel [79]. However, the lack of aromatic compounds makes F-T fuels susceptible to the fuel leakage issues described earlier (**Section 1.4**), currently limiting their use in aviation to blends of up to 50% with conventional fuels. The recently approved FT-SPK/A variation is a potential solution to this, whereby the minimum aromatic content necessary for elastomer seal swell is added to a F-T fuel by alkylation of light aromatic

compounds (e.g. Benzene) from non-petroleum sources, which can be tailored for the lowest achievable sooting tendencies [73].

Unfortunately, the F-T process produces high quantities of CO₂, especially in the case of CTL fuels which have been shown to produce well-to-wake CO₂ emissions over twice those of conventional fuels without Carbon Capture and Storage (CCS) technologies, and 10% higher with CCS [5], [62]. Additionally, GTL and CTL fuels are derived from fossil fuels, which limits their suitability in the long term. BTL fuels can avoid this issue through carbon capture at their feedstocks, as mentioned in *Section 1.4*, allowing for lifecycle GHG emissions up to 95% lower than conventional fuels [63]. It is noted that PTL fuel generation is a promising emerging technology employing the F-T process [80], but is not yet approved for use in aircraft by ASTM D7566 [73].

2.2.2. Hydroprocessed Esters and Fatty Acids (HEFA) Fuel

The manufacture of HEFA fuels utilises a process of catalytic hydrogenation, deoxygenation, hydro-isomerization, and hydrocracking to convert bio-derived, triglyceride-rich unsaturated fats and oils into iso-paraffin rich SPK Biojet fuels [56]. Fuels produced through this conversion process have also been referred to as Hydrotreated Renewable Jet fuel (HRJ), or Hydrotreated Vegetable Oils (HVO) [63], [68]. However, the accepted terminology now adopted by the ICAO is HEFA [64]. The HEFA conversion process is outlined in *Figure 2-5*.

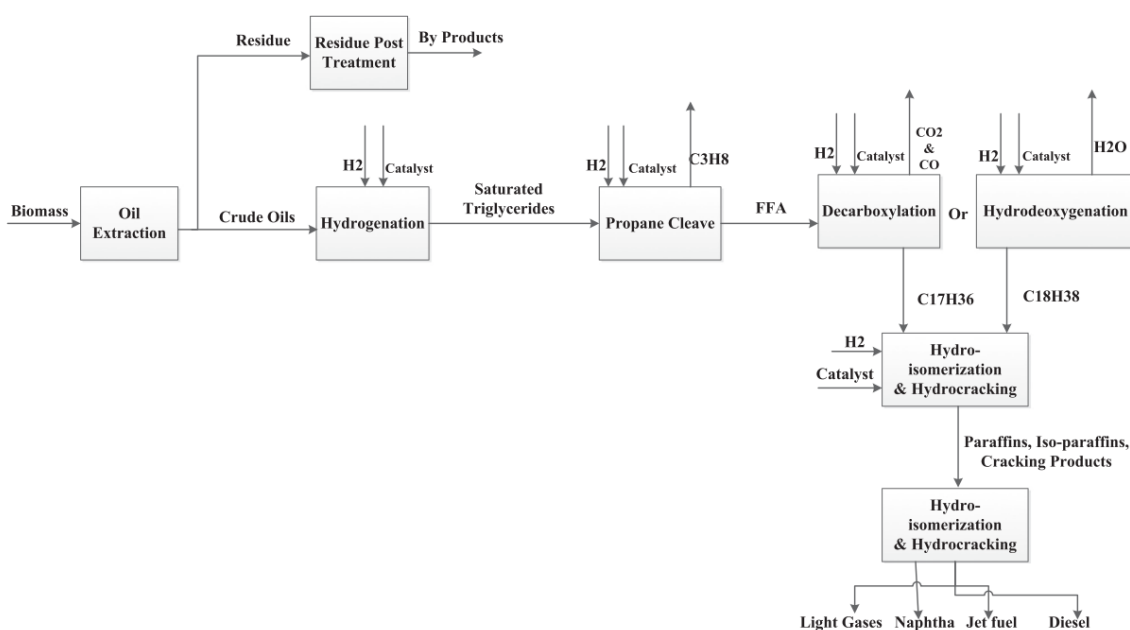


Figure 2-5 - HEFA conversion process [63]

During conversion, unsaturated triglyceride compounds from biomass feedstocks are first converted into saturated triglyceride compounds through catalytic hydrogenation. This is followed by a propane cleave step, yielding three moles of Free Fatty Acids (FFA's) and one mole of propane. The FFA's undergo continued catalytic hydrogenation to remove CO₂, CO, and H₂O, before a final hydrocracking process where the resultant long carbon-chain compounds are broken down into lengths suitable for use in aircraft. Additionally, other hydrocarbon products useful to other sectors are produced. Typical HEFA fuels are indistinguishable in composition from F-T fuels, containing high cetane numbers, low aromatic contents, and negligible sulphur contents [16].

A wide variety of biological feedstocks can be used in the HEFA manufacturing process, including camelina, jatropha, soybean and rapeseed crops, beef tallows, and marine algae. HEFA fuels also best demonstrate the need for consideration of land usage during SAF production, as mentioned in **Section 1.4**, which can greatly limit the viability of potential SAF from any of the conversion processes in this section. A shift to alternative fuel production would likely require the repurposing of high carbon stock or key natural carbon capture sites towards alternative fuel production could result in increases to fuel lifecycle CO₂ emissions well above those of conventional aviation fuels. For example, a worst-case scenario for HEFA fuels manufactured from palm oil and soy crops is predicted to result in lifecycle CO₂ emissions several times those produced by conventional fuels, as a result of land space usage alone [5], [62]. This is shown in **Figure 2-6**.

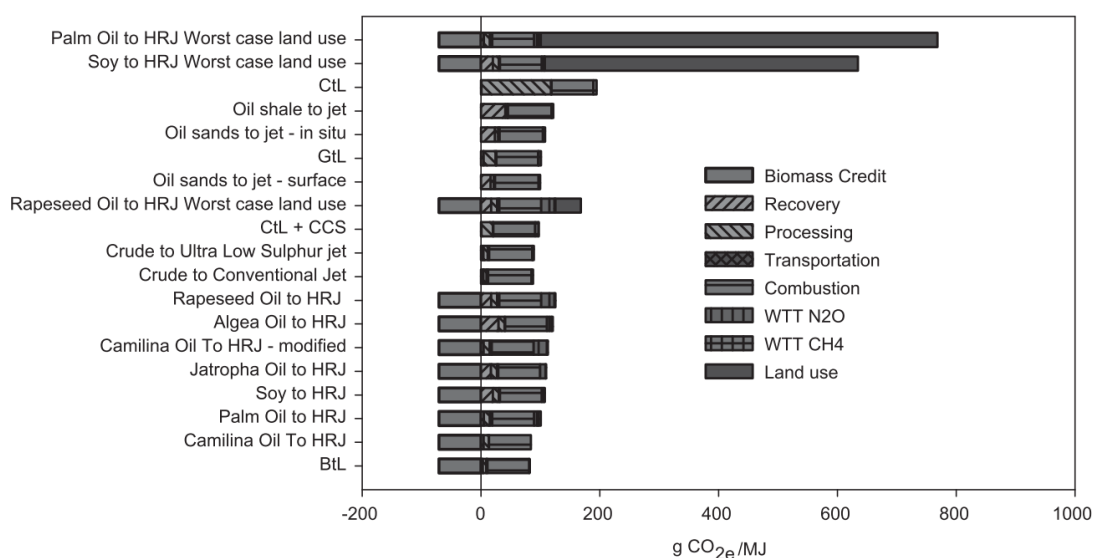


Figure 2-6 - Predicted lifecycle CO₂ emissions for various aviation fuels [5]

2.2.3. Alcohol-to-Jet (ATJ) Fuels

ATJ fuels are SPK fuels derived from alcohols such as methanol, ethanol, n-butanol and iso-butanol [63]. The ATJ conversion can be summarised by a three-step process of alcohol dehydration, oligomerization of small hydrocarbons into larger unsaturated hydrocarbons and finally, hydration of the unsaturated paraffins into saturated paraffins [63]. Refinement of the resultant mixture into hydrocarbons of suitable carbon chain lengths for aviation is then achieved through traditional fractionation. While many ATJ fuels have been shown to exhibit very low quantities of aromatic hydrocarbons in favour of n- or iso-paraffins, similarly to F-T and HEFA fuels, some ATJ fuels have been known to exhibit less favourable physiochemical properties for aviation in comparison to other low-aromatic SAF. Won *et al.* [81] found that the Derived Cetane Number (DCN) of a Gevo ATJ (POSF 10151) was almost three times less than conventional Jet A-1 fuels, which would be expected to result in low extinction strain rates and subsequently, narrower flame stability limits. ATJ fuels have also demonstrated poor ignition behaviours, attributed to high iso-paraffin content they often exhibit [82].

2.2.4. Catalytic Hydrothermal Conversion Jet (CHCJ) Fuel

Catalytic Hydrothermal Conversion Jet (CHCJ) fuels, also known as Catalytic Hydrothermolysis Jet (CHJ) fuels, are biojet fuels produced by Catalytic Hydrothermolysis, also called HydroThermal Liquefaction (HTL). This was originally developed by the Applied Research Associates (ARA) and Chevron Lummus Global (CLG) to produce the ReadJet fuel [83]. CHCJ fuels have seen increasing development in recent years, and the conversion process was approved under ASTM specifications for use in aircraft up to 50% by volume blend in 2019. The CHJ process employs a supercritical water process at high temperatures and pressure (250 - 450°C and 100 - 350 bar) in the presence of a catalyst to convert triglyceride compounds from organic matter into fuel hydrocarbons, from which those suitable for aviation fuels can be refined through a number of hydrotreating, hydrocracking, hydroisomerisation and conventional refinery process' including fractionation [63], [73], [84]-[86]. An example CHCJ process is outlined below in **Figure 2-7:**

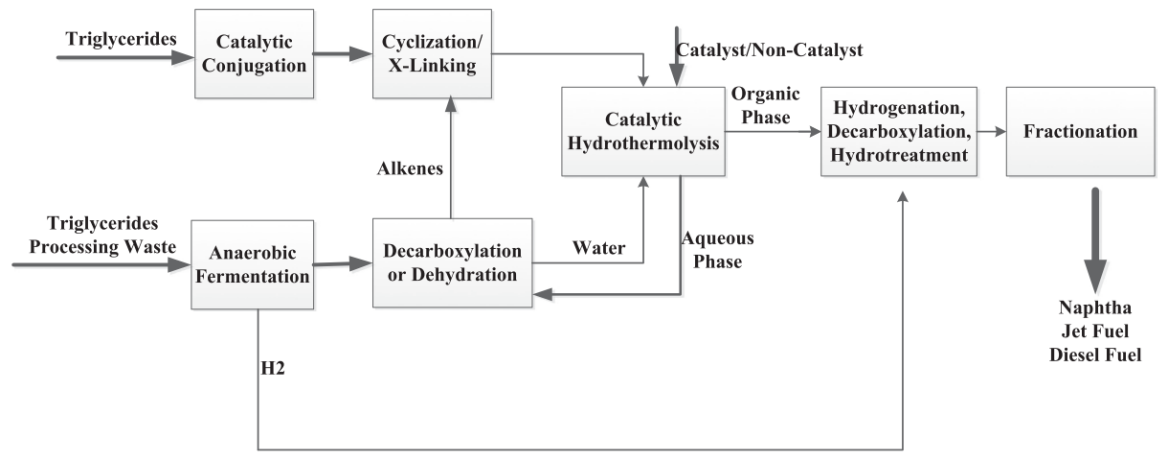


Figure 2-7 - CHCJ conversion process [63]

CHCJ fuels typically retain relatively high quantities of aromatic compounds. For example, Schripp *et al.* [87] found that the Readijet fuel produced from waste oils and fats exhibited an aromatic content of 20.9% vol., 5.3% vol. higher than a reference Jet A-1. This can worsen nvPM emissions compared to most of the aforementioned SAF, but does enhance their drop-in capabilities and prevents fuel leakage issues from inadequate seal swell. Luning Prak *et al.* [85] carried out a detailed chemical analysis of the hydrocarbon components and properties of a CHCJ fuel, finding that a CHCJ fuel was mostly similar to a Jet A fuel, but contained a narrower molecular weight range of alkanes and aromatics, and a similar concentration of cycloalkanes to n-alkanes and i-alkanes, as opposed to the higher abundance of alkanes found in Jet-A. It was commented that the absence of heavier alkanes in CHCJ may result in a lower freezing point compared to Jet-A, which would be beneficial especially for flights in colder climates.

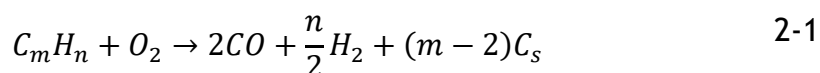
Suitable feedstocks for the production of CHCJ fuels include biological waste fats, oils and greases [87], plant oils from triglyceride-based crops such as jatropha, soybean, camelina and tung crops [84], and microalgae feedstocks [88]. It has also been highlighted that CHCJ fuels using offshore marine algae farms as feedstocks could offer possible reductions to life cycle greenhouse gas emissions of up to 76% compared to conventional jet fuels, with the transportation stages contributing the majority of CO₂ produced using this technology [88]. The Readijet fuel is highlighted as the first SAF to be used unblended to power both commercial and military aircraft, and is stated to allow for 50% reductions in particle

emissions, 1.5% lower specific fuel consumption (increasing aircraft range) and 80% lifecycle CO₂ compared to conventional Jet A-1 [83].

2.3. Chemical Effects on nvPM Emissions

2.3.1. Chemical Mechanism of nvPM Formation

As mentioned, nvPM forms through incomplete combustion reactions in locally rich, high temperature flame regions, which most often occur in the primary combustion zones of gas turbine combustors (**Section 1.3**). Mishra and Chandel [25] give a general equation for the production of incomplete combustion products from hydrocarbon mixtures in rich fuel-air mixtures ($\phi > 1$), as in **Equation 2-1**.



In this model, nvPM is formed alongside CO and hydrogen, the latter of which provide hydrogen radicals useful for combustion. However, the formation of nvPM is rather more complex than gaseous chemistry, undergoing a multistage life cycle including particle-particle reaction chemistry and kinetic interactions alongside gaseous reactions. This has been studied in great detail in previous studies [18], [89]-[93]. A visual representation of the key stages of nvPM formation is shown in **Figure 2-8**.

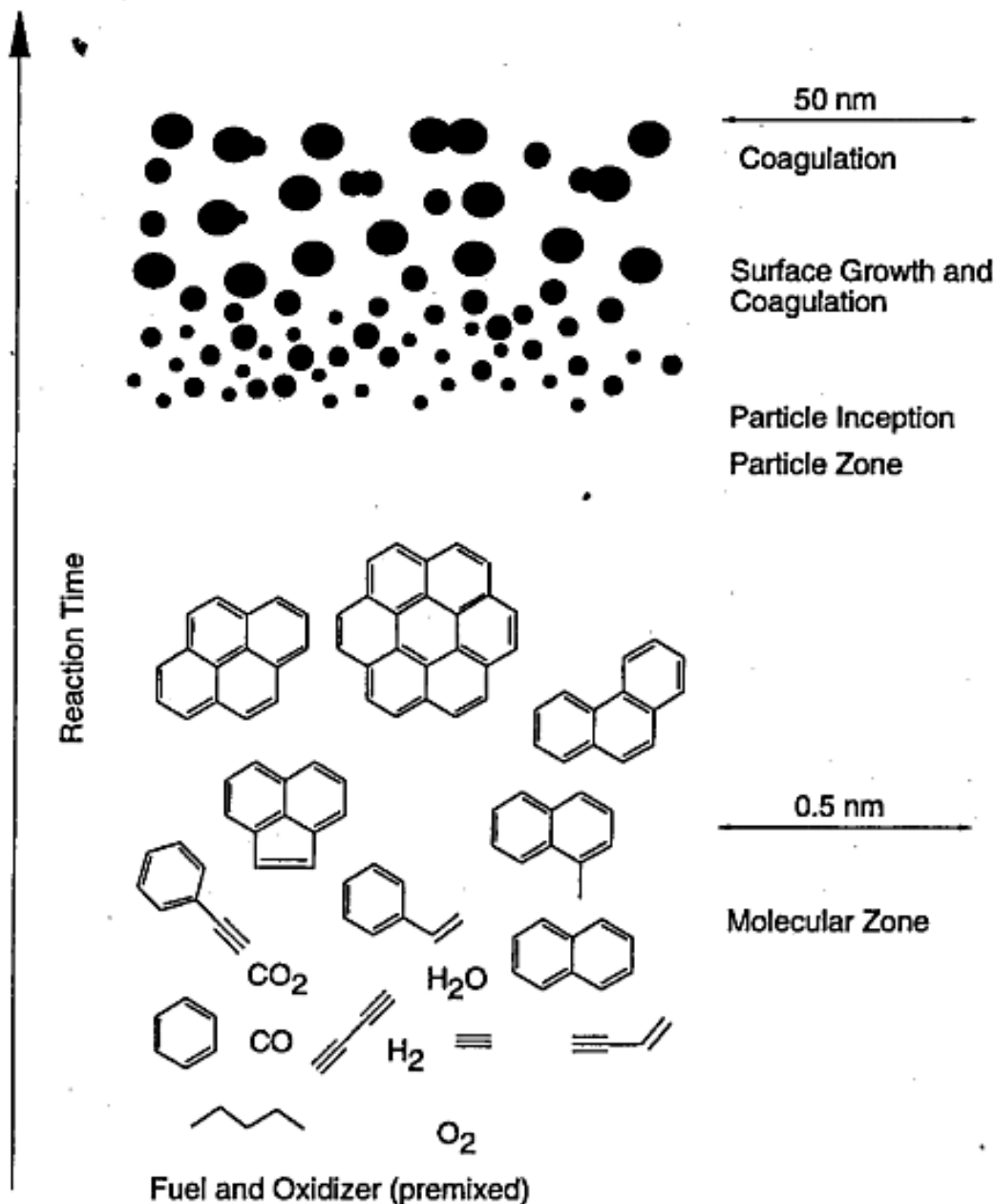


Figure 2-8 - Soot particle formation during fuel combustion [91]

The first stage of nvPM formation is referred to as nucleation or inception, during which gaseous hydrocarbon molecules transition into the particle phase. It may be assumed that nucleated particles are solid, but it is argued that they are in fact liquid-like nano-particles [18]. Nucleation occurs through the condensation of large, multi-ringed aromatic structures, referred to as Polycyclic Aromatic Hydrocarbons (PAHs), which are considered to be the primary soot precursor species [89]. PAH molecules form from lighter aromatic compounds (mono-aromatics and di-aromatics) commonly found in unburnt jet fuels, through chemical growth reactions in fuel rich combustion [90]. Acetylene (C₂H₂) is

generally considered as the key reactive species propagating growth [89], [90], [92]. Current soot models assume that the point of nucleation occurs with the formation of Pyrene ($C_{16}H_{10}$), containing four benzene rings and which forms initial soot particles through pyrene-pyrene dimerization reactions [90].

Additional nvPM formation is known to occur from the pyrolytic fragmentation and growth of smaller aliphatic compounds (n-paraffins, i-paraffins and cyclo-paraffins) into larger aromatic structures. Kumal *et al.* [94] explains that the growth reactions acting on pyrolyzed paraffin fragments are effectively the same as those by which PAH molecules are formed from lighter aromatic compounds. However, the formation of PAH molecules from lighter components requires more growth reactions and higher energy input, which increases the residence time of nucleation. This essentially imposes a kinetic delay on the reaction mechanism, during which time additional turbulent mixing can occur, helping to improve fuel and air distribution and further reduce nvPM formation rates [94]. As such, nvPM formed from aromatic compounds is the dominant mechanism in aircraft combustors.

Following the transition from the heavy PAH phase to the particulate phase, nascent soot particles begin to lose hydrogen atoms through dehydrogenation reactions, leaving behind graphite-like carbon structures [89]. At the same time particles continually gain mass through both surface growth reactions and particle-particle collisions. Surface growth reactions are similar to the growth reactions in the formation of heavy PAHs, occurring on radical sites on the soot particle surface [27]. Meanwhile, particle-particle collision interactions include coagulation (coalescence) or agglomeration (aggregation). Coagulation refers to a scenario where two particles fuse into a single spherical particle, while agglomeration describes when solid particles join at a surface level with very little loss of surface area, forming “fractal” structures [18]

As mentioned in **Section 1.3**, the addition of secondary air through the combustion liner in later combustion regions causes a portion of the nvPM produced to oxidise into CO_2 and CO . The competing processes of nvPM formation and oxidation mean that exhaust nvPM emissions are effectively the net result of these two processes. Soot particles may undergo oxidation reactions with OH , O and O_2 molecules, with OH radicals acting as the main oxidisers of PAH and soot in fuel rich flames, and O_2 in fuel lean flames [27], [95]. Rates of oxidation by OH

radicals are normally dominant in gas turbine combustor settings, and are encouraged by hotter inlet temperatures and flame temperatures. Oxidation by O₂ is limited, especially at higher pressures, and only impacts emissions under specific conditions such as fuel rich flames that are strongly mixed with air, which can occur at the front end of a combustor [18].

As mentioned in **Section 1.3**, rates of nvPM formation and particulate morphologies are affected by engine combustor designs and operating conditions. Rates of nvPM formation are increased by higher temperatures and pressures due to enhanced rates of chemical kinetic reactions [96]. Rates of particle nucleation and surface growth are highly temperature dependant, where low temperatures (<1500 K) result in insufficient chemical kinetic rates for PAH growth into nvPM with combustion timescales, while higher temperatures (<1900 K) also slow PAH ring growth due to thermodynamic instability [18]. Meanwhile, increased temperature in later combustion zones helps to encourage particle burnout, but at the risk exacerbating NO_x formation [18]. Increased combustor pressures also encourage nvPM formation by increasing combustion flammability limits, allowing for richer combustion to be possible where nvPM formation is higher [16].

2.3.2. Emissions Reductions through the use of Low-Aromatic Fuels

As previously mentioned, many SAF exhibit significantly reduced aromatic content in favour of paraffinic compounds, and so exhibit a greater dependence on the slower, pyrolytic reactions prior to particle nucleation described in the previous section. Kumal *et al.* [94] describes the kinetic delay this causes as a shift in the “starting point” of the soot formation lifecycle further from nucleation, giving a representation of the difference in soot formation life cycles between a conventional Jet A-1 fuel and a low-aromatic CHCJ biofuel derived from camelina crop, as shown in **Figure 2-9**. The authors found that, when used to operate a T-85 turbojet engine, the latter produced lower exhaust EC concentrations of smaller particle sizes as result of the kinetic delay to nucleation.

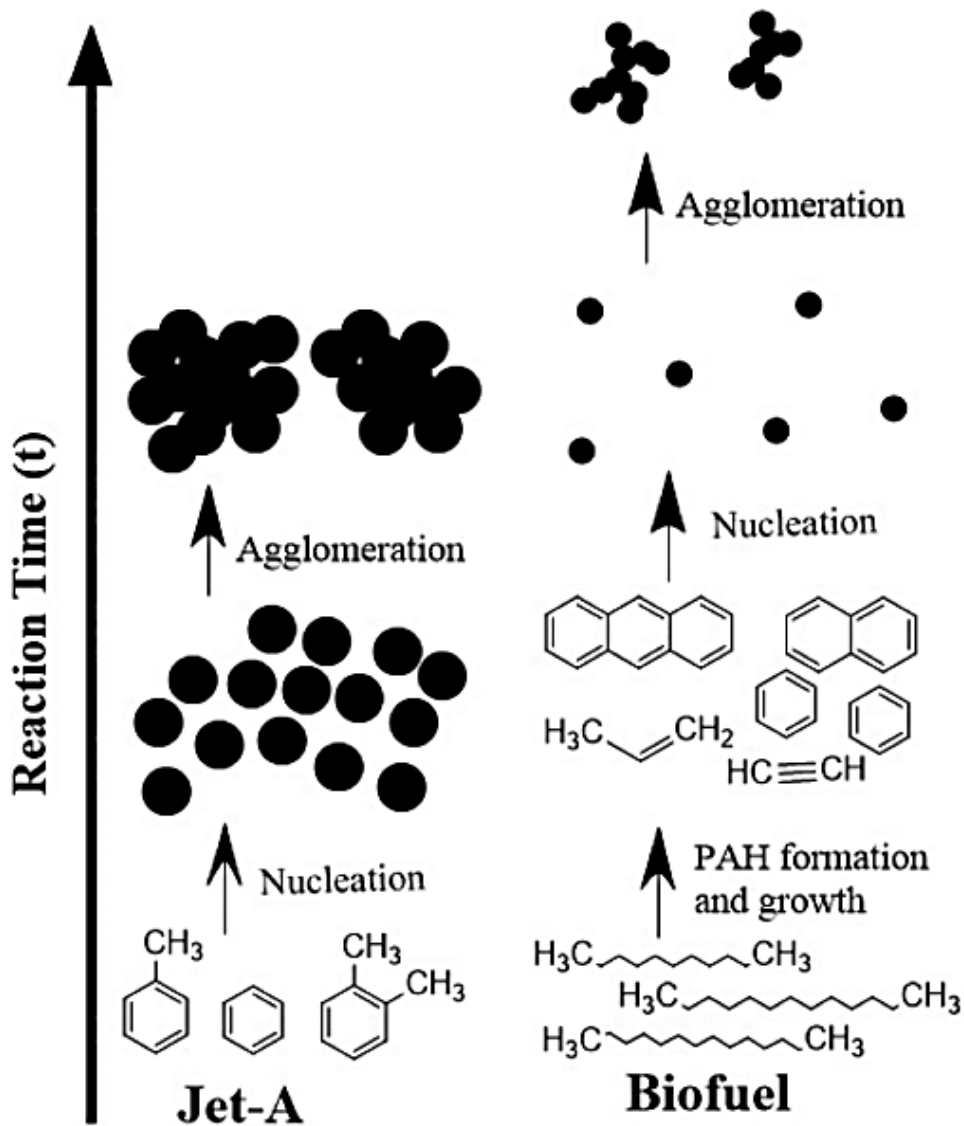


Figure 2-9 - Comparison of nvPM formation for a Jet-A fuel compared to a camelina-derived CH biofuel [94]

Improved understanding of the link between fuel composition and nvPM using drop-in fuels and SAF has been attained from numerous experimental campaigns undertaken in recent years. This includes experimentation with real world aircraft engines, APUs, and fundamental laboratory combustors. Although GTL and CTL fuels do not classify as SAF, they are perhaps the most widely documented drop-in fuel to date. GTL fuels have been consistently shown to greatly reduce nvPM emissions from aircraft, attributed to characteristically low aromatic contents. Blends of GTL with conventional fuels demonstrated that reductions in sooting tendencies were proportional to increased percentage compositions of GTL. Typical reductions in particle mass and number of 50-95% have been observed relative to conventional JP-8 [71], [72], [74], [97], [98] and Jet A-1 [99] fuels. Reductions in particle average diameters of 10-50% have been

observed [74], [98], [99]. CTL fuels have also been studied in aircraft engine sampling [97], [100], demonstrating similar nvPM reductions to GTL fuels, although reductions are often lower than GTL fuels.

Higher reductions in nvPM for GTL fuels relative to conventional fuels have been observed at lower power conditions compared to higher powers [101], [102]. Particle number is generally affected to a higher degree than mass, and in some cases (e.g. low power conditions), reductions >99% have been observed for neat F-T fuels [71], [97]. Timko *et al.* [102] attributed this to lower combustion temperatures and pressures, and less efficient mixing promoting areas of high local fuel/air ratio where soot formation is high, indicating a greater influence of spray properties at low power conditions. Some studies have also observed reductions in NO_x and CO emissions in the order of 5-10% for F-T fuels [74], [97], especially at idle conditions. When testing GTL and CTL fuels in an APU, Lobo *et al.* [99] commented that, at low power conditions, increasing CO emissions appeared to correlate with increasing fuel aromatic content. However, other authors have observed negligible variations to gaseous emissions [100]. It is likely that this is associated with the fuel spray, which is known to significantly affect gaseous emissions from aircraft.

More recent studies have explored the emissions characteristics of ICAO/ASTM approved SAF. A HEFA fuel derived from beef tallow was tested during the NASA AAFEX-II experiments, and was found to allow for similar reductions in nvPM to F-T fuels [72]. ATJ fuels have seen increasing attention in the last few years [81], [87]. Schripp *et al.* [87] tested a low aromatic ATJ fuel in a CMF56-5C4 engine, observing reductions in particle mass up to 70% compared to the reference Jet A-1 fuel. Alongside the ATJ fuel, the authors also tested a high-aromatic CHCJ fuel, which was found to increase particle number and mass by as much as 60%, which correlated with a higher aromatic content, acting as an example of an SAF which does not necessarily offer reductions to nvPM emissions over conventional fuels.

The reductions in nvPM emissions typically associated with SAF can also allow for reductions in the contrails formed by aircraft. Voigt *et al.* [34] measured the contrail formations from a research aircraft operating at altitude using a range of conventional and conventional/SAF fuel blends. It was found that the ~50% reductions in soot emissions associated with the fuel blends resulted in 45-74%

reductions in contrail ice crystal emissions indices, since the nucleation sites were reduced. An observed increase in emitted H₂O from the blended fuels condensing onto fewer nucleation sites was found to slightly increase ice crystal sizes. However, theoretical studies were referenced suggesting that larger ice crystals would experience faster sedimentation and sublimation, which would lead to a shorter contrail lifetime in the atmosphere. The overall conclusion was that the reduction in initial ice crystal number was critical in determining radiative forcing effect, and that the lower values associated with less sooty SAF blends would allow for decreased contrail extinction, energy deposition, and warming through radiative forcing.

2.3.3. Linking Chemical Properties to nvPM

Predicting the sooting tendencies across aviation fuels is often complicated by the large quantity and variability of components present. Bulk descriptors of fuel molecular composition are usually employed in understanding fuel sooting tendencies. Because of the significance of aromatic compounds in nvPM formation, as observed across the aforementioned experimental studies, total aromatic content has previously been used as a singular (first order) descriptor of nvPM emissions. However, while reducing aromatic compounds in fuel compositions is one of the most effective ways of reducing aircraft nvPM emissions, using total aromatic content to relate fuel compositions to nvPM emission rates is somewhat of an oversimplification. This is for two main reasons. First, aromatic content does not account for the nvPM produced by aliphatic compounds. Secondly, variability in the sooting tendencies of aromatic compounds exists, most notably between mono-aromatic and di-aromatic families, as was effectively demonstrated by Brem *et al.* [103]. Past experimental data has allowed for the establishment of a general hierarchy of the sooting tendencies across the hydrocarbon classes found in aviation fuels, as given by Calcote and Manos [104]. This hierarchy is as follows, from the lowest (n-paraffins) to highest (polyaromatics) sooting compounds:

n-paraffins < *iso-paraffins* < *olefins* < *cyclo-paraffins (naphthenes)* < *alkynes* < *mono-aromatics* < *di-aromatics* < *polyaromatics (PAH)*

Fuel hydrogen content (or H/C) ratio is now widely considered as the most robust parameter correlating fuel composition to measured nvPM formation, and

has been found to provide the strongest correlation with observed nvPM emissions in previous studies [18], [87], [103], [105], [106]. The use of hydrogen content in PM emissions studies dates back to Schalla and McDonald [107], who suggested that the degree of hydrogen saturation within a hydrocarbon was closely linked to its tendency to soot. As hydrocarbon molecules become less saturated with hydrogen atoms, the free radicals instead form inter-carbon bonds and change the structure and chemical classification of the molecule. With decreasing hydrogen saturation, hydrogen branches are replaced by intermolecular double or triple carbon bonds. These are harder to break than hydrogen functional groups, reducing the available energy from combustion of the molecule. Decreasing hydrogen saturation also correlates with the transition from straight chained or branched molecules to the ringed structures characteristic of cycloalkanes and aromatic compounds described above. Recently, empirical hydrogen content correlations have proven powerful tools in understanding both nvPM number and mass emissions taken using ICAO compliant measurement systems and representative gas turbine rigs, an example of which is shown in **Figure 2-10** [105], [106].

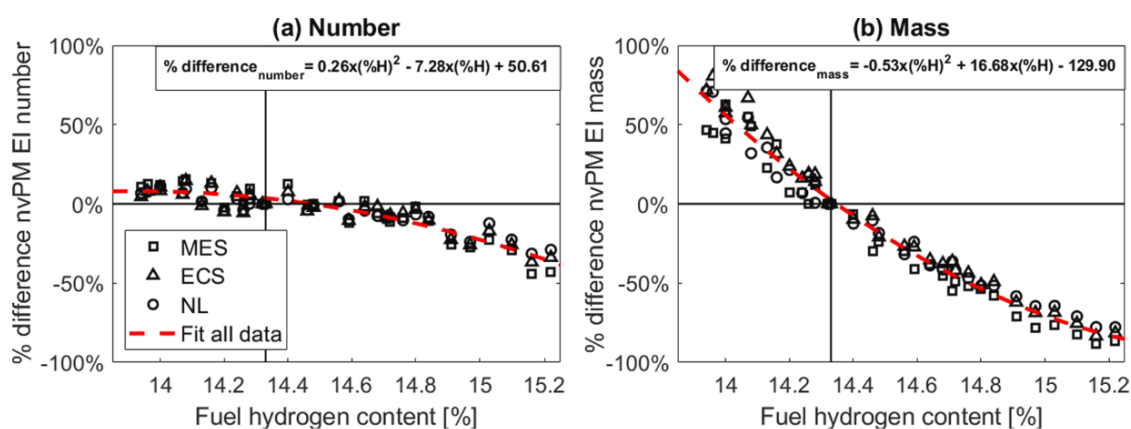


Figure 2-10 - Correlating nvPM number and mass emissions to hydrogen content [106]

Empirically correlating experimentally derived sooting tendencies of fuels using (sole) fuel physicochemical properties can prove a simple but effective tool for researchers. However, it has been known for some time that the numerous influences affecting nvPM formation limit the effectiveness of first order parameters in predicting fuel sooting tendencies. Yang *et al.* [108] suggested that first-order parameters could not be used to adequately describe the dependencies between fuel physicochemical properties and tendencies to soot, and that the added detail provided by compound (“lumped”) parameters composed of several first order

parameters was more suitable. Fuel chemical properties considered in the limitation of nvPM emissions alongside total aromatic content are hydrogen content (mass), di-aromatic content, and smoke point.

Some authors [109], [110], suggest that large quantities (e.g., 20-30% vol.) of di-aromatic compounds in hydrocarbon fuels can increase nvPM emissions above hydrogen content correlations. Rosfjord [110] studied the sooting tendencies of fuels up to 30% Naphthalene content by volume, finding a slightly better correlation between measured soot formation and a compound parameter composed of both Hydrogen content and Naphthalene content ($R^2=0.93$) compared to Hydrogen content alone ($R^2=0.87$).

$$q''_{rad} \propto H^{-1.65} \quad 2-2$$

$$q''_{rad} \propto H^{-1.2}(100 - DA)^{-0.4} \quad 2-3$$

While these trends were determined using flame radiation experiments, representative of soot formation in the combustor, Yang et al. [108] later found the second correlation was the best compound parameter available in the literature for predicting exhaust soot emissions, indicating the significance of di-aromatic compounds soot formation. Naegeli and Moses [109] found that a naphthalene (di-aromatic) content of 20% wt. added to a fuel used in a gas turbine combustor served to increase soot emissions above a hydrogen content trend equivalent to a decrease in hydrogen content by 1% wt. However, it should be noted that these quantities of di-aromatics are much higher than ASTM limits for jet fuels, and so discrepancies to hydrogen content trends can become negligible compared to combustor uncertainties.

Secondly, hydrocarbon sooting propensities can vary for hydrocarbons of equal carbon and hydrogen numbers as a result of differences in fuel molecular structure and isomerisation. Botero *et al.* [111] used a wick burner and a DMS-500 particle analyser to determine the Particle Size Distributions (PSD's) of aliphatic components typically found in petroleum and diesel flames. The authors found that branched iso-paraffins and cyclo-paraffins had a greater tendency to soot and produced larger particles compared to straight chained n-paraffins of the same carbon number. Because the hydrogen content across n-paraffins and iso-paraffins would be expected to remain constant, this acts as an example of a case where Hydrogen content cannot fully describe sooting tendencies. As described in

Section 2.1, iso-paraffins exhibit reduced reactivities compared to n-paraffins, which can worsen combustion characteristics. Further experimental evidence of this is found in counterflow flame tests using ATJ fuels, which exhibit higher sooting tendencies compared to other drop-in fuels of similar hydrogen contents. Xue *et al.* [75] used a non-premixed counter flow burner and Laser-Induced Incandescence (LII) instrument to study the soot formation behaviour of three low aromatic alternative fuels: an FT-SPK, HEFA-Camelina, and ATJ fuel. The FT-SPK and HEFA fuels exhibited molecular weights similar to the Jet A-1, while the ATJ fuel displayed a higher value attributed to a higher i-paraffin content. This given as an explanation for higher measured soot emissions observed for the ATJ fuel, despite exhibiting a similar hydrogen contents to the F-T and HEFA fuel.

2.4. Atomisation in Gas Turbines

As discussed in **Section 1.3.1**, combustion of liquid fuels in gas turbine combustors first requires the breakup of fuel jets or sheets into smaller droplets, which evaporate faster than the bulk liquid and so allow fuel to enter the flame zone as an evenly mixed fuel-air gas. The breaking up of bulk liquid into fine droplets is called atomisation. The goal of atomisation is to maximise the specific area to volume ratio of the spray, which, along with the high temperature conditions experienced in the combustion chamber, increases rates of fuel evaporation [16]. A wide variety of fuel atomisers may be employed to achieve atomisation in aircraft gas turbine engines. Different types of atomiser induce droplet breakup through different processes, exhibit their own unique advantages and disadvantages, and are influenced differently with respect to operating variables and fuel properties.

Atomiser designs commonly utilised in aircraft include pressure atomisers and airblast atomisers. For pressure atomisers, liquid is injected through a small orifice by a high pressure differential. The energy induced by the pressure differential across the orifice is converted into kinetic energy, encouraging turbulent disturbances within the liquid. Meanwhile, airblast atomisers inject liquid at a relatively low injection pressure, and induce instabilities on the bulk liquid by the transferal of kinetic energy from relatively large volumes of air moving at relatively low velocities (typically 60-120 m/s) compared to other atomiser designs such as air-assist atomisers. While this is a comparatively

restricted range of operating velocities to other atomiser types, giving airblast atomisers comparatively narrow stability limits, they are nevertheless ideal for use in continuous flow operations such as aircraft engines, where the large volumes of required combustion air are readily available [112], [113]. This air helps to pre-mix reactants across the different combustion power ranges, often resulting in reduced nvPM formation compared to other atomisers [113]. For this study, airblast atomisers are the primary focus instead of pressure atomisers, and will be described in more depth henceforth.

2.4.1. Atomisation Mechanisms

2.4.1.1. Classical Atomisation

The process of atomisation typically follows the classical mode of liquid breakup, which considers the breakup of bulk liquid from instabilities which formed on a liquid surface. This stems from the breakup of a liquid jet from instabilities originally described by Lord Rayleigh [114]. These instabilities grow to eventually overcome the forces binding the liquid together, causing it to separate into smaller geometries. The ease in which these instabilities form and mechanism by which droplets break up is heavily controlled by turbulence, making the Reynolds number (Re) a useful dimensionless variable when applied to the study of atomisation.

$$Re = \frac{\rho UL}{\mu} \quad 2-4$$

Following injection of fuel from an atomiser, atomisation can effectively be separated into primary atomisation and secondary atomisation. Primary atomisation describes the initial breakup of liquid into large droplets or ligaments, caused by internal forces and turbulent profiles within a liquid sheet or jet counteracting the physical forces binding the liquid together. Secondary atomisation is the subsequent breakup of the droplets formed from primary atomisation into smaller droplets as a result of aerodynamic forces acting on the liquid surfaces. For low viscosity fluids (water, jet fuel), the breakup of droplets in a flowing stream (e.g. coflowing air) is best described by the Weber (We) number, which is a dimensionless variable defined as the ratio of the external aerodynamic pressure forces against liquid surface tension forces, which act to bind the droplet together. When the surface tension forces are overcome by the

external aerodynamic forces then droplet breakup will occur. Therefore, a high Weber number indicates an increased likelihood of droplet breakup leading to finer atomisation. Weber number is defined in **Equation 2-5**:

$$We = \frac{\rho_a U_R^2 L}{\sigma_L} \quad \text{where } U_R \approx U_a \text{ for low liquid flowrates} \quad 2-5$$

Where L is a characteristic length, most commonly given as the diameter of a spherical droplet with aerodynamic pressure forces applied to it and U_R is the relative velocity between the air and fuel. Another key dimensionless number used in atomisation studies was derived by Ohnesorge, as described by [112] who studied the breakup of a jet at increasing Re number. It was found that jets of lower Re number tended to break up through internal oscillations free of air friction (Rayleigh breakup mechanism). At higher Re numbers, the influence of air friction induces oscillations in the jet, which transitions to a wave-like breakup mechanism. Finally, very high Reynolds numbers cause the jet to immediately transition to secondary atomisation, where droplet break up is very fast. These stages are shown in **Figure 2-11**.

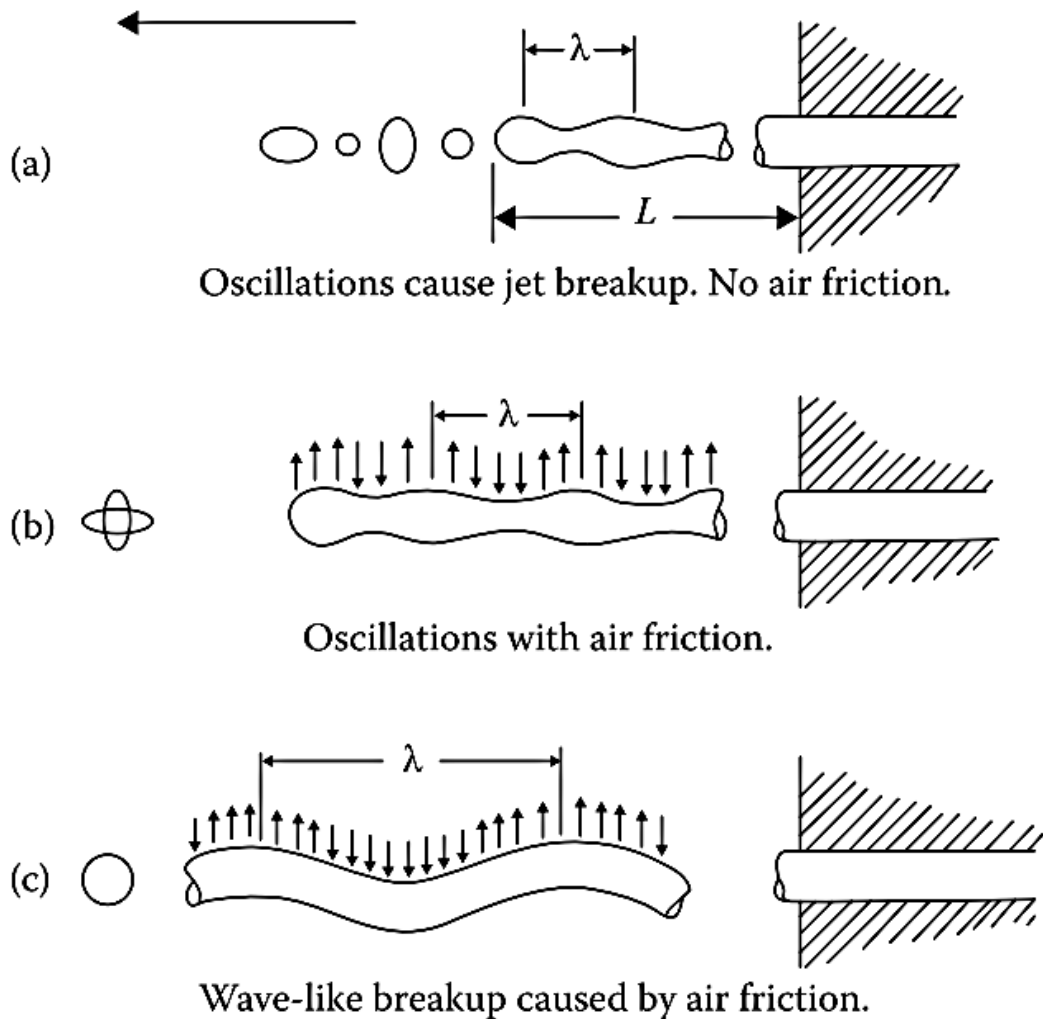


Figure 2-11 - Examples of liquid jet breakup mechanisms [112]

The dimensionless number used to characterise each stage of breakup with respect to Re number was the Ohnesorge (Oh) number, which acts as a measure of resistive fuel property forces within a jet, including viscosity, and given by **Equation 2-6**.

$$Oh = \frac{\sqrt{We}}{Re} = \frac{\mu}{\sqrt{\rho\sigma L}} \quad 2-6$$

Airblast atomisers may be separated into two categories. Plain jet atomisers introduce fuel as a jet (e.g. through a central orifice) which is then atomised by large volumes of air. Prefilming airblast atomisers introduce fuel as a flat or conical sheet using a prefilming surface (or “lip”). This increases the surface area of the fluid in contact with the air stream, maximising the aerodynamic forces applied to it [16]. Prefilming airblast atomisers are known to exhibit superior atomisation performance over plain jet airblast atomisers, and

are associated with excellent atomisation at elevated ambient pressures [112]. For atomisers which introduce liquid as a sheet as opposed to a jet, breakup of the liquid follows the wavy sheet mechanism, as shown in **Figure 2-12** [112].

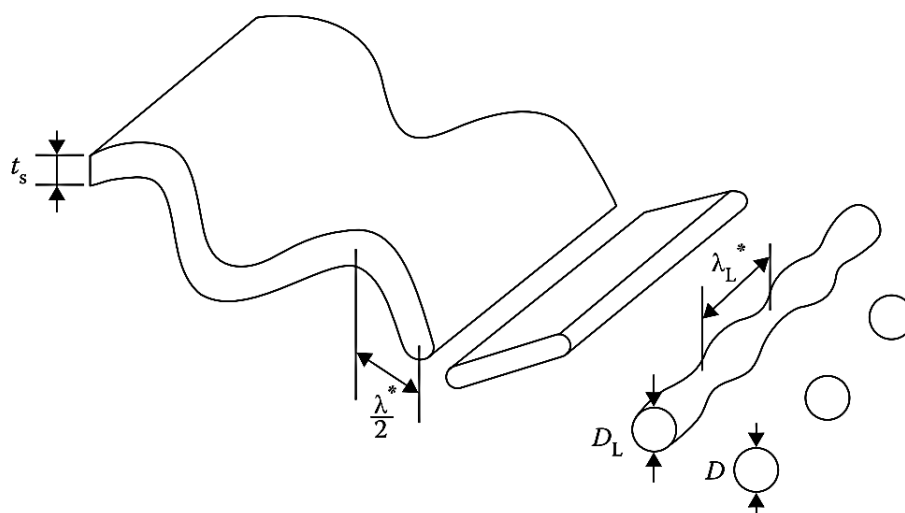


Figure 2-12 - Wavy jet breakup [112]

2.4.1.2. Prompt Atomisation

For airblast atomisers, an alternative mode of atomisation to the classical regime first described by Lefebvre [115] is the prompt mode of atomisation. This is found in cases where the aerodynamic forces acting on the liquid film are so great that atomisation occurs almost instantaneously, bypassing the normal method of wavy instability formation. The authors noted that both the classical “wavy-sheet” breakup mechanism and the prompt mechanism could occur at any flow condition in prefilming airblast atomisers, but would likely be more prevalent at very high flowrates. Prompt atomisation is also encouraged in atomisers with steep angles of impingement between the air and the liquid, or where there is a very high relative velocity between the liquid sheet and the air. Lefebvre and Balal [16] state that it is common for atomisers to follow the classical regime more closely at low We numbers, and transition to the prompt regime as flowrates and We numbers increase. Unlike classical atomisation regimes, prompt atomisation serves to decouple the quality of the atomised spray from the effects of liquid viscosity, which can potentially allow for greater fuel flexibility in aircraft engines.

2.4.2. Characterising Atomisation Quality

In a hypothetical perfect atomiser, liquid is assumed to instantaneously evaporate and evenly mix with air before combustion, thereby behaving as a premixed gaseous flame. In practice however, polydisperse liquid sprays are generated by aircraft atomisers often approximating a normal or log-normal Particle Size Distribution (PSD). An example is as shown in **Figure 2-13**.

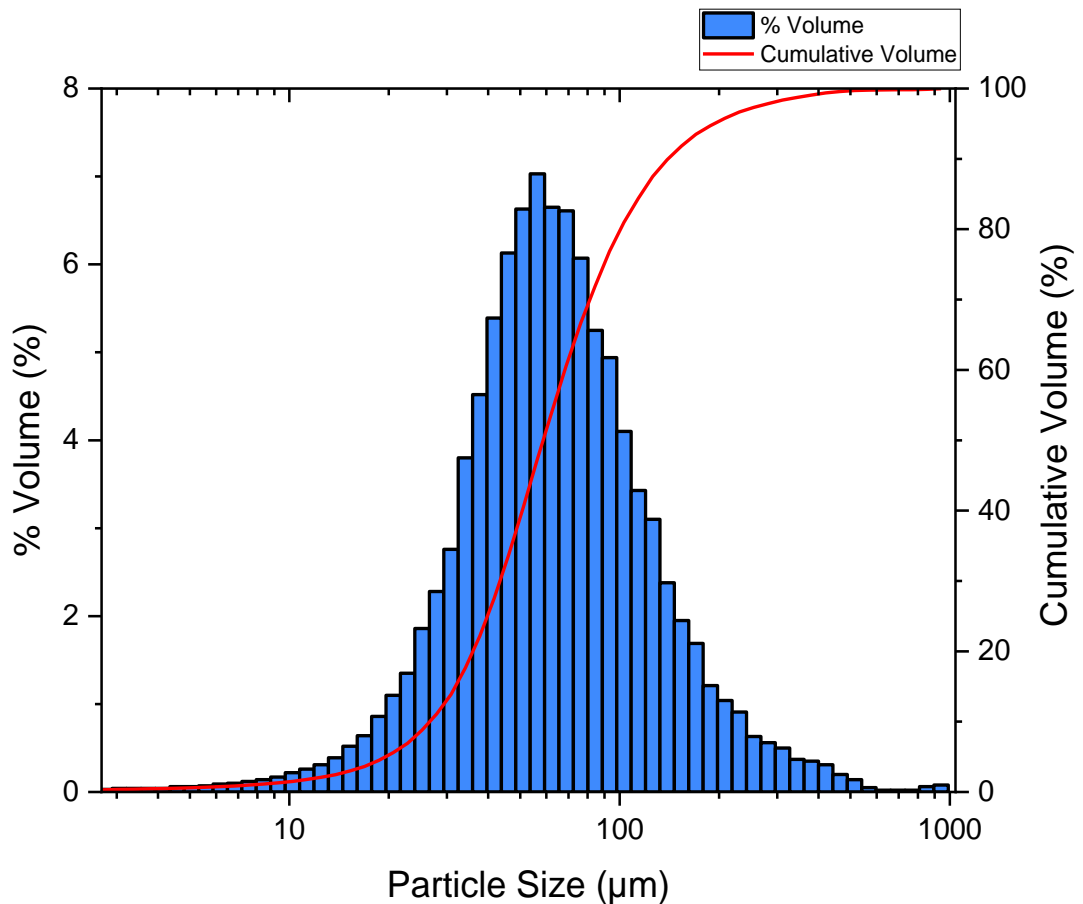


Figure 2-13 - Typical Particle Size Distribution (PSD) for a spray

Characterisation of atomisation quality can be achieved by determining key statistical parameters relating to the PSD of the spray. Often it is useful to use mean diameters to summarise the PSD of an entire spray. A commonly used parameter is the Arithmetic Mean Diameter (AMD, D_{10}), representative of the mean diameter of the spray calculated on a number basis, given in **Equation 2-7**.

$$AMD, D_{10} = \frac{\sum_{i=1}^n d_i}{n} \quad 2-7$$

Undoubtedly the most common variable used for combustion scenarios is the Sauter Mean Diameter (SMD, D_{32}), defined as the ratio of the total volume of droplets in the spray to the total surface area of those droplets. This measure is representative of a single droplet of the same ratio of volume to surface area as the total spray [112]. SMD values help to define the evaporation characteristics of a spray and so are most useful for combustion applications, with low values indicating fine atomisation and vice versa. However, it should be noted that SMD values are volume weighted, and the presence of even a few larger droplets present in a spray can skew values towards larger droplet size more significantly than a number weighted average such as AMD. The equation for SMD values is given by *Equation 2-8*.

$$SMD, D_{32} = \frac{\sum_{i=1}^n d_i^3}{\sum_{i=1}^n d_i^2} \quad 2-8$$

It is worth mentioning some other volume-based variables commonly used in droplet size characterisation. The $D_{0.1}$, $D_{0.5}$ (also called the Mass Median Diameter, MMD), and $D_{0.9}$, which describe droplet sizes below which 10%, 50%, and 90% of the spray volume lies, respectively. These variables can be useful, as they provide additional information on the PSD shape and range of droplet sizes, as shown in relation to typical airblast atomiser spray drop size frequency curve (Rosin-Rammler distribution), shown in *Figure 2-14*. The D_{peak} describes the most frequent droplet size of the distribution, located at the peak of the curve. However, while these variables are useful as a background for droplet size characterisation, SMD will be the sole volume-based variable utilised for this work henceforth.

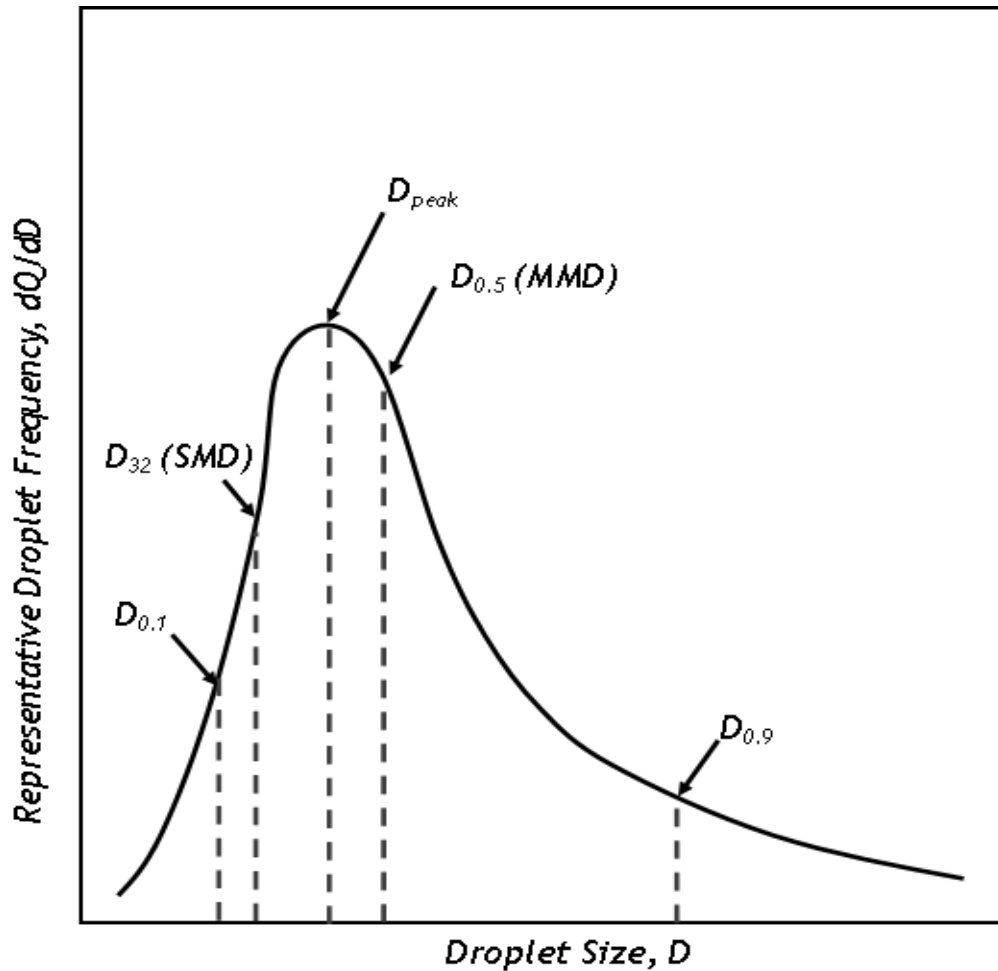


Figure 2-14 - Airblast spray droplet frequency distribution with several mean diameter locations, recreated from [112]

2.4.3. The Impact of Atomisation Quality on Emissions

Atomisation is known to impact rates of emissions in gas turbines [16], [18]. In combustion settings, fine sprays are required for high volumetric heat release, good light-up behaviour, and wider combustor operating condition ranges [16], [116]. Coarser liquid sprays exhibit reduced specific surface area to unit volume of droplets, which slows evaporation rates and increases the likelihood of larger droplets propagating downstream of the primary zone. Large liquid droplets which reach the flame zone undergo “droplet burning”, during which they burn as diffusion (“envelope”) flames from the outside of the droplet inwards, as in **Figure 2-15**. Droplet burning is less efficient compared to well-mixed gaseous combustion, exhibiting higher combustion residence times, leading to reduced overall uniformity of fuel-air mixing [116].

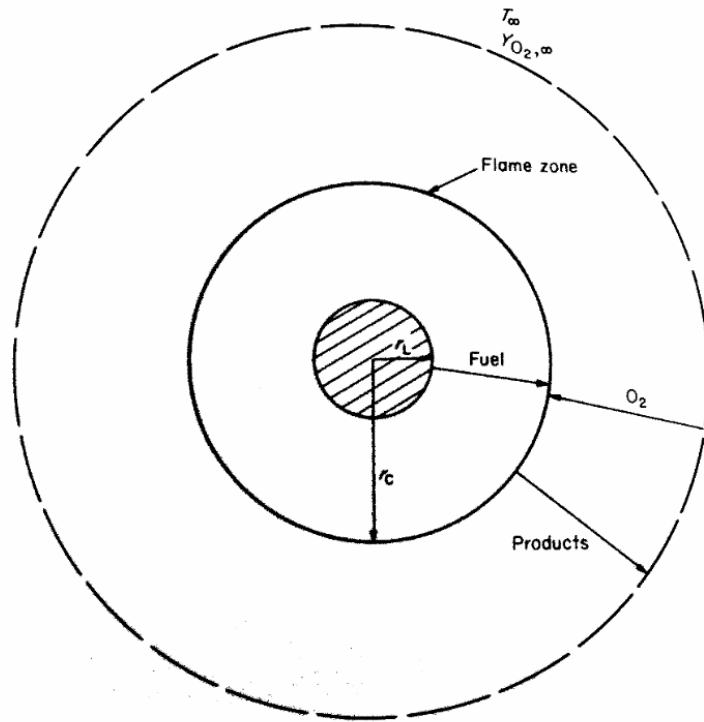


Figure 2-15 - Droplet burning [116]

Localised rich zones coupled with the longer residence times of low-speed recirculating flows can exacerbate nvPM emissions under these conditions, especially for RQL type combustors where primary zones are very rich [18]. CO and UHC formation are also worsened due to the increased residence time for evaporation of larger droplets, which reduces the time available for combustion reactions necessary to convert fuel hydrocarbons to CO_2 , thereby decreasing the overall efficiency of combustion [16]. Poor atomisation may be especially prominent at low power conditions, since atomisation quality and combustion efficiency general improves with increased power settings [18]. It is therefore desirable among gas turbine engine manufacturers to prevent both droplet burning and uneven mixing by designing atomisers which produce highly uniform fine sprays across all engine operating conditions. Even a small number of large droplets may be expected to promote droplet burning in gas turbine settings, and this demonstrates how SMD values can prove useful in liquid combustion settings, since larger droplets holding higher liquid volumes would be expected to skew measured SMD values more significantly than smaller ones. It is suggested that sprays with SMD values between 40-80 μm should be utilised in gas turbine combustion [117].

While the effects of fuel chemistry on nvPM formation are well documented, to the authors' knowledge, there appear to be fewer studies exploring the impact of fuel physical properties and atomisation quality on nvPM formation in gas turbines. This may be due to the anticipated small variations expected compared to fuel chemistry, but are nevertheless, believed to be worth investigating in the context of SAF. Rink and Lefebvre [19] demonstrated that emissions of nvPM, CO, and UHC were worsened by poorer atomisation quality. The authors used a specially designed combustor operating with a diesel oil fuel to isolate the impacts of three different SMD sizes (30 μm , 70 μm , and 110 μm) on soot formation while keeping all other conditions constant, finding that 50% reductions in soot exhaust concentration levels could be achieved when the fuel spray was reduced from 110 μm to 30 μm , with this effect becoming more prominent as combustor pressure and equivalence ratios increased. However, the fuel utilised was a diesel fuel and not representative of aviation fuels.

Zahmatkesh and Moghiman [118] undertook computational simulations using a turbulent flame model combustor. Flames generated using fine droplets (15-50 μm) were found to produce a higher number of soot particles near the atomiser compared to coarse droplets (50-120 μm). The particles produced however were much smaller, and would subsequently oxidise more rapidly in comparison, resulting in considerably lower soot mass fraction by the combustor exit, as shown in **Figure 2-16**. It is noted that these variations of SMD values are considerably higher than expected from drop-in fuels, which are ideally intended to replicate the physical properties of a Jet A fuel.

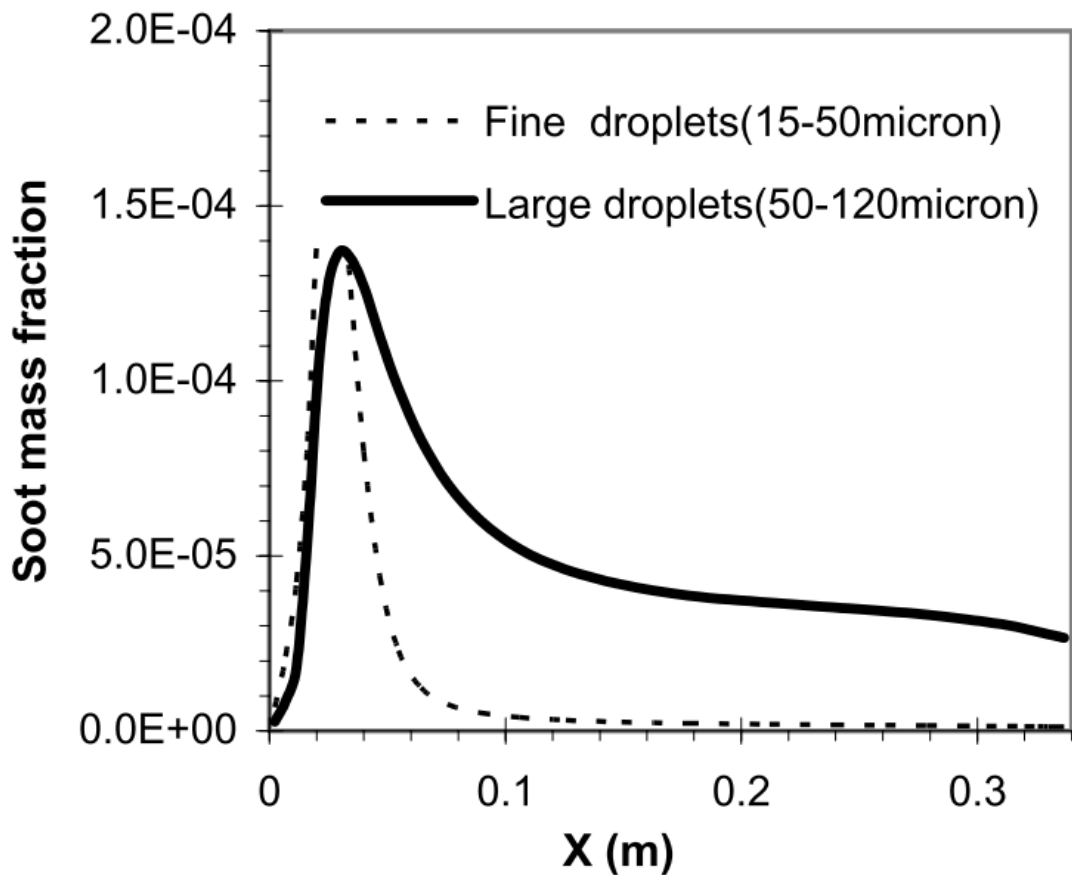


Figure 2-16 - Variation in modelled soot formation in a model combustor for sprays of differing droplet sizes [118]

2.4.4. Factors Affecting Atomisation for Airblast Atomisers

A number of physical factors influence the atomisation quality produced by an airblast atomiser. As mentioned, essentially the only prerequisite for droplet breakup in airblast atomisers is the presence of a relative velocity (U_R) between the fuel liquid and the fluid medium it interacts with [112]. Intuitively, a higher airspeed of the atomising air at the point of interaction with the liquid will result in improved droplet breakup, and this has been observed in the work of [112], [113]. However, it may be noted that a key drawback with airblast atomisers is that they experience very poor atomisation below a certain air velocity threshold (~ 40 m/s), as observed by [119], which makes them prone to poor atomisation at low power conditions [16].

Assuming the operating conditions of aircraft atomisers are held constant, atomisation effectiveness can be assumed to be solely dependent on variations in fuel physical properties. These can effectively be separated into two categories: 1) fuel properties directly resisting the breakup of liquid into smaller volumes such

as surface tension, viscosity, and density, and 2) evaporative properties affecting subsequent evaporation rates of the droplets before combustion, such as vapour pressure and volatility. The main physical properties directly resisting atomisation are surface tension, viscosity, and density, any increase in which typically results in reduced atomisation and a coarser spray. Of these properties, surface tension and viscosity are thought to have the most significant impacts. Surface tension is effectively responsible for physically binding a liquid together and resisting the breakup of large droplets into separate smaller geometries [112]. As such, surface tension plays a key role in resisting the breakup of bulk fluid in atomisation. Meanwhile, liquid viscosity is responsible for resisting any changes to a fluid's surface geometry, and plays a somewhat more complex role in the atomisation process. Additionally, more viscous fluids impart a higher resistance to the formation of wavy instabilities key to classical breakup mechanisms. Liquid fuel density is generally considered to reduce atomisation quality [120], although to a relatively smaller degree compared to surface tension and viscosity. Particularly in the case of jet fuels, which typically exhibit a narrow range of densities [112].

Some recent studies have explored the impacts of varying fuel physical properties across drop-in fuels on atomisation characteristics. For example, Charalampous and Hardalupas [121] measured variations in density, dynamic viscosity, kinematic viscosity, and surface tension of +5%, -5%, -10% and +5% for an HRJ fuel compared to a reference JP-8, respectively. These variations were found to have a minimal effect on the external morphology of the jet produced from a plain orifice atomiser, but did influence the internal morphology, which could in turn influence atomisation performance by increasing turbulent disturbances responsible for primary jet breakup. Vouros *et al.* [122] explored the differences in sprays produced by a generic full cone pressure atomiser operating with conventional reference Jet A-1 and representative drop-in fuels. The drop-in fuels consisted of a base GTL fuel (99% paraffins), which was blended with pure hydrocarbon components to determine the impact of different hydrocarbon families. These blends included an 80% Paraffin-20% Aromatic blend (P-Ar), 60% Paraffin-40% Naphthene blend (P-N) and a 50% Paraffin-30% Naphthene-20% Aromatic blend (P-N-Ar). Differences in physical properties across fuels were found to differ by up to 10%, resulting in variability to SMD values of 10-20% across the fuels. The Jet-A1 fuel was found to produce the largest SMD values, while the highly paraffinic fuel produced the smallest. Dafsari *et al.* [123]. explored the impact of

varying fuel viscosity on the spray quality produced by a pressure swirl atomiser by altering the preheat temperature of the fuel. It was found that increasing viscosity served to decrease atomisation quality, with liquid viscosity having a greater effect on cone angle even than injection pressure. Peak SMD values were found to increase by 45 μm (66%), while average SMD values were found to increase by 36 μm (74%).

However, to the authors' knowledge, studies exploring the variability of spray properties across airblast atomisers operating with drop-in fuels are very few. It may be noted that airblast atomisers are considered less sensitive to liquid viscosities than most atomisers since the low airspeeds make Reynolds number less sensitive to viscosity changes [124]. Reeves *et al.* [124] suggested that variability in SMD values produced by airblast atomisers, with respect to surface tension and viscosity, could be described by the correlation given in **Equation 2-9**.

$$SMD \propto \sigma^{0.35} \mu^{0.05} \quad 2-9$$

Where σ is surface tension and μ is dynamic viscosity. Other authors have suggested different weightings for the impacts of each property, and the impact of viscosity in atomisation especially is thought to be not well understood [112]. However, realistic ranges in the exponents for each property in **Equation 2-9**, based on previous experimental studies, are suggested as 0.2-0.6 for surface tension and 0.06-0.2 for viscosity [125].

2.4.5. Prefilming Airblast Atomiser Empirical Correlations

Towards the end of the 20th century, much work was undertaken in studying the sprays generated by atomisers, including prefilming airblast atomisers. For most of these studies, empirical correlations were derived from individual droplet size datasets for atomisers of varying designs and across a range of specified atomisation conditions. These correlations are effectively a means of benchmarking the performance of an atomiser and allow predictions of SMD changes with regards to different atomiser features and fuel properties. Most of the correlations were also derived using the prefilming airblast atomiser design given in **Figure 2-17**. This design used two air channels surrounding the prefilming surface along which liquid fuel is directed, with a central pintle employed to channel the inner air towards the atomising lip.

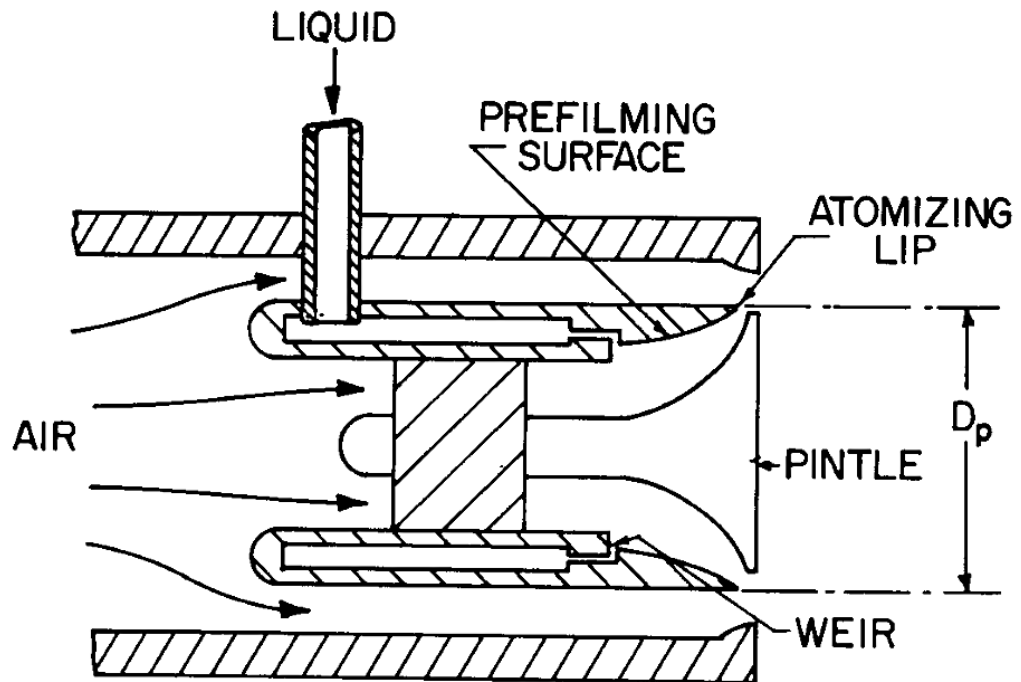


Figure 2-17 - Pintle type prefilming airblast atomiser [16]

However, variability in atomiser designs and tested range of conditions mean that SMD values predicted from different equations can vary significantly and caution must be used when attempting to fit them to experimental droplet size data. This was demonstrated by Gepperth *et al.* [126], who compared calculated SMD trends from several correlations found in the literature alongside their own experimental droplet size data. It was concluded that, while published SMD correlations typically are able to adequately capture the general trends of experimentally measured data, they could differ from both each other and the authors own experimental data across varying flow conditions by orders of magnitude in some cases. The best option is therefore to characterise atomisers individually for an expected range of operating conditions using experimental data, with respect to a given characteristic variable.

Most empirical correlations relating to the classical regime of atomisation stem from the general dimensionless equation defined by Lefebvre and Balal [16] (**Equation 2-10 and Equation 2-11**). This effectively separates the parameters affecting atomisation into two terms: the first dominated by aerodynamic forces and incorporating the We number, and the second dominated by viscous fuel properties described by the Oh number.

$$\frac{SMD}{L_c} = \left(1 + \frac{1}{ALR}\right)(AWe^{-0.5} + BOh^{0.5}) \quad 2-10$$

$$\frac{SMD}{L_c} = A \left(\frac{\sigma}{\rho_a U_a^2 L}\right)^{0.5} \left(1 + \frac{1}{ALR}\right) + B \left(\frac{\mu_L^2}{\sigma \rho_L L}\right)^{0.5} \left(1 + \frac{1}{ALR}\right) \quad 2-11$$

The characteristic length (L_c) is an arbitrarily chosen value typically used to represent the effect of changing the atomiser scale. The value of L is another characteristic length chosen for We number calculations, and is often assigned as the prefilming diameter (D_p). Lefebvre and McDonell [112] explain that, while the above equation is generally applicable to prefilming airblast atomisers, improvements can be made based on practical observations of atomiser tests. Raising the exponent of $\left(\frac{\sigma}{\rho_a U_a^2 D_p}\right)$ from 0.5 to 0.6 was believed to make the equation more robust to the Re number of the liquid stream and Mach number of the airstreams, which are affected by physical phenomena not understood at the time of writing. Similarly, the addition of the term $\left(\frac{\rho_L}{\rho_a}\right)^{0.1}$ was thought to account for experimental observations of airblast sprays where higher density liquids push the point of atomisation further downstream, delaying atomisation. This yields the modified equation given by **Equation 2-12**.

$$\frac{SMD}{L_c} = A \left(\frac{\sigma_L}{\rho_a U_a^2 D_p}\right)^{0.6} \left(\frac{\rho_L}{\rho_a}\right)^{0.1} \left(1 + \frac{1}{ALR}\right) + B \left(\frac{\mu_L^2}{\sigma_L \rho_L D_p}\right)^{0.5} \left(1 + \frac{1}{ALR}\right) \quad 2-12$$

Although the assignment of L_c is somewhat arbitrary, the choice of L_c is a crucial component in airblast empirical equations. The prefilming of the liquid into a thin sheet prior to coming into contact with atomisation air has been highlighted as an important variable in atomisation studies. As such, film thickness (t) is a valid choice for L_c . In the original document for the Parker-Hannifin type nozzle [127] liquid film thickness (t) is described simply as a feature of the fuel path annulus geometry. In many cases this may prove an adequate representation of the film thickness, and so thinner films can be achieved by implementing narrow fuel channels into airblast atomiser designs.

Studies by Rizkhalla *et al.* and Lefebvre [113], [120] explored the effects of air and fuel properties on atomisation behaviour with the inclusion of t as the characteristic variable, leading to the following generic correlation:

$$SMD = \left\{ A \frac{(\sigma_L \rho_L t)^{0.5}}{\rho_A U_A} \left(1 + \frac{\dot{m}_L}{\dot{m}_A} \right) \right\} \quad 2-13$$

$$+ \left\{ B \left(\frac{\mu_L^2}{\sigma_L \rho_A} \right)^{0.425} t^{0.575} \left(1 + \frac{\dot{m}_L}{\dot{m}_A} \right)^2 \right\}$$

Using experimental data and known values of film thickness (t), the constants A and B were determined for the atomiser used, giving the equation:

$$SMD = \left\{ 6.5 \times 10^{-4} \frac{(\sigma_L \rho_L)^{0.5}}{\rho_A U_A} \left(1 + \frac{\dot{m}_L}{\dot{m}_A} \right) \right\} \quad 2-14$$

$$+ \left\{ 1.2 \times 10^{-4} \left(\frac{\mu_L^2}{\sigma_L \rho_A} \right)^{0.425} \left(1 + \frac{\dot{m}_L}{\dot{m}_A} \right)^2 \right\}$$

Jasuja [128] undertook experiments using kerosene, gas oil and heavy fuel oils. Using the same equation, the authors found that values $A = 9.0 \times 10^{-4}$ and $B = 0.75 \times 10^{-4}$ gave the best correlations to the lower viscosity kerosene and gas oil fuels. However, an increasing disparity between experimental and predicted data was evident for the higher viscosity heavy oil fuel. Aiming to develop a correlation able to accurately describe a wider range of fuel viscosities, the authors modified the correlation given by Rizkhalla *et al.* [109] by reducing the exponent of the $(1+1/AFR)$ term, and tuned the A and B constants to their own dataset. This equation is given as:

$$SMD = \left[(1.0 \times 10^{-3}) \frac{(\sigma_L \rho_L)^{0.5}}{(\rho_a U_A)} \right. \quad 2-15$$

$$\left. + (0.6 \times 10^{-4}) \left(\frac{\mu_L^2}{\sigma_L \rho_a} \right)^{0.425} \right] \left(1 + \frac{\dot{m}_L}{\dot{m}_A} \right)^{0.5}$$

El-Shanawany and Lefebvre [129] explored the effect of general linear scale on atomisers, using the prefilming diameter (D_p) as the characteristic length rather than film thickness. This was justified by the fact that increasing atomiser scale served to increase film thickness at the same rate as D_p . Similarly to Jasuja, the authors utilised a range of fuels of varying fuel properties. This included water, kerosene, and a kerosene/Hyvis polybutene no. 05 blend with an absolute

viscosity an order of magnitude higher than unblended kerosene. It was found that increasing linear size served to reduce atomisation quality, with a general correlation of $SMD \propto D_p^{0.43}$ (water sprays) given. However, ultimately this observation was attributed to the increase in film thickness associated with larger atomisers. Low viscosity liquids were dependant on surface tension described by $SMD \propto \sigma_l^{0.6}$. For liquids of higher viscosity, the following correlation was suggested:

$$SMD = \left\{ A \left(\frac{\sigma_L}{\rho_A U_A^2} \right)^{0.6} \left(\frac{\rho_L}{\rho_A} \right)^{0.1} D_p^{0.4} \left(1 + \frac{\dot{m}_L}{\dot{m}_A} \right) \right\} \quad 2-16$$

$$+ \left\{ B \left(\frac{\mu_L^2 D_p}{\sigma_L \rho_L} \right)^{0.5} \left(1 + \frac{\dot{m}_L}{\dot{m}_A} \right) \right\}$$

Using the dataset provided by Rizkhalla *et al.* to determine A and B constants, this becomes:

$$SMD = \left\{ 0.073 \left(\frac{\sigma_L}{\rho_A U_A^2} \right)^{0.6} \left(\frac{\rho_L}{\rho_A} \right)^{0.1} D_p^{0.4} \left(1 + \frac{\dot{m}_L}{\dot{m}_A} \right) \right\} \quad 2-17$$

$$+ \left\{ 0.015 \left(\frac{\mu_L^2 D_p}{\sigma_L \rho_L} \right)^{0.5} \left(1 + \frac{\dot{m}_L}{\dot{m}_A} \right) \right\}$$

Elsewhere [16], a dimensionless form of this equation has been provided with the hydraulic diameter of the air exit duct (D_H) assigned as the characteristic variable, while the characteristic length used for calculation of We number is kept as the prefilming diameter. The hydraulic diameter in these studies was assumed as the orifice outlet diameter at the atomiser exit plane, yielding the following correlation:

$$\frac{SMD}{D_H} = \left\{ 0.33 \left(\frac{\sigma_L}{\rho_A U_A^2 D_p} \right)^{0.6} \left(\frac{\rho_L}{\rho_A} \right)^{0.1} \left(1 + \frac{\dot{m}_L}{\dot{m}_A} \right) \right\} \quad 2-18$$

$$+ \left\{ 0.068 \left(\frac{\mu_L^2}{\sigma_L \rho_L D_p} \right)^{0.5} \left(1 + \frac{\dot{m}_L}{\dot{m}_A} \right) \right\}$$

Across all of the aforementioned studies, it was found that, for fuels of relatively low viscosity such as gasoline, kerosene, and water, the second term tended to become negligibly small, and atomisation is dominated by the first term. This removes viscosity as a factor affecting atomisation and considers We number

as the sole descriptor of total atomisation forces. The same is true in cases where the prompt mechanism proposed by Lefebvre (**Section 2.4.1.2**) is dominant, such as in atomisers operating at high flow conditions and with steep relative angles of inclination between fuel and air paths. Because atomisers may transition from classical to prompt atomisation as air flowrates increase, Lefebvre and Balal [16] state that it is not uncommon for a particular equation to be most applicable under low flow conditions, only to prove inferior to another under high flow conditions where different physical atomisation processes may come into effect.

As with the general form of the classical predictive equations, a general equation for prompt atomisation can be defined for individual atomisers, described below:

$$SMD = 3t \left[1 + \frac{CWe}{1 + \left(\frac{1}{ALR}\right)} \right]^{-1} \quad 2-19$$

Where $We = \rho_l U_a^2 t$, which it may be noted uses the density of liquid as opposed to density of air for calculation, and assigns film thickness (t) as the characteristic dimension (L). In their original study, the value of C calculated was 0.00175, resulting in the following correlation:

$$SMD = 3t \left[1 + \frac{0.00175We}{1 + \left(\frac{1}{ALR}\right)} \right]^{-1} \quad 2-20$$

Tareq *et al.* [117] studied the atomisation characteristics of a prefilming airblast atomiser nozzle based on the Parker-Hannifin design [127] operating using water and Jet A-1, finding that the average SMD produced by a prefilming airblast atomiser decreased by approximately 30 μm for Jet A-1 over water. It is noted that this atomiser is of similar design to the atomisers employed in this study, which will be described in further detail in subsequent sections. Linear regression was employed to determine optimal values of A and B in the equation proposed by Lefebvre (**Equation 2-11**), using prefilming diameter to calculate We number and film thickness as the characteristic length. Unlike the previous studies, it was decided that the varying properties of water and Jet A-1 (particularly surface tension) were such that the two fuels required separate A and B constants. These were determined using extensive PDA data at varying locations downstream of the

atomiser. As such, empirical correlations derived using water were not recommended for prediction of Jet A fuels. However, it is hypothesised that the properties of drop-in fuels are similar enough to each other to allow for a single empirical correlation, which could help to relate any impacts of spray quality on observed combustion behaviour and emissions in experimental work. The resultant correlations are given by *Equations 2-21 and 2-22*, while *Figure 2-18* shows variations in calculated A and B values with increasing distance from the atomiser exit:

$$\frac{SMD}{t} = 1.299 \left(\frac{\sigma}{\rho_a U_a^2 D_p} \right)^{0.5} \left(1 + \frac{1}{ALR} \right) + 34.184 \left(\frac{\mu_L^2}{\sigma \rho_L D_p} \right)^{0.5} \left(1 + \frac{1}{ALR} \right) \quad (Water) \quad 2-21$$

$$\frac{SMD}{t} = 5.243 \left(\frac{\sigma}{\rho_a U_a^2 D_p} \right)^{0.5} \left(1 + \frac{1}{ALR} \right) + 22.995 \left(\frac{\mu_L^2}{\sigma \rho_L D_p} \right)^{0.5} \left(1 + \frac{1}{ALR} \right) \quad (Jet A - 1) \quad 2-22$$

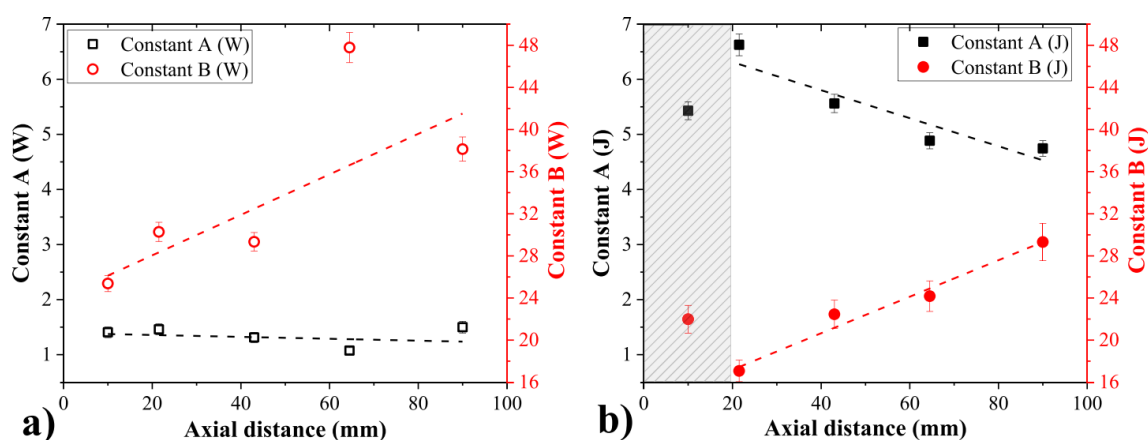


Figure 2-18 - A and B regression coefficients [117]

2.5. Cone Angles

In addition to the atomisation quality itself, the cone angle of the spray produced by an atomiser requires consideration in gas turbine combustion, acting as an effective measure of droplet dispersion and spatial distribution [117]. Generally, it is thought that increased cone angle is preferable for combustion since it is accompanied by improved atomisation, better fuel-air mixing and a

more even dispersion of droplets within the combustor volume [123]. Wider cone angles also reduce flame penetration downstream of a combustor, bringing the flame closer to the atomiser exit, helping to improve flame stability and increasing the AFR at which Lean BlowOut (LBO) occurs [130]. This is an advantage of prefilming airblast atomisers, which generally exhibit wide cone angles across most operating conditions [112]. However, it should also be considered that very wide cone angles have also been seen to increase nvPM concentrations in the primary zone [25].

For airblast atomisers, spray cone angles are mainly influenced by atomiser designs, fluid flow rates, combustor operating pressures, and fuel properties. Tareq *et al.* [117] commented on the impacts of fuel properties and pressure drop (dP/P) on the spray cone angle produced by a prefilming airblast atomiser, finding that switching from water to Jet A-1 increased the cone angle from 45° to 57.5° , as shown in **Figure 2-19**. The higher cone angles are observed for the Jet A-1 spray, which was attributed to the significantly lower surface tension compared to water. This outweighed the anticipated decrease in cone angle as a result of the higher viscosity of Jet A-1.

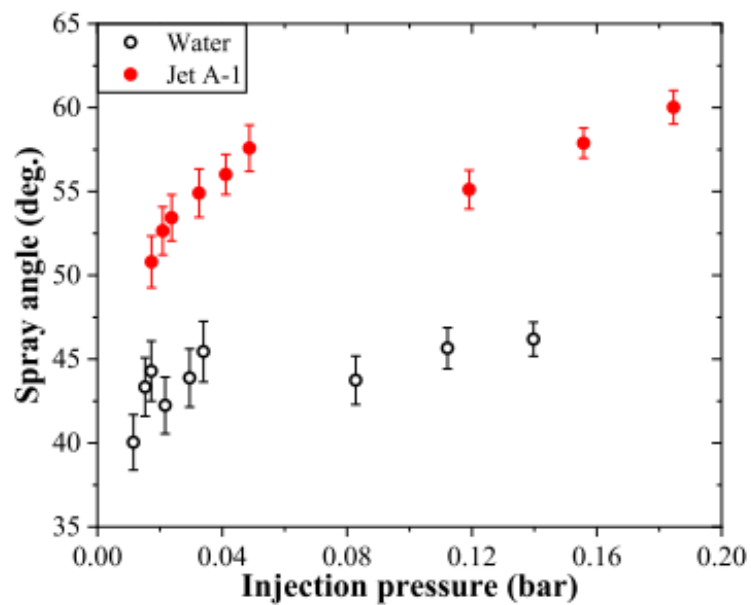
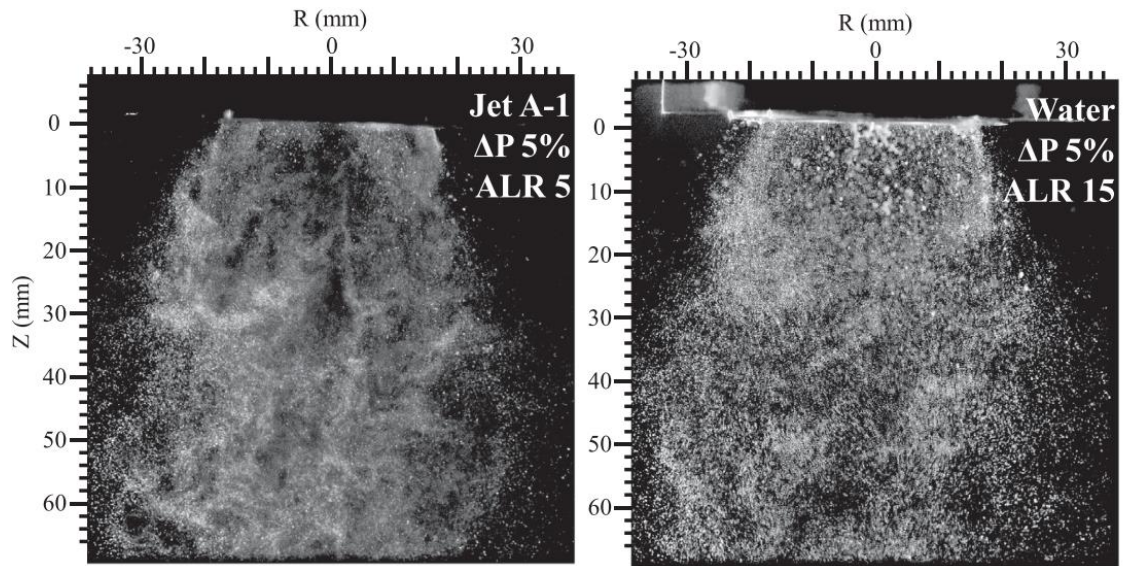


Figure 2-19 - Example of the differences across Jet A-1 and water sprays for a prefilming airblast atomiser [117]

Airblast atomiser spray structures have been described as typically less affected by ambient pressures compared to other atomiser designs at constant AFRs [112]. However, predicting the impact of ambient pressure and other operating conditions on spray cone angles can be complicated by the interdependencies between variables in combustion environments. Increasing the pressure drop across an airblast atomiser is known to narrow the cone angles, while also improving atomisation due to higher air velocities [131]. However, when ambient pressure is increased at a constant fuel flowrate, but the air flowrate is adjusted to match the atomiser pressure drop, spray cone angles have been seen to decrease [131], [132]. An example of this provided by Zheng *et al.* [131] is shown in *Figure 2-20*.

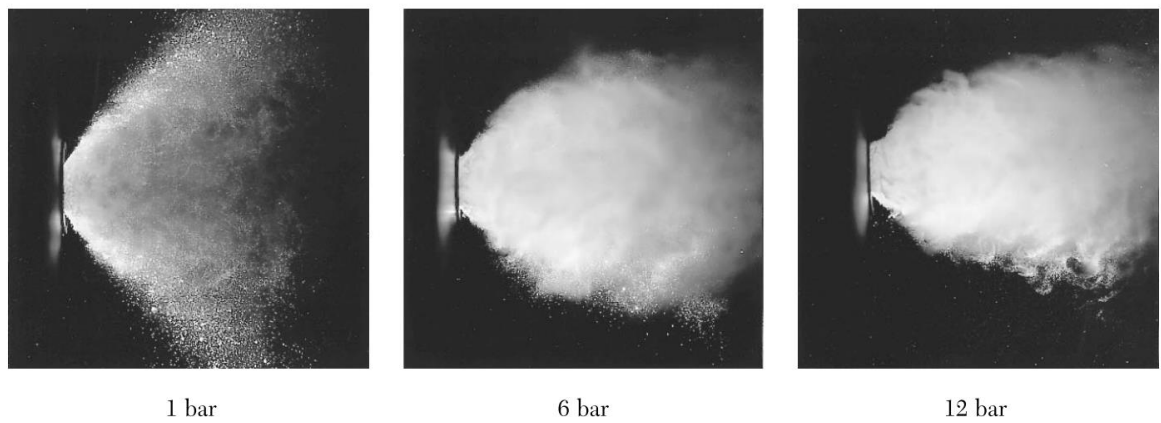


Figure 2-20 - Airblast atomiser sprays at increasing ambient pressures at a fuel flowrate of 35 g/s, and dP/P of 0.05 [131]

In the same study [131], pressure was increased for a constant dP/P and AFR, achieved by increasing both air and fuel flowrates. This is considered representative of increasing power conditions in real world aircraft. Increasing fuel flowrate alone had been shown to increase cone angles, with the effect being greatest with increasing distance from the atomiser exit. This effect was seen to outweigh that of the decrease in cone angle due to increased ambient pressure. As such, increasing power conditions in aircraft gas turbine settings is associated with a widening of the spray cone angle. It was therefore concluded that the fuel/air momentum ratio could be used to best correlate with spray variations, with increased values resulting in larger SMD values and wider cone angles.

2.6. Summary and Gap Analysis

Most SAF contain an inherently low aromatics content, allowing for reductions to nvPM number, mass, and size. It is universally agreed that hydrogen content is the best descriptor for nvPM emissions, with high hydrogen content fuels allowing for reductions of (%). However, while hydrogen content is accepted as the strongest first order descriptor of nvPM emissions rates, evidence has been found that rates of nvPM emissions are influenced by additional factors outside of first order compositional properties. Authors have suggested that first order parameters are unsuitable for adequately describing nvPM emissions produced in combustion, and compound parameters are preferable.

It is known that rates of nvPM formation are influenced by atomisation in gas turbines, both in terms of droplet sizes and spray dispersion. For aircraft, nvPM

emissions are at their worst at high power conditions, but this is because of factors such as increased operating temperatures and pressures accelerating nvPM formation chemistry, rather than a result of atomisation. However, at low power conditions such as aircraft idling on a runway, atomisation quality may play a more significant role in exacerbating the nvPM emissions produced, presenting a concern most notably towards the LAQ near airports. The presence of larger droplets in a spray can worsen nvPM through the droplet burning phenomena, allowing for localised rich spots where nvPM formation rates can be exacerbated, while also promoting CO and UHC, and reducing overall combustion efficiency. This has the potential to be especially problematic for RQL combustors operating with airblast atomisers, both because of the high equivalence ratios in RQL combustor primary zones, and the sharp decline in atomisation quality associated with airblast atomisers at low airspeeds.

Fuel surface tension, viscosity, and density can all impact the atomisation quality produced by prefilming airblast atomisers, but the relative significance of each property appears to be not well understood. This is best demonstrated for the case of viscosity, which is generally considered to have a low impact on atomisation quality, even to the point of negligibility in cases where prompt atomisation is dominant. Therefore, the relative impacts of these properties likely differ across operating conditions. Authors have previously derived empirical correlations describing sprays generated by prefilming airblast atomisers across different conditions and with different fuels. However, these appear to be applicable only to the specific atomiser designs, operating ranges, and fuel properties used in each study, which supports the above observation.

Overall, there appear to be very few studies attempting to compare the atomisation quality across conventional fuels and SAF, and quantify the subsequent impact this could have on nvPM emissions. This is likely due to the fact that most SAF are near drop-in and exhibit only small differences in fuel physical properties compared to conventional fuels, there does appear to be some increase in attention given to this subject. Therefore, a closer examination of the impacts of atomisation properties on nvPM in addition to hydrogen content is warranted, which could help to provide greater insight into the operability of SAF compared to conventional jet fuels and promote 100% SAF powered flights.

3. Experimental Facilities and Apparatus

The main focus of this study was the accumulation and analysis of experimental data, for which a number of experiments were undertaken over the course of this project, the results of which are presented in later chapters. Combustion tests using a generic RQL research combustor were undertaken for the measurement of nvPM emissions produced by SAF, allowing also for an assessment of combustion performance towards refinement of the design. Alongside this, the atomisation and spray characteristics of the airblast atomisers developed for the combustor were investigated, using a variety of measurement techniques.

This chapter will describe the experimental facilities used for the duration of the study.

3.1. Fuel Analysis Techniques

3.1.1. Nuclear Magnetic Resonance (NMR) Spectroscopy

NMR spectroscopy is a popular and well-developed tool used for non-destructive compositional analysis of chemical compounds. Detailed descriptions of the principles of NMR techniques have been given by Keeler [133] and Carreras [134]. NMR techniques use magnetic fields and radio wave emissions to determine the relative quantity of particular atoms in a compound based on a physical phenomenon called nuclear spin. When NMR-active nuclei (^1H , ^2H , ^{13}C and ^{15}N) within compounds placed are in a strong magnetic field, their magnetic dipoles align in the direction of the field in one of two orientations: one parallel to the direction of the field and one opposite to the direction of the field (antiparallel). The parallel orientation corresponds to the lowest energy level of the nucleus, while the antiparallel orientation corresponds to the highest energy level, resulting in a difference in energy levels of ΔE . The effect of the magnetic field causes a precession movement in the atoms, which spin around the axis of orientation similar to a spinning top losing momentum. The frequency of the precession movement is known as the Larmor frequency. A Radio-Frequency (RF) pulse, of a frequency close to the Larmor frequency, directed at the sample perpendicularly to the direction of the external magnetic field causes the axis of precession spin to temporarily rotate into the xy plane, referred to as excitation. Following the radio pulse, the axis of spin gradually moves back into orientation

with the external magnetic field, emitting radio energy in the process. A sinusoidal energy signal, referred to as Free Induction Decay (FID), then presents as an intensity peak of a given frequency when modified by a Fourier transform. This intensity peak allows users to determine the relative abundance of a particular atom in a compound.

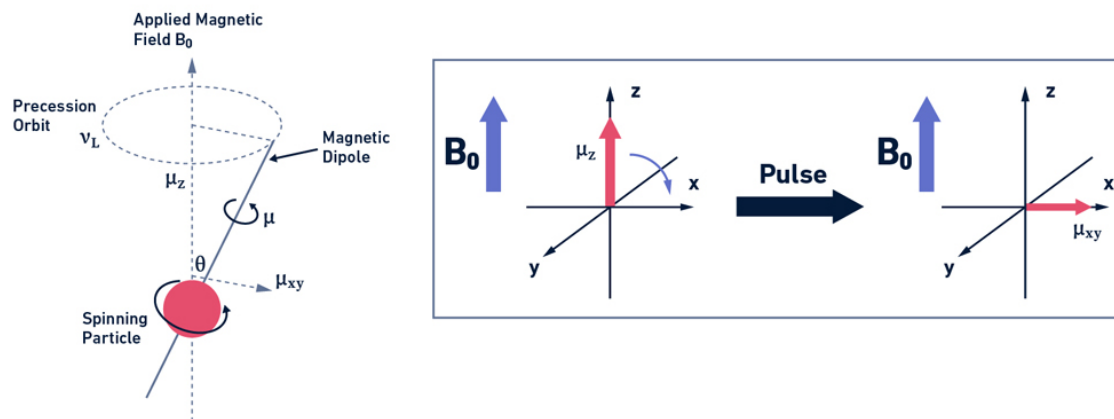


Figure 3-1 - NMR principles showing nuclear spin precession movement for an atom in an external magnetic field (left) and the effect of an applied radio pulse (right), [134]

NMR spectroscopy is an established method of aviation fuel analysis, which has been highlighted as especially useful in providing details of complex mixtures such as aviation fuels by determining average descriptors of their chemical structures [135]. ASTM methods utilising NMR describe the determination of total hydrogen content and aromatic carbon content in hydrocarbon fuels. However, NMR is most often used to determine the total hydrogen content in aviation fuels using low resolution NMR spectroscopy. ASTM methods D3701 [136] and D4808 [137] use continuous wave NMR for the analysis of the hydrogen content of hydrocarbon fuels. The former is given as the more specialised technique for use with aviation fuels, while the latter is a more general method applicable to a range of hydrocarbons.

ASTM D7171 [138] is similar to D3701 and D4808, but uses pulsed NMR spectroscopy as opposed to continuous wave spectroscopy, able to determine the hydrogen content of aviation fuels within an optimal hydrogen content sampling range of 10.5-15.5% wt. NMR spectroscopy measurements following ASTM D7171 were undertaken and provided for fuels in this project by DLR (German Aerospace Center). Repeatability standard deviations were also provided across fuel data provided.

3.1.2. Gas Chromatography (GC)

Modern GC test methods allow for detailed compositional analysis of hydrocarbon fuels. A typical GC system consists of a column through which a vaporised sample passes along with an inert carrier gas. The need for vaporised samples means that GC is only suitable for analysis of volatile organic and inorganic compounds, and is well suited to hydrocarbon forensics. Different species transit the column at different rates due to differences in chemical and physical properties. Species exiting the column are detected using a variety of methods, and the output is a 2D chromatogram profile, with a retention timeline used to differentiate compounds plotted against a detection signal indicating the abundance of said compound. ASTM methods specify a number of detection methods which may be utilised with GC depending on the desired measurement compounds, varying significantly in complexity. A relatively simple method used to determine total saturate, olefin and aromatic contents by volume uses a fluorescent dye chromatograph (ASTM D1319 [139]). Other ASTM GC methods are used to determine quantities of aromatic compounds (mono-, di-, and total) in aviation fuels, using refractive index detection (ASTM D6379 [140]) or Vacuum UltraViolet (VUV) absorption spectroscopy detection (ASTM D8267 [141]).

While GC methods can prove useful for aviation fuel compositional analysis, the complexity and large number of species present can make accurate analysis of a fuel difficult. An evolution of one-dimensional GC, originally described by Liu and Philips [142], introduces an extra dimension to the measurement plane by using two separation columns rather than a single column, separated by a modulator. This technique is called comprehensive 2D GC or GCxGC. This method may be paired with a variety of detection methods following the second column, including but not limited to Mass Spectrometry (MS) or Flame Ionisation Detection (FID) [143]. GCxGC is now a relatively mature analysis technique, affording significant improvements in accuracy, measurement sensitivity, and resolving power over 1D GC [143]. The extra dimension also improves upon GC retention line plots by allowing for differentiation between compounds of similar retention times, reducing a phenomenon called coelution. Overall, this results in better component identification and dramatically increases the number of measurable compounds from a few hundred to several thousand, making 2D GCxGC better

suited for complex mixtures of chemical compounds such as aviation fuels [144], [145].

An example of data collected using 2D GCxGC, determined for a reference Jet A-1 fuel used in this study, is given in **Figure 3-2**

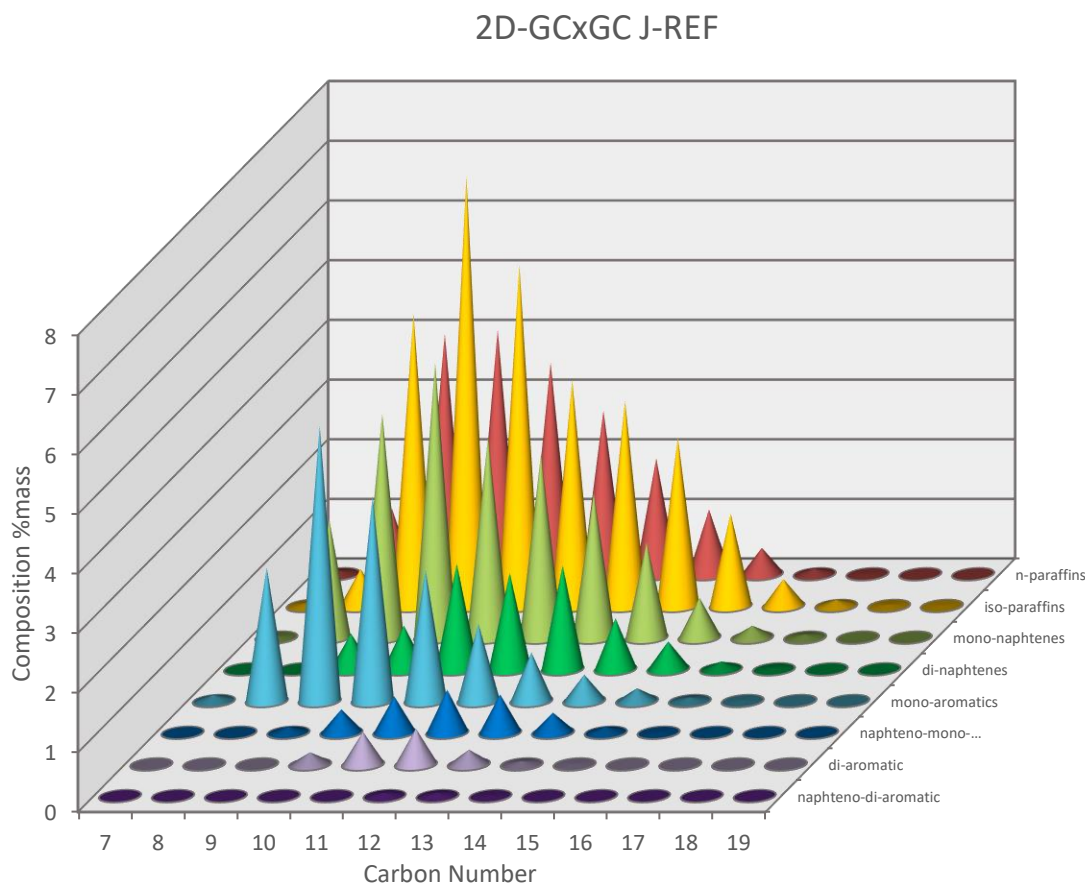


Figure 3-2 - Typical jet fuel hydrocarbon compositional data determined using 2D GCxGC

In addition to compositional data, 2D GCxGC can be used to determine fuel hydrogen content using the weighted method described by Vozka et al. [146]. The weighted hydrogen method effectively calculates a summed average of hydrogen content against carbon content for each molecule, weighted by the relative abundance. This method is shown in **Equations 3-1 to 3-3**:

$$\text{Chemical formula} = C_n H_m \quad 3-1$$

$$H_i = \frac{(m \times M_H)}{(m \times M_H) + (n \times M_C)} \quad 3-2$$

$$H_{wt.\%} = \sum_1^i H_i \times Wt_i$$

Hydrogen content values calculated from 2D GCxGC have been shown to exhibit strong agreement with values obtained through NMR, offering improvement over more simplistic ASTM methods [146]. Fuel molecular weights (MW) can also be calculated from GCxGC data using the weighted average method. MW values for individual components are determined by the sum of the number of Carbon and Hydrogen atoms multiplied by the respective molar masses of each element. Weighted averages are determined as in **Equations 3-4 and 3-5**.

$$MW_i = (m \times M_H) + (n \times M_C) \quad 3-4$$

$$MW_{Total} = \sum_1^i MW_i \times Wt_i \quad 3-5$$

3.2. GTRC Generic RQL Combustor

For the purposes of alternative fuel testing, a small-scale <250 kW non-proprietary RQL combustor was designed and manufactured within Cardiff University. Over the course of this work, two combustion liners and numerous atomisers were developed in conjunction with undergraduate students and utilised for later experimentation involving SAF. The design was a can-type combustor based on the work of Makida *et al.* [147], chosen to allow for full control over flow processes/ambient conditions and greater ease of modelling compared to full in-production aircraft engine combustor systems. The general design consisted of two main components: a prefilming airblast atomiser manufactured using Additive Manufacturing (AM), and a combustion liner manufactured using traditional machining.

3.2.1. AM Atomiser Design

Design of the atomisers utilised for this project were influenced by the atomiser developed by the Parker-Hannifin company [127], as shown in **Figure 3-3**. Additional design choices relating to the atomiser dimensions were influenced by Makida *et al.* [147].

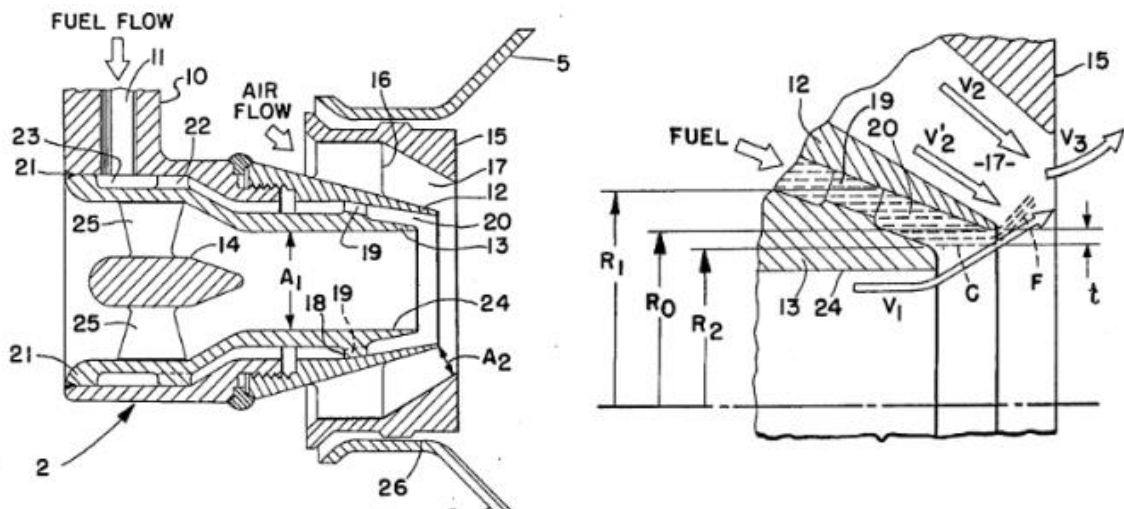


Figure 3-3 - Parker-Hannifin atomiser design (left) and interaction between air and fuel flows at the atomiser exit (right) [127]

In the Parker-Hannifin design, air is provided to the atomiser from a single source and partitioned into an inner and outer air channel. Each air channel contains a swirler assembly, which houses inclined blades (vanes) employed to turn the air relative to the axial direction and add swirl. Fuel is pumped through a narrow annular channel between the two air channels, which also contains swirler blades helping to distribute liquid evenly. Expanding air exiting the inner air channel immediately contacts the fuel distributed along the prefilming surface, whose radius is labelled as R_0 . The initial film thickness (t) is defined by the atomiser geometry as a function of the radial thickness of annulus formed between the inner air channel wall (of radius R_2) and the prefilmer surface. The exit planes of the three fluid channels are offset from each other, allowing for the desired interaction between the air and fuel.

The initial prototype airblast atomiser design, used in the GTRC generic RQL burner was developed prior to the start of this project (**Figure 3-4**), with further details available elsewhere [2].

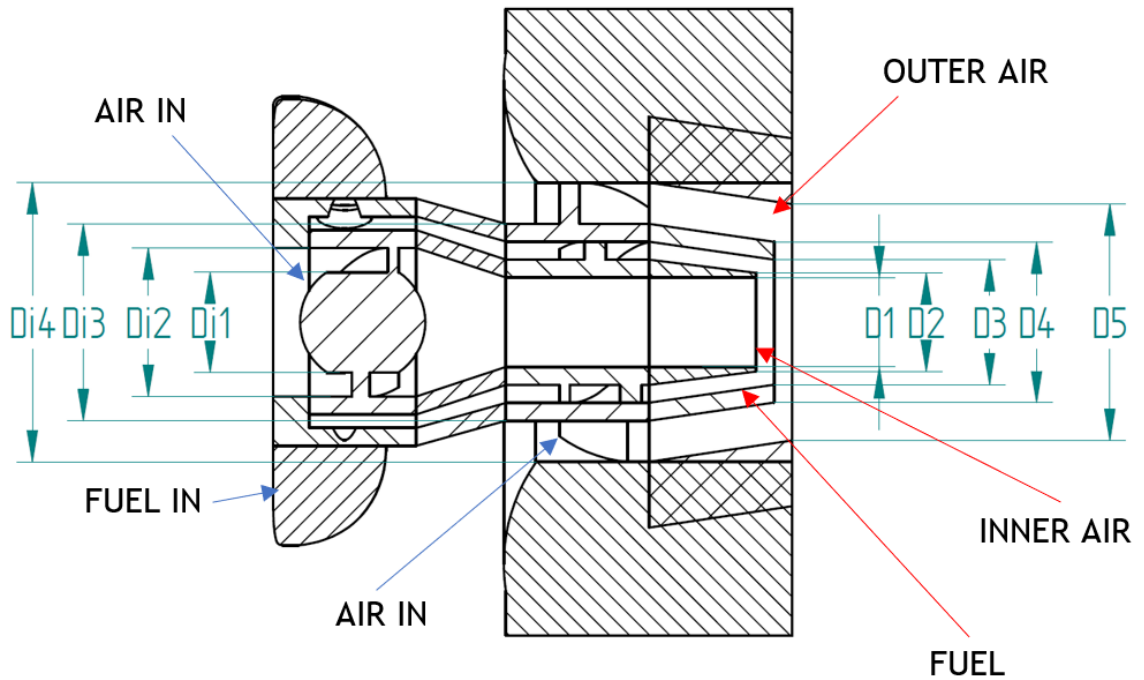


Figure 3-4 - RQL atomiser prototype design

As mentioned, the original atomiser developed for the RQL combustor was made using Additive Manufacturing (AM), also referred to as Additive Layer Manufacturing (ALM). The decision to use AM had been made as such a part could not be manufactured using traditional methods in the School of Engineering’s workshops and would have been prohibitively expensive to manufacture as a one-off part at a specialist manufacturer. AM has seen significant strides in development over recent years, with applications in a wide range of industrial sectors [148]. In contrast to typical subtractive machining methods, AM techniques gradually “build” components by the addition and joining of raw materials, usually on a layer-by-layer basis. AM techniques require only a suitable CAD file before manufacture without the need for auxiliary tooling, with the only modifications necessary concerning the placement of manufacturing supports required to support the weight of the part as it is formed. This makes more complex parts possible and allows for greater freedom in component designs.

Aircraft parts produced through AM can be designed with intricate internal geometries and specialised for application in aircraft in ways not possible with traditional machining. Internal cavities allow for significant weight reductions allowing for decreases in aircraft fuel consumption (a process referred to as *lightweighting* [149]) or can facilitate internal cooling air channels or embedded

electronics [148]. AM typically results in considerably reduced material wastage compared to subtractive manufacturing methods, with wastage reductions as high as 90% having been reported [148]. This is particularly appealing for aerospace where expensive, high-quality materials are required such as aerospace-grade metal alloys. Parts ordinarily requiring expensive and time-consuming multi-part assemblies can be manufactured as fully integrated parts in one build. This reduces overall part counts, assembly costs, and potential for failure through reduction in the number of joints, although is limited by manufacturing chamber sizes [148]. AM techniques are relatively underutilised in aerospace at the current time, but are steadily becoming more common, having been successfully used in the manufacture of in-service aircraft components. A GE LEAP engine fuel nozzle (**Figure 3-5**) manufactured using AM was able to combine 20 parts into one print, saving on assembly costs, while also reducing part weight by 25% [150]. An example of lead time reductions through the use of AM are the front bearing housings developed by Rolls Royce for the Trent series engines, yielding lead time reductions of 30% [151].

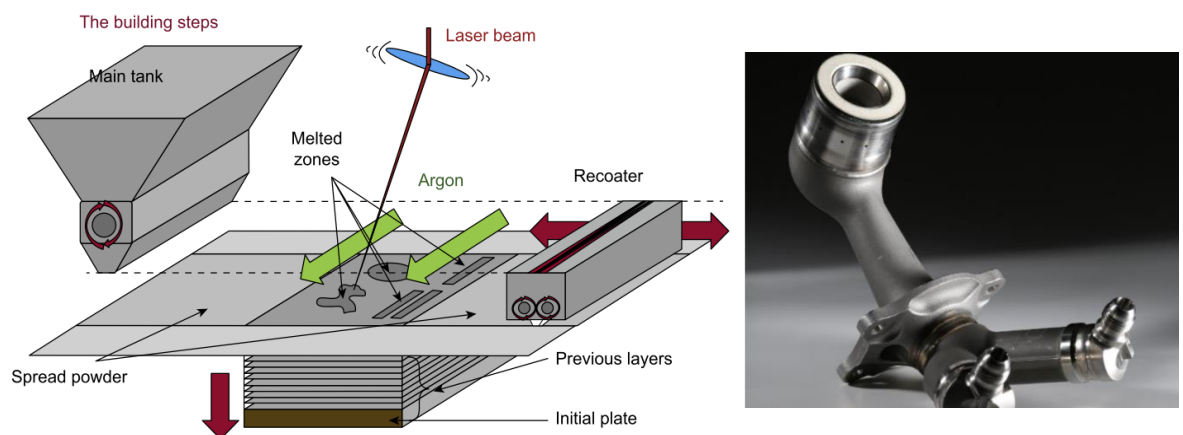


Figure 3-5 - Typical powder bed fusion process [152] (left) and General Electric LEAP engine atomiser (right)

Limiting the more widespread use of AM in aerospace are certain key drawbacks and obstacles requiring further research and development. Manufacturing tolerances of AM parts require improvement, having demonstrated a lack of repeatability across parts [148]. Uncertainties surrounding the mechanical properties and fatigue life of parts produced using recently matured AM processes is also of concern, especially considering the strict quality requirements of safety critical aerospace components. Additionally, coarse surface finishes are often associated with AM parts as a result of the fused grains

of metal powder, which can affect fatigue life [148]. Because of this, a degree of post processing (surface finishing e.g., electropolishing) is often required. To control the above concerns, development of international quality standards concerning AM [153] is on-going, but overall the progress of AM replacement of traditional manufacturing techniques is slow owing to the constantly evolving nature of AM as an emerging technology [148].

The lack of tooling requirements and improved part complexities associated with AM processes allow for the most significant cost reductions over traditional machining when applied to low volume, high complexity part production [149]. AM is therefore most applicable for rapid prototyping applications, in which a number of components are designed and produced with iterative modifications to their design features, and subsequently categorised through experimentation. This was ideally suited to further atomiser development in refining the prototype design in this project, given the internal complexity and relatively small size of the atomiser, and given the timescales available. Atomisers produced in this work were manufactured from 316L Stainless Steel using Selective Laser Melting (SLM), a subcategory of powder bed fusion techniques, in which a high-powered laser is directed onto a bed of fine metal powder to weld together individual layers of the material. Fresh layers are applied after each welding process, allowing the part to be built up layer by layer over a matter of hours. Manufacturing was undertaken using a Renishaw AM250 Selective Laser Melting (SLM) machine equipped with a modulated ytterbium fibre laser ($\lambda=1071$ nm) within Cardiff School of Engineering's advanced manufacturing research centre. All atomisers were manufactured using the recommended processing parameters supplied by Renishaw and utilised in development of the prototype atomiser [2]. Parts were printed with a chessboard strategy at a laser power of 200 W, hatch distance 110 μm , powder layer thickness 50 μm , point distance 6 μm , exposure time 50 μs , and a 67° rotation angle between layers. The stainless-steel powders nominal particle range was given by Renishaw as 5-40 μm .

3.2.2. Combustion Liner

Design of the combustion liner had been similarly influenced by the design choices of Makida *et al.* [147], and developed prior to the start of this project in Cardiff University. The Mk. I design was devised as a generic research combustor

setup representative of a small aircraft engine. In this initial design, a ring of cooling holes were included in the combustor dome to provide film cooling to the upstream sections of the combustor and provide an air sheath to the spray. Four quench air holes were placed at the end of the primary zone, angled normally to the liner, and aligned in an opposing orientation in an effort to afford improved ignition and LBO behaviour in comparison to axially symmetric orientations [147]. Inserts in these air holes were subsequently used to optimise the diameter, and hence pressure differential across the combustor at a given air flow rate. A ring of dilution holes and three rings of cooling holes were located further downstream in axially symmetric orientations. A render of the Mk. I burner is shown in **Figure 3-6**.

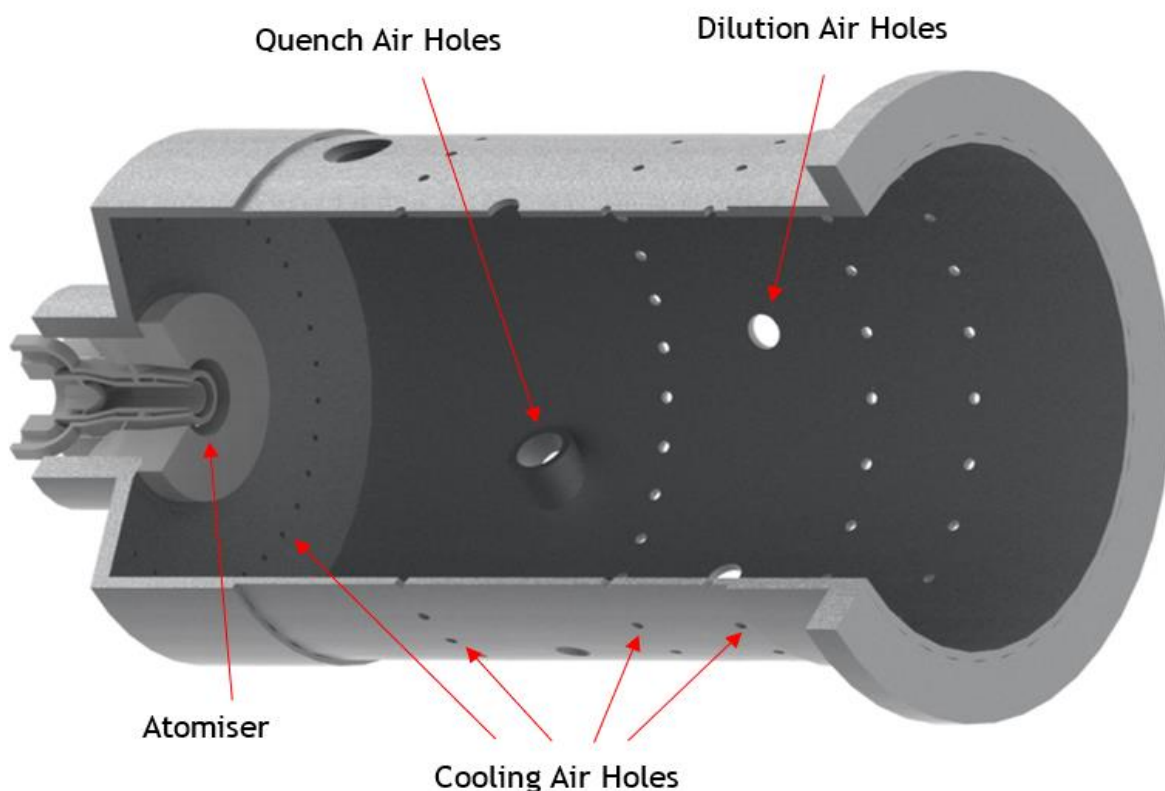


Figure 3-6 - Mk. I RQL combustor with atomiser placement

3.3. NvPM Emissions Sampling and Measurement

3.3.1. HPOC

Combustion emissions testing using the aforementioned GTRC generic RQL combustor was performed in the High-Pressure Optical Chamber (HPOC) developed by Cardiff University's Gas Turbine Research Centre (GTRC), shown in

Figure 3-7. Further details of the HPOC can be found elsewhere [154]. This system is capable of undertaking combustion tests at elevated pressures and temperatures, rated up to 16 bara and 933 K. Quartz glass windows allow for observation of combustion equipment during operation.

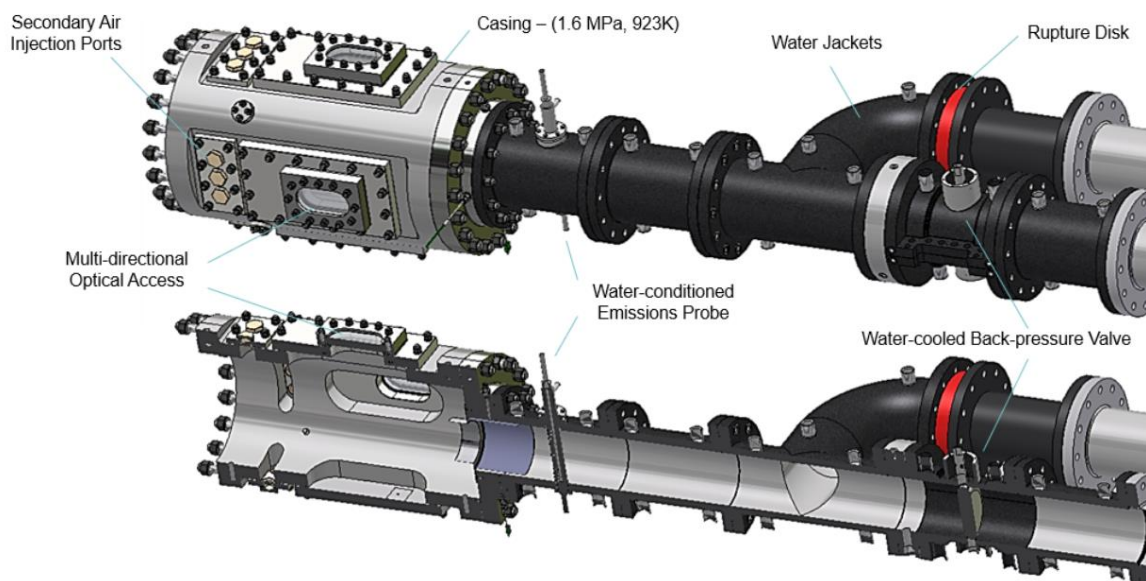


Figure 3-7 - GTRC HPOC Setup

For collection of exhaust samples, a 9-point equal area ‘piccolo’ sampling probe was used (**Figure 3-8**). This probe housed 9 orifices of 1.2 mm diameter, spaced to encompass equal cross-sectional area sections in the exhaust column. A central orifice is located at the approximate centre line of the exhaust column piping, while the remaining orifices are spaced to account for annular areas of equal cross-sectional area. The probe was water cooled to 433 K and housed in an exhaust column with a diameter of ~170 mm. The probe is shown in **Figure 3-7** positioned approximately 400 mm from the combustor outlet, but it should be noted that the configuration of the sample probe varied across emissions testing, and was positioned at a point further downstream during later testing.



Figure 3-8 - Piccolo sampling probe

Mounting of the RQL combustor into the HPOC during combustion experimentation is shown in **Figure 3-9**. Fuel and primary air were supplied into the HPOC via a fuel/air lance connected to the atomiser. Secondary air was directly supplied into the HPOC to the combustor liner. Primary and secondary air flows were dried to a fixed dew point of -17°C using a Beko Drypoint RA DPRA960, supplied from two Atlas Copco GA45VSD variable speed drive compressors and independently regulated using an Emerson CMF025M and a CMF050M ($\pm 0.35\%$), respectively. Fuel supply was regulated using a Bronkhorst mini-CORI-FLOW M14 Coriolis mass flow controller ($\pm 0.2\%$). Nominal preheat temperatures of 30°C , 80°C and 120°C were used for the fuel, primary air, and secondary air flows, respectively. The preheating of each fluid flow was intended to eliminate uncertainties associated with flow behaviours or fuel physical properties caused by day-to-day variability of ambient temperature. Local temperatures were monitored using thermocouples positioned at various stages of the HPOC, in order to monitor fluid preheat temperatures, combustor temperature, and exhaust temperature. Static pressure taps were located on the primary air inlet line, in the HPOC casing, and in the front face of the combustor liner, so as to measure pressure drop values across the atomiser and combustor liner during operation.

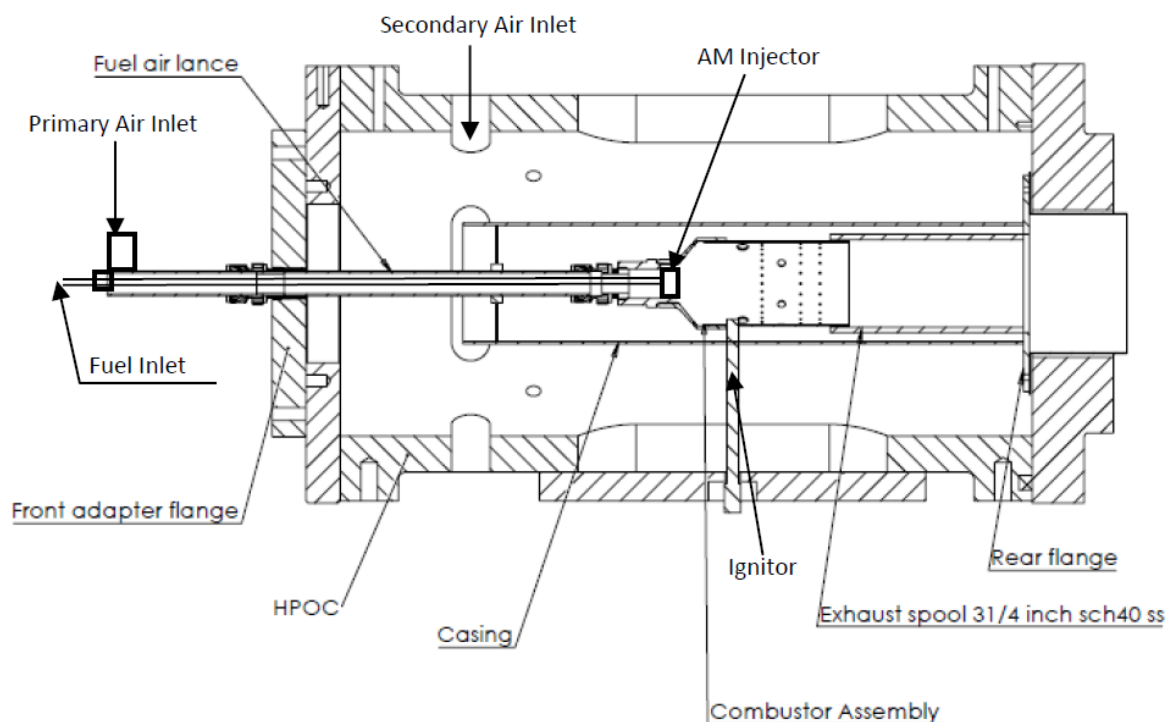


Figure 3-9 - HPOC setup with RQL combustor placement

3.3.2. European Mobile Reference Sampling and Measurement System

Measurement of nvPM emissions in this project was undertaken using the European (EUR) mobile nvPM reference sampling and measurement system. The reference system is a fully ICAO compliant mobile unit containing several instrumentation modules for nvPM measurement. Extensive details of the design, development, and benchmarking of this system may be found in the SAMPLE III project reports [155], [156]. This system was used previously during the A-PRIDE test campaign [101] and the ITAKA 2 campaign [106].

Following collection by the sampling probe, the exhaust is conditioned in a water-cooled (433 K) heat exchanger (1 m long 3/8" ID) before passing through into an 83 cm long dilution box, housing a primary splitter and dilution stage (Dekati DI-1000). The primary splitter inlet marks the beginning of the transfer section, and is used to separate exhaust samples to be sent to the different measurement systems, including a dedicated gaseous measurement system (raw CO₂ and additional gaseous measurements) and the EUR reference nvPM sampling and measurement system. Exhaust bound for the reference system first passes through a 2 m long, 8 mm ID, anti-static (carbon loaded) polytetrafluoroethylene (PTFE) sample line heated at 433 K and into the primary dilution stage. This stage is designed in accordance with ICAO Annex 16 Vol. II, and is included so as to suppress particle coagulation, water condensation, and volatile particle nucleation, helping to ensure the measurement of non-volatile particulates only. Exhaust is diluted with filtered nitrogen by a recommended dilution factor of 8-14 using a Dekati Di-1000 dilutor. The diluent temperature is maintained using a nitrogen heater and multiple thermocouples, so as to ensure the exhaust is cooled to 333 K.

Exhaust exiting the dilution box is transported to the reference system via a 25 m, 8 mm ID, anti-static carbon loaded PTFE sample line (WINKLER) maintained at 333 K. The reference system itself, shown in **Figure 3-10**, is a portable and modular unit containing the instrumentation necessary for full characterisation of exhaust nvPM emissions according to ICAO protocol. Exhaust enters the system through a 1 µm sharp-cut cyclone, also maintained at 333 K using a bespoke oven module designed and developed in Cardiff University. The cyclone uses vortex separation to remove particles larger than 1 µm from the exhaust stream, which may form in the system as a result of line shedding events.

These particles can result in blockages to narrow orifices and skew measurement readings. A second splitter section consisting of two three-way splitters combined into a single unit is utilised to send exhaust gases to the various measurement instruments.

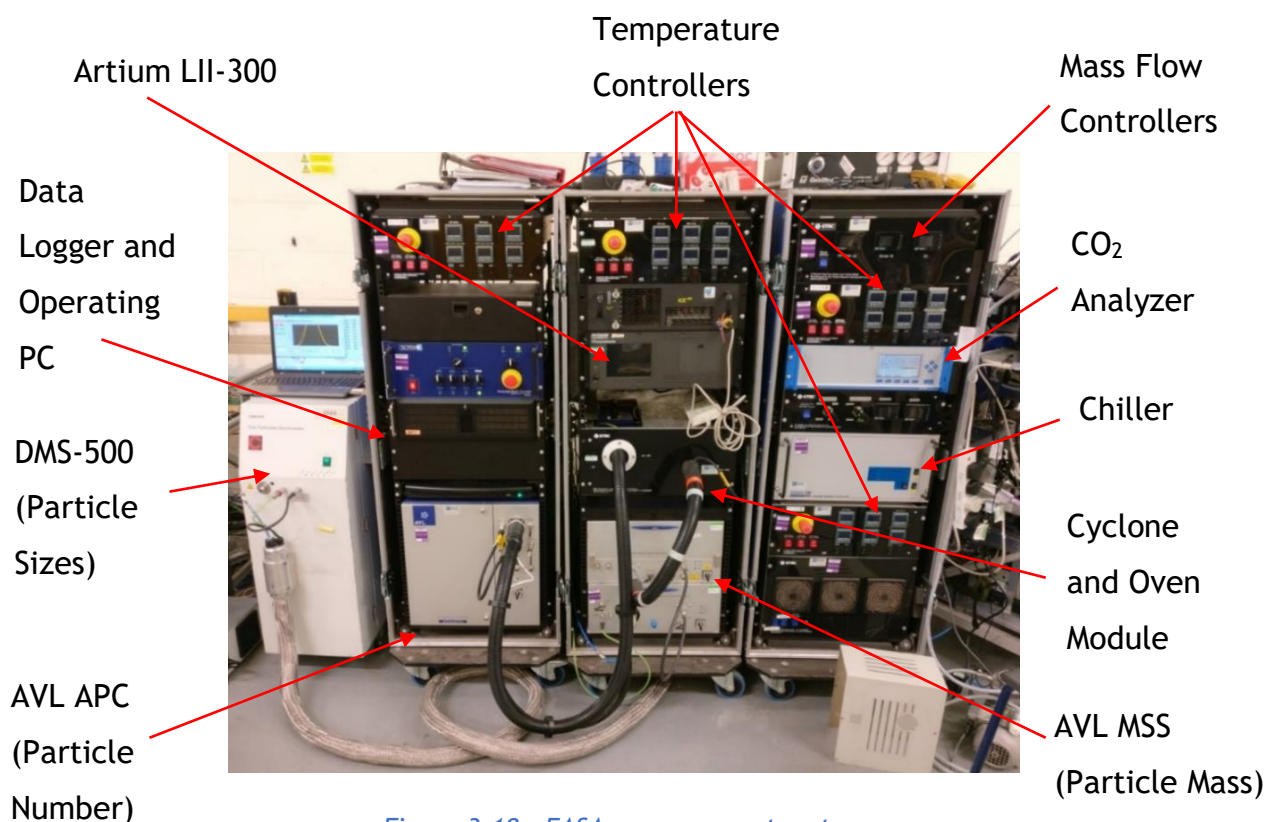


Figure 3-10 - EASA measurement system

3.3.2.1. Measurement Uncertainty

Calculation of measurement uncertainties is achieved using standard calculations outlined in ICAO documentation. Aircraft particulates generally present as log-normal PSD plots, with particle sizes plotted against particle number. Fluctuations from mean values across the chosen measurement period are represented as standard deviations (σ), which is the standard metric for assessing variability across log-normal distributions including nvPM PSD data. The calculation for standard deviations is given in **Equation 3-6**. A standard deviation of $\pm 1\sigma$ from the mean is representative of 68% confidence interval, and $\pm 2\sigma$ is representative of a 95% confidence interval.

$$\sigma = \sqrt{\frac{1}{n} \sum_{i=1}^{i=n} (y_i - \mu)^2} \quad 3-6$$

Where n is the number of repeats, y_i is the current measurement value, and μ is the mean value. Propagation of uncertainties is necessary when presented metrics are determined from multiple measurement systems each with a characteristic measurement uncertainty. Separate equations are utilised for when metrics are determined using addition/subtraction or multiplication/division of measurements. The relevant equations are shown in **Equations 3-7 and 3-8**:

$$\text{When } z = y_1 \pm y_2 \quad U_{total} = \sqrt{U_1^2 + U_2^2} \quad 3-7$$

$$\text{When } z = y_1 \frac{\times}{\div} y_2 \quad U_{total} = \sqrt{\left(\frac{U_1}{x_1}\right)^2 + \left(\frac{U_2}{x_2}\right)^2} \quad 3-8$$

3.3.2.2. nvPM Particle Number Measurements

Current ICAO specifications for the measurement of particle number require the use of a Volatile Particle Remover (VPR) in series with a Condensation Particle Counter (CPC). The VPR is included to remove volatile components such as unburned fuel or organic carbon prior to measurement in the CPC, ensuring the measurement of only nvPM. In a CPC, particles are mixed with super-saturated gas, which condenses onto their surfaces and causes them to enlarge to sizes detectable by an optical detector [157].

Measurements of nvPM particle number are achieved in the EUR reference system by an AVL APC489-CS Advanced Particle Counter, consisting of an ICAO compliant VPR leading to an n-butanol based TSI 3790E CPC. The VPR consists of numerous components including: 1) a primary dilution stage containing a rotary “chopper” dilutor, a catalytic stripper, and a secondary dilution stage. Upon entering the VPR, exhaust samples are diluted in the primary dilution stage to a dilution factor between 10:1 and 200:1 using heated air. This acts as a pre-treatment stage, preventing inaccuracies associated with modification of the sample composition in the evaporation tube. The exhaust exits the primary dilutor through a 2 m flexible sample line, before entering the Catalytic Stripper heated to 350°C, in which volatile components are evaporated and removed from non-volatile components. Finally, the sample passes to the secondary dilution unit which uses cool air to dilute the sample by a dilution factor between 10:1 and 15:1. This serves to reduce the sample temperatures to <35°C and reduce particle

concentrations to appropriate levels, so as to be suitable for measurement by the CPC. Data is recorded during operation at 1 sample/second.

The uncertainty of the APC is calculated as the combined uncertainties across the VPR and CPC according to ICAO regulations. These are a secondary dilution factor tolerance of $\pm 10\%$ from calibrated values for the VPR, and a counting accuracy of $\pm 10\%$ for the CPC. This yields an overall uncertainty of $\sqrt{10^2 + 10^2} = 14.1\%$.

3.3.2.3. nvPM Mass Measurements

Two separate instruments for nvPM mass concentration measurements are incorporated into the EUR reference system, namely, an AVL Micro-Soot Sensor (MSS) and an Artium Laser Induced Incandescence analyser (LII-300). The MSS operates according to the photoacoustic effect, using a modulated laser to excite nvPM particles with strong light absorption properties (ie. black carbon). The modulated expansion and contraction of the air surrounding the particles, caused by cyclic heating and cooling, is measured as an acoustic wave by a microphone. The LII uses a pulsed laser to heat particles to 2500-4500 K, and measures the subsequent thermal incandescent light radiation using photodetectors. The nature of both measurement techniques make them highly selective, and ensure only black carbon is measured. which also requires that both instruments are calibrated regularly against EC measurements taken using the NIOSH 5040 Thermo-Optical Transmittance (TOT) test method [158]. As with the APC, data is recorded by the LII and MSS at 1 sample/second. Outputs of the MSS and LII are to be within $\pm 10\%$ of the calibration method, which itself has an uncertainty of $\pm 16.7\%$, yielding an overall uncertainty of $\sqrt{10\%^2 + 16.7\%^2} = 19.5\%$.

3.3.2.4. nvPM Particle Size Measurements

Current ICAO documentation does not prescribe particle size measurements. However, size measurements are useful for understanding the impact of SAF on nvPM compositions, and required for the bin-by-bin correction procedure outlined in discussed in **Section 3.4.2**. Measurement of particle sizes was undertaken using a Cambustion Ltd DMS-500 fast response differential mobility spectrometer, able to detect particles in the range of 5-1000 nm, at concentrations of 10^3 - 10^{11} particles/cm³. Particle sizes are determined through electrical classification. Aerosol particles are charged using a unipolar diffusion

charger (corona discharge) and deflected by an electrical field onto a series of electrometer rings housed within a classifier column. The particle trajectories (and subsequent electrometer ring contacted) are defined by the particle electrical mobility, which is the ratio of electrostatic forces resulting from particle charging to the aerodynamic drag forces induced by the fluid medium. Volatile components could theoretically be detected by the DMS-500, but are assumed in this study to be negligible due to the inclusion of dilution stage following ICAO Annex 16 and typically low UHC values experienced during combustor testing. Particle size data output from the DMS-500 is given in the form of a time dependant PSD plot following a log-normal distribution shape. Time resolved averages of particle sizes are represented by the Geometric Mean Diameter (GMD), while the width of the measured distribution is given by the Geometric Standard Deviation (GSD).

3.4. nvPM Loss Corrections

3.4.1. Particle Loss Mechanisms

In ICAO compliant systems, particle losses occur between the combustor exits and the measurement instrumentation, caused by nvPM particles adhering to flow path surfaces during emissions sampling. Because of this, along with the long sampling lines (up to 35 m) prescribed, losses can be as high as 50% for nvPM mass and 90% for particle number [24]. The mechanisms of particle loss are known to affect nvPM emissions in ICAO compliant measurement setups, as have been summarised previously [18], [159], [160], and are represented in *Figure 3-11*.

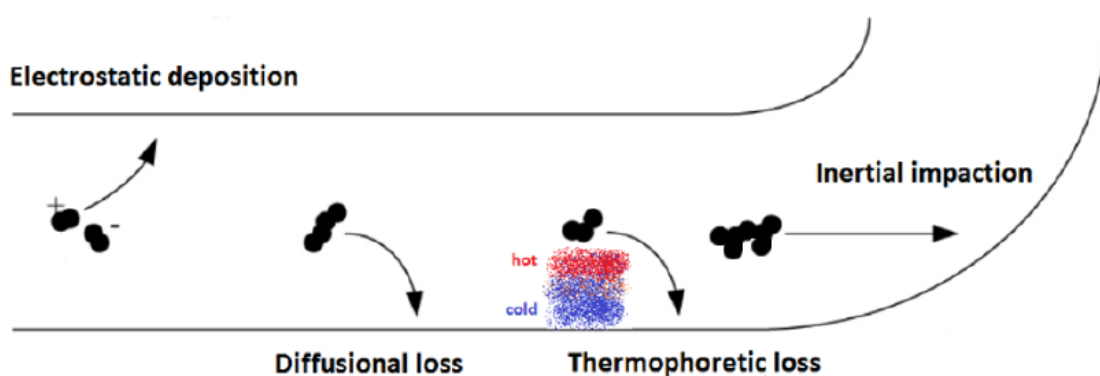


Figure 3-11 - Particle system loss mechanisms [160]

Thermophoretic losses occur as a result of local temperature gradients in the sampling system. In areas of high temperature, gas molecules of the carrier gas stream possess higher kinetic energy than those in cooler regions. Suspended particles experience higher rates of collisions from these gas molecules on the higher-temperature facing side, which pushes particles into cooler regions [159]. Temperature gradients typically occur in regions between hot exhaust gases and cooler walls of the sampling system, resulting in deposition of particles onto the walls. The prescription of heated lines and careful monitoring of temperatures at points in the system by ICAO documentation, helps in the control and estimation of thermophoretic losses. Thermophoretic losses affect all particle sizes (in the size range witnessed in aircraft exhaust) to a similar degree, and tend to be responsible for the majority of reductions to aircraft particulate mass through loss mechanisms [18]. Corrections for thermophoretic losses have been included in ICAO documentation for some time, with a correction factor (k_{thermo}) included as a standard practice for the calculation of emissions indices. These are given in **Equations 3-9-3-11**

$$k_{thermo} = \left(\frac{T_{wall} + 273.15}{T_{exhaust} + 273.15} \right)^{-0.38} \quad 3-9$$

$$\begin{aligned} EI_{nvPM \text{ number-meas}} [\#/kg_{fuel}] & \quad 3-10 \\ & = \frac{nvPM_{num-STP} \times DF_2 \times 22.4 \times 10^6}{CO_{2 \text{ dil}} \times (M_C + \alpha \times M_H)} \times k_{thermo} \end{aligned}$$

$$\begin{aligned} EI_{nvPM \text{ mass-meas}} [g/kg_{fuel}] & \quad 3-11 \\ & = \frac{nvPM_{mass-STP} \times 22.4 \times 10^{-6}}{CO_{2 \text{ dil}} \times (M_C + \alpha \times M_H)} \times k_{thermo} \end{aligned}$$

Diffusion losses refer to the dispersion of particles across concentration gradients. Particles in regions of high concentrations are transported to areas of low concentration by forces from collisions between particles and gas molecules, referred to as Brownian motion. Smaller particles (typically <50 nm, [159]) hold lower kinetic energy during transit than larger particles, and so are more severely affected by gas molecule interactions, leading to higher losses. As a result, losses via the diffusion mechanism are highly size dependant in nature. Diffusion losses account for the majority of losses by particle number, although a relatively small percentage of losses by mass, which are attributed to loss mechanisms affecting

larger particles. The size dependant nature of diffusion losses skews particle size distributions towards larger sizes (increased right tail), resulting in larger measured GMD values at the end of the sampling system than would have been witnessed at the combustor exit.

Additional losses in ICAO compliant measurement systems include bend losses, electrostatic losses, and inertial losses [160]. These are calculated as penetration efficiencies, detailing the losses to particles as a percentage as shown in **Figure 3-12**. However, as can be seen, the primary loss mechanism affecting nvPM sampling in the size ranges typical of aircraft emissions are thermophoretic losses and diffusional losses, while other mechanisms typically only impact larger particles which hold more mass.

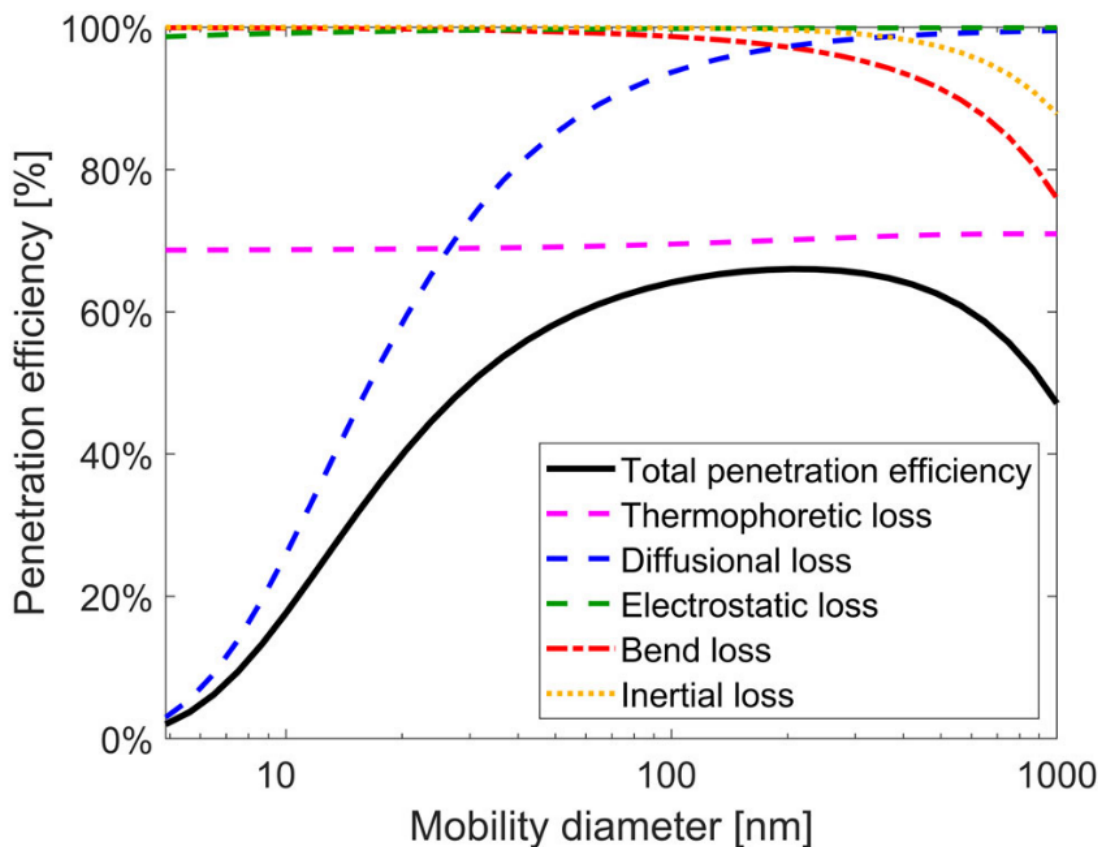


Figure 3-12 - Particle penetration (transport) efficiency vs. particle diameter for a typical ICAO compliant sampling system [161]

3.4.2. Size Dependant System Loss Correction Methodology

Accounting for system losses in SAF studies is of importance due to the typically smaller nvPM particles produced by high hydrogen content fuels when compared to conventional Jet A1 fuels (**Section 2.3.2**). The smaller particle sizes result in higher diffusional losses during sampling, leading to an underprediction

of measured particle concentrations, and an overprediction of their achievable emissions reductions compared to conventional fuels at the combustor exit. It is critical that this is prevented for accurate reporting of nvPM emissions produced by aircraft so as to meet current and future nvPM standards. It is therefore important to include system loss corrections in SAF studies for an accurate assessment of the emissions benefits associated with SAF and for the study of the atmospheric impact of nvPM emissions from aircraft.

Updated versions of the Annex 16 document have introduced new data processing methods for the standard and accurate reporting of aircraft emissions. Recently, this has included corrections for system losses associated with the required sampling and measurement methodology. Loss correction values (k_{sl}) are applied to measured nvPM concentrations, so as to be representative of nvPM concentrations at combustor exits or Engine Exit Planes (EEP). This is encouraged in the Annex 16 document for inventory and modelling purposes [24]. Correction factors for mass ($k_{sl-mass}$) and number ($k_{sl-number}$) are used to correct thermophoretic loss-corrected emissions indices, following *Equation 3-12*.

$$EI_{EEP} = EI_{thermo\ corrected} \times k_{SL} \quad 3-12$$

3.4.2.1. ARP6481 Regulatory Method

The current regulatory method for the prediction of system losses other than those caused by thermophoresis is the ARP6481 protocol [162], also outlined in appendix 8 of the annex 16 document [24] and the AIR 6504 document [163]. The method utilises the United Technologies Research Group (UTRC) model to predict the penetration efficiencies associated with sampling, including those in the sampling lines, and additional losses and counting efficiencies associated with the VPR and CPC. A value of GMD at the EEP is then iteratively estimated using a Chi-square minimisation, until the losses to particles yield a GMD value comparable to a value estimated at the measurement instrument using measured mass and number inputs. Using this value of GMD, a log-normal size distribution is produced with an assumed GSD of 1.8, stated as typical of aircraft size distribution plots collected from past experimentation [163]. $k_{sl-number}$ is then predicted as the ratio between the sum of the modelled PSD output, and the same distribution multiplied by the penetration efficiencies calculated in the first step. $k_{sl-mass}$ is

predicted by converting the modelled PSD output into the mass space using an assumed particle density of 1 g/cm³, and then following the same method.

3.4.2.2. Bin-by-Bin Method

Issues with regulatory method have been highlighted by Durand and co-workers, particularly relating to the assumptions made in simulation particle size distributions [160], [161]. It has been shown that, in cases in which GMD values are very small (<20 nm), the regulatory method will significantly underpredict values of k_{st} . [160] This is a crucial consideration in SAF studies, in which particle sizes are typically reduced by the reduction of aromatic compounds. Rather than the regulatory method, nvPM loss correction factors were calculated for this project using the bin-by-bin method, as outlined in [106]. This differs from the regulatory method in that correction factors are estimated using additional particle size measurements, rather than relying on the above-mentioned assumptions. For the purposes of this project, this tool was a black box computational tool written for MATLAB requiring inputs of the sampling system dimensions and aerosol properties, as well as nvPM mass data and PSD data, to determine outputs of k_{st} values. Measured PSD data taken for the DMS-500 is separated into 38 size bins for the 5-1000 nm range, and used as an input alongside measured mass concentrations. An example of nvPM data corrected by the bin-by-bin method compared to data corrected for thermophoresis only is shown in **Figure 3-13**.

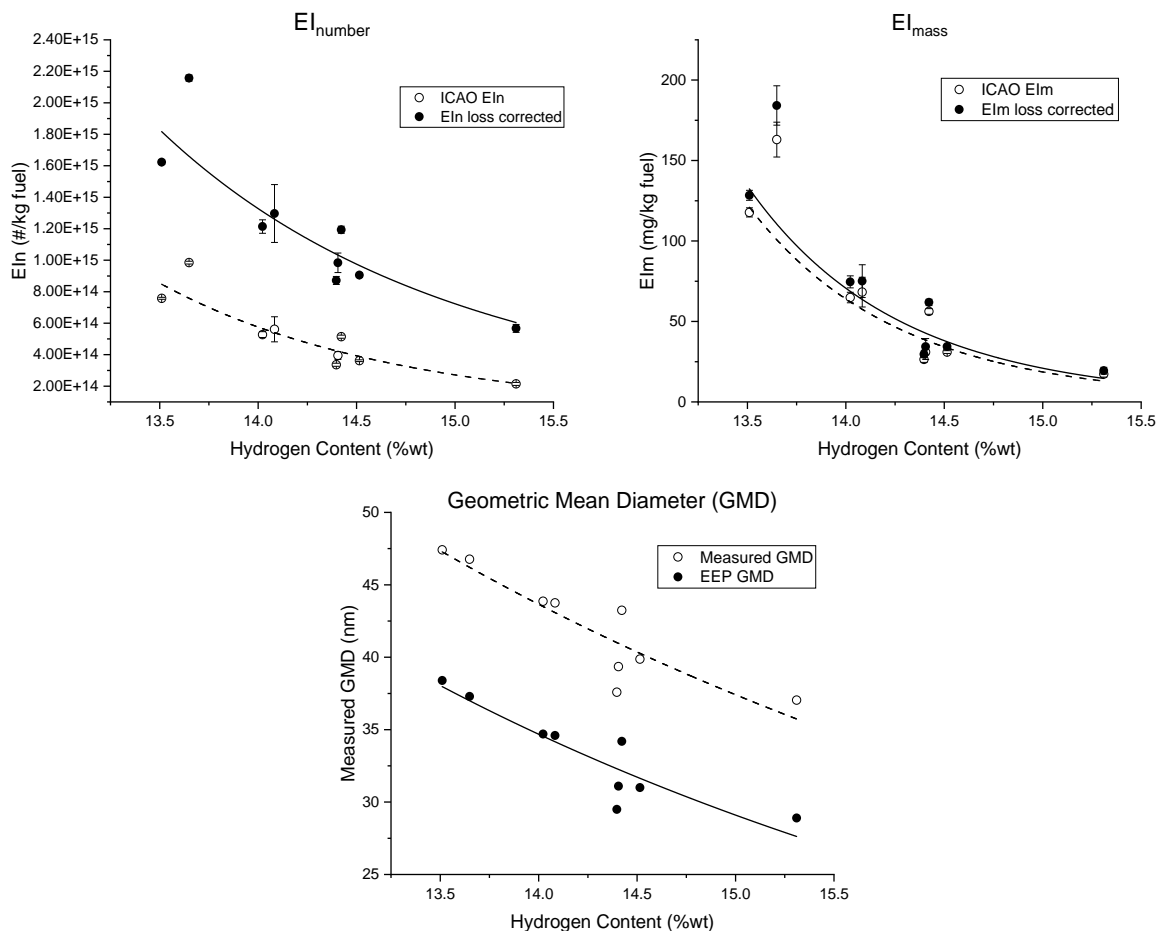


Figure 3-13 - Impact of system loss corrections on nvPM emissions

3.4.3. Specific Energy Corrections

Standard EI's may be further corrected for variations in fuel specific energy (a.k.a. net heat of combustion, MJ/kg), which were recorded for fuels in this study following ASTM D4809/3338 [137], [164]. Although this is not prescribed in ICAO Annex 16 documentation, variations in specific energy would be expected to slightly impact results due to higher rates of heat release associated with higher specific energy fuels, such as high hydrogen content SAF. Corrections for fuel specific energies are useful in preventing systematic errors as a result of varying fuel energy release during combustion, but are typically not included in emissions studies due to the relatively small impacts they have. For example, Durand *et al.* [106] found that the inclusion of energy corrections would impact nvPM results by no more than <2% and so did not include them in their work, but did comment that these corrections are important for LAQ studies. Energy corrections were included in the work of Timko *et al.* [102], who presented calculations for energy weighted EI's, where nvPM emissions are presented per unit of energy release during combustion (g/kJ or #/kJ), as opposed to per unit mass of fuel burnt. The

equation given for the calculation of ENERGY-EI values is given in **Equation 3-13** [102].

$$ENERGY - EI = \frac{EI}{\Delta H_x} \quad 3-13$$

Lobo *et al.* [99] suggested an alternative method of adjusting fuel flowrates used during experimentation so as to maintain a consistent power across fuels of different specific energies, relative to a chosen reference fuel. In their study, this fuel was a reference Jet-A1, and so mass flowrates were described as representative Jet A-1 equivalent flowrates. It may be noted that primary AFRs would be affected by the change in fuel mass flowrate when using this method, which would likely impact nvPM formation rates. Primary AFRs may be held consistent in research settings by also scaling the accompanying flowrates of air, but it is important to note that this is not representative of aircraft engine operation using SAF.

$$\dot{m}_{equiv\ Jet-A1} = \dot{m}_x \left(\frac{e_x}{e_{Jet-A1}} \right) \quad 3-14$$

3.5. Gaseous Measurements

3.5.1. Measurement System

The ICAO specifies that measurements of CO₂, CO, NO_x, NO, and total unburned hydrocarbons (UHC) should be undertaken during engine testing. ICAO compliant systems for gaseous measurements should follow the guidelines outlined in ICAO Annex 16 Appendix II [24]. Gaseous measurements taken during this project were collected using compliant Signal Group Ltd gas analysers at the end of a 10 mm OD, 25 m PTFE heated line (160°C) connected to the primary splitter before dilution. Non-Dispersive Infrared (NDIR) analysers were used for the measurement of CO₂ and CO. A 4000VM Chemiluminescent Analyser (CLA) was used for the determination of NO_x. Finally, a 3000HM heated flame ionisation detector (FID) analyser was used for the measurement of UHC. The gas analysers used in this study conformed to the maximum allowable uncertainty limits, all of which are given as full-scale deflection percentages, given in **Table 3-1**.

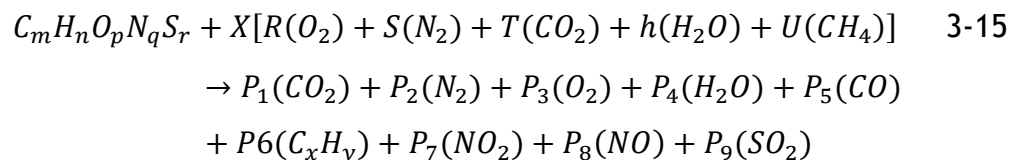
Table 3-1 - Gas Analysis Uncertainties

	NDIR		CLA	FID
	CO ₂	CO	NO _x	UHC
Measurement Total Range	0-10%	0-2500 ppm	0-2500 ppm	0-5000 ppmC
Resolution	±0.5% or ±100 ppm	±0.5% or ±1 ppm	±0.5% or ±1 ppm	±0.5% or ±0.5 ppm
Repeatability	±1% or ±100 ppm	±1% or ±2 ppm	±1% or ±1 ppm	±1% or ±0.5 ppm
Stability	±2% or ±100 ppm	±2% or ±2 ppm	±2% or ±1 ppm	±2% or ±1.0 ppm
Zero Drift	±1% or ±100 ppm	±1% or ±2 ppm	±1% or ±1 ppm	±1% or ±0.5 ppm
Noise	±1% or ±100 ppm	±1% or ±1 ppm	±1% or ±1 ppm	±1% or ±0.5 ppm
Linearity	2%	2%	2% or ±2 ppm	2%
Span Gas	2% or ±100 ppm (CO ₂ in zero air)	2% or ±2 ppm (CO in zero air)	2% or ±1 ppm (NO _x in zero nitrogen)	2% or ±0.05 ppm (propane in zero air)

A standard uncertainty for the analysers was estimated as the Root Mean Square (RMS) of the uncertainties, equal to $RMS = \sqrt{0.5^2 + 1^2 + 2^2 + 1^2 + 1^2 + 2^2 + 2^2} = \pm 3.9\%$. Additional uncertainties associated with individual analysers are corrected for using the method described in the following section.

3.5.2. Gaseous Corrections

Raw values of gaseous data were processed using the matrix method outlined in SAE Aerospace Recommended Practice (ARP) 1533C [165], using a pre-developed Excel tool. The SAE correction tool uses gaseous inputs to estimate the chemistry balance associated with the combustion of 1 mole of a chosen hydrocarbon fuel into its products (*Equation 3-15*)



Where $P_1 - P_9$ are moles of each respective constituent product. It may be noted that P_9SO_2 is not mandatory in these calculation and was omitted for this study. A series of simultaneous equations are established to calculate the values of P_1-P_9 , as well as the total moles of exhaust products (P_T) and the ratio of the moles of dry air to one mole of fuel (X). The inputs required for gaseous corrections are:

- Raw concentrations of CO_2 (dry), total NO_x , CO , UHC, and ambient hydrocarbons (assumed =0).
- Fuel type (kerosene), molar constants for carbon, hydrogen, oxygen, and nitrogen, and fuel specific energy.
- Instrument coefficients.
- Dew point (assumed as $1.8^\circ C$).

Included in the correction tool are procedures to correct for measurement interferences encountered during sampling. These are:

- Interference of O_2 on CO_2 (O_2 Broadening),
- Interferences of CO_2 and H_2O on CO and NO_x measurements,
- The efficiency of the NO_x analyser,
- Effects of the basis of measurement (semidry or wet),

Corrections were applied to account for the interferences to gas analyser measurements caused by the multiple gases in the measured exhaust. These either have a fixed interference effect across all values (zero-shift interference), or an interference effect which scales with measured concentration levels (concentration factor interference). O_2 is known to interfere with NO emissions combustor exit oxidation reactions, through a process known as O_2 broadening, and has a concentration factor effect. CO_2 and H_2O are known to apply a zero-shift interference to CO and a concentration shift interference to NO_x measurements. The chemiluminescent analysers used for NO_x measurement can measure NO or total NO_x emissions directly, while concentrations of NO_2 are determined by the difference between the two. When NO_x is measured, this is

determined by converting the NO₂ in the exhaust mixture to NO using ozone, and measuring the resultant NO emissions. Because this conversion process is not 100% efficient, conversion efficiency corrections need to be undertaken. NO_x conversion efficiencies are typically between 0.9-1.0. Corrections are also required to account for the relative dryness of the exhaust sample (semidry or wet). The NDIR gas analyser used for measurements of CO and CO₂ requires a dryer, which removes the majority of water vapour from the gaseous composition through cooling of the gas to 3°C. Since there is still water present in gas at the chiller operating temperature, a correction factor must be included for the remaining water vapour present during sampling.

The instrument coefficients used for calculations in this work are given in **Table 3-2**. It is noted that these values are given as sample coefficients in SAE documentation, rather than values determined from the instruments themselves, which could not be obtained at this time. This is highlighted as an additional uncertainty impacting gaseous emissions.

Table 3-2 - ARP 1533C Gas Analysis Tool Instrument Coefficients

CO ₂ NDIR	CO NDIR		NO _x CLA			Semi-Dry Gas
O ₂ Broadening	CO ₂ Interference	H ₂ O Interference	CO ₂ Interference	H ₂ O Interference	NO _x Conversion Efficiency	Humidity Vol. Fraction
J	L	M	L1	M1	NO _{x,n}	
0.09	-1.3	-4.5	0.14	0.28	0.95	0.00607

Similar to nvPM emissions, outputs of the correction tool are given as EI values, with the units of mass of the gaseous emission per unit of fuel burned. This is achieved for CO, NO_x, and UHC respectively using **Equations 3-16-3-18**.

$$EI_{CO} = \frac{P_5 \cdot M_{CO}}{m(M_C + \alpha M_H)} \times 1000 \quad 3-16$$

$$EI_{NOx} = \frac{(P_7 + P_8) \cdot M_{NO2}}{m(M_C + \alpha M_H)} \times 1000 \quad 3-17$$

$$EI_{UHC} = \frac{P_6 \cdot M_{C_xH_y}}{m(M_C + \alpha M_H)} \times 1000 \quad 3-18$$

Fuel-to-Air ratio (F/A) is determined from the combustion equation as a comparison against known mass flowrate inputs. F/A ratio is determined assuming dry air and ignoring the presence of trace species in both fuel and air, using the following equation:

$$\frac{F}{A} = \frac{m(M_c + \alpha M_H)}{X(M_{air})} \quad 3-19$$

Finally, calculation of combustion efficiencies is achieved on an enthalpy basis using fuel specific energy measurements and relative quantities of CO and UHC, given that these compounds exist as a result of reduced combustion efficiencies. Calculations do not factor in the impacts of NO_x and H₂ or the dissociation of combustion products. In SI units, combustion efficiency is given by **Equation 3-20**.

$$\eta_b = \left[1 - 10109 \frac{EI_{CO}}{H_c} - \frac{EI_{CxHy}}{1000} \right] \quad 3-20$$

3.6. Malvern Spraytec97 Laser Diffraction Experimentation

3.6.1. Measurement Principle

Measurement of the atomiser spray characteristics was undertaken through an established laser diffraction methodology, using a Malvern Spraytec97 particle sizer. This instrument provided an efficient assessment of the spray Particle Size Distributions (PSD's) produced by the atomisers across a wide range of atomisation flow conditions. The working principle for the Malvern Spraytec97 is shown in **Figure 3-14**. A 1 mW (class 2) laser with a wavelength between 630-680 nm (red) and a beam diameter of 10 mm is directed perpendicularly through the spray and scattered by the droplets. Scattered light is refracted through a Fourier lens and directed into a series of concentric photodetector rings, each of which produce an electric output signal proportional to the intensity of light incident upon it. Larger particles diffract light to a higher degree compared to smaller particles, causing more light to be directed to the outer rings. The resultant scattering profile is then compared to a background measurement and processed to give the distribution of droplet sizes within a representative section of the total spray. Undiffracted light is focused to a small pin hole slot at the centre of the photodetector, passing through to an additional detector which is used to measure

droplet obscuration and ensure that optimal droplet densities are present in the spray for accurate sizing. The typical quoted accuracy for the instrument is $\pm 3\%$ of local values, and the RMS precision is $\pm 1\%$ of the median diameter.

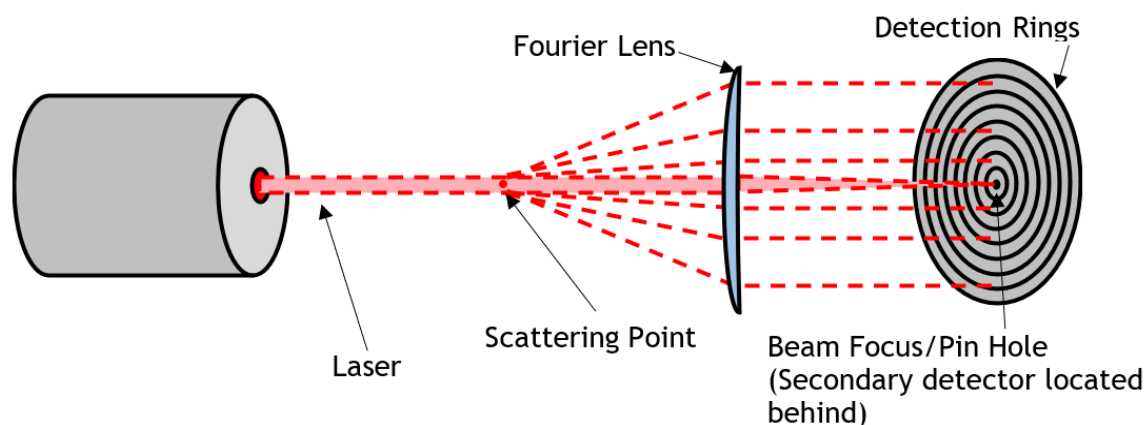


Figure 3-14 - Malvern Spraytec97 measurement principle

A 450 mm curvature diameter lens was used, giving the system an effective measurement range of 2.5-1040 μm particle size. Smaller lenses allow for smaller size detection ranges, but were not used for this project due to the larger sizes expected at low atomiser flowrates. The system was used to record time resolved PSD data calculated from the scattering signal by the RTSizer for Windows™ version 5.50 software package. The time history was automatically calculated and exported as standard averages within the system software, with an example of the outputs given in *Figure 3-15*.

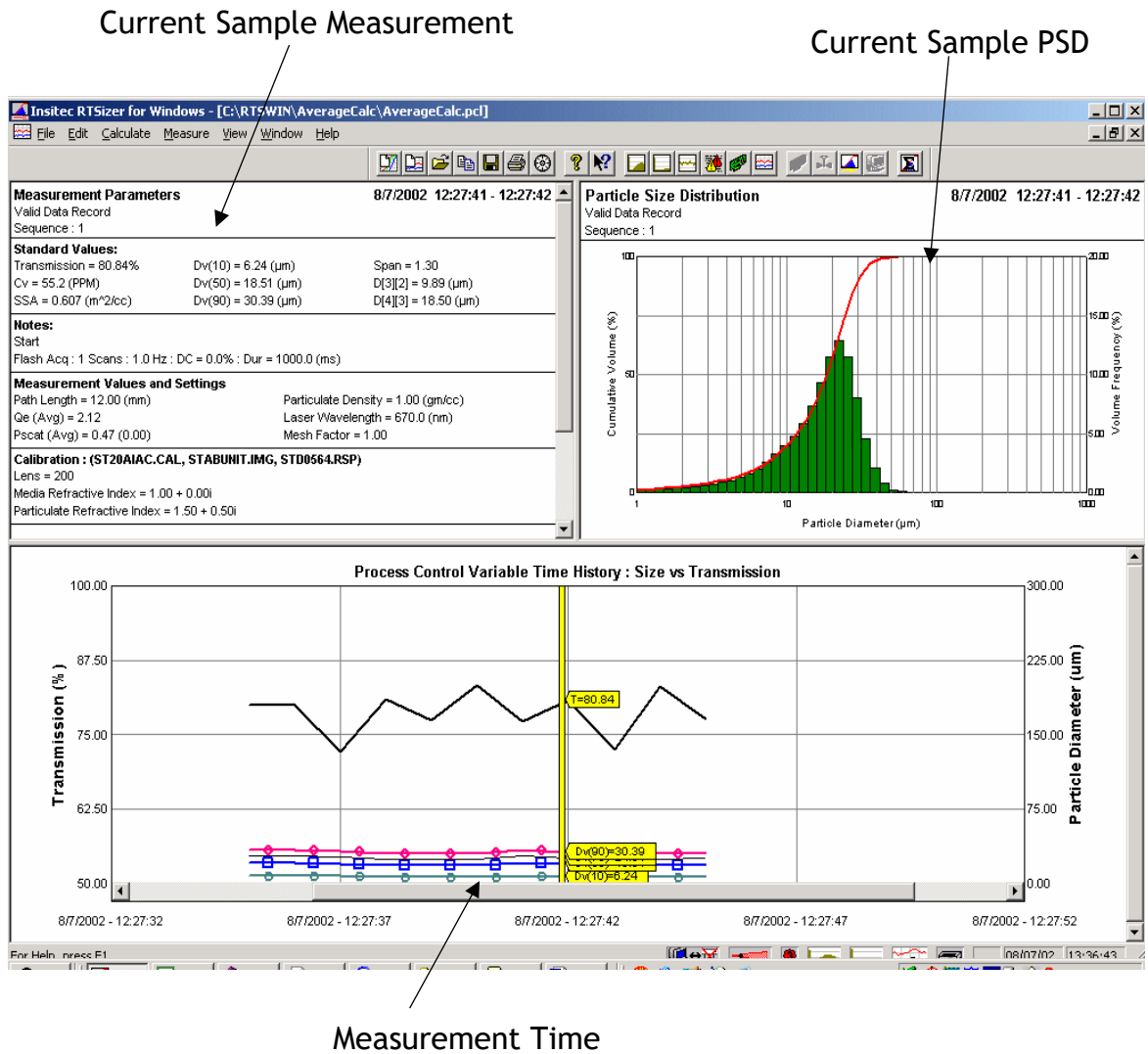


Figure 3-15 - Malvern Spraytech97 system outputs

3.6.2. Calibration

Adjustment of the detector module alignment, as directed in the instrument user manual, was undertaken each day before the start of experimentation. This was achieved by adjusting the location of the detector module relative to the laser using the adjustment screws as shown in *Figure 3-16*.

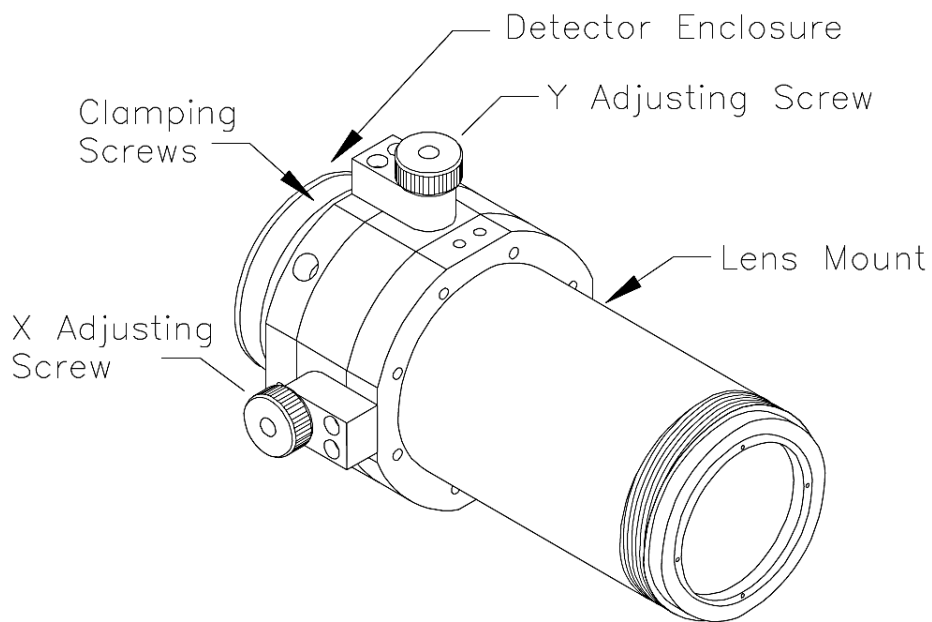


Figure 3-16 - Malvern Spraytec97 optics receiver module

As previously described, laser light entering the central pin hole of the detector passes to a detector positioned behind it, which is used during calibration of the instrument, and reported as ring 1. Calibration is achieved to ensure that the laser focal point is positioned at the central point of the detector, resulting in a high intensity reading for ring 1. An appropriate transmission signal intensity of >1500 is suggested by the manufacturer, with all other rings reading minimal intensities, as is shown in **Figure 3-17**.

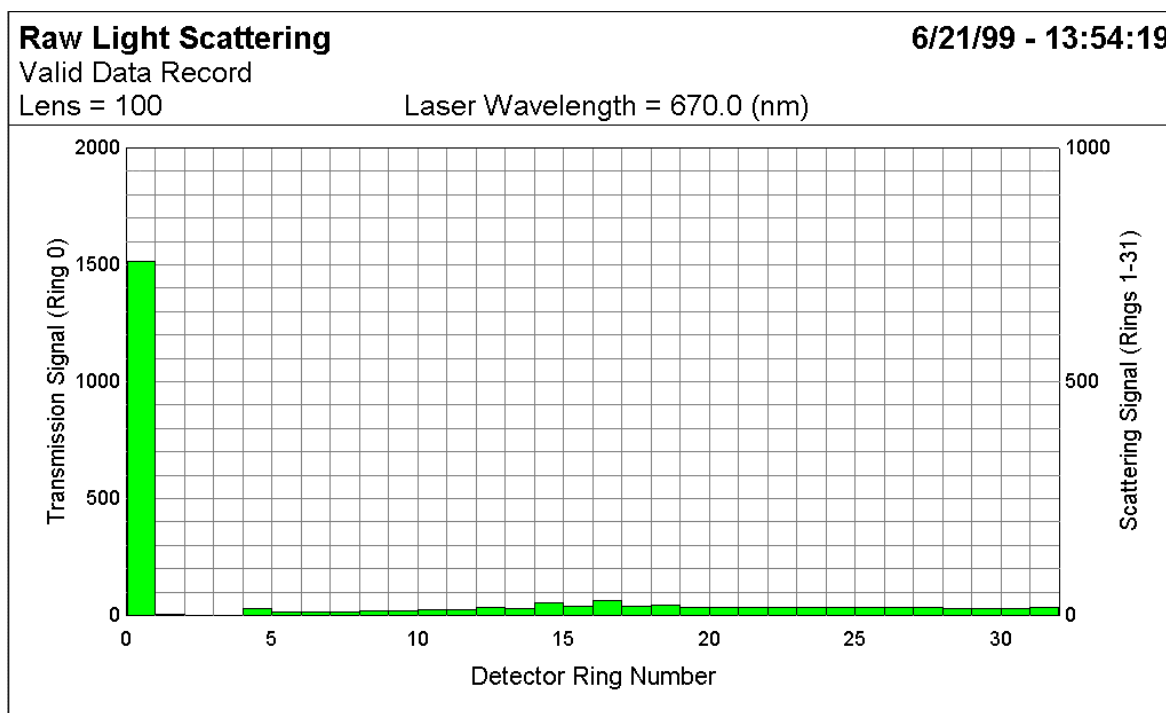


Figure 3-17 - Recommended background calibration signal

3.6.3. Experimental Setup

Laser diffraction experimentation was undertaken using only water as the operating fluid, since the laboratory was not equipped with suitable safety measures for aviation fuel testing. This afforded an experimental setup in a normal laboratory without the risk of accidental fire or explosion, deemed appropriate for preliminary assessment of the atomisation quality generated across atomiser designs. A representation of the experimental setup is given in **Figure 3-18**.

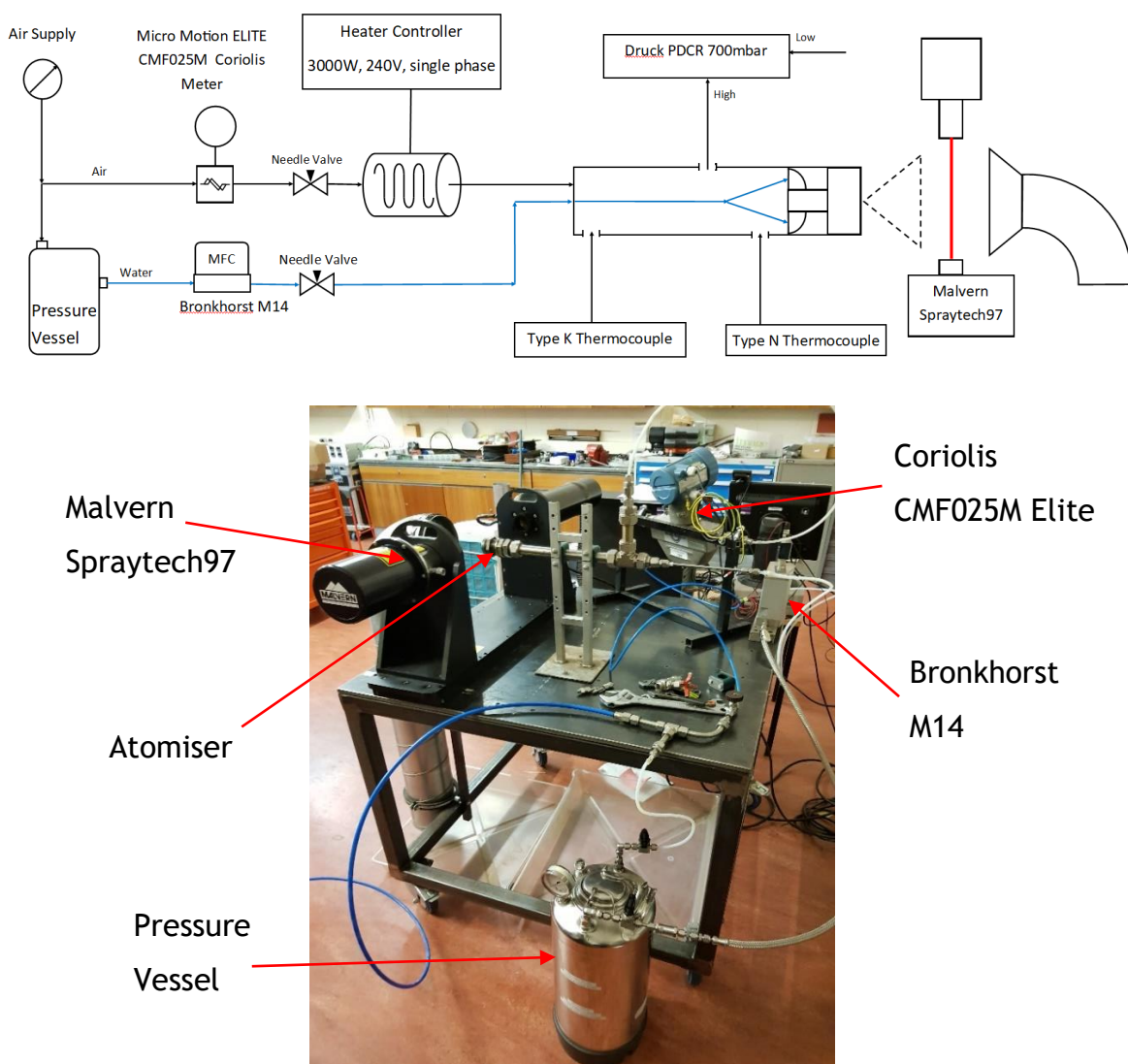


Figure 3-18 - Malvern Spraytec97 measurement setup diagram and photograph

Air was supplied to the atomiser using a Micro Motion ELITE CMF025M Coriolis meter with a quoted accuracy of $\pm 0.35\%$ at a nominal gas flow rate of 1.5 g/s. The Coriolis meter was sized so as to provide high enough accuracy at the low air flowrates to be used in the experiment. A 3 kW Watlow Cast-X electric heater

was used to preheat the air and was positioned after both the mass flow controller and control valve. Temperature at both the heater outlet and fuel injector inlet were monitored using type K and type N thermocouples, respectively. A separate air supply was used to provide sheath air to the Malvern system, so as to protect the laser and detector optic modules from a build-up of liquid droplets.

Water was delivered from in a pressurised storage vessel and regulated using a Bronkhorst M14 mass controller, with an accuracy of $\pm 0.2\%$ of the reading at a nominal mass flowrate of 2.8 g/s, and a quoted zero stability point of 0.0017 g/s.

Static pressure losses were measured using a DRUCK PDCR 10/35L differential pressure sensor with an operating range of 700 mbar and an accuracy of 0.08% full scale. The upstream (high) static pressure point was measured just before the atomiser, using a wall tap point as recommended by Benedict [166], as shown in *Figure 3-19*. Since the resultant spray was unconfined, the downstream (low) pressure was taken as atmospheric pressure. The wall tap was manufactured by perpendicularly drilling a 1.5 mm hole into a Swagelok 1" union part, with an outer 3 mm ID pipe (5 mm OD) soldered onto the external wall used to connect the pressure line. The inside of the part was deburred to limit the effect of rough edges on the pressure drop readings. The outer pipe was counterbored into the union wall slightly for stability. This was kept as shallow as possible (~0.5 mm) to allow the wall tap itself to remain as long as possible within the available wall thickness and attain an adequate L/D ratio. Given the 5 mm thick union, the resultant length of the wall tap was 4.5 mm, resulting in an L/D ratio of 3, well over the recommended minimum value of 1.5. The tap was positioned to be 2.5 D upstream of the atomiser, as recommended for static pressure loss measurements by Liptak [167].

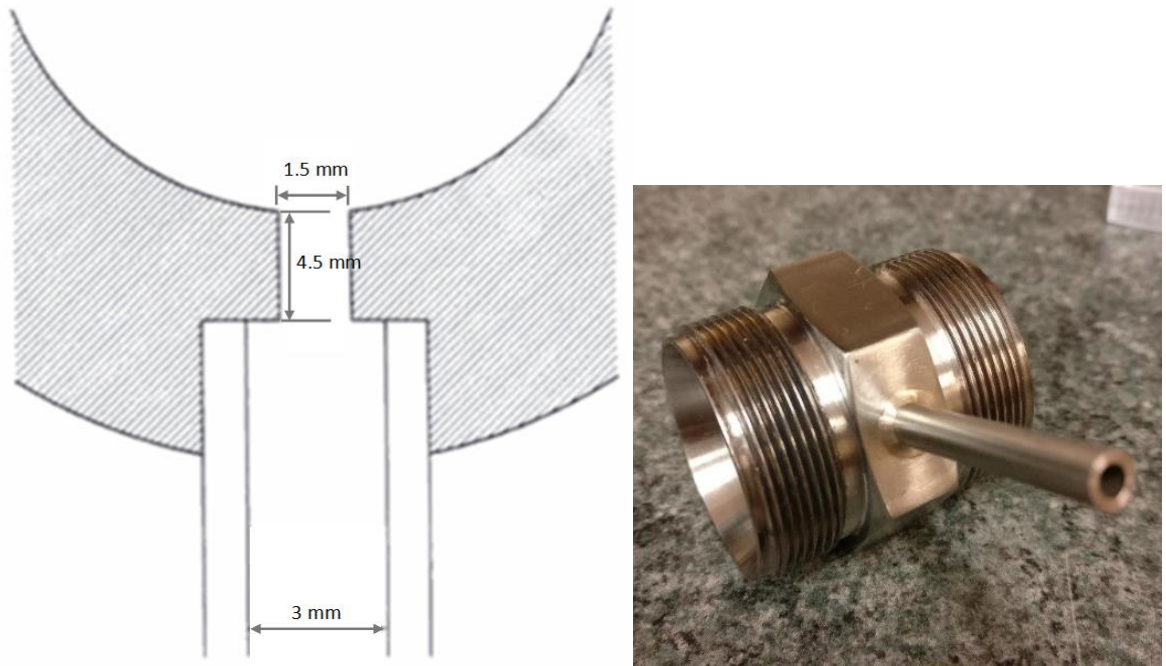


Figure 3-19 - Schematic and photograph of manufactured pressure tap

3.7. High Speed Imaging (HSI)

3.7.1. Overview

Visualisation of the spray behaviour across atomisers over a wide range of operating conditions was undertaken using backlit High-Speed Imaging (HSI). Experimentation was undertaken using the GTRC's dedicated spray booth, which was an enclosed space with transparent viewing windows intended for optical analyses of atmospheric fuel sprays in a safe operating environment. Atomisers were oriented vertically using the same housing developed for the laser diffraction experiments. An additional pressure tap section was used, located further upstream to the original pressure tap section described in **Section 3.6.3**, as a comparison to static pressure readings taken close to the atomiser. High speed images were taken using a Photron Fastcam APX-RS camera, controlled using the accompanying viewer v.3 software. High powered directional LED lights set to trigger along with the HSI camera were used to illuminate a reflective white background behind the spray so as to provide backlighting for the images. The experimental setup is shown in **Figure 3-20**. Both water and jet fuel were used during testing, with 2000 JPEG images collected per test point. A 50-image background was taken at the start of each series of tests using the setup, along with a calibration image with a visual scale, both of which were necessary for subsequent image processing.

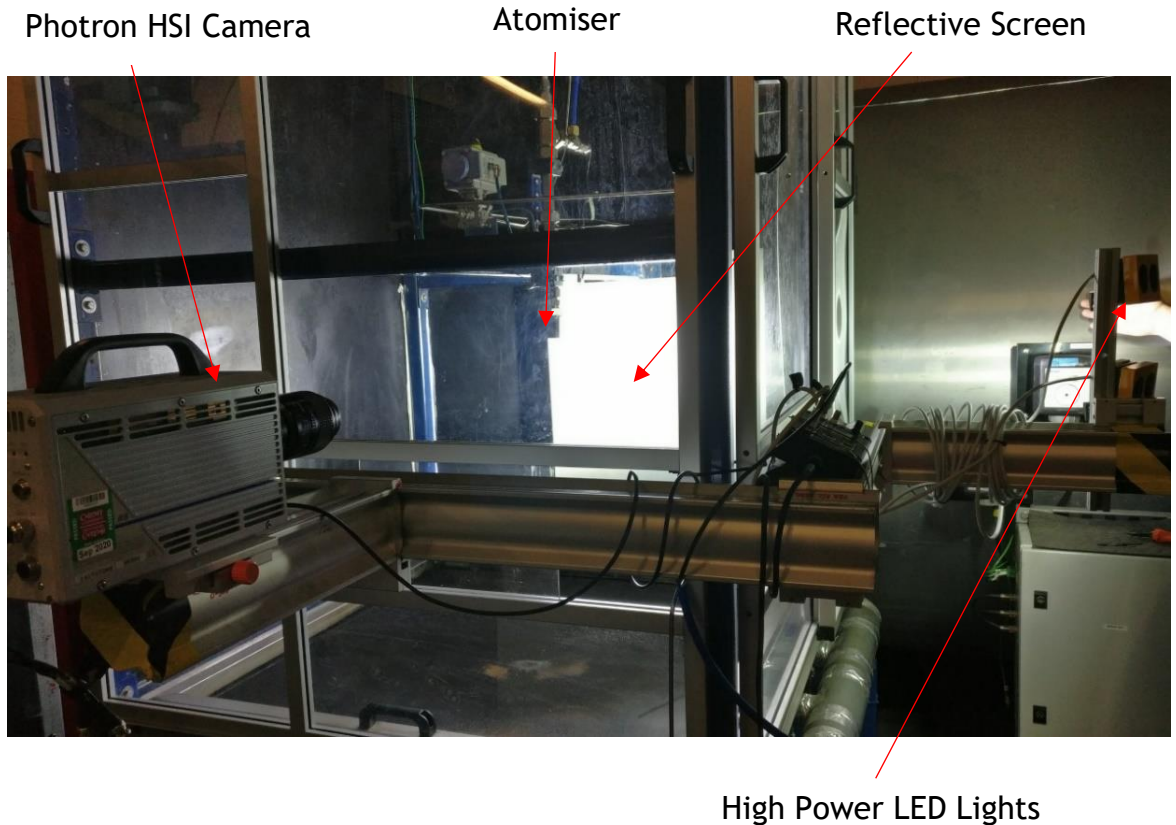


Figure 3-20 - GTRC spray booth with HSI setup

3.7.2. Image Processing Method

Image processing was undertaken using the open source ImageJ software developed by the National Institutes of Health - Laboratory for Optical and Computational Instrumentation (LOCI, University of Wisconsin) [168]. The wide variety of image processing tools made this software ideal for the rapid analysis of the 2000 image stacks. In built image tools were used to provide enhanced contrast images of the spray, averaged images of the spray across the sample time, and measurement of spray cone angles. A particle sizing tool also exists in ImageJ which affords an approximate analysis of particle sizes through image detection, but it was found that this feature was unable to be effectively used due to the camera magnification chosen to capture the entire spray profile, which was measured as approximately $125 \mu\text{m}^2$ per pixel at the focal plane. As discussed, the collected images were processed as 2000 image stacks of 8-bit greyscale images of pixel intensities between 0 (black) and 255 (white) following the following method:

- 1) **Importation of image stacks:** - A 2000-image stack of the spray and the corresponding background 50-image stack were imported into ImageJ.

- 2) **Averaging of background image:** - The background stack was averaged into a single background image using *Image>Stacks>Z-Project>Average Intensity*
- 3) **Inversion of the images:** - both the 2000 image stack and averaged background images were inverted, ensuring the spray would appear as bright droplets against a dark background.
- 4) **Light intensity background correction:** - This step was required to reduce noise in later thresholding stages and to overcome a subsequently observed issue believed to be caused by a slight dimming of the LED lights immediately following start of operation (possibly while the cooling fans were brought to full speed). Once the images were inverted (see step 3) the reduction in light intensity resulted in a gradual increase in average intensity of the images in the stack, as shown in *Figure 3-21*.

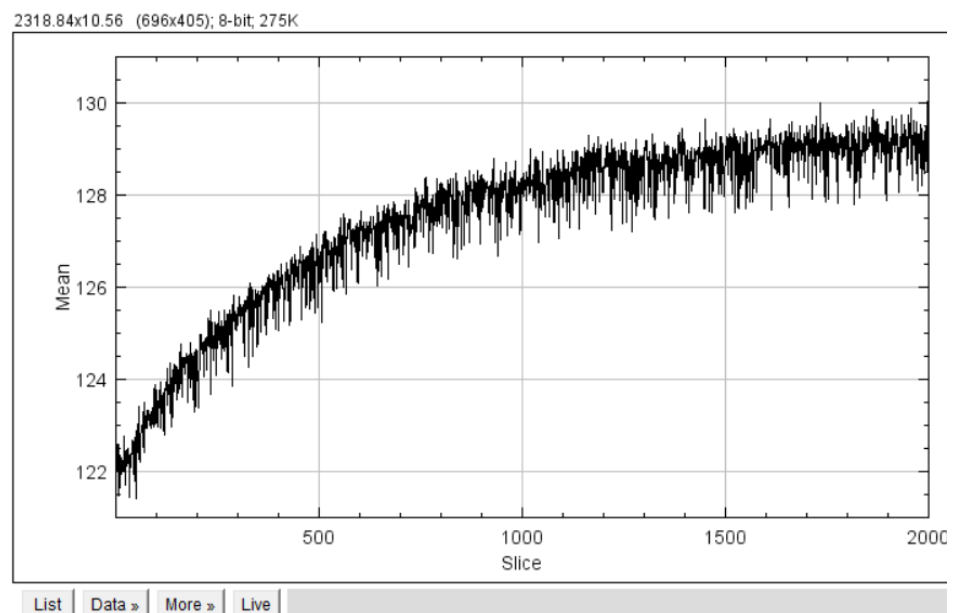


Figure 3-21 - Uncorrected intensity signal across all 2000 images of a typical image stack (intensities inverted)

To correct for this, a bespoke “*Background Correction*” macro was developed. The macro was operated by creating an average intensity control image of the final 100 images of the original stack, in which the light intensity was thought to have stabilised. The brightness intensity of each image in the stack was then measured and individually brightened or darkened to match that of the final average by applying an LUT to each image. The offset between each image and the control image was calculated as the difference in brightness intensities, and subtracted from

the min and max values of the LUT. The resultant image intensity plot after corrections is shown in figure with the same scale as *Figure 3-22*.

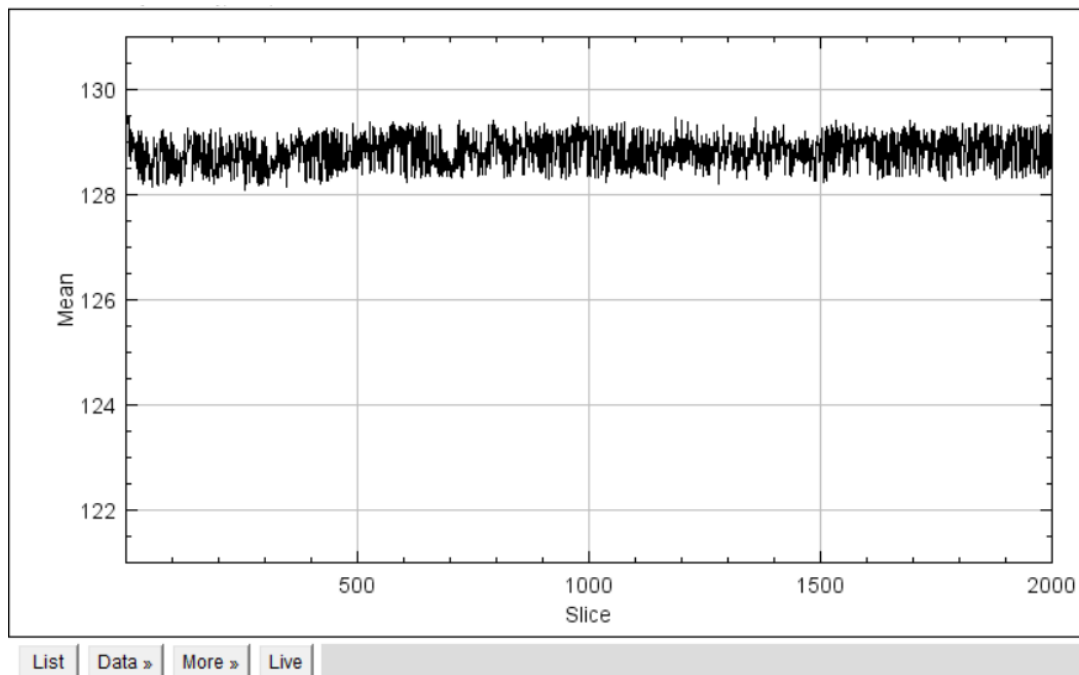


Figure 3-22 - Corrected intensity signal

- 5) **Background subtraction from image stacks:** - The averaged background image was subtracted from the processed stack using the function *Process>Image Calculator*.
- 6) **Isolation of single image:** - Each image was isolated from the stack using *Image>Stacks>Tools>Make Substack*. In order to better visualise the spray, the contrast of the images was then increased using the “enhance contrast” feature, with the number of saturated pixels set to 0.6%. Because this also brightened the background, a second macro (“*Background Residual*”) was written in order to correct the resultant images for residual brightness of the background from any offsets between the average background image and the spray images. The measured intensity of this section was subtracted from the entire image to ensure that pixel intensities in background sections of the image were as close to 0 as possible. This helped to improve image clarity and isolate the liquid droplets from the background. An example of the enhanced contrast function is shown in *Figure 3-23*, showing the same image without and with the corrections.

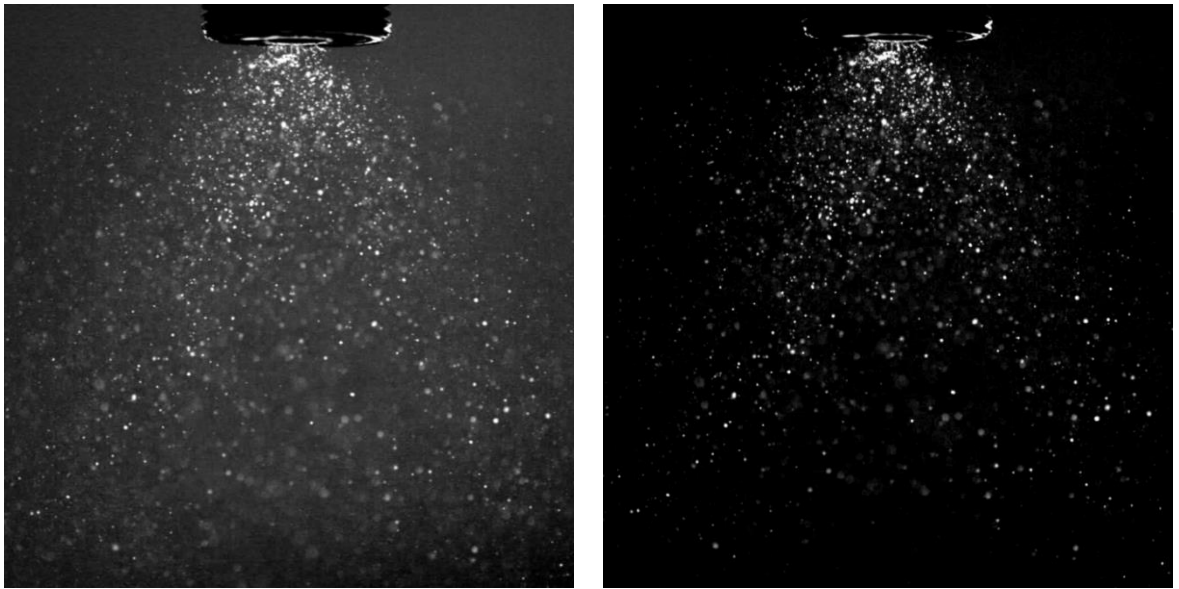


Figure 3-23 - Effect of correcting for residual background illumination

- 7) **Generation of standard deviation plot:** - A visualisation of the spray structure was generated using the standard deviation feature in ImageJ. Standard deviation plots display greater intensities for pixels in which light intensities are more transient, with higher intensities generated where droplets appear more frequently. This method would therefore act as a rudimentary particle tracking feature and provide a visualisation of the core region of the spray, as has been explored in previous studies [169]-[171]. Before this was undertaken, images were binarized to a 1% background level threshold, as shown in *Figure 3-24*. In doing so, particularly small droplets were removed from the spray, and the visible spray pattern would consist of larger droplets holding the majority of the spray volume.

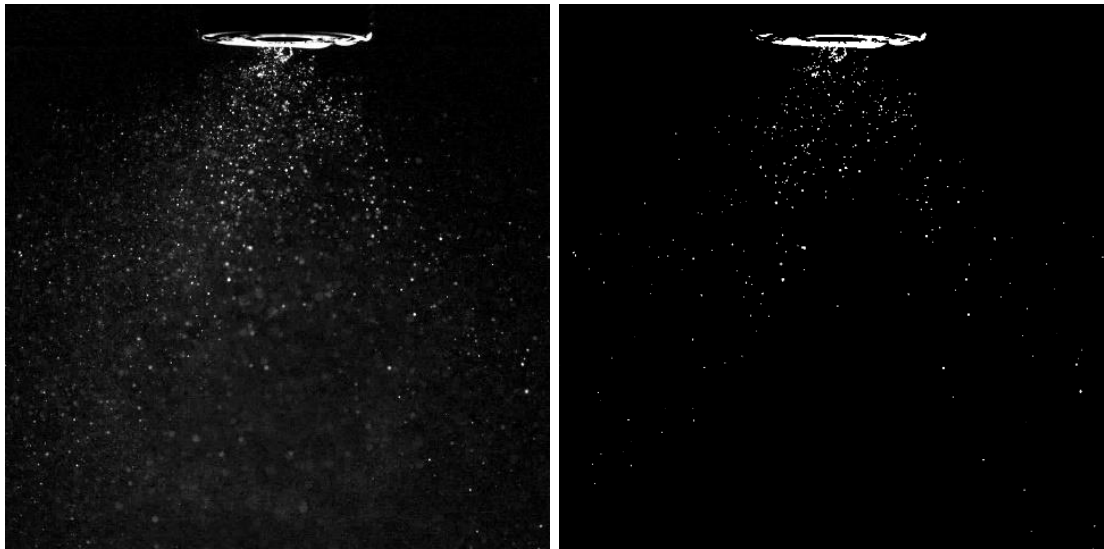


Figure 3-24 - Images before (a) and after (b) thresholding

The standard deviation image was then created of the spray using *Image>Stacks>Z-Project>Standard Deviation*. For ease of visualisation, a false colour “Royal” LUT filter was applied. An example of the resultant image is shown in *Figure 3-25*.

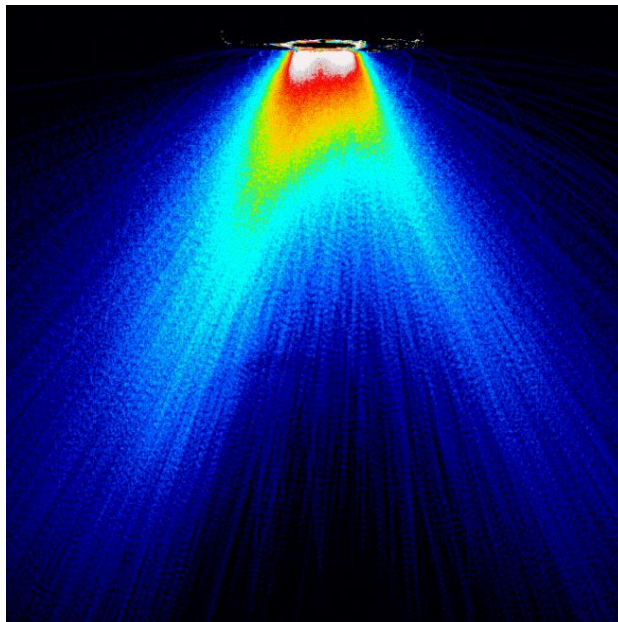


Figure 3-25 - STD plot following thresholding

- 8) **Spray cone angle measurements:** - To determine spray cone angles, background subtracted images (as of step 5) were converted to standard deviation plots, and binarized to a threshold of 80%. This produced a black and white image that was found to consistently offer a good indication of the core spray profile, an example of which is shown in *Figure 3-26*. A

similar method has been utilised in previous spray studies for measuring spray cone angles [123]. The spray angle could be measured using the angle measurement tool in ImageJ. Half-angles to the vertical were measured on both sides of the spray by drawing a line from a point at the spray cone edge 40 mm vertically downstream of the atomiser exit, to the atomiser fuel channel exit. To determine the vertical distance, a scaling factor for the conversion of pixels into mm was set using the accompanying calibration images. The overall cone angle (θ_c) was determined as a summation of the two half angles.

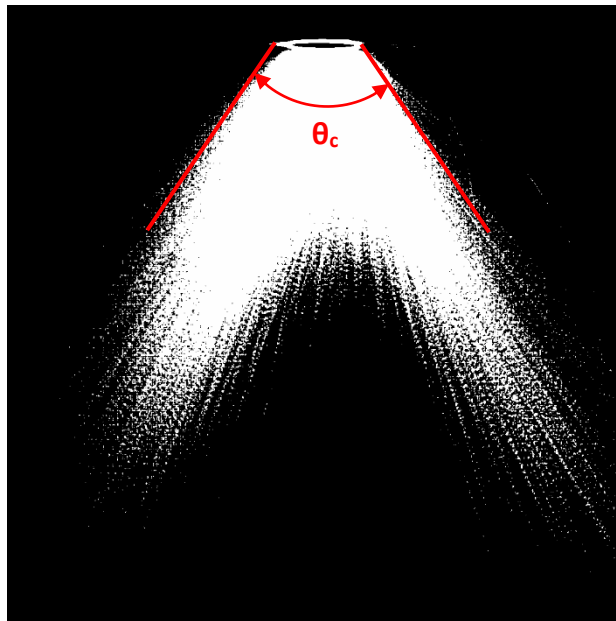


Figure 3-26 - Spray cone angle measurement

3.8. Phase Doppler Anemometry (PDA)

Phase Doppler Anemometry (PDA) is a single point light scattering technique used to non-intrusively determine spray characteristics, including droplet sizes and velocities. The operating principle incorporates laser Doppler and phase Doppler principles, first described by Bachalo and Houser [172]. When two laser beams focused onto a control volume encounter a spherical particle, they experience individual scatter according to Lorenz-Mie theory. Although this theory dictates that light is scattered in all directions, placement of a detector at a particular position relative to the incident angle of light results in one of the three main modes of scatter becoming dominant. These modes are reflection, 1st order refraction and 2nd order refraction, as shown in **Figure 3-27**. The interaction

between scattered light from the two light sources, as a result of spatial relative phase differences, generates an optical interference fringe pattern at the detector. As the particle moves through the control volume, the difference in light scattering causes the fringe pattern to appear to move at the Doppler difference frequency (f_D) from the point of view of the detector. A receiver lens housed by the detector module focuses light onto a photodetector, which observes light as a Doppler burst signal.

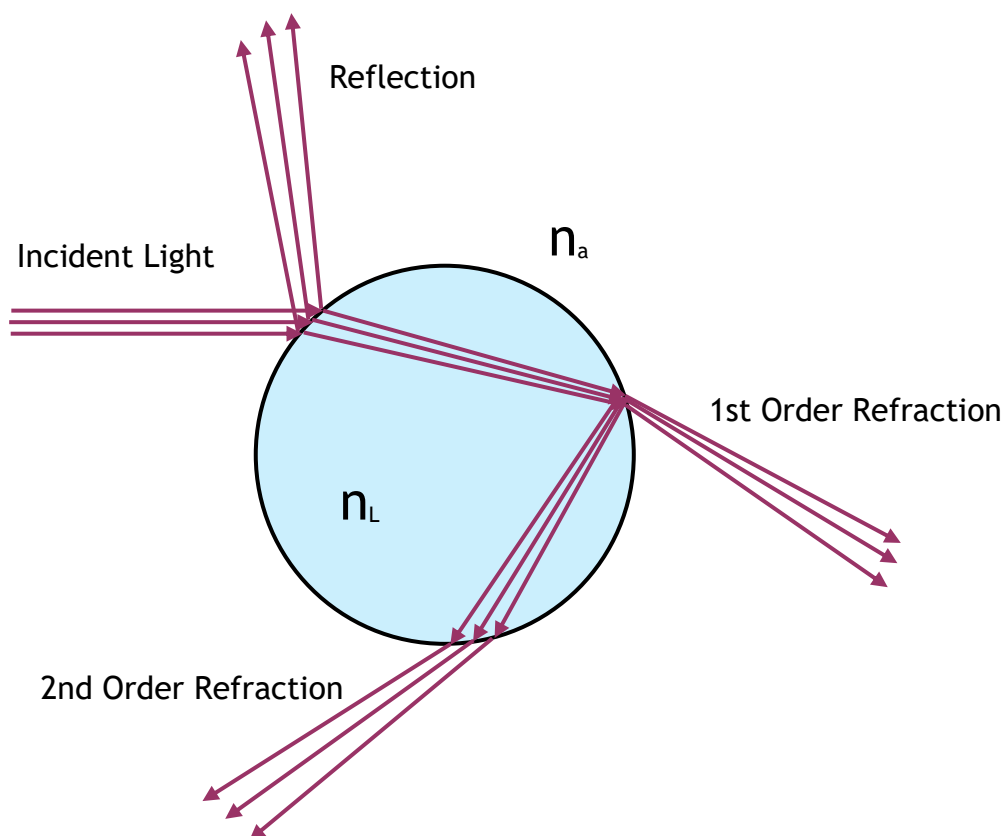


Figure 3-27 - Refraction of coherent light through a liquid particle (reproduced from Dantec homepage [173])

Factors affecting the Doppler difference frequency are droplet velocity, beam intersection angle, and the wavelength of the light. As such, detection of light signals allows for the determination of both particle sizes and velocities. Particle velocities may be detected from a single Doppler burst signal, according to **Equation 3-21**:

$$U = \frac{\lambda}{2 \sin(\frac{\theta}{2})} f_D \quad 3-21$$

Where θ is the offset angle of incidence between the two laser beams and λ is the wavelength of the light [172]. Particle velocities are detected in one plane

only depending on the orientation of the lasers, and so multiple pairs of laser beams at different wavelengths are required for categorisation of a droplet moving through 3D space.

The use of multiple detectors is the key feature separating a PDA system from an LDA system, and the feature allowing for the detection of particle sizes. Light rays from the two laser beams refracted by a particle towards two detectors experience differences in optical path lengths due to the scattering effect, leading to a phase offset (ϕ) between measured Doppler burst signals. The degree of scattering differs as a result of particle sizes (D) and the refractive index (n_{liquid}) of the particle relative to the air medium. Typically, larger particles scatter light to a higher degree than smaller particles, which results in a greater difference between optical path lengths and a larger phase offset. As such, particle sizes can be determined by this offset, alongside knowledge of the beam intersection angle, wavelength of the light, and the angle of observation [172]. For refraction dominant signals, particle sizes are determined from **Equations 3-22 and 3-23**:

$$\phi = \frac{-2\pi D}{\lambda} \frac{n_{rel} \sin \theta \sin \Psi}{\sqrt{2(1 - \cos \theta \cos \Psi \cos \rho)(1 + n_{rel}^2 - n_{rel} \sqrt{2(1 + \cos \theta \cos \Psi \cos \rho)})}} \quad 3-22$$

$$n_{rel} = \frac{n_{liquid}}{n_{air}} \quad 3-23$$

Where ρ is the scattering angle, and Ψ is the angle between the light rays incident on the receiving optics prior to detection.

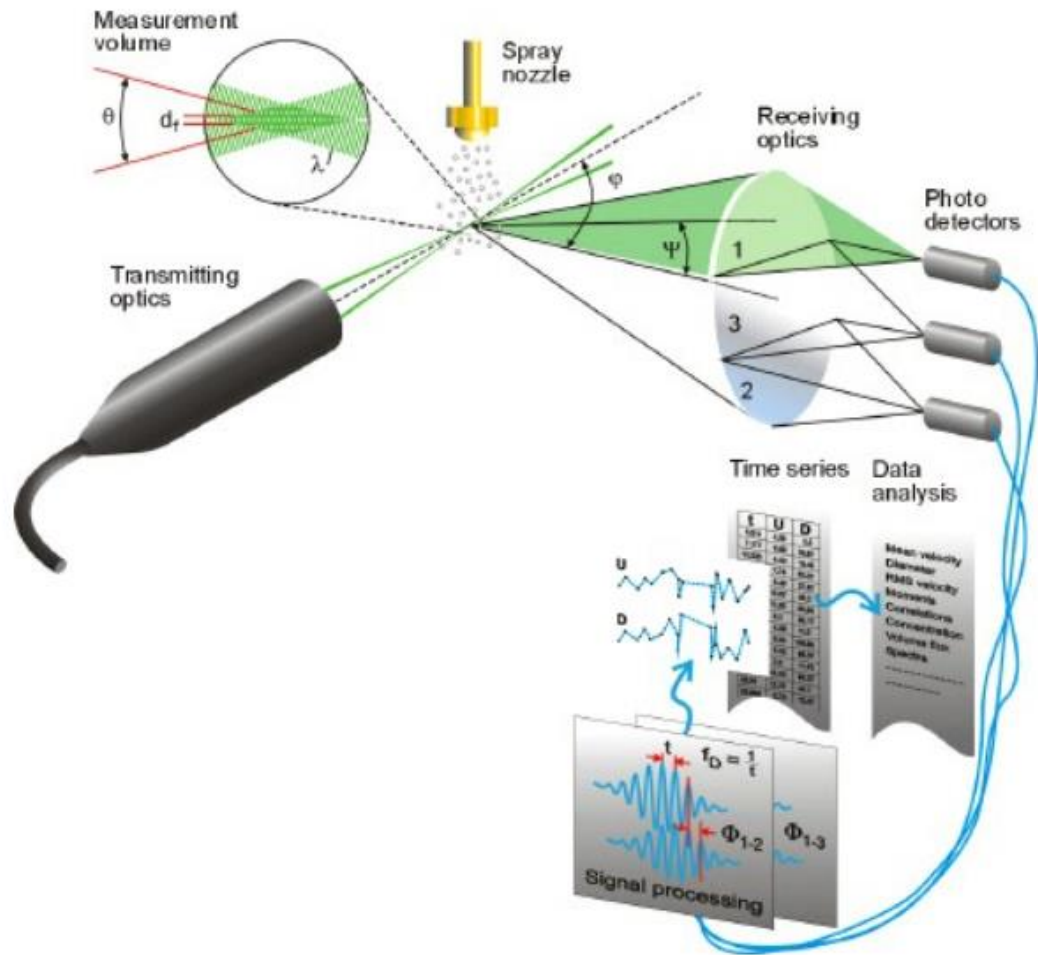


Figure 3-28 - PDA measurement principle [173]

Unlike the Malvern laser diffraction instrumentation which uses a laser passing through the full width of the spray (*Section 3.6*), PDA is always used to determine spray characteristics at a single measurement point. As a result, determination of global spray characteristics for a non-homogenous spray, as would be expected from an airblast atomiser, requires collection at multiple test-point locations in the spray. To account for localised variations in spray characteristics at different regions of spray, Weighted Mean Sauter Mean Diameter (also called WMSMD or global SMD) calculations were undertaken, as in previous spray studies [117], [123]. This method assigns an average scalar value to a spray based on collected SMD measurements taken across multiple axial positions, as given in *Equation 3-24*.

$$WMSMD = \frac{\sum_{r=1}^{r=R} SMD \times n_r}{\sum n_r} \quad 3-24$$

In theory, WMSMD values determined from PDA data collected at multiple points along a central line at a fixed distance away from the atomiser exit, could be used to replicate the test procedure of the Malvern Spraytech97 described in *Section 3.6.1*. However, given that atomisers generate complex flow fields, it is noted that using a global average in this way is somewhat of an oversimplification. Additionally, it is important to note that previous studies [174] have found that the two measurement principles are affected by separate uncertainties, which have been seen to cause significant disparities between datasets collected from the two measurement techniques, although general trends may be comparable.

A Dantec Fiber PDA system was utilised for experimentation in this work. A multiwavelength laser generated by a Coherent Innova 70C system, operating at ~2.5 W, is separated into its component colours by passing through a Dantec splitter optics system. Two colours were utilised for testing: green ($\lambda=514.5$ nm) and blue ($\lambda=488$ nm). Two beams are produced for each colour, necessary so as to produce a fringe pattern when scattered from a measurement volume. The green laser pair was orientated vertically and used to measure particle axial velocity components, while the blue laser pair was orientated horizontally and used to measure particle radial velocities. The receiver module, which houses a series of focusing lenses and three detectors, was positioned at 69° relative to the direction of incident light, within the recommended range of 1st order refraction dominant scattering ($30-70^\circ$) and close to the Brewster angle of the fuels used [172], [173]. Individual values of specific gravity and refraction index were provided for the fuels. The maximum particle size detectable by PDA instrumentation is limited by the point where the separate light rays are again in phase. As such, a focusing lens built into the receiving optics is coupled with an aperture plate to give a characteristic particle size measurement range, which should ideally be tailored for the expected size range of the measured spray. Of the three commercially available aperture plates for the detector module, plate B was used, giving a maximum measurement size of ~260 μm .

4. Assessment of Additive Manufacturing (AM) in the Development of Prefilming Airblast Atomisers

4.1. Overview

As outlined in *Section 3.2*, a generic RQL combustor had been designed prior to the beginning of this project. Initial unconfined combustion trials indicated that the original concept atomiser [2] was capable of a sustained spray flame, with stability observed when operating with Jet A-1 across a range of AFR from 3.7-4.2. The pressure drop characteristics of the atomiser were generally favourable, but a stable flame was only achievable at pressure drops between 4.9-6.1%, somewhat higher than the recommended range of 3-4%. Additionally, the atomiser exhibited poor ignition behaviour and was prone to extinguishing when changing operating conditions, which would likely lead to difficulties with combustor operability over long test campaigns. The poor ignition performance and stability only at higher pressure drop values suggested that the original atomiser was not able to generate high enough air velocities for good atomisation quality in the desired 3-4% pressure drop range, at which conditions the atomiser may have experienced the characteristic breakdown of atomisation quality associated with airblast atomisers at low air velocities. This would lead to coarse sprays with large droplets, potentially leading to erratic and unpredictable rates of nvPM formation during later emissions testing.

As such, it was decided that the atomiser was unsuitable for subsequent emissions experimentation, and the decision was made to develop further atomisers that more closely replicated proven concepts [147], towards improving atomiser performance. AM techniques, as outlined in *Section 3.2.1*, were used to rapidly prototype numerous designs with subtly variable geometries, so that predicted performances (e.g. dP/P , SMD, cone angle etc.) could be empirically validated towards the selection of an optimised design. Two separate design phases were utilised over the course of this study. The phase I atomisers were developed for use with the pre-existing the Mk. I RQL combustor (*Chapter 5*), with a second phase of atomiser designs developed alongside the Mk. II combustor, as detailed later in this thesis (*Chapters 6 and 7*).

4.2. Design Considerations

4.2.1. Atomiser Features

One of the key features in the design of atomisers of this type are the inner and outer air swirler assemblies. As mentioned in **Section 1.3.1**, swirling air is employed in atomisers in order to establish a recirculation zone, helping to stabilise the flame, and to evenly distribute the fuel and air within the pre-flame zone, ensuring uniform and efficient combustion free from local variations in equivalence ratio. Swirler assemblies were first designed according to the standard straight bladed profile outlined by Lefebvre and Balal [16], which employ a constant angle of inclination along the profile of each blade. Blades were designed as helical threads, using standard helical trigonometry to achieve a target angle of inclination (θ). This is represented in **Figure 4-1**.

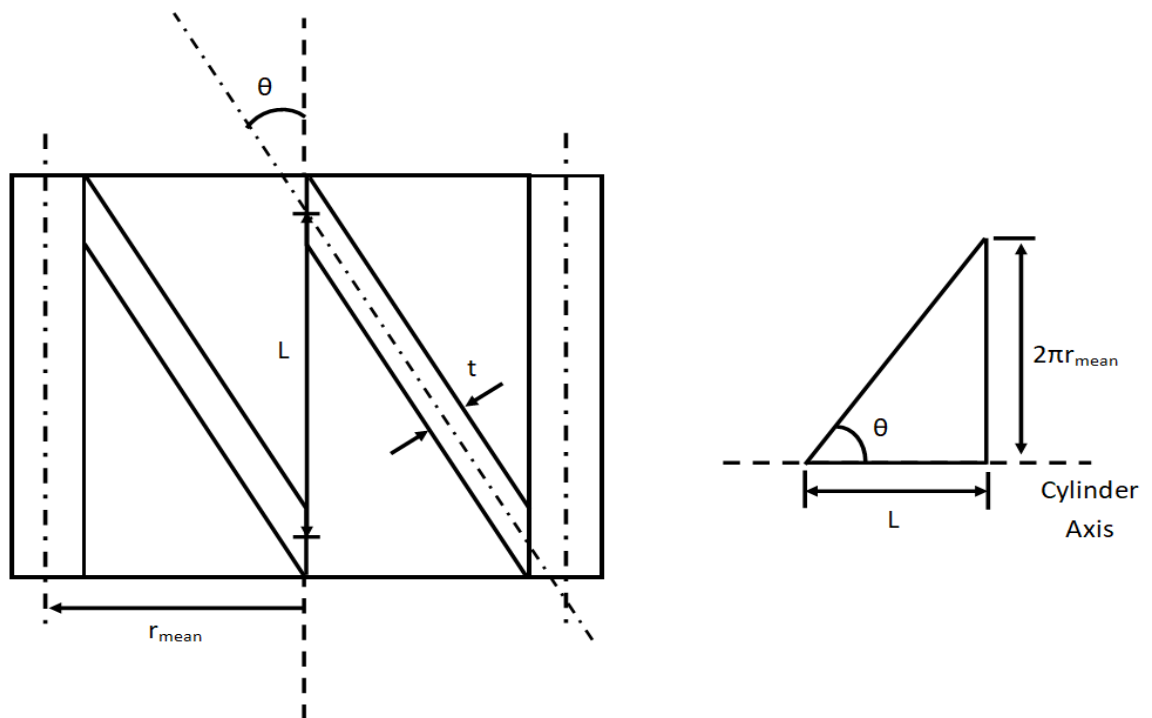


Figure 4-1 - Representation of a straight bladed swirler assembly [16], and trigonometry for a helix

Figure 4-2 shows examples of inner and outer air swirler assemblies used for the phase I atomiser designs.

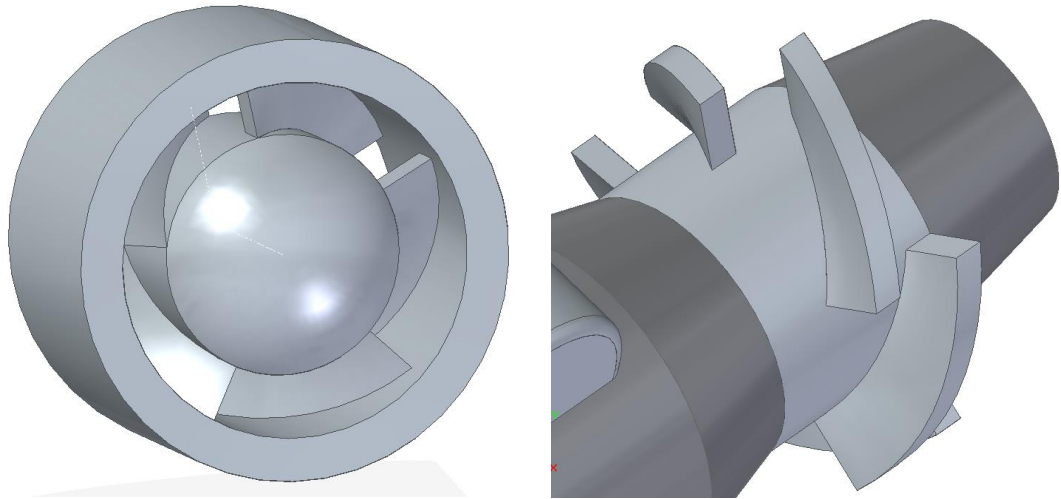


Figure 4-2 - Inner (left) and outer (right) air swirlers

In this work, the average air velocities (U_a) produced by the atomisers was calculated from mass continuity. Given velocity distributions are expected to vary across the 3D flow field produced by an atomiser, previous atomisation studies have employed U_a as a global measure of air velocity, made up of both axial (U_{axial}) and whirling components (U_{whirl}). For these calculations, it was assumed that the air velocity through the swirler assemblies (which were the narrowest constrictions through each respective air channel) and the velocity of air exiting the atomiser would be relatively unchanged. Therefore, a summation of the turned area through both of the swirler assemblies (A_a) could be used to calculate U_a . Air was assumed as an incompressible fluid, and the effective area through the swirler assemblies was assumed to be equal to the geometric areas (ie. $C_d=1$). This meant that calculated velocities were approximations of true exit velocities, but were deemed suitable to understand velocity trends across atomisers for the purposes of subsequent empirical categorisation.

Values of A_a through each set of swirlers was calculated using trigonometry, as shown in **Figure 4-3**. For atomisers of relatively thin swirler blade profiles, empirical atomiser characterisation can discount the blockage of the blades in the determination of flow area, and so the inlet area is equal to the free swirling area (A_{fsw}). However, due to the small scale of the atomisers and limitations in manufacture techniques, the blade thickness were significant compared to the swirler assembly area in this study. It was therefore necessary to equate the inlet area (A_{in}) to the free swirling area minus the blockage area of the blades. As such, the equations used for determination of turned atomiser flow area and average predicted velocity are given in **Equations 4.1.-4.4**.

$$x = t_b \sec \theta \quad 4-1$$

$$A_{in} = \left(\frac{\pi}{4}\right) (D_{sw}^2 - D_{hub}^2) \quad 4-2$$

$$- [\text{no. of blades} \times x \times \left(\frac{D_{sw} - D_{hub}}{2}\right)]$$

$$A_a = A_{in} \cos \theta \quad 4-3$$

$$U_a = \frac{\dot{m}}{\rho_a \sum A_a} \quad 4-4$$

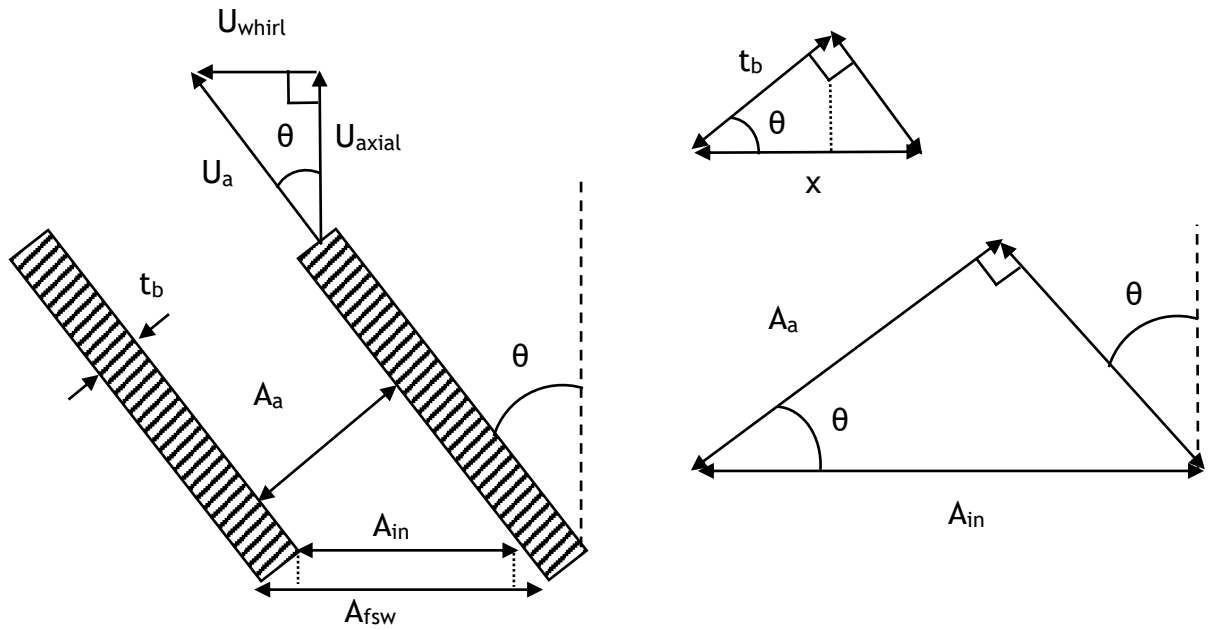


Figure 4-3 -Swirler assembly effective flow area calculations

The degree of swirl generated by an atomisers was calculated using the geometry-based swirl number and shown in **Equation 4.5** [16].

$$S_n = \frac{2}{3} \left[\frac{1 - (D_i/D_o)^3}{1 - (D_i/D_o)^2} \right] \tan \theta \quad 4-5$$

Where D_i and D_o refer to the inner and outer diameters of the free swirling area, respectively, while θ is the blade angle. As such, swirl is typically enhanced for swirler assemblies with narrower free swirling areas and higher blade angles. It is noted that angles $>60^\circ$ are not recommended as they can result in flow stall at the atomising edge, leading to rapid deterioration of atomisation quality [175]. Recommended swirl numbers for atomisers in aircraft combustors are above 0.6, above which flow recirculation can be achieved, and values above 0.8 may be

considered as strongly swirling [176]. As noted by Aigner and Wittig [175], swirl may also be applied to the fuel sheet prior to atomisation, helping to spread the liquid into an even, thin sheet. The effect of swirler blade configuration (the individual directions in which fuel and air is turned relative to each other) for twin fluid atomisers is also a consideration, as was explored by Chin *et al.* [177]. The authors found that optimal atomisation performance was achieved through the use of an inner air stream co-rotating with the fuel stream, and with a counter-rotating outer airstream. As such, all atomisers in this study were manufactured following this configuration.

While straight helical blades were initially used in the developed atomiser designs, it has been observed that curved bladed designs are more efficient in swirling atomisation air and are generally recommended as superior for the design of airblast atomisers. Curved blades allow for lower kinetic energy losses, reduced likelihood of blade stalling, and reduction of wakes which can adversely affect atomisation quality [16]. This can allow for reduced SMD values and improved flame stability over straight blades at matched fluid mass flowrates [178], [179]. Straight swirler blades are thought to be typically easier to design and manufacture, but this benefit is made redundant by the improved drawing and manufacturing complexity capabilities of CAD and AM used for production. For the later atomisers, curved blades were designed by extruding blade surface areas of a chosen thickness along a custom-made blade path imprinted onto the swirler hub. This path initially ran parallel to the direction of oncoming air before curving following a circular arc, with the blade angle determined according to the angle of the circular segment used to calculate the arc length (α), as highlighted in **Figure 4-4**.

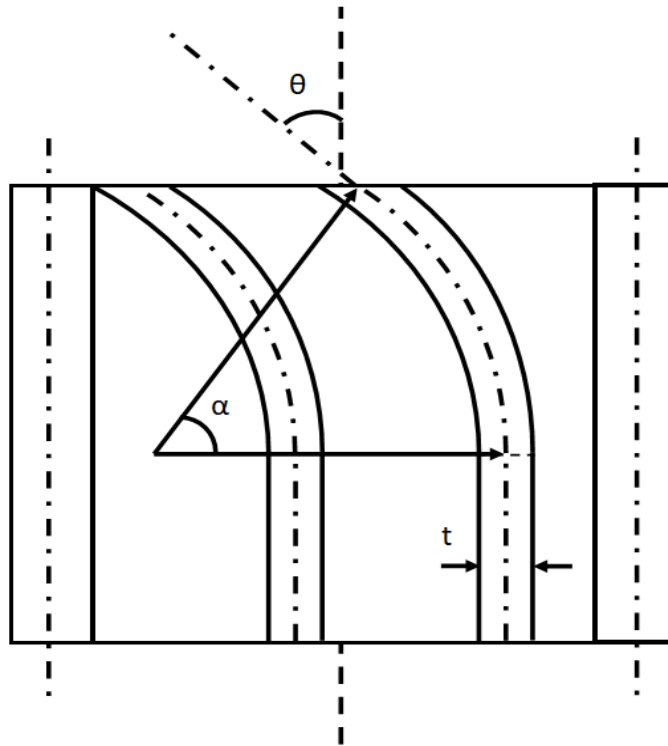


Figure 4-4 - Curved bladed swirler assembly

Recommendations for designing air passages following the swirler assemblies are given by Simmons *et al.* [127]. In their original patent, an optimal constriction ratio between the exit cross sectional area and the free swirling area (A_{fsw}) was given as 80-90%. For the inner air channel, air exiting the swirlers immediately enters a region of expansion, which then constricts into a central channel of length (L_i), recommended as 1.5-2 times the diameter of the channel (D_1) [127]. The expansion region was a carryover from the original atomiser design due to the rounding of the swirler hub, but would be expected to result in additional kinetic energy losses through expansion, reducing the overall efficiency of the atomiser. Therefore, some of the atomiser designs developed in this study included a conical extension (bullet) in this region, so as to gradually reduce the cross-sectional area in the post blade channels. For the outer air channel, air exits the atomiser and contacts the fuel sheet at an angle of inclination (θ) to the horizontal, which is defined by the passage dimensions. Steep angles of inclination are known to promote the prompt mode of atomisation (described in **Section 2.4.1.2**), with outer air channel inclinations of 30° seen to induce the transition in the work of Lefebvre [115].

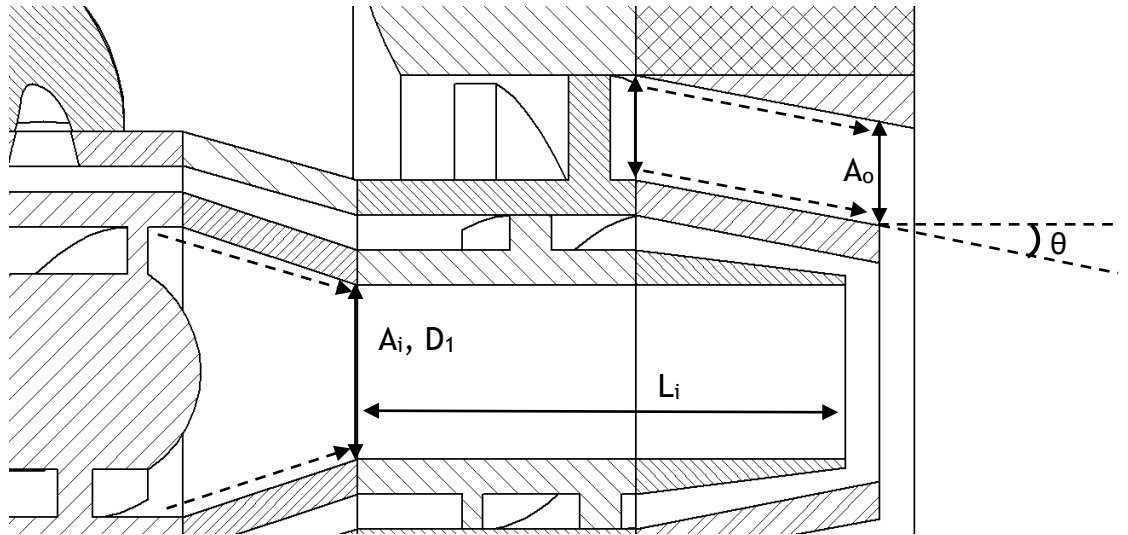


Figure 4-5 - Additional air flow path dimensions

The final key design consideration was the prefilming surface against which liquid fuel forms into a thin film, which are unique features of prefilming airblast atomisers. In the Parker-Hannifin atomiser concept, fuel is introduced into an annular passage running between the central inner air channel and outer air channel. As the fuel exits the channel, the liquid forms a thin film on the upper surface of the fuel channel, due to the centrifugal motion of the fuel exiting the fuel swirlers and the aerodynamic forces exerted by the expanding inner air (**Figure 4-6**). As such, the film thickness is governed by the dimensions of the fuel annulus and prefilmer. As seen, air exiting the inner air channel contacts the fuel film in the small region between the inner air orifice exit plane and the end of the prefilmer, referred to as the prefilming zone length (L_p). Simmons [180] describes two separate families of atomisers based on varying prefilmer length, namely, the long prefilming type and the “zero-length” prefilming type. However, the effect of prefilmer length was not a consideration for the atomisers used in this project, and was kept consistent throughout designs. The thickness of the prefilmer (t_p) is taken as the annular width of the prefilmer at the furthest point, and should ideally be kept as narrow as possible to prevent liquid accumulation. As described by Inamura *et al.* [181], thicker prefilmer edges are prone to liquid accumulation, causing a wider droplet size distribution and larger droplets in the primary atomisation region, which detrimentally impact combustion. However, it is noted that secondary atomisation acting on these larger droplets results in smaller droplets by the secondary atomisation region. Hence, dependencies between SMD values and prefilmer thickness are limited beyond the primary atomisation zone. Thick or uneven liquid films have also been shown to significantly worsen

atomisation quality [182], and as such, the value of t was kept relatively small and constant throughout this project.

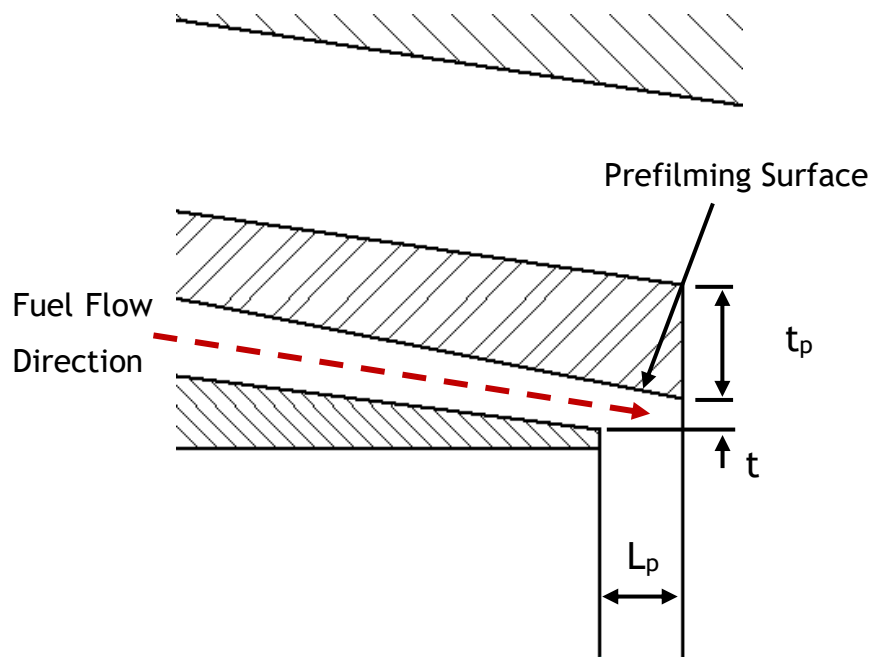


Figure 4-6 - Atomiser prefilmer dimensions

4.2.2. Static Pressure Loss Calculations

In most aircraft engine designs, air enters the combustor section from a single source following the compressor section. Air is then partitioned along various flow paths so as to achieve the desired air supplies and AFRs at key points in the combustor section. The quantities of air through each flow path is determined by the component pressure resistivities imparted on the air, caused by changes to the flow path geometry. Knight and Walker [183] explain that this can be represented as a pressure circuit network, spanning the combustor air path, containing a number of individual series and parallel circuits containing resistive elements. Aircraft components exhibit characteristic pressure resistivities (loss factors) which can be estimated from knowledge of component geometries. As air passes through each component, the frictional losses and flow separation imparted by each component causes a dissipation of kinetic energy proportional to the total air mass flowrate, measured as a drop in static pressure (P_s). Static pressure refers to the ambient pressure of the fluid while unaffected by fluid movement. This differs from dynamic pressure (q), which is imparted by the motion of a fluid, an example of which can be observed by the wind imparting

a force against a flat object. In a fluid where dynamic pressure is measured parallel to the flow direction, the value of q is equal to $\frac{1}{2}\rho V^2$. The sum of these two pressure components describes the total (stagnation) pressure (P_T) in the system, as shown in **Equation 4.6**.

$$P_T = P_s + q = P_s + \frac{1}{2}\rho U^2 \quad 4-6$$

In fluid mechanics, one often encounters the scenario of fluid motion through closed systems. The motion of laminar, incompressible fluid in a system free from kinetic energy losses is described by Bernoulli's equation. In a horizontally flowing system (ie. no change in net height between the inlet and outlet), the motion of a fluid is controlled by the total pressure acting on the system alone. As such, the system will maintain a constant stagnation pressure throughout, with any change in dynamic pressure is mirrored by the inverse of static pressure and vice versa. Changes in dynamic pressure in a closed system, result from cross sectional area changes, the simplest of which is a circular orifice. In a perfect orifice or well-rounded nozzle, flow can be considered frictionless, and Bernoulli's equation between two points is represented by **Equation 4.7**.

$$P_1 + \frac{1}{2}\rho U_1^2 = P_2 + \frac{1}{2}\rho U_2^2 \quad 4-7$$

Aircraft components are representable as real restrictions such as sharp-edged orifices, with kinetic energy losses generally represented by a coefficient of discharge (C_d), defined as the ratio between the actual and theoretical mass flowrates through the restriction. Similarly, the fraction of the cross-sectional area of a vena contracta to the orifice is represented by the Coefficient of Contraction (C_c). Additionally, frictional losses have small effects on the actual velocity of the jet compared to the theoretical velocity, the ratio of which is described by the coefficient of velocity (C_v). In the case of a real nozzle, the term effective flow area is used to refer to an equivalent idealised cross-sectional area of a theoretically perfect nozzle ($C_d = 1$) that is representative of the actual geometric cross-sectional area (A_{geo}) with real losses ($C_d < 1$). As such, the effective area of a given nozzle will always be lower than the actual area, and is represented in **Equation 4.8**.

$$A_{eff} = C_d A_{geo} = \frac{\dot{m}}{\sqrt{2\rho\Delta P}}$$

A representation of the flow field across a real orifice plate flowmeter, and the accompanying static pressure profile is shown in **Figure 4-7**. In agreement with Bernoulli's theory, static pressure is seen to increase immediately before the orifice, then sharply drops after the orifice. The lowest static pressure in the system occurs along the same vertical plane as the vena contracta (P_2) where the cross-sectional flow area is most constricted, and velocity is highest. This decrease occurs through the conversion of static pressure to dynamic pressure, which increases the fluid velocities at this point. Determination of maximum air velocities can therefore be determined by the static pressure differential (ΔP) between P_1 and P_2 . These are useful measures for determining atomiser air velocities and in understanding atomisation behaviour, but are not representative of the component losses described by Knight and Walker [183]. Following the vena contract, the expansion of the effective flow area causes the air velocity to slow, causing a drop in dynamic pressure. Most of the kinetic energy is converted back into static pressure further downstream of the orifice, but in real systems, a portion of the original kinetic energy is permanently lost. For orifice plates, static pressure losses are typically 10-50% of starting values [184], but this will differ by component. An additional loss observed is the gradual decline in static pressure as a result of friction losses at flow boundary layers.

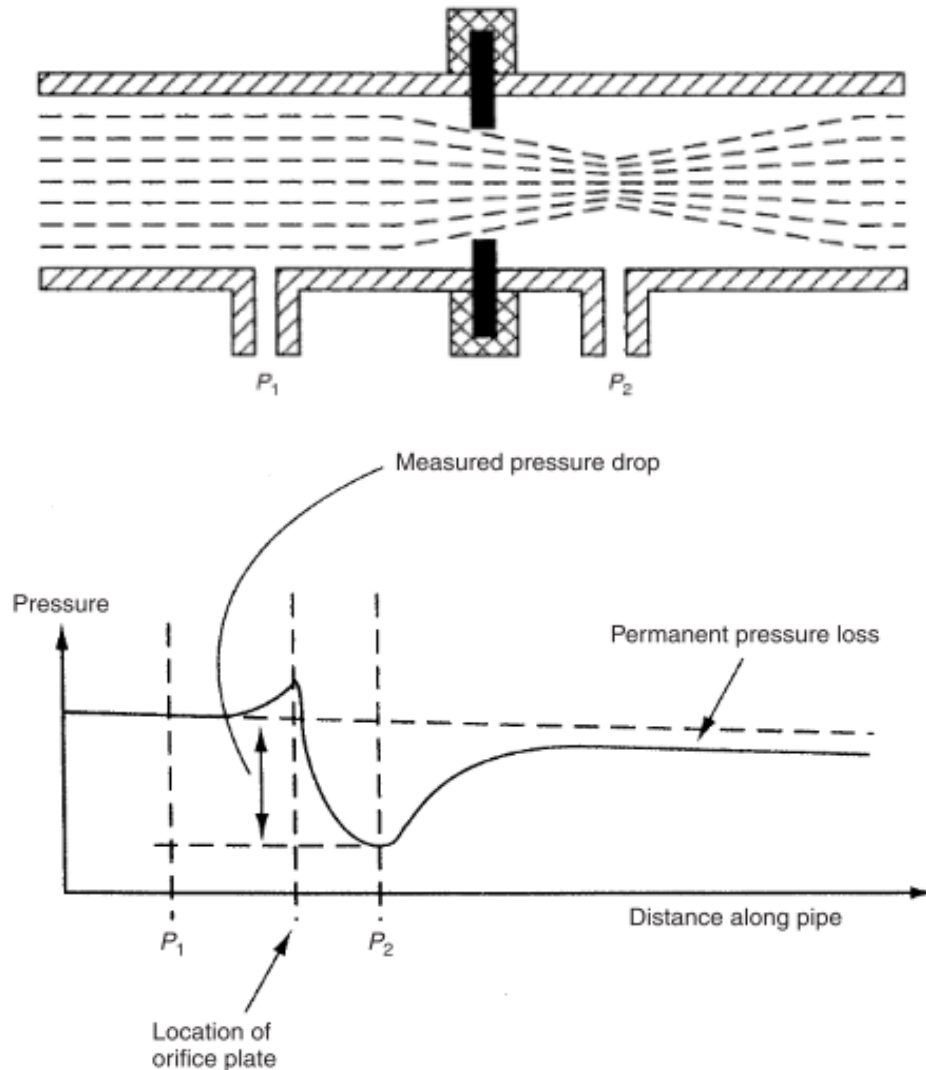


Figure 4-7 - Static pressure profile across a simple orifice [184]

The above theory forms the basis of the method proposed by Knight and Walker [183], whereby pressure losses result from inefficiencies in pressure recovery in regions of expansion, and other minor losses such as friction. Losses between two points of a reference area of constant cross-sectional area are estimated for components of known geometries from empirical knowledge of kinetic energy dissipation across typical gas turbine components. At the conceptual design stage this can allow the user to tune combustor design features before manufacture. The term ϕ is used as the characteristic pressure resistivity for a component, which remains constant across all flow conditions, and relates to pressure drop following **Equation 4.9**. Pressure differentials across a component are effectively analogous to voltages in a conventional electrical circuit, while the mass flow rates of air represent the current. Components follow the same theory as series and parallel electrical circuits, in which elements in series produce a pressure resistivity equal to the sum of each element (**Equation**

4.10.), while parallel circuits have an equal pressure drop across them (**Equation 4.11**).

$$P_1 - P_2 = \phi_1 \frac{1}{2} \rho V_1^2 \quad 4-9$$

$$\Delta P_{series} = \sum_{i=0}^n \Delta P_i \quad 4-10$$

$$\Delta P_{parallel} = constant \quad 4-11$$

Component pressure resistivities are determined relative to a reference area, which remains constant between the upstream and downstream measurement locations. This is arbitrarily chosen, and can be any fixed area sufficiently large in comparison to the component areas. In aircraft combustors, this is often taken as the annulus area surrounding the combustor, or the flame tube (combustion liner), given as A_F [183].

4.2.2.1. Expansion/Contraction Losses

Expansion pressure losses occur in flow paths where sudden expansions in flow area are encountered and can be determined solely from knowledge of the expansion ratio between relative flow areas. The equations for determining pressure resistivity for an expansion region, as outlined by Knight and Walker [183], is given in **Equation 4.12**.

$$\phi = (\lambda - 1)^2 \text{ where } \lambda \text{ is the expansion ratio } \left(\frac{A_2}{A_1} \right) \quad 4-12$$

Losses occur in sections where a sudden contraction occurs from the expansion of air between the vena contracta and actual pipe area, as shown in **Figure 4-8** [185]. These losses are expected at the entrances of atomiser air channels, as well as across the air holes in the combustion liner. Losses are dependent on the C_d of the contraction region. Standard values for various geometries have been extensively determined [185]. Sharp circular entrances to a pipe typically have C_d values of 0.6, which incur higher losses than rounded entrances, which exhibit C_d values of 0.8. The equation given by Knight and Walker [183] is presented in **Equation 4.13**.

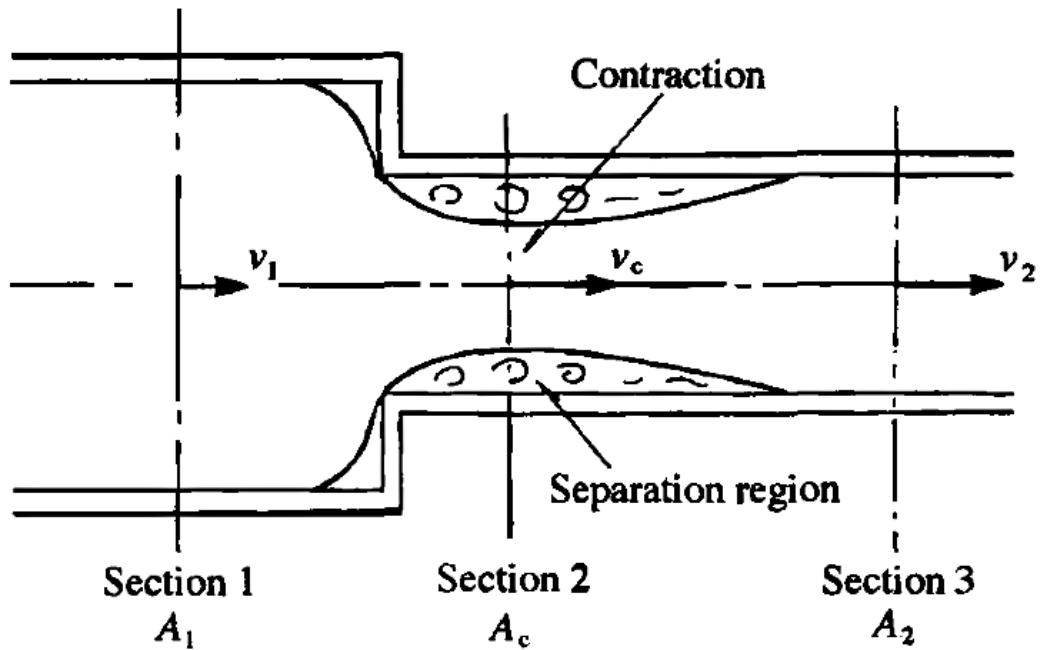


Figure 4-8 - Flow entering a contraction [185]

$$\phi_{ref} = \left(\frac{A_F}{A_2}\right)^2 \left(\frac{1}{C_d} - 1\right)^2 \quad 4-13$$

4.2.2.2. Swirler Losses

Knight and Walker [183] also explain that the losses in a swirler assembly are the result of two factors: 1) Dissipation of a whirl velocity component in the turning of the air through the blades and 2) blade profile losses. The former is essentially represented by the expansion of air following the narrowest restrictions between swirl blades. The latter is a combination of numerous losses against the blade profile determined from empiricism, including friction, flow separation, and secondary losses as a result of 3-dimensional effects. The equation for the pressure resistivity of a generic, bladed swirler is given by **Equation 4.14** [16], [183].

$$\phi_F = \left\{ \left[(1 + K_{sw}) \left(\frac{A_F}{A_{annulus}} \right)^2 \sec^2 \theta \right] \right\} - 1 \quad 4-14$$

$$\text{Where } A_{annulus} = \left(\frac{\pi}{4}\right) (D_{sw}^2 - D_{hub}^2)$$

Total blade losses are represented by the term K_{sw} . As discussed earlier, A_F is defined as the cross-sectional area of the flame tube, but can essentially be considered as the area the atomiser expels air into, provided this is then scaled relative to the chosen reference area. Detailed empirical studies have been undertaken to understand the individual losses expected across different atomiser geometries, with values of K_{sw} generally assumed as 0.15 for curved blades and 0.3 for straight bladed designs. It should be noted that Knight and Walker [183] refer to thin blades in their study, and it is expected that relatively thick blades may realistically require even larger values of K_{sw} due to additional kinetic energy dissipation. This can be understood from the pitch/chord ratio (σ), of which values of 0.7 were recommended. The thickness/pitch (t/s) ratio is described as a means of correcting blade losses for blade thicknesses, however this work will instead factor in the area blocked by the blade thicknesses into values of A_{in} used in determining losses. Since the blade thicknesses in the atomisers developed by Knight and Walker [183], were defined perpendicularly to the turned air direction, a modified version of their equation is presented in **Equation 4.15** which accounts for the blockage of the blades, observed in this study.

$$\phi_F = \left\{ [(1 + K_{sw}) \left(\frac{A_F}{A_{in}} \right)^2 \sec^2 \theta] \right\} - 1 \quad 4-15$$

4.2.2.3. Mass Flow Calculations

Figure 4-9 shows the total pressure losses considered through the inner and outer airpaths across an atomiser design (highlighted red). For entrance losses, standard values of C_d were chosen for the entrances based on their geometries used. C_d was taken as 0.6 for sharp circular entrances, and 0.8 for annular and rounded circular entrances. Individual pressure resistivity values for each airpath are summed into a single value of ϕ_F . In line with the recommendations of Knight and Walker [183], these are then used to calculate the percentage of air mass flow (\dot{m}) partitioned through each parallel air path using **Equations 4.16**. The overall pressure resistivity across the parallel system ($\Phi_{overall}$) is constant across the two airpaths, and is calculated using **Equations 4.17**.

$$\dot{m}_x = \frac{100}{\sqrt{\frac{\phi_x}{\phi_1}} + \sqrt{\frac{\phi_x}{\phi_2}} + \dots + \sqrt{\frac{\phi_x}{\phi_n}}} \quad 4-16$$

$$\Phi_F = \phi_1 \left(\frac{\dot{m}_1}{\dot{m}_{total}} \right)^2 = \phi_1 \left(\frac{\dot{m}_2}{\dot{m}_{total}} \right)^2 = \dots \phi_n \left(\frac{\dot{m}_n}{\dot{m}_{total}} \right)^2$$

The ratio of inner to outer air mass flow is an important consideration to ensure operational stability for atomisers of this type, with Simmons *et al.* [127] suggesting an optimal range of outer/inner mass flow ratios between 1 and 2, whilst ensuring the exit air velocities are kept approximately equal across flow paths. Based on this, fuel and airflows can be matched to achieve the desired pressure drops, power requirements, and to maintain the suggested optimal AFR of between 0.5-4.

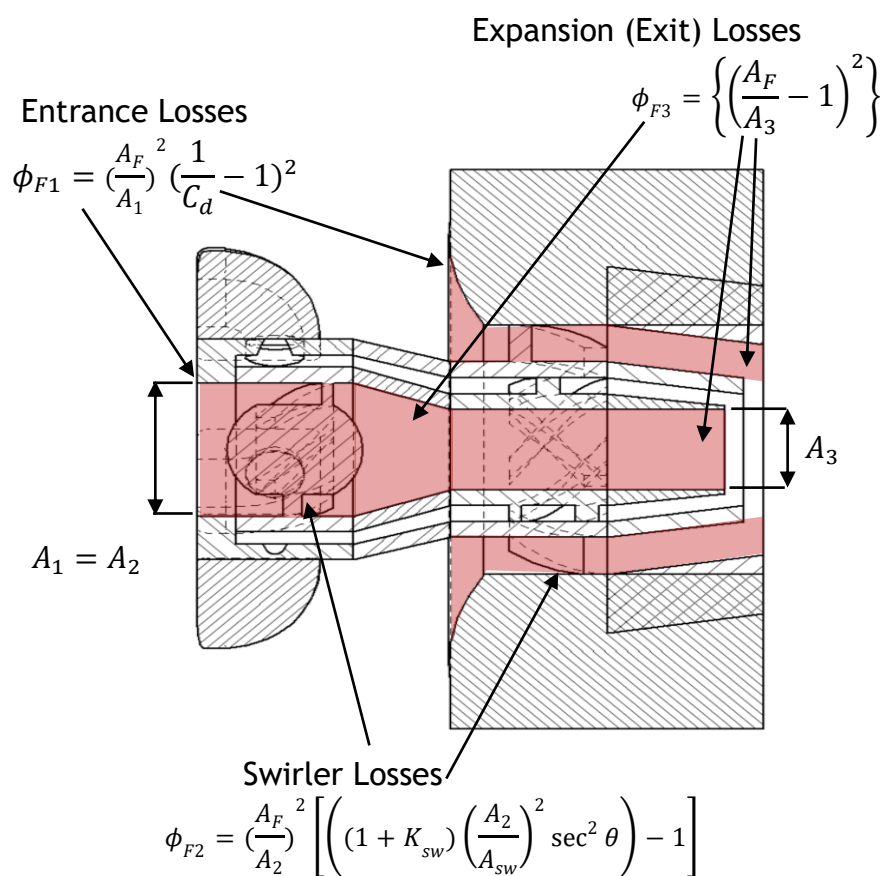


Figure 4-9 - Representation of pressure losses across atomiser air channels

In this study, an additional pressure loss was included to account for a partial blockage caused upstream of the nozzle air inlet caused by a Swagelok part required to connect the atomiser fuel supply. Physical measurements of the pipe and the Swagelok part were used to determine the cross-sectional area at each point, separating the part into three contraction regions. Values of ϕ were then determined using **Equation 4.13**. A schematic of the Swagelok part is shown in **Figure 4-10**.

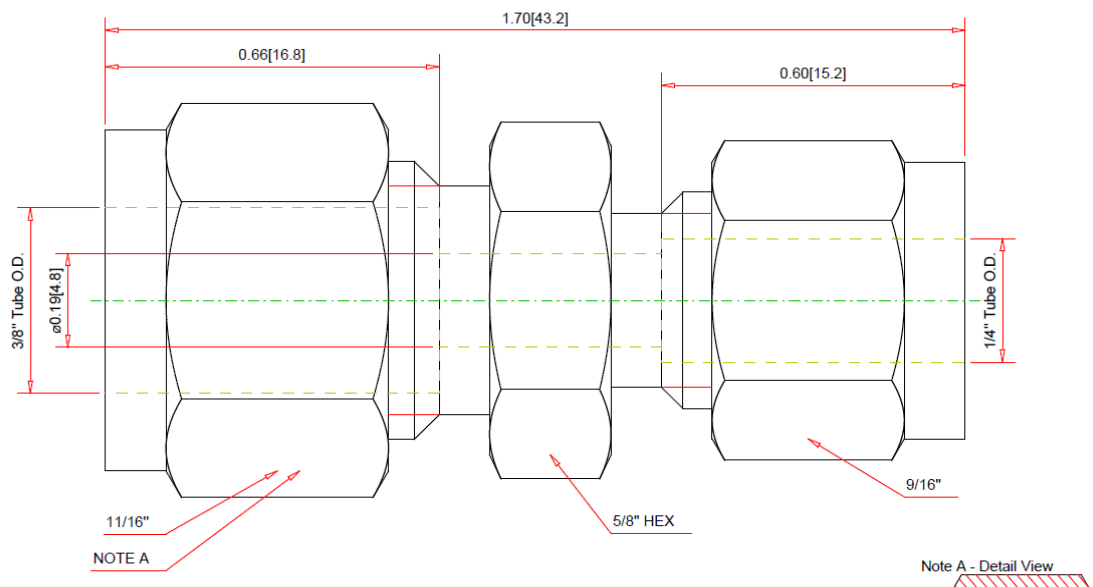


Figure 4-10 - Swagelok 1/4" to 3/8" connector

Once individual pressure resistivities are determined, a global pressure loss factor is used to determine the total pressure drop expected across the entire combustion system. The law of mass conservation dictates that the dynamic pressure will remain constant between two points if the reference area remains constant, and so the loss of kinetic energy is reflected in a static pressure loss. Therefore, the global pressure loss factor is given as the ratio of total static pressure loss across the combustor to the reference (inlet) dynamic pressure, with total static pressure losses determined using **Equation 4.18**. Knowledge of the pressure loss factor enables the determination of the total pressure drop across a given combustor (or other component) as a ratio of the combustor reference (ambient) pressure. For real world engines, this ratio is normally kept in the range of 3-4% [16].

$$\phi_{overall} = \frac{\Delta P_{atm}}{q_{ref}} \quad 4-18$$

It is noted that a number of minor pressure losses are not accounted for in this methodology, including kinetic energy losses due to friction against wall surfaces, as described in the Fanning equation [183]. While these losses are typically small in conventionally manufactured atomisers, AM parts (without surface treatment) typically exhibit higher average surface roughness values (R_a), and hence may experience further loss of kinetic energy due to flow shear against the wall surfaces. Increased surface roughness associated with AM generated

swirlers has previously been shown to noticeably increase measured pressure drop values, leading to a decrease in both C_d and axial velocities [186], [187]. The magnitude of these deviations is dependent on atomiser design, but it has been observed that as much as a 16% higher pressure drop may be associated with an AM swirler that has not had post surface treatment ($R_a = 8.31\text{-}11.09 \mu\text{m}$) vs. a traditionally manufactured swirler ($R_a = 0.67\text{-}1.76 \mu\text{m}$) as a result of surface roughness [186]. Surface roughness measurements were undertaken on the first AM atomiser concept, using a Taylor Hobson Form TalySurf Series 2 profilometer (see [2]), and indicated R_a values for flat surfaces parallel to the atomiser build direction of $12.3 \mu\text{m} \pm 3.0 \mu\text{m}$ following manufacture, while angled surfaces exhibited roughness values of almost double, at $25.2 \mu\text{m} \pm 3.0 \mu\text{m}$.

Additionally, the pressure loss method outlined assumes incompressible flow, which may be an oversimplification considering the small scale of the atomisers and levels of turbulence expected at the operating conditions used. Significant compression through the narrow atomiser channels may be expected to result in additional expansion losses not accounted for in the current methodology.

4.3. Phase I Atomisers

4.3.1. Design

The primary aim of the first set of developed atomisers was to enhance the swirl characteristics compared to the original prototype atomiser, towards achieving a shorter flame, while maintaining the favourable pressure loss characteristics. It was hoped that this would also lead to an improvement in atomiser stability and ignition behaviour. The first design (I-A) was nearly identical to the original concept design [2], and serves as a baseline design. The only notable change over the original atomiser was a reduction in fuel annular thickness from 0.75 mm to 0.37 mm, achieved by narrowing the outer fuel channel diameter (D_3) so as not to impact the effective area through the air channels. This was the narrowest that could be achieved using the AM facilities available in Cardiff University. For the next atomiser design (I-B), the swirl angle of the outer air blades was increased from 45° to 60° , increasing the amount of swirl produced by

the atomiser, so as to more closely replicate the design proposed by Makida *et al.* [147].

For the next atomiser design (I-C), the effective areas of the outer air channels were increased, so as to reduce the anticipated pressure drop values to levels comparable to the original prototype atomiser, whilst maintaining the higher degree of swirl. Atomiser I-D was designed using the same dimensions as atomiser I-C, with added modifications included with the intention of reducing atomiser pressure drop. This included an internal “bullet” for the inner air swirler assembly, allowing for a gradual reduction of effective area within the inner air channel, thereby reducing static pressure losses as a result of expansion into the original cavity. The entrance to the inner air channel (D_{i2}) was also rounded in an effort to further reduce pressure losses, based on the principle that a higher C_d is observed in the case of rounded circular orifices compared to sharp circular orifices. The outer diameter of the fuel channel at the atomiser exit (D_3) was slightly rounded in the hope that this would encourage fuel to travel in the direction of the inner air flow towards the counterrotating outer air flow. However, it is noted that this design step slightly increased both the film thickness and prefilming diameter of the atomiser. Atomiser I-D is shown in **Figure 4-11**, and a summary of the phase I atomisers is given in **Table 4-1**.

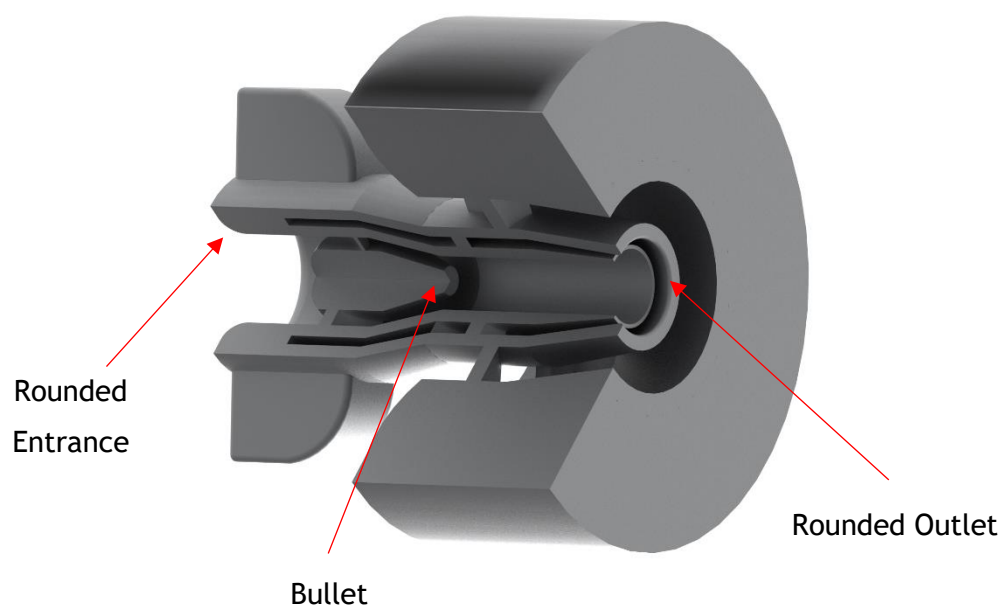


Figure 4-11 - CAD Render of Atomiser I-D

Table 4-1 - Phase I Atomiser Modifications

Atomiser	Prototype	I-A	I-B	I-C	I-D
Inlet					
D _{i1}	5.60	5.60	5.60	5.60	5.60
D _{i2}	8.30	8.30	8.30	8.30	8.30
D _{i3}	11.00	11.00	11.00	11.00	11.00
D _{i4}	15.60	15.60	15.60	17.00	17.00
Outlet					
D ₁ /mm	5.00	5.00	5.00	5.00	5.00
D ₂ /mm	5.50	5.50	5.50	5.50	5.50
D ₃ (D _p) /mm	6.98	6.24	6.24	6.24	6.36
D ₄ /mm	8.98	8.98	8.98	8.4	8.4
D ₅ /mm	13.20	13.20	13.20	14.00	14.00
Film Thickness (t) /mm	0.75	0.37	0.37	0.37	0.43
t _p	1.00	1.00	1.00	1.08	1.02
L _i	14	14	14	14	14
Inner Air Swirler					
Blade Angle /°	45	45	45	45	45
No. of Blades	5	5	5	5	5
Blade Thickness (t _b)	0.707	0.707	0.707	0.707	0.707
Inner Air Swirl Number	0.848	0.848	0.848	0.848	0.848
Outer Air Swirler					
Blade Angle /°	45	45	60	60	60
No. of Blades	5	5	5	5	5
Blade Thickness (t _b)	0.849	0.849	1.039	1.039	1.039
Outer Air Swirl Number	0.861	0.861	1.491	1.448	1.448
Calculated Effective Area (A _{eff}) / mm ²	74.27	74.27	52.17	66.45	66.45
Inner/Outer Air Area	3.621	3.621	2.246	3.135	3.135
Other					Extended Inner Swirler Hub

Atomisers were manufactured in a face down orientation, as shown in **Figure 4-12**. The atomisers were removed from the baseplate by hand using workshop tools. Internal supports required wire erosion techniques. It was decided that the amount of post processing required to remove the supports should be improved, especially since damage to the atomiser faces was later observed. A 1” BSPP screw thread was cut into the outer surface, required to mount the injector in the combustor. As can be seen, spare atomisers of the designs already described were printed in-case of misprints or damage during the finishing manufacture stages, but were not required and hence were not finished or tested during this study.

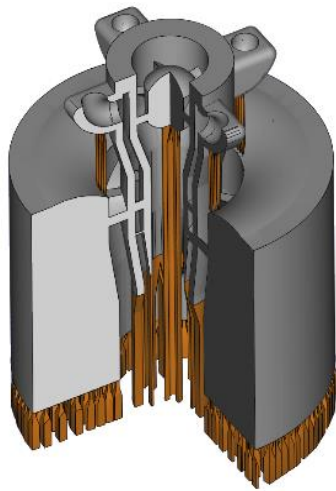


Figure 4-12 - Phase I atomiser manufacturing CAD file with supports (left) and printed atomisers (right)

4.3.2. Assessment of Flow Behaviour

Using the method outlined in **Section 4.2.2**, predictions for pressure drop values and outer/inner air ratios were determined for the atomisers developed, with predicted values given in **Table 4-2**. It is noted that the ratios are outside of the range of 1-2 recommended by [127], which was further considered in the Phase II designs.

Table 4-2 - Predicted Airflow Partitioning

Atomiser	Inner Air Mass Flowrate (%)	Outer Air Mass Flowrate (%)	Outer/Inner Air Mass Ratio
I-A	19.1	80.9	4.2
I-B	27.3	72.7	2.7
I-C	21.1	78.9	3.7
I-D	22.3	77.7	3.5

Figure 4-13 shows predicted pressure drop trendlines compared to empirically measured values taken using the Malvern experimental setup (**Section 3.6.3**). Calculations were performed using a value of A_F equivalent to a circular area of diameter=200 mm. It was found that smaller values of A_F resulted in lower prediction of pressure drop values, but predicted pressures were seen to converge at higher values, and hence 200 mm was deemed sufficient. It is evident that the predicted pressure losses, from using the theory of Knight and Walker [183], are

significantly underpredicted compared to measured values, possibly in part to the physically small flow paths and unaccounted surface roughnesses. For atomisers I-B, I-C, and I-D, predicted pressure drop values are approximately 50% of those determined from experimentation. Slightly better agreement is found for atomiser I-A, which ranged between 80-90% of measured values. However, it is believed that the better agreement was a result of visible gaps through the outer air swirler assembly as a result of the lower blade angles of 45° , shown in **Figure 4-13**. These gaps were a carryover feature of the original atomiser, which were highlighted as undesirable features since a portion of the outer air would be allowed to pass through the swirler assembly unturned. The reduced blockage is expected to have reduced the measured pressure drop due to lower constriction of effective area, but would also reduce the effectiveness of swirl for the atomiser.

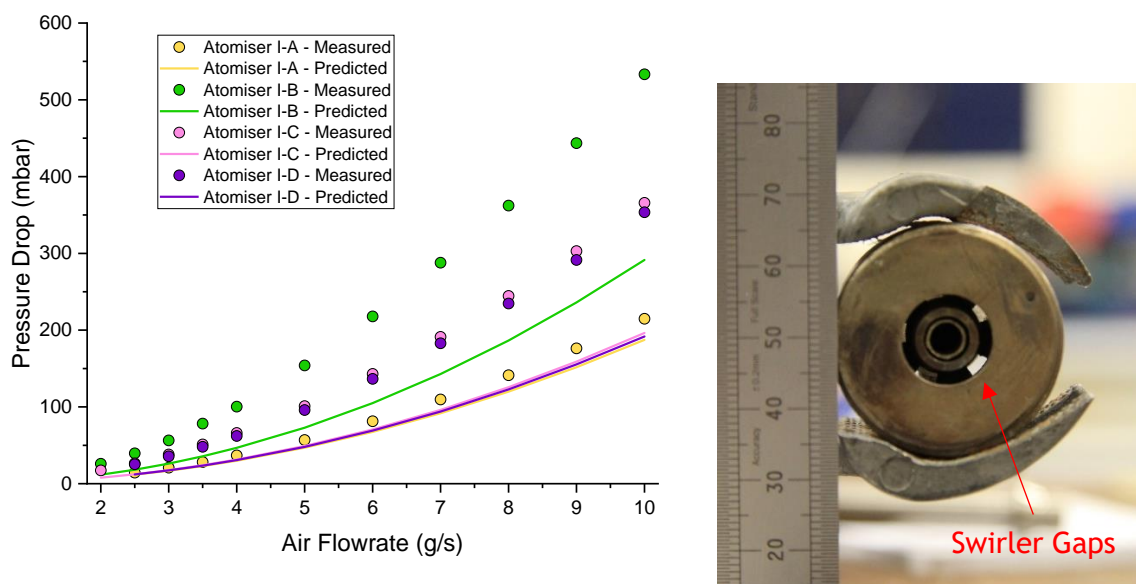


Figure 4-13 - Measured pressure loss values vs. predicted trends (left) and swirler gaps visible in the original atomiser (right)

The higher angle of inclination utilised for the other atomiser designs rectified this issue and eliminated these gaps, but at the cost of the higher measured pressure drop. Coefficients of discharge values were determined using the turned area (A_a) through the two swirler assemblies and experimental values of mass flowrate, air density, and pressure drop, using **Equation 4.19**. C_d values for the atomisers across operating conditions are shown in **Figure 4-14**. Across all atomisers, measured values of C_d were non-constant and were found to tend slightly upwards at higher flow conditions.

$$C_d = \frac{\dot{m}}{A_a \sqrt{2\rho\Delta P}}$$

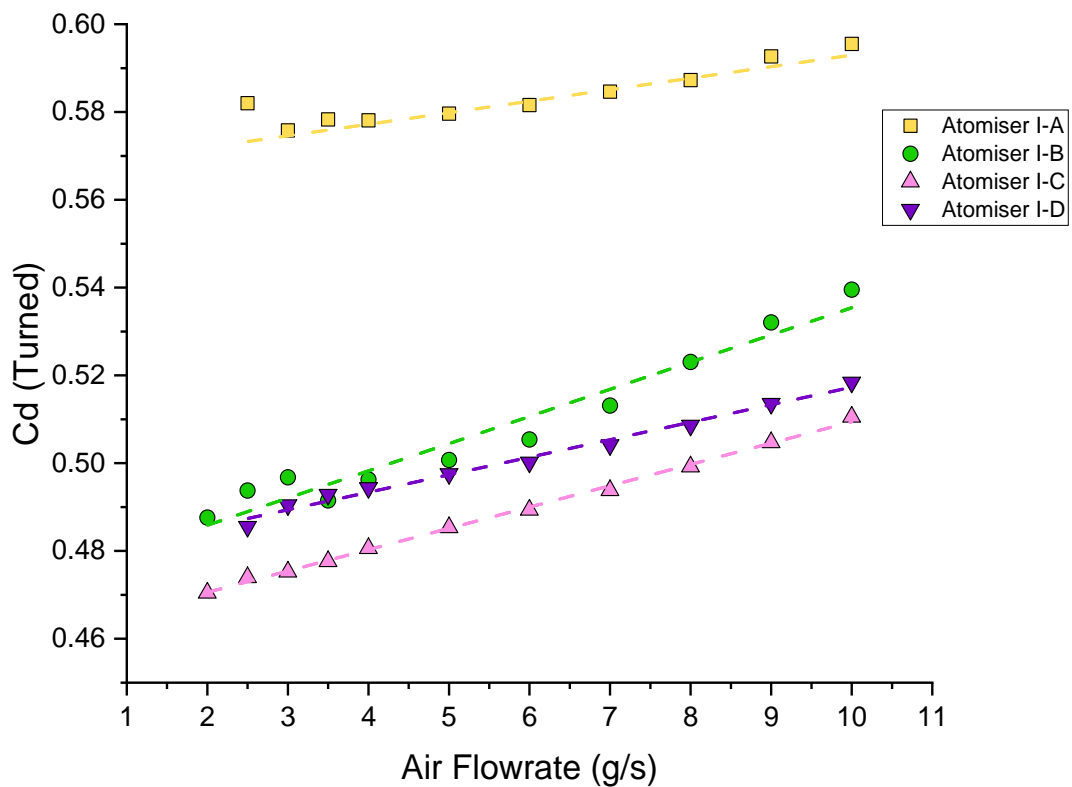


Figure 4-14 - Calculated C_d values across phase I atomisers

It is noted that the discrepancies between predicted and measured pressure drop values, as well as coefficients of discharge, are similar between atomisers I-B, I-C, and I-D. As such it may be expected that velocity and pressure drop characteristics might be adequately described by calculated values of A_a , indicating that the method may be somewhat relevant for atomisers in the same family (ie. sharing key design features with different effective areas). However, this would require a correction factor, and the method lacks fidelity overall. Therefore, pressure drop calculations were only used to guide later design of the atomisers in this project, rather than to accurately predict what the given pressure drop of any given atomiser design would be.

4.4. Phase II Designs

The second phase of designs was developed following combustion tests using atomiser I-D and the Mk. I combustor, described later in **Chapter 5**. To simplify the post-printing manufacturing required to remove the support structures from the atomiser outlets when manufactured in the face-down

orientation, and in response to defects observed with several atomisers during Phase I, Phase II atomisers were designed to be printed in a face up orientation.

The first atomiser design (II-A) was effectively a reprint of atomiser I-D using the above-mentioned manufacturing techniques. Atomiser II-B was then designed to incorporate the same effective areas as II-A but with a reduction in prefilmer thickness (t_p), hoped to reduce the number of large droplets in the near atomiser region as a result of accumulation. This was achieved by reducing the diameter of D_4 and D_5 , ensuring that only the prefilmer thickness and the angle of inclination of the outer air channel would be affected by the change. Overall, the steeper angle and reduced distance between the outer air and fuel channel exit orifices was hoped to improve interaction between the fuel and outer air.

Atomisers II-C and II-D were designed in an effort to better satisfy the design suggestions outlined by Simmons *et al.* [127] in the original Parker-Hannifin design. Atomiser II-C targeted the ratio between the inner air channel diameter (D_1) and the length of the channel (L_i). All atomiser designs up to this point had utilised a value of D_1 equal to 5 mm, and a value of L_i equal to 14 mm, yielding a length/diameter ratio 2.8, outside the recommended range of 1.5-2 given by Simmons [127]. To account for this, D_1 was increased to 6 mm, and L_i was reduced to 12 mm, yielding a ratio of 2. For atomiser II-D, it was decided that the air channel areas should be sized in an effort to achieve the recommended inner/outer air mass flow ratio of 1-2 given by [180]. Because the aforementioned pressure loss method was shown to underpredict witnessed losses for the previous atomiser designs, the ratio between inner/outer A_a values was instead used as a proxy for understanding relative mass flow. This resulted in a design employing a widening of the flow area through the inner air swirl assembly, yielding a ratio of outer/inner air A_a of 1.66.

For the final atomiser design (II-E), curved blades were utilised for both the inner and outer swirler assemblies. This design results in reduced blockage compared to straight blades, which can cause undesirable gaps to appear in the air channels. To prevent these, it was decided that curved bladed designs would house more blades of smaller blade thicknesses while maintaining the same effective flow areas through the swirler assemblies of a comparable straight bladed design. As such, seven blades were utilised in the outer air channel swirler

in the case of II-E compared to the five used in earlier designs, with the blade thickness reduced to maintain the same approximate value of A_a as atomiser II-D.

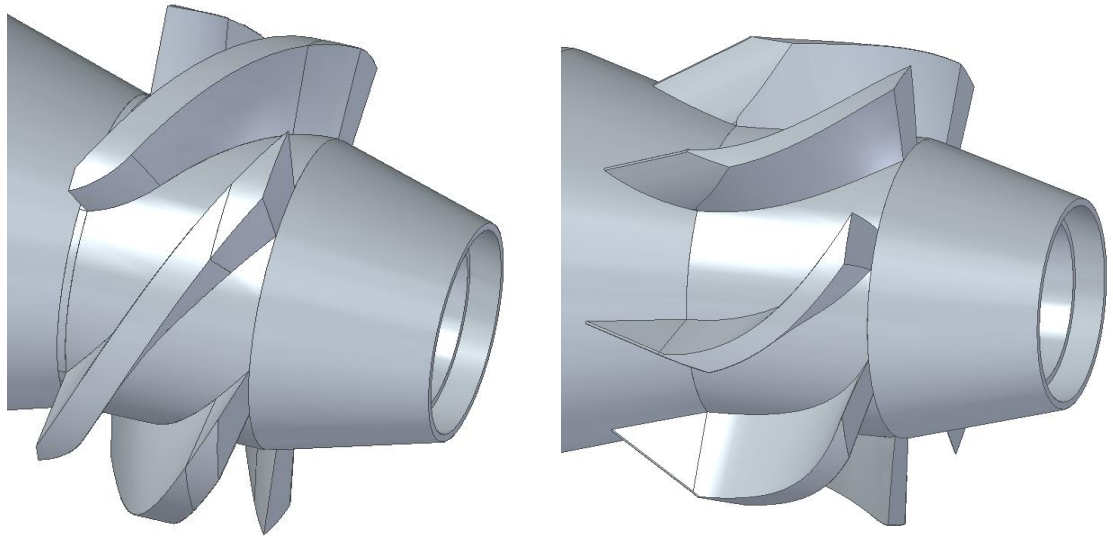


Figure 4-15 - CAD Images of straight blades (left) vs. curved blades (right)

A summary of the design changes is given **Table 4-3**

Table 4-3 - Phase II Atomiser Dimensions

Atomiser	II-A	II-B	II-C	II-D	II-E
Inlet					
D _{i1} / mm	5.6	5.6	6.2	4	4
D _{i2} / mm	8.3	8.3	9.5	9.5	9.5
D _{i3} / mm	11	11	11	11	11
D _{i4} / mm	17	17	17.4	17.4	17.4
Outlet					
D ₁ / mm	5.00	5.00	6.00	6.00	6.00
D ₂ / mm	5.50	5.50	6.50	6.50	6.50
D ₃ (D _p) / mm	6.24	6.24	7.24	7.24	7.24
D ₄ / mm	8.40	6.74	7.74	7.74	7.74
D ₅ / mm	14.00	13.07	14.00	11.42	11.42
Film Thickness (t) / mm	0.37	0.37	0.37	0.37	0.37
t _p / mm	1.08	0.25	0.25	0.25	0.25
L _i / mm	14	14	12	12	12
Inner Air Swirler					
Blade Angle / °	45	45	45	45	45
No. of Blades	5	5	5	5	5
Blade Thickness (t _b) / mm	0.71	0.71	0.71	0.71	1
Swirl Number	0.848	0.848	0.838	0.750	0.750
Outer Air Swirler					
Blade Angle / °	60	60	60	60	60
No. of Blades	5	5	5	5	7
Blade Thickness (t _b) / mm	1.2	1.2	1.2	1.2	0.84
Inner Air Swirl Number	1.448	1.448	1.437	1.437	1.437
Calculated Effective Area (A _a) / mm ²	64.04	64.04	75.12	83.69	80.05
Inner/Outer Air Area	2.985	2.985	2.275	1.656	1.912
Other Modifications				Inner air bullet	Inner air bullet, curved blades

Utilising the face up orientation reduced the number of supports necessary for supporting internal atomiser components, and allowed for thinner orifice faces to be designed at the atomiser exit since no support area was necessary. However,

the orientation resulted in the swirler blades requiring supports, and so small flat areas needed to be included onto the swirler blade faces to accommodate them. Additionally, the thicker cylindrical area used to hold the first phase atomisers into the piping during operation could no longer be manufactured, since this would require an unfeasibly large volume of supports. To remedy this problem, atomisers were printed with significantly reduced outer area, requiring a simple separate part to be conventionally manufactured and silver soldered to each Phase II atomisers, to enable fixing into the combustion liner. **Figure 4-16** shows the reversed atomiser orientation used for the manufacture of the Phase II atomiser designs.



Figure 4-16 - Phase II atomiser manufacturing technique (failed atomiser highlighted)

The manufacturing strategy was shown to be effective in producing the atomisers, and significantly reduced post processing time following manufacture. However, it can be seen that atomiser II-B (highlighted) failed during the first print, and was subsequently remanufactured at a later date. As with the previous designs, it was also found that some designs were affected by powder blockages in the narrow fuel channels, which required removal following manufacture. For atomiser II-A, the blockage could not be removed, preventing subsequent spray testing for this atomiser.

4.5. Assessment of Manufacturing Quality

As highlighted in **Section 3.2.1**, issues with manufacturing tolerances are known to impact the quality of AM generated parts. Dimensional analysis of the atomisers developed in this project was undertaken using two separate

measurement techniques: physical measurement of the atomisers using a set of electronic Vernier callipers with a precision of ± 0.005 mm, and measurement via image detection using a MATLAB image processing code. Measurements using the Vernier callipers were repeated three times with each atomiser rotated between measurements. Due to the small thickness of the fuel channel, measurements of D_2 could not be undertaken.

Image processing was undertaken using high quality digital photographs of the atomisers, an example of which is shown in **Figure 4-17**. Each image included a scale positioned along the orifice exit plane, which was used for the conversion of pixels into mm using the MATLAB *imtool* feature. Images were sharpened and binarized using the “Canny” edge detection algorithm, with a threshold set to between 0.1-0.2. The *bwareaopen* feature was utilised in an effort to reduce noise during edge detection, so as to remove features of a set pixel count. Settings were optimised for each image due to differences in lighting and general variation across the images. For each circular feature, measurements were made by placing a data cursor in MATLAB in five points. The first was at the approximate centre of the atomiser. Four additional points (top, bottom, left, and right) were taken along horizontal and vertical axis relative to the centre point (± 5 pixels) until the cursor encountered an edge, which would register as an intensity of 1 (white pixel) as opposed to 0 (black pixel).

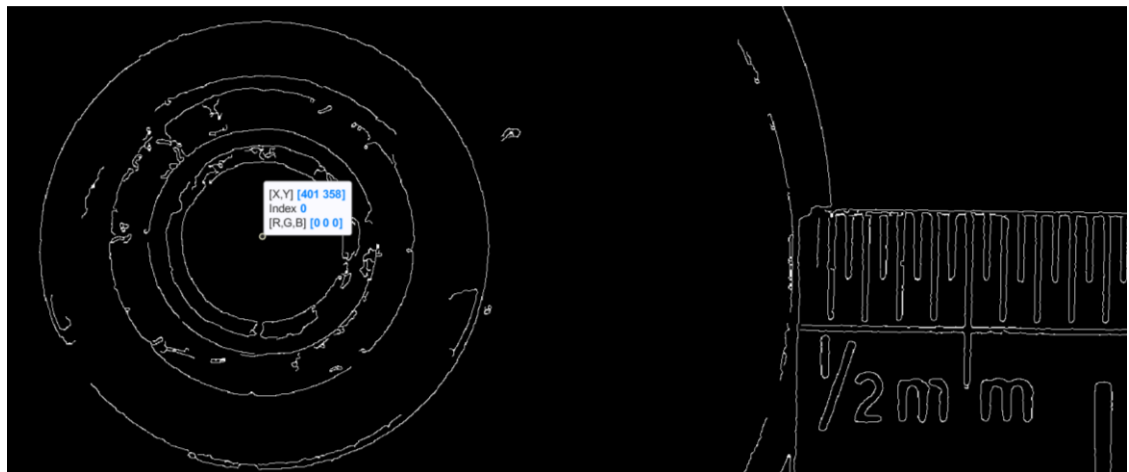
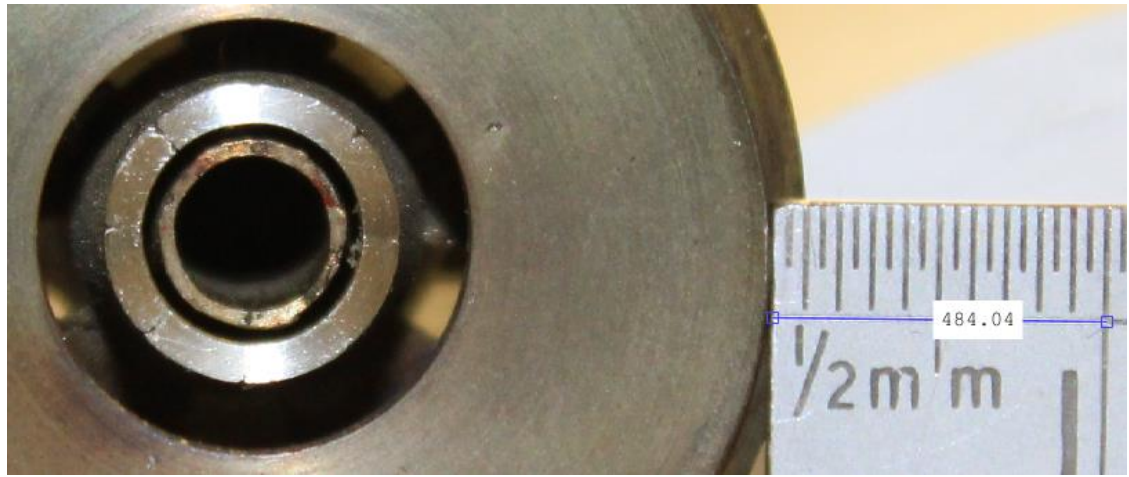


Figure 4-17 - Unprocessed image (top) and binarized image used for dimensional analysis (bottom)

While the edge detection algorithm was generally able to isolate the edges of the atomiser, it is noted that noise was still encountered during processing. This was mostly due to imperfections in the atomiser surface face, which were identified as edges by the program. Additional noise was encountered for some atomisers as a result of slight blurring due to the offset between exit planes across the three atomiser channels. The dimensions measured by the two measurement techniques for the Phase I and Phase II atomisers, respectively, are presented in *Table 4-4 and Table 4-5*

Table 4-4 - Phase I Atomiser Measurements

Diameter / mm ²	Prototype	I-A	I-B	I-C	I-D
CAD (mm)					
D ₁	5.00	5.00	5.00	5.00	5.00
D ₂	5.50	5.50	5.50	5.50	5.50
D ₃	6.98	6.24	6.24	6.24	6.36
D ₄	8.98	8.98	8.98	8.40	8.40
D ₅	13.20	13.20	13.20	14.00	14.00
Physical Measurements (mm ± deviation to CAD)					
D ₁	4.77 (-0.23)	4.68 (-0.32)	4.65 (-0.35)	4.65 (-0.35)	4.72 (-0.28)
D ₂	-	-	-	-	-
D ₃	6.63 (-0.35)	6.23 (-0.01)	6.20 (-0.04)	6.29 (+0.05)	6.21 (-0.15)
D ₄	8.93 (-0.05)	8.74 (-0.24)	8.88 (-0.10)	8.53 (+0.13)	8.66 (+0.26)
D ₅	12.91 (-0.29)	12.77 (-0.43)	13.00 (-0.20)	13.19 (-0.81)	13.89 (-0.11)
Image Processing (mm ± deviation to CAD)					
D ₁	4.69 (-0.31)	-	4.74 (-0.26)	4.74 (-0.26)	4.75 (-0.25)
D ₂	5.63 (+0.13)	-	5.51 (+0.01)	5.49 (-0.01)	5.68 (+0.18)
D ₃	6.62 (-0.36)	-	6.18 (-0.06)	6.36 (+0.12)	6.24 (-0.12)
D ₄	8.90 (-0.08)	-	8.94 (-0.04)	8.35 (-0.05)	8.61 (+0.21)
D ₅	13.06 (-0.14)	-	13.04 (-0.16)	13.23 (-0.77)	13.91 (-0.09)

Table 4-5 - Phase II Atomiser Measurements

Diameter / mm ²	II-A	II-B	II-C	II-D	II-E
CAD (mm)					
D ₁	5.00	5.00	6.00	6.00	6.00
D ₂	5.50	5.50	6.50	6.50	6.50
D ₃	6.24	6.24	7.24	7.24	7.24
D ₄	8.40	6.74	7.74	7.74	7.74
D ₅	14.00	13.07	14.00	11.42	11.42
Physical Measurements (mm ± deviation to CAD)					
D ₁	4.72 (-0.28)	4.62 (-0.38)	5.75 (-0.25)	5.74 (-0.26)	5.76 (-0.24)
D ₂	-	-	-	-	-
D ₃	6.05 (-0.19)	5.98 (-0.26)	7.06 (-0.18)	7.07 (-0.17)	7.04 (-0.20)
D ₄	8.57 (+0.17)	6.99 (+0.25)	8.00 (+0.26)	7.98 (+0.24)	7.98 (-0.24)
D ₅	13.77 (-0.23)	12.94 (-0.13)	13.71 (-0.29)	11.37 (-0.05)	11.19 (-0.23)
Image Processing (mm ± deviation to CAD)					
D ₁	4.73 (-0.27)	4.86 (-0.14)	5.98 (-0.02)	5.74 (-0.26)	5.76 (-0.24)
D ₂	5.17 (-0.33)	5.28 (-0.22)	6.37 (-0.13)	6.41 (-0.09)	6.37 (-0.13)
D ₃	6.05 (-0.19)	5.91 (-0.33)	6.98 (-0.26)	6.90 (-0.34)	6.97 (-0.27)
D ₄	8.59 (+0.19)	6.72 (-0.02)	7.60 (-0.14)	7.66 (-0.08)	7.54 (-0.20)
D ₅	13.59 (-0.41)	12.79 (-0.28)	13.54 (-0.46)	11.28 (-0.14)	11.01 (-0.41)

The results indicate that deviations between the CAD and manufactured parts of ± 0.2 mm were common across the atomisers. The largest deviation observed was for atomiser I-C, which showed an offset between both measurement techniques and the CAD file dimensions of -0.8 mm (-6%) for D₅. It is noted that this may be significant enough to impact flow behaviour between atomiser I-C and I-D, possibly explaining the slightly reduced pressure drop for I-D reported in **Section 4.3.2**. Although the two atomisers were designed with the same value of D₅, measurements indicate differences of ~ 0.7 mm. Agreement between the two measurement techniques was generally good (often within 0.1 mm), with a maximum difference of 0.4 mm observed.

4.6. Chapter Summary

Rapid prototyping using AM was successfully utilised to understand and optimise the design of prefilming airblast atomisers. Atomisers were designed using empirical methods, such as calculation of flow areas and estimation of pressure losses. It was found that a fundamental pressure loss prediction methodology (developed in the 1950's and based on large conventionally manufactured injectors) used during the atomiser design phase lacked fidelity and significantly underpredicted measured values, at least to the level of detail implemented. This is highlighted as the biggest obstacle in the accurate development of atomisers, since atomiser performance cannot be properly categorised until subsequent experimentation, and so the effectiveness of key design features required confirmation using empirical assessment. The methodology did however offer confidence in predicting general trends across atomisers sharing similar key features. It is therefore suggested that empirical methods would be most effective in refining atomisers of similar designs (e.g. changes to effective area), rather than for assessing the exact impact of significantly changing key design features.

AM has been shown to be a useful rapid prototyping tool for the progressive design of atomisers over a short timescale, notwithstanding manufacturing drawbacks associated with AM parts. An assessment of part tolerances using physical measurements and an image processing technique indicated deviations between CAD files and manufactured parts of as much as 0.8 mm (6%). Also, as anticipated, rough inner flow surfaces were observed across all of the atomisers, with part failures associated with the removal of metal powder from small flow paths common, independent to the orientation of printing during manufacture. However, it was seen that significant improvement in terms of post-print finishing was observed by redesigning the atomisers, so as the more complicated outlet geometries were printed face-up, removing the requirement for support structures on their surfaces and affording thinner/sharper edges which were less likely to be damaged during part removal from the baseplate. Details of the atomisation and combustion performance of the atomisers are provided in subsequent chapters.

5. Characterisation of nvPM Emissions from Alternative Fuels (Mk. I Combustor)

The Mk. I RQL combustor was used for an experimental campaign as part of the H2020 JETSCREEN (JET fuel SCREENing and optimisation platform for alternative fuels) program. The main aim of this program was to characterise the emissions behaviour of various aviation fuels, including certified SAF, in a representative aircraft combustor operating over a range of ambient conditions and AFRs, and generate a full emissions dataset. Concentrations of nvPM mass and number, and particle size distributions were measured using the European reference system and DMS-500 setup described in *Section 3.3*. Measured concentrations were to be corrected for system losses using the bin-by-bin correction method (*Section 3.4*), so as to be representative of emissions at the combustor exit plane. The fuels tested were 3 conventional Jet A-1 fuels, 3 SAFs, and 3 blends of conventional fuel and SAF. In accordance with ICAO annex 16 [24], gaseous measurements of CO₂, CO, UHC, and NO_x were also undertaken. Gaseous measurements were corrected for known interferences following the process outlined in *Section 3.5.2*. The full dataset was provided in an accompanying publication to this work, so as to facilitate future modelling studies exploring the impacts of fuel properties on nvPM emissions produced by SAF [1].

With regards to the research focus of this study, the key objectives of this experimental campaign were:

- To examine the emissions characteristics and performance of the RQL combustor operating with a newly developed atomiser and a range of conventional fuels, SAF, and blended fuels.
- To explore the typical variability in fuel properties (chemical and physical) across the tested fuels using detailed fuel analysis.
- To use measured fuel physical properties to provide an estimate of the expected variability in atomisation quality across the fuels.
- To assess the quality of the previously established hydrogen content trend with line loss corrected nvPM data.
- To examine the impacts of other fuel properties and operating conditions, to see if emissions trends can be linked to more than one fuel property.

5.1. Operating Conditions

During experimentation, four test pressures were utilised (1-2.4 bara) with fuel flowrates chosen for an initial power output of ~30 kW at unpressurised conditions, which was subsequently scaled with pressure. The chosen power conditions would facilitate the maximum thermal rating (250 kW) of the HPOC within the facilities current maximum pressure rating (16 bar). Primary air was supplied to the atomiser at mass flowrates chosen to maintain a dP/P of 3-5% across pressure conditions, which was deemed representative of aviation cannular combustion systems [16]. This theoretically maintained atomisation air velocities across increasing combustor operating pressures, whilst also maintaining similar primary and global AFRs. Secondary air was supplied to the combustor at mass flowrates chosen to reduce the combustor equivalence ratio 0.3-0.4, as is recommended for RQL combustors (*Section 1.3.2*).

The operating conditions were not fully representative of modern, in-production aircraft engines, and were instead chosen to allow sufficiently long measurement times for all of the desired test conditions with the available fuel reserves. *Table 5-1* displays the averages of the operating conditions taken across the study with uncertainties representing recorded variability of conditions over different fuels. Conditions A-E are assigned to specific operating conditions at which air and fuel flowrates were replicated, but scaled for the specific operating pressure, thereby representative of an increase in thrust setting for a real-world aircraft engine.

Table 5-1 - Fuel, air and atmospheric conditions of test matrix

Combustor Pressure (bara)	Condition	Fuel Mass Flowrate (g/s)	Primary Air Mass Flowrate (g/s)	Secondary Air Mass Flowrate (g/s)	Primary AFR (predicted from atomiser flowrates)	Global AFR	Global Equivalence ratio (ϕ)
1.03 ± 0.01	A	0.71 ± 0.00	2.10 ± 0.00	30.02 ± 0.04	3.0	45.5	0.322
1.03 ± 0.01	B	0.71 ± 0.00	2.42 ± 0.01	30.02 ± 0.05	3.4	45.9	0.318
1.03 ± 0.01	C	0.81 ± 0.00	2.09 ± 0.01	30.01 ± 0.05	2.6	39.8	0.367
1.03 ± 0.01	D	0.81 ± 0.00	2.42 ± 0.01	30.01 ± 0.05	3.0	40.2	0.363
1.44 ± 0.01	C	1.21 ± 0.00	3.12 ± 0.01	44.98 ± 0.08	2.6	39.9	0.367
1.41 ± 0.02	D	1.21 ± 0.00	3.62 ± 0.01	45.00 ± 0.08	3.0	40.3	0.362
1.92 ± 0.01	A	1.41 ± 0.00	4.18 ± 0.01	60.00 ± 0.14	3.0	45.6	0.321
1.89 ± 0.04	B	1.41 ± 0.00	4.81 ± 0.01	60.02 ± 0.12	3.4	46.1	0.318
1.93 ± 0.01	C	1.61 ± 0.00	4.19 ± 0.02	60.13 ± 0.11	2.6	40.0	0.366
1.86 ± 0.07	D	1.61 ± 0.00	4.81 ± 0.02	60.01 ± 0.13	3.0	40.4	0.363
1.93 ± 0.01	E	1.61 ± 0.00	4.19 ± 0.02	70.12 ± 0.17	2.6	46.2	0.318
2.41 ± 0.01	C	2.01 ± 0.00	5.25 ± 0.11	74.96 ± 0.28	2.6	40.0	0.367
2.37 ± 0.01	D	2.01 ± 0.00	6.02 ± 0.03	75.08 ± 0.21	3.0	40.4	0.363
2.41 ± 0.01	E	2.01 ± 0.00	5.23 ± 0.02	87.54 ± 0.24	2.6	46.2	0.318

5.2. Fuel Properties

A total of nine fuels were used during experimentation: three conventional Jet A-1 fuels, three SAF, and three blends of conventional fuel and SAF mixed on a volume basis. The three conventional fuels consisted of a reference Jet A-1 fuel (J-REF), a high aromatic Jet A-1 fuel (J-HA), and a low-aromatic Jet A-1 fuel which had undergone a de-sulphurisation process (J-LA). A high aromatic CHCJ fuel (A-HA) was included as one of the SAFs tested, with a total aromatic content consisting almost entirely of mono-aromatics. The other SAF were two ATJ fuels, one with a moderate aromatic content (A-MA), and the other composed almost exclusively of i-paraffins and with negligible aromatic content (A-LA). The blended fuels were mixtures of conventional fuels and SAF, blended at ratios conforming to ASTM D7566 [73]. Fuel blends were mixed using the fuels already mentioned, with the exception of a low aromatic HEFA fuel with a hydrogen content of 15.369 ± 0.007 % wt. The three blends were mixtures of 70% J-REF/30% A-LA (B-REF), 51% J-HA/49% HEFA (B-HE1), and 70% J-LA/30% HEFA (B-HE2). All three blends exhibited relatively similar total aromatic contents, which were somewhat lower than expected for conventional Jet A-1 fuels, but above the minimum 8% vol. limit for drop-in fuels specified in **Section 1.4**. It is noted that the fuel descriptors will be used in the remaining text and are illustrative of the composition of the fuel, with (J-) indicative of a conventional Jet-A1 Fuel, (A-) highlighting alternative fuels (SAF) and (B-) for blends of conventional and alternative fuels. The aromatic content within the fuel is subsequently detailed as either the reference level (REF), Low aromatic (LA), medium aromatic (MA) or high aromatic (HA). Finally, HEFA fuels are indicated by (HE).

5.2.1. Chemical Properties

Fuel chemical properties were determined via. NMR spectroscopy (ASTM D7171) and 2D GCxGC, as discussed in **Section 3.1**. ASTM D7171 was used to directly determine the hydrogen contents across fuels. 2D GCxGC data, provided by the French Institute for Petroleum (IFPEN) was used to determine the relative proportions (% wt.) of hydrocarbons, separated by chemical family and carbon number. This was undertaken for all fuels following emissions experimentation, except for fuel A-MA for which fuel reserves had been depleted. For this fuel, pre-

existing compositional data was used, which had been determined using mass spectrometry and GC-FID methods.

As a comparison to ASTM D7171 results, additional hydrogen content values were calculated from 2D GCxGC data using the weighted average method outlined in **Section 3.1.2**. Hydrogen content and total aromatic content values accumulated through ASTM D7171 and 2D GCxGC are shown in **Figure 5-1**. Repeatability values for the ASTM D7171 test method given by the testing facility are included as error bars.

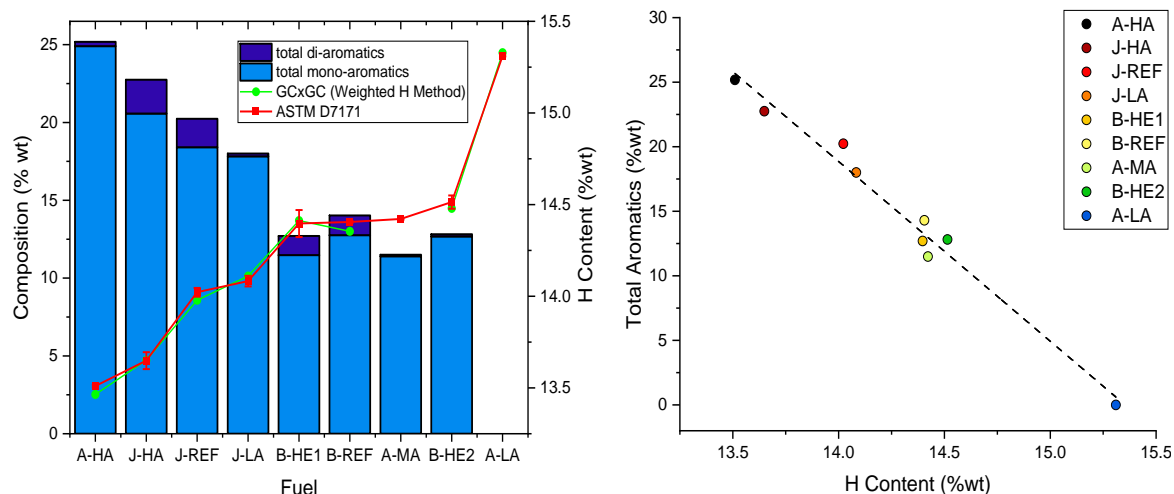


Figure 5-1 - Hydrogen contents and total aromatics contents of the fuels tested.

As can be seen, fuel A-HA exhibited the highest total aromatics content and lowest hydrogen content. Fuel J-HA exhibited the highest di-aromatic content of all fuels, but a lower total aromatic content and hydrogen content in comparison to A-HA. Total aromatic content exhibited good agreement with hydrogen content, although subtle variations were observed, potentially due to differences in hydrocarbon compounds making up each family. Good agreement was observed between hydrogen content values determined by ASTM D7171 and those calculated from GCxGC data, with a maximum discrepancy of 0.087% wt. However, since fuel A-MA was missing from the 2D GCxGC, only the results of the ASTM D7171 method will be presented herein for consistency, with fuel hydrogen content ranging from 13.51% (A-HA) to 15.31% (A-LA).

A full summary of the measured fuel components is shown in **Figure 5-2**. This demonstrates the added detail afforded by 2D GCxGC in determining component variability within the main hydrocarbon families already highlighted. For example, fuel B-HE1 and B-HE2 exhibit similar total aromatic contents (0.12%

wt. measured difference) and cyclo-paraffin contents, but B-HE2 shows a slightly higher hydrogen content. Within these classifications, B-HE1 exhibits higher quantities of di-cycloparaffins and cyclo-monoaromatics, as well as a relatively significant di-aromatic content and a lower proportion of n-paraffins. These molecules are less hydrogen rich than smaller, single ringed cycloparaffins and monoaromatics, and so appear to result in the lower hydrogen content. However, it should also be noted that the standard deviations of the two fuels overlap, and so discrepancies could also be attributed to fuel compositional measurement uncertainties. B-HE1 also exhibited a lower total aromatic content compared to B-REF, but a relatively higher proportion of cyclo-monoaromatics and a higher overall cycloparaffin content. As a result, the two fuels display near identical hydrogen contents, indicative of the significance of larger ringed compounds.

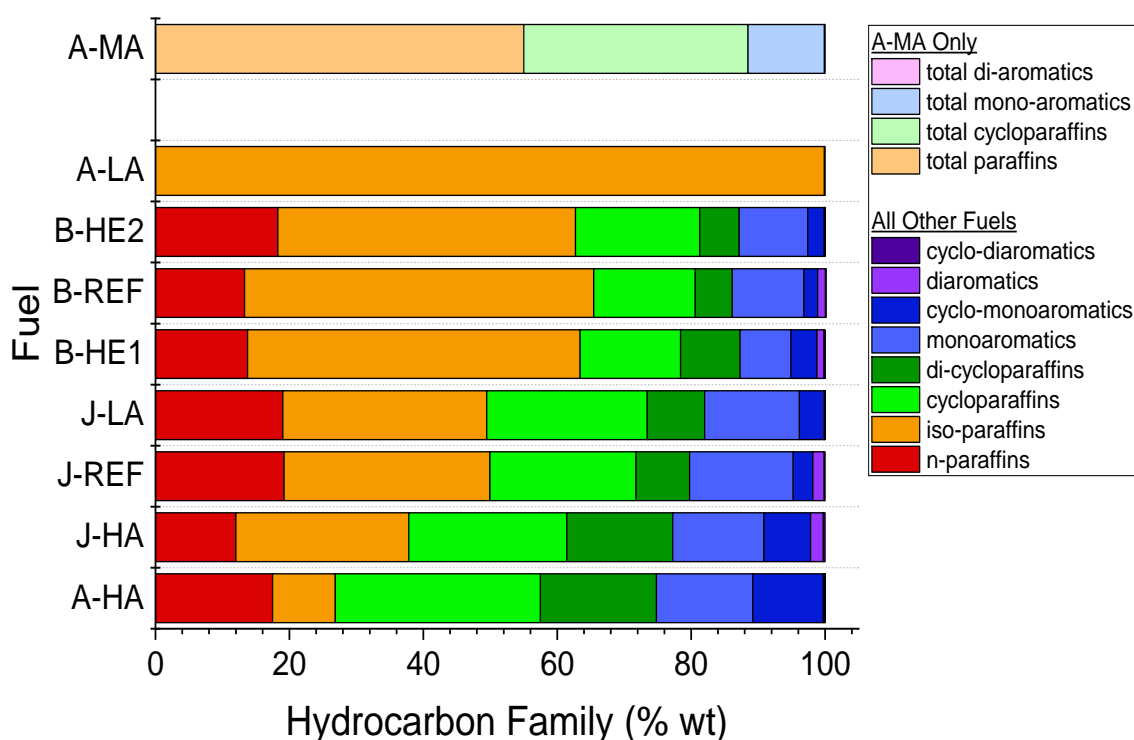


Figure 5-2 - Compositions of fuels by main hydrocarbon families (GCxGC)

So as to better understand the relationship between the established hydrogen content trend and fuel compositions, with the overall impact on nvPM emissions, measured hydrogen contents and GCxGC fuel compositional data have been examined more closely. It is expected that a higher proportion of hydrogen-saturated compounds (ie. paraffins) would show a direct correlation with hydrogen content, while less saturated compounds may show an inverse correlation. **Figure 5-3** shows the correlations between fuel hydrocarbon families and hydrogen

content. The data shows that, with respect to measured hydrogen content, there exists the expected direct correlation with paraffin content, and inverse correlations with cycloparaffin, mono-aromatic, and di-aromatic content. With the exception of di-aromatic content, good agreement is generally observed between compared variables. Some scatter is noted, especially for the case of cycloparaffins for fuels at ~14.4% wt. hydrogen content, with cycloparaffin content varying by ~10 %wt. between A-MA and B-REF, despite very similar hydrogen contents. Di-aromatic content shows very poor agreement with hydrogen content when all fuels are considered, but does appear to show two separate inverse linear correlations, each with a much better correlation with hydrogen content. It was considered whether this could have been a result of fuel analysis uncertainty, such as the quantities of diaromatic being near the limit of detection for the test method. However, given the limit of detection of GCxGC methods is typically very low (<0.01), and that measured di-aromatic contents are well above this for all fuels except A-LA, the measurements of diaromatic content are considered accurate.

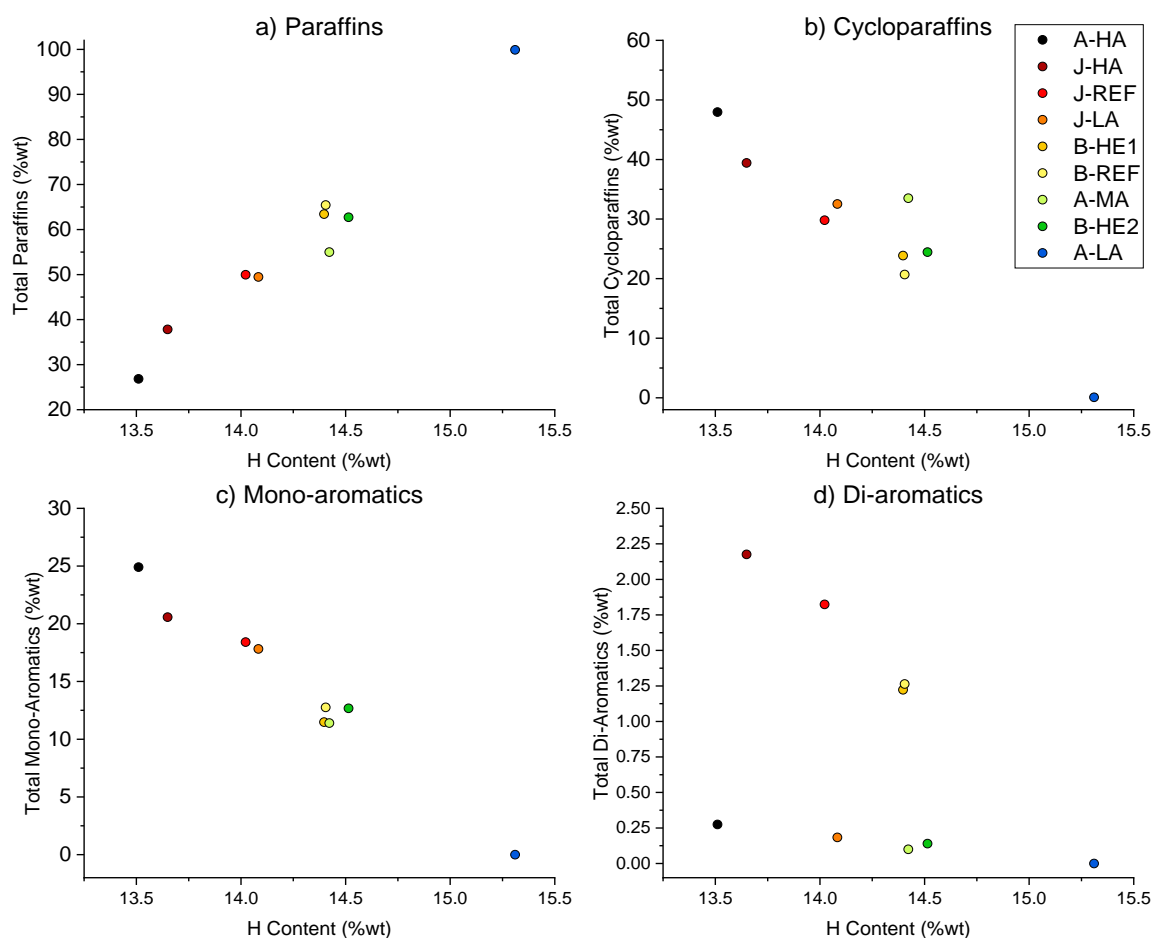


Figure 5-3 (a-d) - Fuel chemical content of paraffins (a), cycloparaffins (b), mono-aromatics (c) and di-aromatics (d) plotted against the fuel hydrogen content.

Molecular weights were determined using GCxGC data and the aforementioned weighted method (*Section 3.1.2*). As seen in *Figure 5-4*, the molecular weights across the tested fuels were typically in the range of 150-170 g/mol, indicating a general 12.5% variability. A notable exception to this was fuel A-LA, which exhibited a significantly higher value above 200 g/mol. While GCxGC data was missing for fuel A-MA, the higher MW for A-LA is attributed to a high content of heavy i-paraffins, as has been previously witnessed for ATJ fuels (see *Section 2.2.3*)

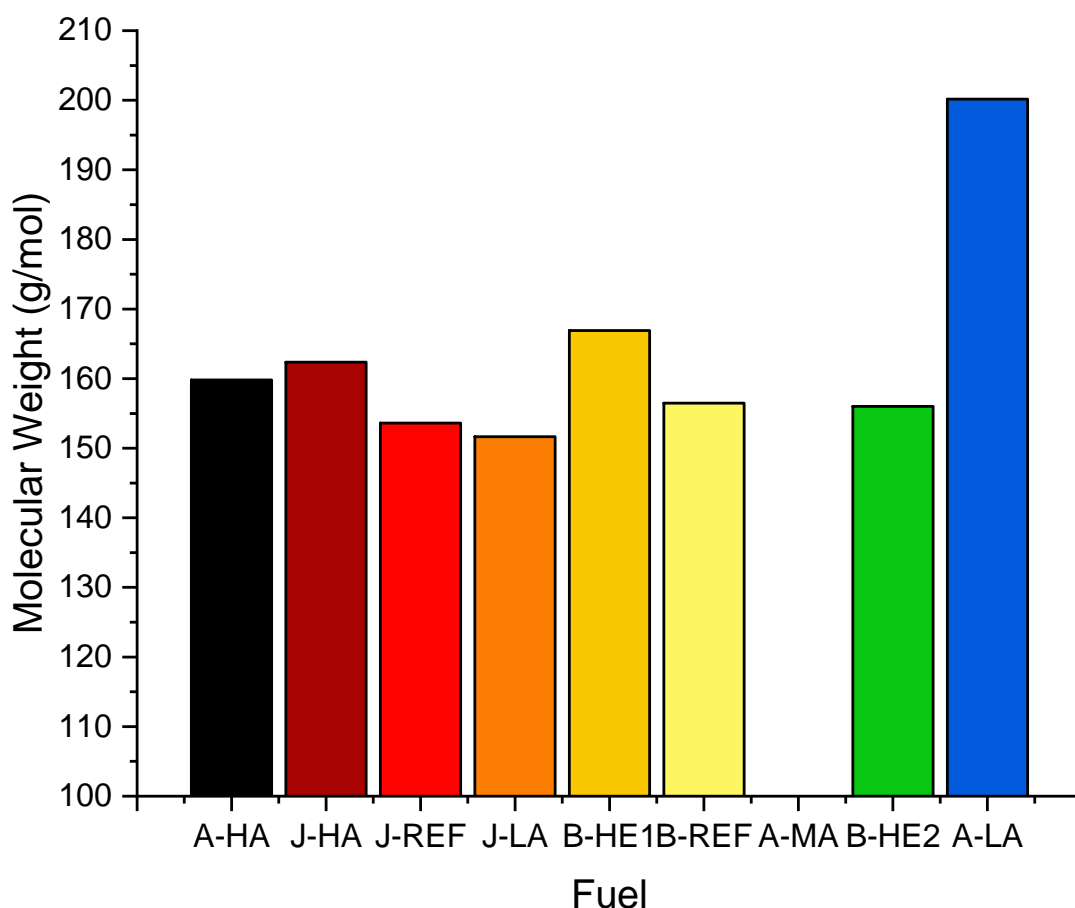


Figure 5-4 - Measured MW values of the test fuels using the weighted method and GCxGC data

5.2.2. Physical Properties

Fuel physical properties were measured using standard test methods within Cardiff University. Kinematic viscosities were determined using an Ostwald BS/U-tube type B viscometer. This technique measures viscosity by drawing each of the test fuels up to a marked point in the tube and measuring the time taken for the level to fall by the forces of gravity to a known point of lower height. A water bath was utilised to maintain fuel temperature at 25°C, as recommended by the manufacturer, and representative of the fuel preheat temperatures used during

emissions testing. Prior to measurement, the viscometer was calibrated at 40°C using a standard fluid, with an associated uncertainty of $\pm 0.22\%$. Fuel density was measured using a Bronkhorst mini-CORI-FLOW M14 Coriolis mass flow controller, operating at 15°C, (the laboratory temperature on the test day), and with a $\pm 0.2\%$ uncertainty. An exception to this was for fuel A-MA, whereby the density had been predetermined using the IP365 test protocol in Cardiff laboratories, and could not be remeasured due to lack of remaining fuel. Dynamic viscosities were determined via calculation from the measured kinematic viscosity and density values, using **Equation 5-1**. Surface tension values were recorded using a KRUSS K10T tensiometer fitted with a platinum Du Noüy ring. The instrumented sample area was thermostated to 298 K \pm 0.1 K using a thermofisher isotemp 500LCU circulator. The individual measurement precision was given as ± 0.05 mN/m.

$$\nu = \frac{\mu}{\rho} \quad 5-1$$

As seen in **Figure 5-5 (a-c)** and **Table 5-2**, the observed variations in physical properties across fuels were significant, especially in the case of viscosity variation, which exhibited a variation across all fuels of $\sim 46\%$, whilst surface tension and density values varied by $\sim 10\%$ and $\sim 8\%$, respectively. It is observed that density exhibits a strong correlation with hydrogen content, with lower hydrogen content fuels generally exhibiting higher values. It is also noted that surface tension values showed a general downward trend with increasing hydrogen content, with the noticeable exception of fuel A-LA, which displayed the highest hydrogen content of all fuels but second highest surface tension value. Finally, it was observed that viscosity showed no apparent trend with hydrogen content.

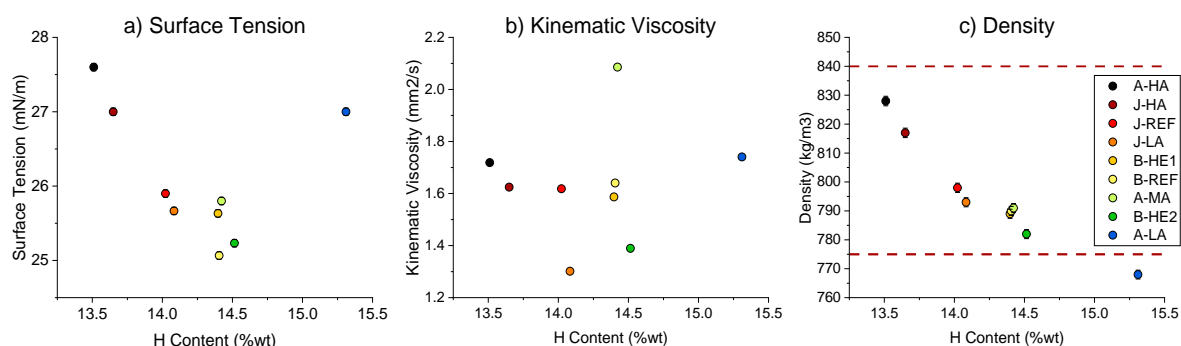


Figure 5-5 (a-c): Fuel physical properties of surface tension, kinematic viscosity and liquid density respectively plotted against hydrogen content. Dashed red lines indicate permissible ASTM specifications for commercial jet fuels where applicable

Table 5-2 - Fuel Physical Properties

Fuel	Hydrogen Content (% wt.)	Total Aromatic Content (% wt.)	Density at 15°C (kg/m ³)	Surface Tension at 25°C (mN/m)	Kinematic Viscosity at 25°C (mm ² /s)	Calculated Dynamic Viscosity (mPa.s)
A-HA	13.51	25.18	828 (+3.8%)	27.60 (+6.6%)	1.719 (+6.2%)	1.423 (+10.2%)
J-HA	13.649	22.75	817 (+2.4%)	27.00 (+4.2%)	1.625 (+0.4%)	1.327 (+2.8%)
J-REF (reference)	14.022	20.24	798	25.90	1.619	1.292
J-LA	14.083	18.01	793 (-0.6%)	25.67 (-0.9%)	1.302 (-19.6%)	1.032 (-20.1%)
B-HE1	14.397	12.70	789 (-1.1%)	25.63 (-1.0%)	1.587 (-1.9%)	1.252 (-3.0%)
B-REF	14.405	14.31	790 (-1.0%)	25.07 (-3.2%)	1.640 (+1.4%)	1.296 (+0.4%)
A-MA	14.422	11.50	791 (-0.9%)	25.80 (-0.1%)	2.086 (+28.9%)	1.650 (+27.7%)
B-HE2	14.514	12.82	782 (-2.0%)	25.23 (-2.6%)	1.390 (-14.1%)	1.087 (-15.9%)
A-LA	15.31	0.00	768 (-3.8%)	27.00 (+4.2%)	1.741 (+7.6%)	1.337 (+3.5%)

An initial estimate of the impact of atomisation quality was achieved using a published correlation proposed by Reeves and Lefebvre [124] (*Equation 2-9*). This was calculated as an arbitrary spray parameter, which was subsequently normalised to J-REF. *Figure 5-6* demonstrates the expected variation of SMD values in % terms as a result of fuel property variations. This trend suggests that variations in fuel physical properties would be expected to impact atomisation by a maximum of ~5% across all fuels, equivalent to only small changes in SMD of up to ~4 µm for the 40-80 µm recommended range. The SMD values produced by the developed atomisers is explored in later sections in this thesis (*Section 6.2 and Section 7.3*).

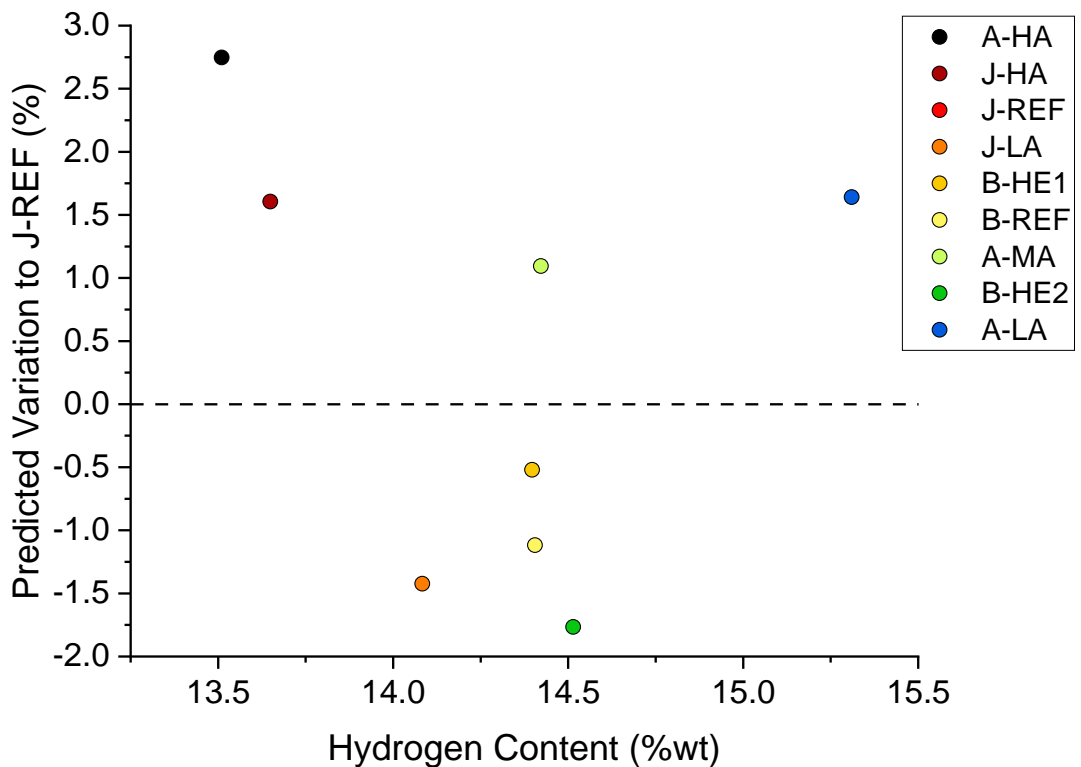


Figure 5-6 - Predicted variability in SMD (with respect to J-REF) for the tested fuels using simple correlation [124]

5.2.3. Energy Content

Gravimetric specific energies (MJ/kg) were determined following ASTM D3338 [164]. For this method, quoted repeatability and reproducibility limits for a 95% confidence interval are 0.021 MJ/kg and 0.046 MJ/kg. From this and knowledge of density values (*Section 5.2.2*), fuel volumetric energy content could be determined. Energy content values plotted against fuel hydrogen content is shown in *Figure 5-7*. Total variation in fuel specific energy was calculated as 3.01%, with fuels of low hydrogen content displaying the most favourable (highest) values. Volumetric energy content showed the opposite trend, with low hydrogen content fuels displaying the highest volumetric energy contents, varying across fuels by as much as 5.66%. These trends are in agreement with previously observed compositional trends [5].

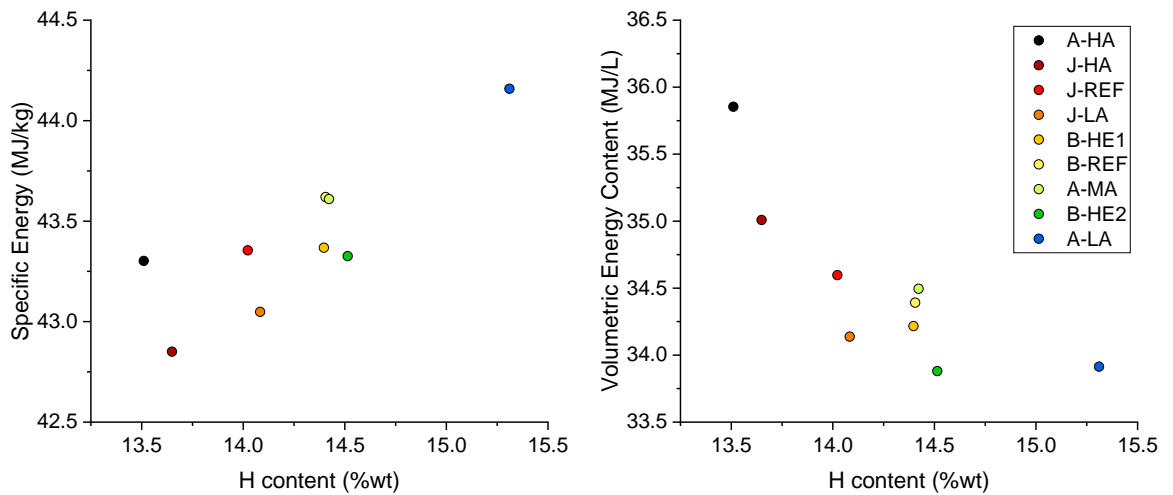


Figure 5-7 - Specific energy content (left) and volumetric energy content (right) as measured by ASTM D3338, plotted against hydrogen content

5.3. Results

5.3.1. nvPM Emissions

Analysis of nvPM emissions for each operating condition was undertaken over individual 30 second time periods, resulting in 30 samples per test point. The recorded data was used to calculate average values and standard deviations, the latter of which gave an indication of the stability of the data. Emission Indices (EI's) calculated from the data provided by the APC and MSS, prior to system loss corrections, and in accordance with ICAO regulations, were found to range between 1.77-364.17 mg/kg for EI_{mass} and 6.41×10^{13} - 1.98×10^{15} #/kg for EI_{number} . Measured nvPM PSDs displayed a generally log-normal, mono-modal distribution, with GMD values seen to range between 26-53 nm, and with associated GSD values of between 1.74-1.93. In agreement with previous literature **Section 2.3.2**, particle sizes were generally seen to decrease with increasing hydrogen content, with some scatter around the non-linear power trendline noted. **Figure 5-8** shows the as-measured nvPM PSDs and GMD values before and after system loss correction procedures for condition C at 1.9 bar, which will be taken as a general reference condition.

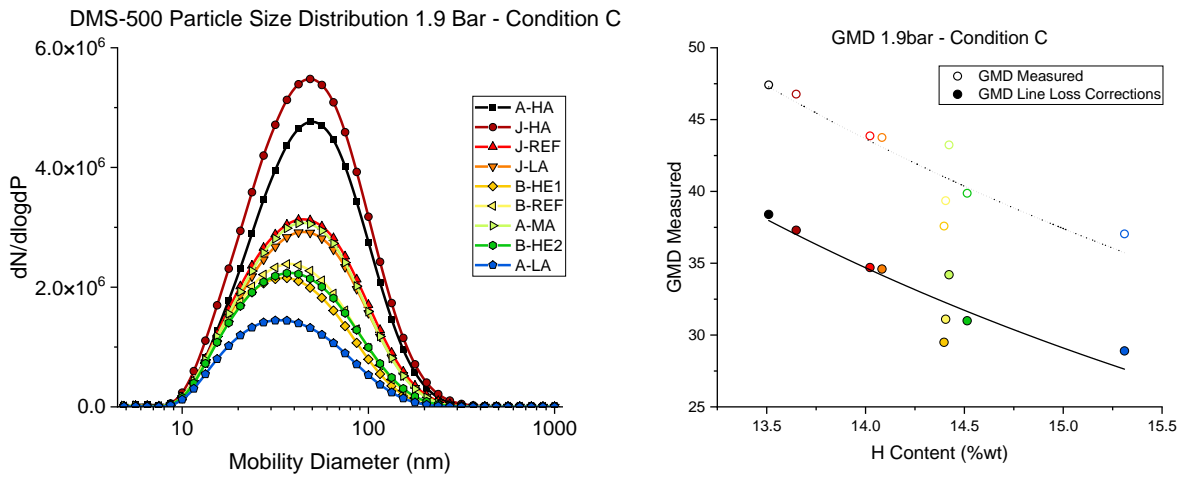


Figure 5-8 - Typical measured PSD across fuels (left) and measured vs. EEP GMD (right)

The representativeness of the EI concentrations and PSDs, mean the fuel trends observed here in this study are relevant to full-scale aviation gas turbine engines. However, given that the major particle loss mechanisms (diffusion), in the sampling system, are known to be size dependant (**Section 3.4**), and that higher hydrogen fuels are known to produce smaller particles (**Figure 5-8**), then direct comparison of EI's does not offer a true comparison of fuel impact on observed nvPM emissions at the combustor exit, which is what is required to understand the impact on local air quality and health. As such, all data from this point onwards will discuss loss corrected emissions.

Following system loss corrections, higher engine exit EI_{mass}, ranging from between 2.12-396.95 mg/kg and EI_{number} values ranging between 2.31x10¹⁴-4.35x10¹⁵ #/kg are predicted, as shown in **Figure 5-9**. As expected, due to the higher loss of smaller particles, engine exit predicted GMD values are smaller than those physically measured at the end of the sampling system, and ranged between 20-44 nm, with associated GSD values between 1.76-2.04. The error bars included represent ±2 standard deviations of the 30-second average, highlighting the measurement stability of the individual test cases rather than repeatability of the result. To aid with visualisation of hydrogen content emission trends, inverse power law trendlines have been included, intended to offer guidance in the prediction of fuel effect on real-world witnessed emissions.

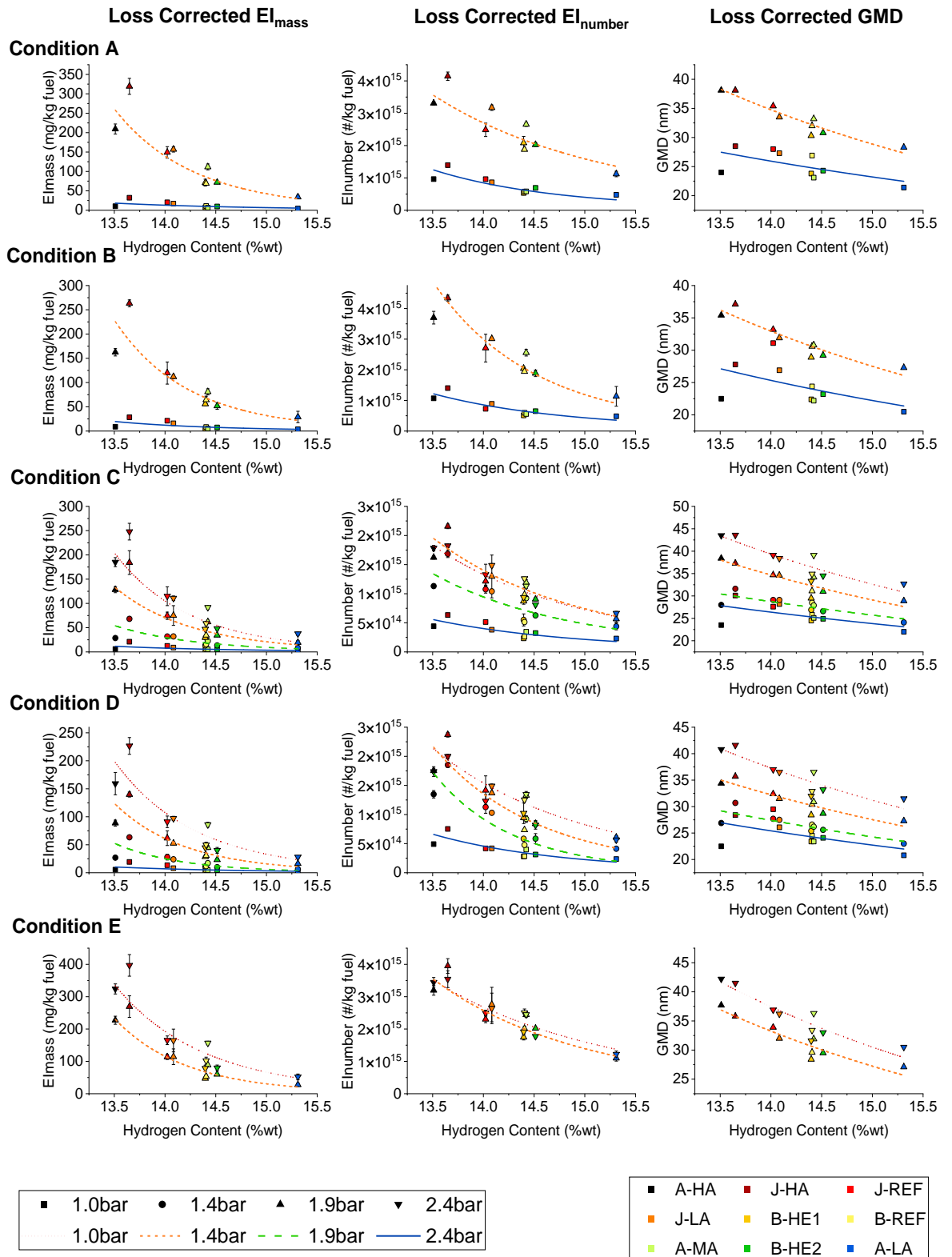


Figure 5-9 - Combustor-exit nvPM EI mass (a), number (b) and measured GMD (c) against fuel hydrogen content at different combustor pressures and rig operating conditions

In agreement with previous uncorrected full-scale engine studies [103], [188] and system loss corrected APU studies [106], across all fuels tested here, decreases in nvPM EI mass, EI number and GMD values are observed with increasing fuel hydrogen content, represented by the power trendlines. The greatest

reductions in nvPM were achieved by A-LA, which exhibited average reductions compared to J-REF for nvPM EI_{number} , EI_{mass} , and GMD of 73%, 54% and 17%, respectively. The highest emitting fuel in this study was J-HA, which increased values of the same variables by 61%, 131% and 10%, respectively compared to J-REF. Considerable scatter to the hydrogen content trendlines is observed across the dataset compared.

In contradiction to the hydrogen content correlation, J-HA exhibits increased nvPM emissions in comparison to A-HA, despite the lower hydrogen content (high aromatic content) of the latter. Fuels B-HE1, B-REF and A-MA, which exhibit similar Hydrogen contents to each other (14.397-14.422 %_{mass}), showed differences in nvPM values of up to ~64% for nvPM EI number, ~71% for nvPM EI mass and ~14% for measured GMD at the condition C, 1.9 bar case. This was especially apparent for A-MA, which generally produced higher emissions compared to the other two fuels. Because the method of determining hydrogen content was consistent across all fuels, these deviations indicate the additional influences affecting nvPM emissions discussed previously. Unfortunately, due to a lack in available fuel and rig-time, systematic errors brought on by day-to-day repeatability (e.g. fluctuations in rig operating conditions, soot built-ups within the combustor can liner walls, line shedding) could not be experimentally determined with only one repeat of each test case possible. However, variations in other fuel physiochemical properties alongside hydrogen content could be considered given that the characteristics were known. As such, physiochemical properties such as surface tension, liquid density, molecular weight etc. which are known to impact sooting tendencies, were considered to understand if these may offer insight into the variation observed around the hydrogen content trends.

5.3.2. Gaseous Emissions

Gaseous emission data were used to offer insight into combustor stability, AFR variability, and combustion efficiency. An example set of gaseous emissions taken at all pressures for condition C is shown in **Figure 5-10**. At this condition, gaseous CO₂ was found to range between 4.98-5.23% for condition C, with a calculated arithmetic mean of 5.11% ± 0.125% (ie. ± 2.44% of the average). Across all conditions, the calculated deviation from the mean fell within the calculated measurement uncertainty of ±3.9% (**Section 3.5.1**) Therefore, it is reasonable to

assume that variations across fuels have no measurable impact on CO₂ emissions, and that repeatability across pressures was high.

NO_x emissions were seen to steadily increase as pressure increased, as was to be expected with increased power conditions and associated flame temperatures. CO and UHC emissions were generally low, indicating high combustion efficiency, but qualitatively were higher at unpressurised conditions. Both emissions were significantly reduced at all pressurised conditions, especially for UHC which was observed to decrease by an order of magnitude. Fuel J-HA produced the highest quantities of CO and UHC emissions, and the lowest NO_x emissions. This is indicative of a lower flame temperature and less efficient, richer combustion than typically observed with the other fuels, also supported by generally lower combustor exhaust temperatures. It is suggested that this effect could have been a result of the poorer predicted atomisation quality for this fuel, which would reduce combustion efficiency and promote droplet burning as described in *Section 2.4.3*. However, the lower emissions observed with fuel A-HA, which had the worst predicted atomisation quality, suggests that the observed trends were not dependant on atomisation alone. It is instead suggested that the combination of atomisation properties and specific energy are responsible.

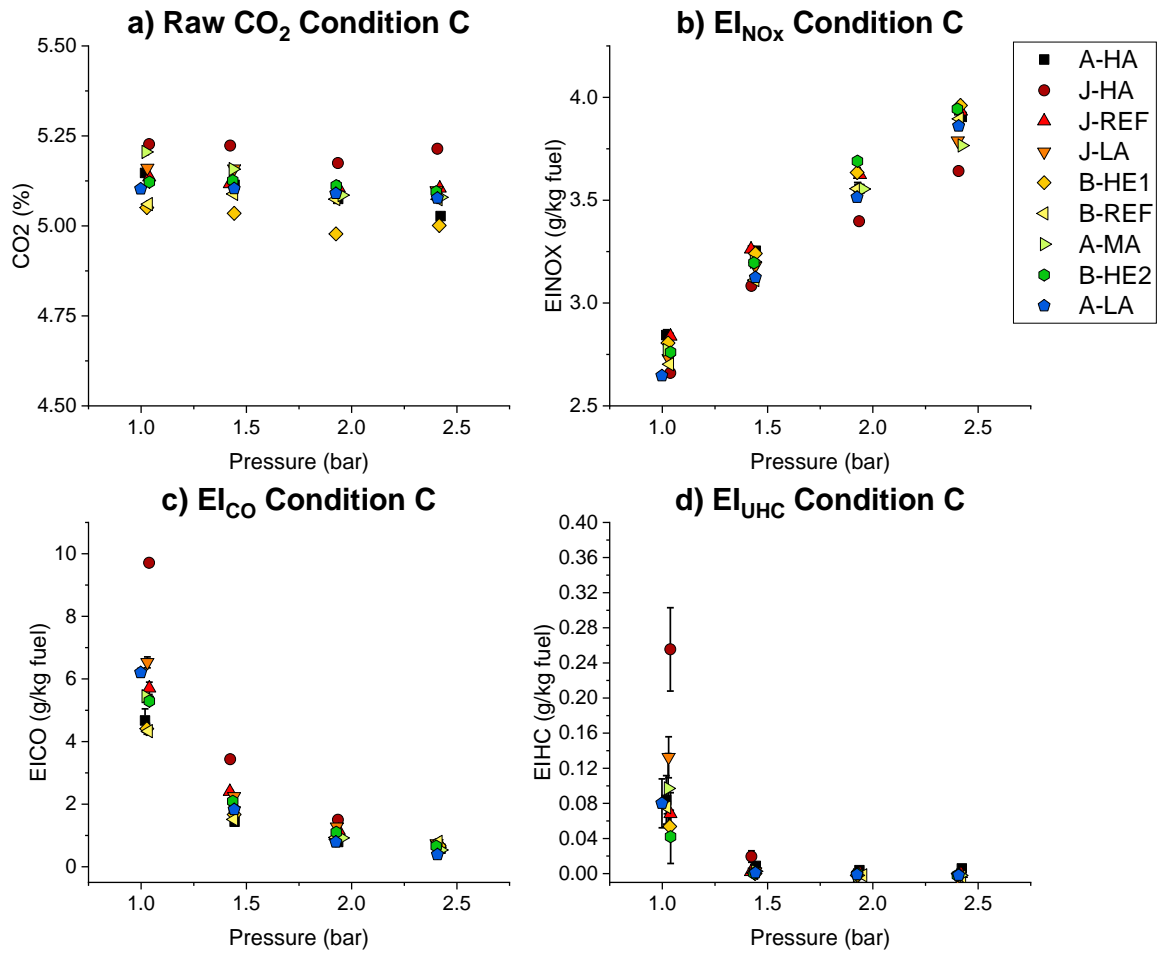


Figure 5-10 - Measured gaseous emissions at condition C at varying pressure for different fuels

Outputs of the SAE gas analysis tool are combustion efficiencies and calculated global AFRs. Combustion efficiencies were generally high across the study (>99.8% for all pressurised conditions). At unpressurised conditions, efficiencies were seen to be slightly lower, reaching a minimum value of 99.26%. Efficiencies were lowest for fuel J-HA, as expected from the higher rates of CO and UHC production also observed.

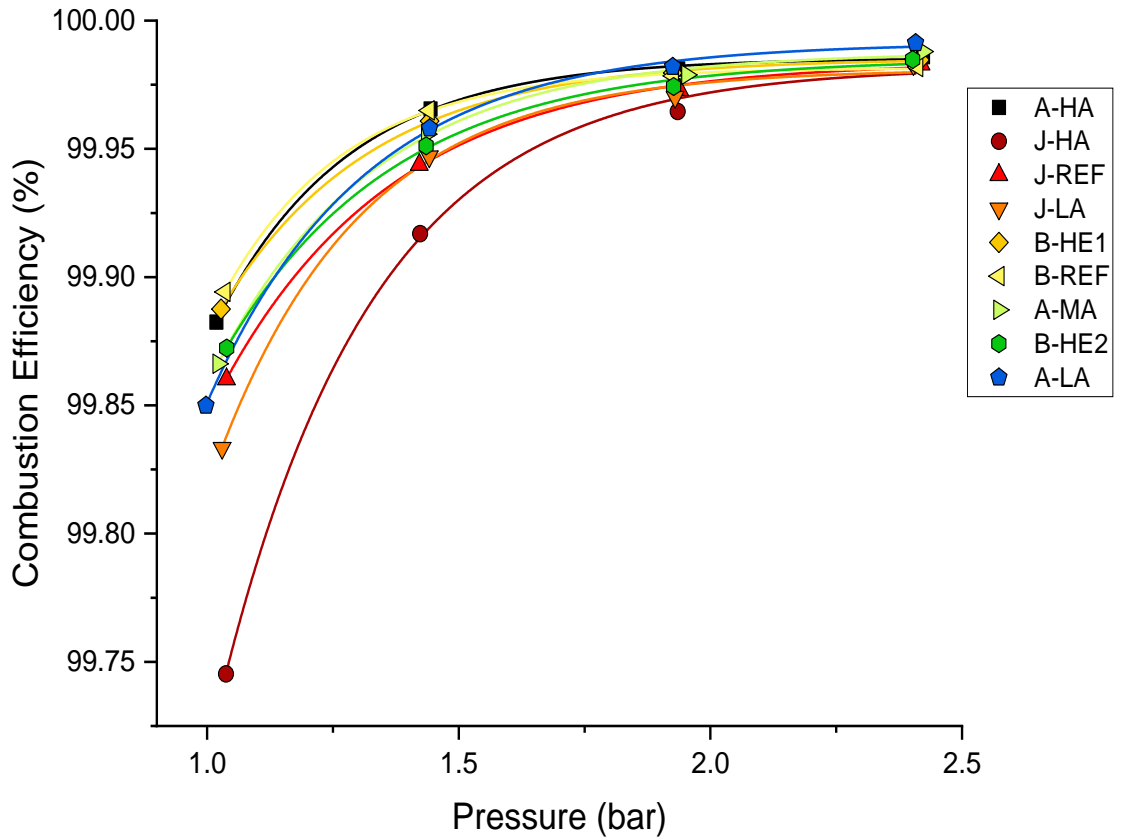


Figure 5-11 - Calculated combustor efficiency across range of pressures for tested fuels

Calculated operating AFRs meanwhile indicate that most fuels operated slightly below the target AFRs calculated from mass flow inputs. Notable exceptions to this are fuels A-HA and B-HE1, which are expected to have operated at or above the target AFRs at higher pressure conditions. Offsets are most likely a result of operator repeatability and hardware uncertainty in fuel and/or air flow controllers. For the case of A-HA, this may explain the large deviation of nvPM emissions from the hydrogen content trend, and the low nvPM emissions compared to fuel J-HA. For comparison, fuel J-HA generally exhibited the highest deviation from target AFRs towards richer combustion and greater nvPM emissions. This indicates that the worsened nvPM emissions associated with fuel J-HA are partly, (if not entirely) a result of a richer than anticipated flame. Fuel B-HE1 also consistently produced lower nvPM emissions compared to fuels of similar hydrogen content across the study, and so is likely affected by the same phenomenon.

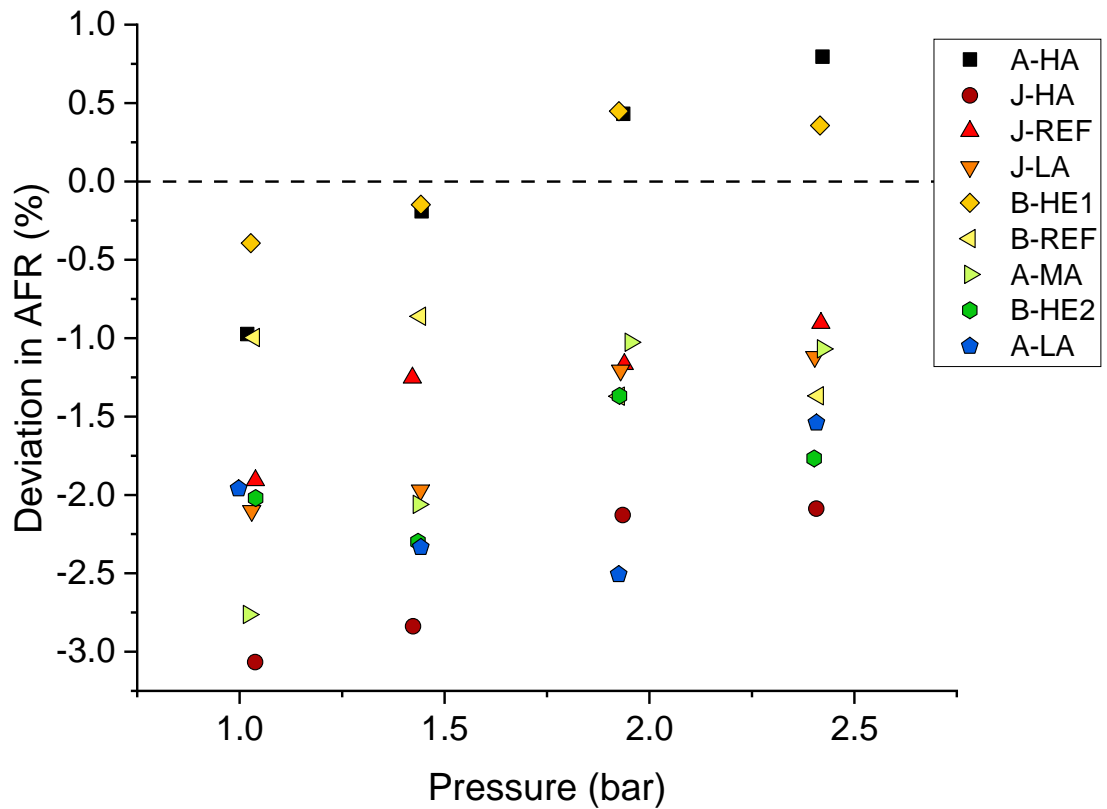


Figure 5-12 - Deviation between AFR calculated from mass flow controllers and calculated from gaseous data

5.3.3. Rig Operating Conditions

Static air pressure drop values across the fuel atomiser were recorded throughout experimentation, which were subsequently assessed to act as a monitor of atomisation stability. Measured pressure differentials during combustion tests were >40% higher than values measured during the atmospheric testing, highlighted in **Section 4.3.2**. It is hypothesised that the reasons for this discrepancy were both a function of the location of the upstream pressure tap, which in the HPOC was located further upstream and behind a bend, and additional losses across both the atomiser and combustion liner as a result of the higher gas temperatures, as discussed by Knight and Walker [183]. **Figure 5-13** shows the difference between measured pressure drop values. Across experimentation it was also observed that certain points were affected by lower-than-expected ambient pressures, which served to drastically increase measured pressure drop. It is thought that these erroneous points were as a result of either soot build-up, or water condensation blocking the in-can pressure tap point, which is supported by the fact that the pressures returned back to expected values following combustor can cleaning and pressure tapping back purge.

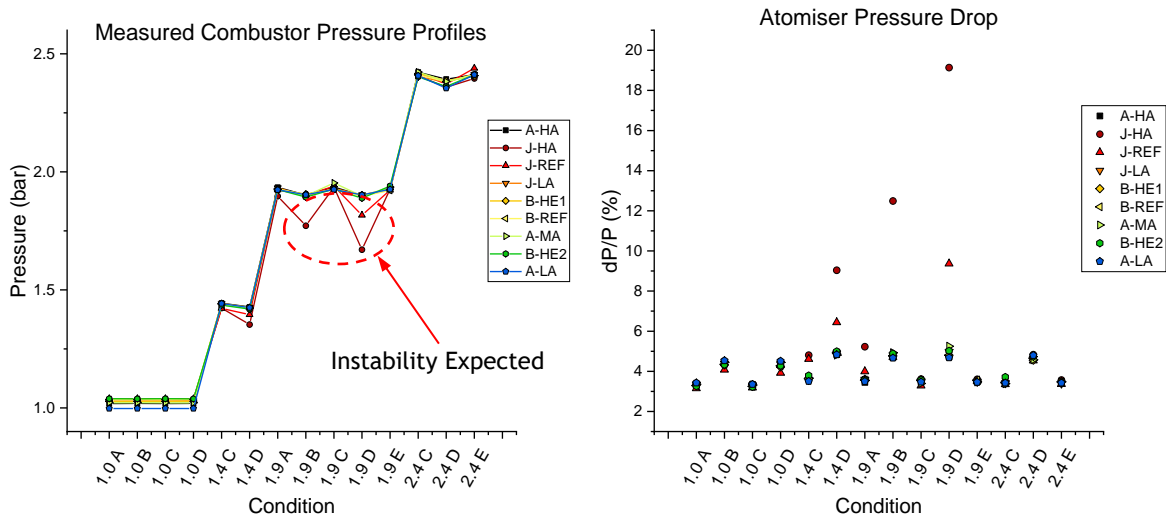


Figure 5-13 (a and b) - Measured combustor liner ambient pressures and atomiser pressure drop across different test cases and fuels.

Figure 5-14 shows the variability in measured exhaust temperatures across the dataset. As would be expected, conditions at higher fuel flowrates (C and D) experience higher combustor temperatures, with an increase in measured exhaust temperatures of circa 60 K observed across all fuels tested. Maintaining the same fuel flowrate with additional secondary air (condition E) serves to cool the flame temperature back to temperatures comparable to lower fuel flowrate conditions (A and B). It is noted that fuel A-HA consistently demonstrates a higher measured exhaust temperature (10-15 K) in comparison to J-HA. This could be a result of the higher specific energy for A-HA, helping to reduce nvPM emissions by raising combustion temperature and encouraging nvPM burnout. This would therefore be a systematic fuel property effect on nvPM. However, another possible cause is the variability in combustion AFRs demonstrated in Figure 5-12, which would instead indicate systematic day-to-day variability.

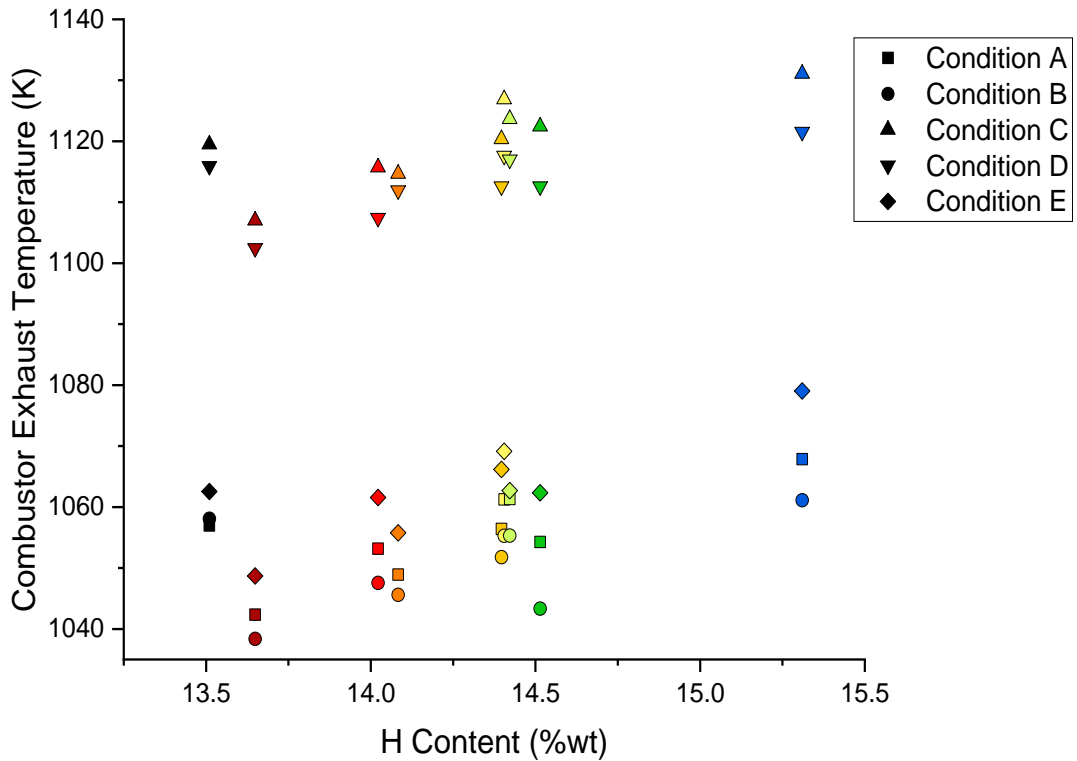


Figure 5-14 - Measured combustor exit temperatures for different test conditions

5.4. Empirical Analysis of Fuel Compositional Effects

5.4.1. Hydrogen Content Trends

As described in **Section 2.3.3**, derivation of normalised trends has been shown to allow for the prediction of emissions across separate experimental campaigns. As such, normalised trends were used in this study for the derivation of hydrogen content trends. Averages of absolute loss corrected nvPM EI concentrations were normalised to the J-REF case for data across the 1.9-2.4 bar pressure conditions, converting data to calculated percentage increases. Error bars presented herein represent the range of data across operating conditions within the chosen data (1.9-2.4 bar). The relatively high pressure cases were chosen, since it was observed that data at the lower pressures experienced higher instability and lower combustion efficiencies. Assessment of the trends was undertaken for the current dataset using unweighted least squares linear regression, so as to determine optimised coefficients and exponents in each case.

Quality of fit was assessed from Coefficient of Determination (COD) R^2 values (**Equation 5-2**), and adjusted R^2 values (**Equation 5-3**). These were determined from the built-in fitting program in Origin 2021 data analysis software.

Of the two, adj. R^2 values are considered more representative of the effectiveness of fit, since the method accounts for the improved fit attained by increasing the number of variables in a correlation. For this, \hat{y} is the predicted value of y from the fitted correlation and p is the number of variables in said correlation.

$$COD R^2 = 1 - \frac{\sum(y_i - \hat{y})^2}{\sum(y_i - \mu)^2} \quad 5-2$$

$$Adjusted R^2 = 1 - \frac{(1 - R^2)(n - 1)}{n - p - 1} \quad 5-3$$

Previous authors using similar experimental setups [105], [106] have used second order polynomial trends to determine hydrogen correlations, the general structure for which is given by **Equation 5-4**, where H_x is the hydrogen content of each fuel. An example of the polynomial fit plotted against normalised nvPM data is shown in **Figure 5-15**.

$$EI \%variation = A(H_x)^2 + B(H_x) + C \quad 5-4$$

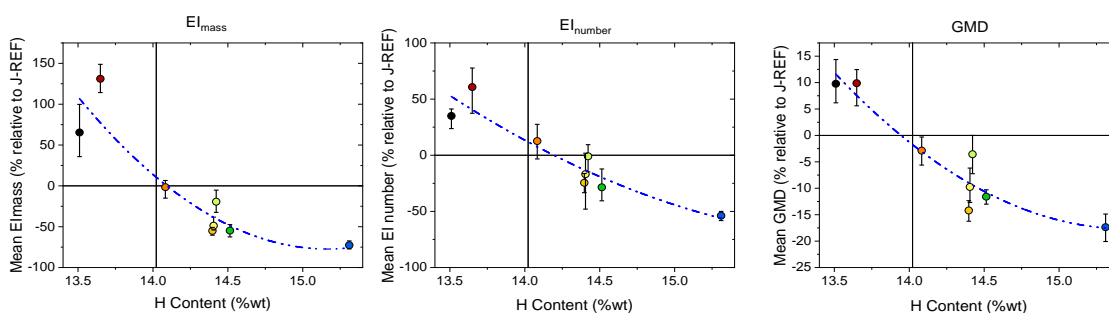


Figure 5-15 - Normalised correlations indicating the impact of fuel hydrogen content (polynomial trend) on nvPM emissions relative to a reference fuel.

Table 5-3 - Coefficients and Quality of Fit for Polynomial Law

	EI _{mass}	EI _{number}	GMD
A	0.671	0.145	0.077
B	-20.367	-4.793	-2.375
C	153.663	38.735	18.196
R^2 (COD)	0.843	0.882	0.905
Adj. R^2	0.780	0.834	0.867

An observation with the proposed polynomial trends is that trends are restricted to the narrow range of fuel hydrogen contents (13-15% wt.) associated

with Jet A-1 fuels. This is typically not an issue given that the hydrogen contents associated with jet fuels and drop-in fuels would be expected to lie in this range. However, it may be noted that, when applied to the dataset discussed here, the local minimum of the polynomial trend is observed to lie within the range of fuel hydrogen contents, tending upwards towards A-LA and higher hydrogen content fuels for EI_{mass} , which is not scientifically consistent. In an attempt to make the proposed correlations more scientifically robust, it was investigated whether more valid trends could be applied, towards both improving the correlation and extending the predicted range.

It is suggested that an inverse power law would provide a better correlation, as this would tend towards a horizontal axis as hydrogen content increased towards 100% wt. **Equation 5-5** is suggested as the inverse power law.

$$EI \%variation = \left[\frac{H_x}{H_{ref}} \right]^n + a \quad 5-5$$

Where H_x is the hydrogen content of each fuel, H_{ref} is the hydrogen content of the reference fuel against which emissions are normalised (in this case, J-REF with a hydrogen content of 14.022% wt.), and a is a fixed constant. The coefficients derived for the trends are given in **Table 5-4**

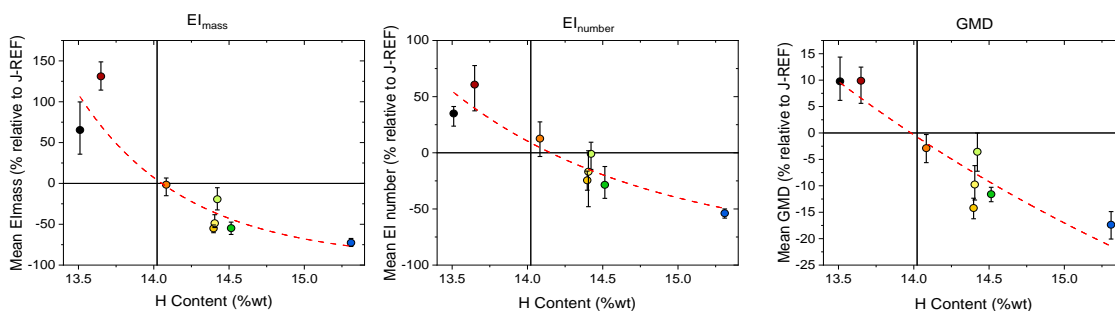


Figure 5-16 - Normalised correlations indicating the impact of fuel hydrogen content (inverse power) on nvPM emissions relative to a reference fuel.

Table 5-4 - Coefficients and Quality of Fit for Inverse Power Law

	El _{mass}	El _{number}	GMD
n	-18.912	-9.969	-2.632
a	0.958	0.912	1.008
R ² (COD)	0.820	0.868	0.865
Adj. R ²	0.789	0.846	0.842

An additional trend is suggested so as to constrain the data towards a 100% reduction in nvPM emissions at 100% hydrogen content (ie. predicting zero nvPM for zero-carbon fuels). This is given by **Equation 5-6**:

$$EI \%variation = k \left[\frac{100 - \%H_x}{100 - \%H_{ref}} \right]^n - 1 \tag{5-6}$$

Where k and n are constants to be derived from experimental results. For this correlation, the numerator will equal zero when hydrogen content is 100%, constraining the trend. The plotted correlation is shown in **Figure 5-17**, with the coefficients derived for the trends given in **Table 5-5**

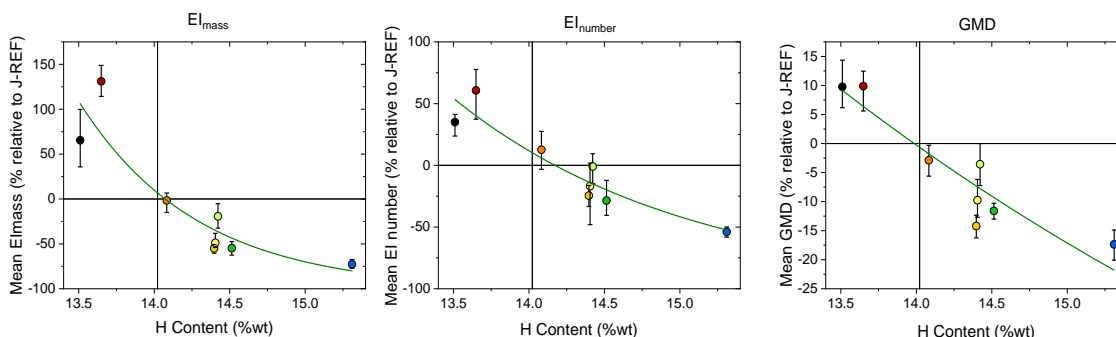


Figure 5-17 - Normalised correlations indicating the impact of fuel hydrogen content (constrained power) on nvPM emissions relative to a reference fuel.

Table 5-5 - Coefficients and Quality of Fit for Constrained Power Law

	El _{mass}	El _{number}	GMD
n	110.960	55.571	15.853
k	1.067	1.102	0.993
R ² (COD)	0.824	0.875	0.855
Adj. R ²	0.795	0.854	0.830

Both power trends are shown to offer good representation of the data, and offer a slightly improved data fit over the previously proposed polynomial trend for EI_{mass} and EI_{number} , as evidenced by a slightly higher R^2 value. However, GMD values appear to be better correlated by the polynomial trend. It is noted that the range of R^2 values across all correlations is lower than ideal, and is likely a result of the aforementioned rig and fuel physical-property scatter affecting the dataset.

5.4.2. Consideration of the Effects of Other Fuel Properties on nvPM Emissions

Total aromatic content was also shown to generally correlate well with nvPM emissions, although the same variability was observed for fuels of similar total aromatic content. **Figure 5-18** shows the impact of aromatic compounds on normalised line-loss corrected EI values as averages across the entire dataset with error bars showing the range of values. While a general trend similar to hydrogen content exists, similar scatter is encountered. It also appears that total aromatic content is a good indicator of nvPM emissions. The power trends were not used for fitting data in this case, since it was specialised for hydrogen content and the constraint in which nvPM emissions tend towards zero at 100% hydrogen content does not apply when considering aromatic content, as paraffins and cycloparaffins produce soot. Instead, the polynomial correlation with individually determined coefficients were used, yielding adjusted R^2 values of 0.707 and 0.768 for EI_{mass} and EI_{number} . This indicates that the polynomial trend gives a better fit with EI_{number} when total aromatic content is used over hydrogen content, although the correlation with EI_{mass} is worsened. Both of these correlations are however worsened compared to the power laws with hydrogen content, hence in support of hydrogen content the best metric for correlating nvPM emissions (**Section 2.3.3**).

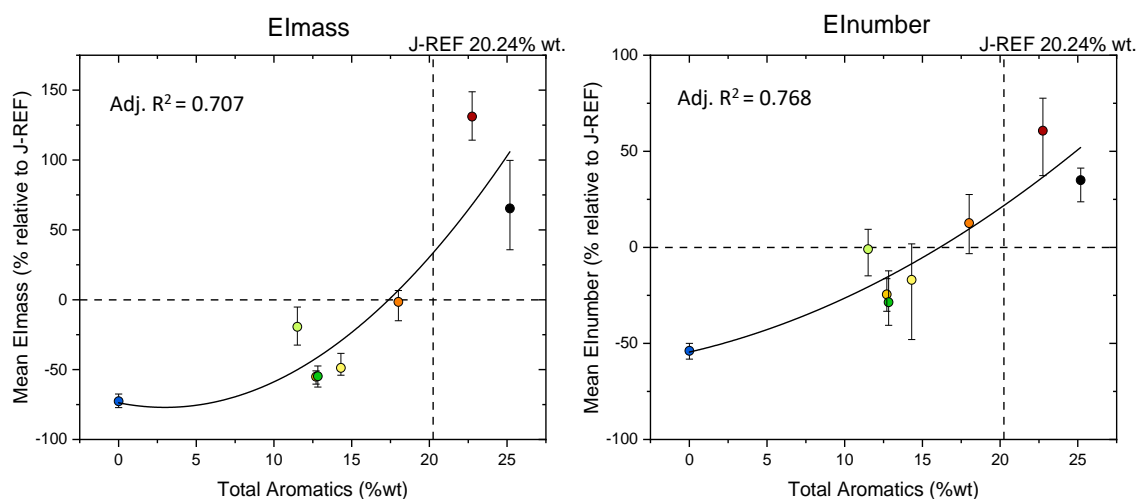


Figure 5-18 - Normalised correlations indicating the impact of fuel total aromatic content on nvPM emissions relative to a reference fuel

Paraffin content, cycloparaffin content and monoaromatic content all show correlations with nvPM emissions, as shown in **Figure 5-19**. In some cases, it was found that one of these variables better described the nvPM trends observed, such as for the case of A-MA, where total paraffin content appears to bring the nvPM data points closer towards a plotted trend line. This was an interesting observation, since this fuel exhibited a particularly high cycloparaffin content (~10% wt. increase) and lower paraffin content in comparison to fuels of similar hydrogen content, despite also exhibiting a lower total aromatic content, and so could indicate that the higher cycloparaffin content accounts for the observed higher nvPM emissions observed for this fuel compared to others of similar hydrogen content. However, these results must be treated with caution because of the different test methods utilised for fuel compositional analysis, which introduces uncertainty, as well as the fact that adjusted R^2 values were overall worsened when using these fuel variables instead of either hydrogen content or total aromatic content. Generally, it appears that paraffin content is able to produce a better fit with nvPM emissions than cycloparaffins or mono-aromatics, with the fit close to that of total aromatic content for El_{number} . Overall, the strength of correlation with nvPM emissions for each fuel property, from best to worst is:

*Hydrogen content > Total aromatics content > Total Paraffins >
Cycloparaffin + Monoaromatics contents*

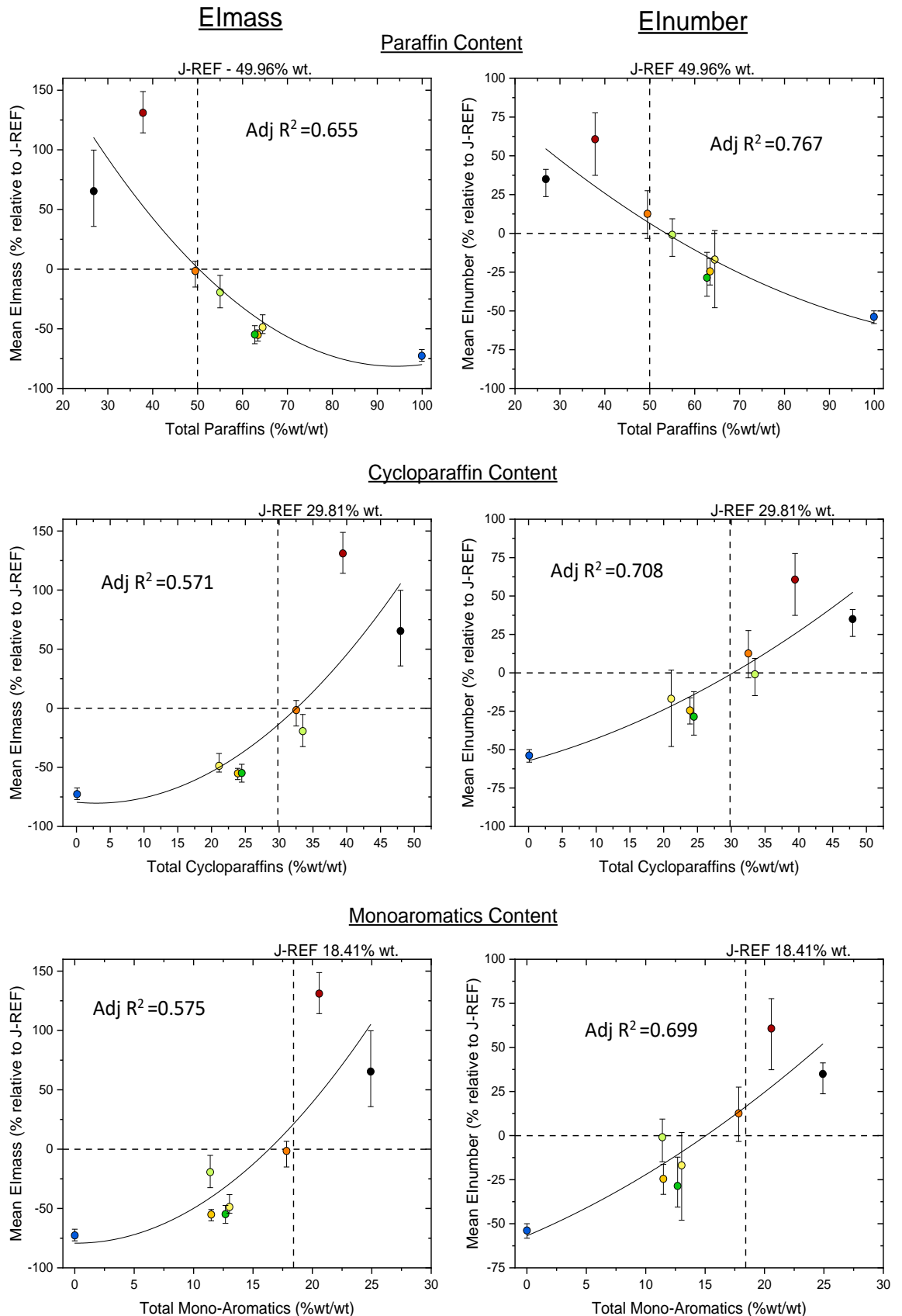


Figure 5-19 - Normalised correlations indicating the impact of paraffin, cyclo-paraffin, and mono-aromatic content respectively on nvPM emissions relative to a reference fuel

Consideration of the influences of fuel physical properties (atomisation performance) were examined for fuels of similar hydrogen content. The fuels in

question were A-MA, B-REF, and B-HE2. Particular focus was directed towards A-MA which exhibited a particularly high dynamic viscosity, and was predicted to produce the worst atomisation quality as a result (See **Figure 5-6**). Across testing this fuel was found to consistently generate higher nvPM emissions in comparison to the other two fuels. As such, it was hypothesised that reduced atomisation quality may have been responsible for the higher emissions observed for this fuel. However, it was found that no consistent trend could be established between individual fuel physical properties of surface tension and viscosity, or predicted variability in SMD, with nvPM emission deviations. The order of fuels was seen to correlate to fuel density most often, but again, scatter across the data points prevented this from being conclusively established. This demonstrates that, while atomisation quality may have an impact on nvPM emissions, the day-to-day variability in rig conditions and AFR had an equal or greater impact on nvPM emissions. Whilst the influence of atomisation effects is not apparent, over the rig uncertainty in this study, this is not to say that they have no effect on nvPM formation since numerous variables are not fully independent of one and other or against nvPM formation.

Another fuel property that could have impacted nvPM results was fuel molecular weight. As mentioned in **Section 2.2.3**, ATJ have been shown to exhibit higher molecular weights (175-180 g/mol) attributed to their relatively higher fractions of heavy iso-paraffin content [75], [81]. Fuel A-LA, and ATJ fuel, exhibited an especially high molecular weight, but was also the only fuel tested with almost no aromatic compounds, and so nvPM emissions for this fuel could not be compared since none of the other fuels were similar enough in hydrogen content for comparisons. Previous studies have indicated that ATJ fuels often exhibit high molecular weights, which can lead to higher nvPM formation in comparison to other low aromatic SAF (ie. F-T and HEFA). This has been experimentally shown in previous counterflow experiments [75]. Being another ATJ fuel, it is suggested that A-MA may also have exhibited a higher molecular weight, accounting for the higher nvPM emissions in comparison to B-REF, and B-HE2. Unfortunately, the molecular weight of A-MA could not be directly established from the current data. It is noted however that Zhang *et al.* [10] comments that a higher viscosity is often an indication of higher fuel molecular weight since fuel physical properties and molecular weight are strongly linked, which may support this hypothesis.

As previously mentioned, di-aromatic content has been highlighted previously as an important secondary factor in nvPM formation. As an examination as to whether variable di-aromatic content across fuels may account for some of the scatter observed, nvPM data was plotted against the compound parameter developed by Rosfjord *et al.* [110], given in **Equation 2-3**. The inverse of this correlation plotted against nvPM emissions is shown in **Figure 5-20**. The constrained power law was subsequently fitted, normalised to the value of the compound parameter calculated using the composition data of J-REF. It was found that using normalised hydrogen content values yielded R^2 values of 0.786 for E_{mass} , and 0.845 for E_{number} . As such, it appears that the correlation does not offer any improvement over using hydrogen content alone for the current dataset, implying that the day-to-day variability across testing outweighed any chemical impacts of di-aromatics.

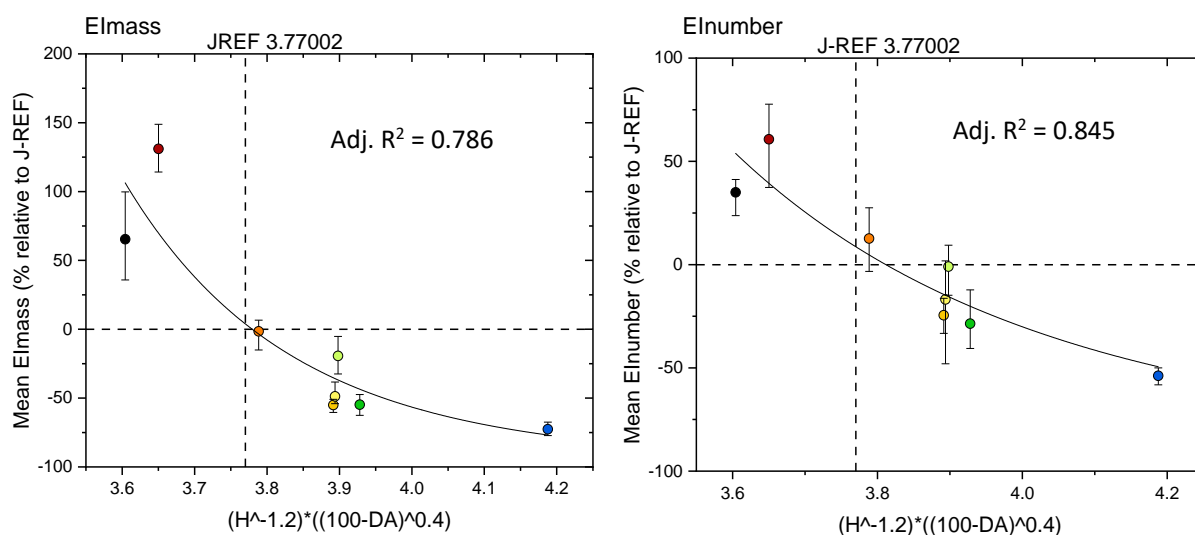


Figure 5-20 - Normalised correlation using a compound parameter of fuel hydrogen and di-aromatic content [108] on nvPM emissions relative to a reference fuel

5.5. Assessment of Correction Procedures

5.5.1. System Loss Corrections

Figure 5-21 demonstrates the values of k_{thermo} , $k_{\text{sl-mass}}$, and $k_{\text{sl-number}}$ for 1.9 bar condition C, calculated using the bin-by-bin correction method highlighted in **Section 3.4.2**.

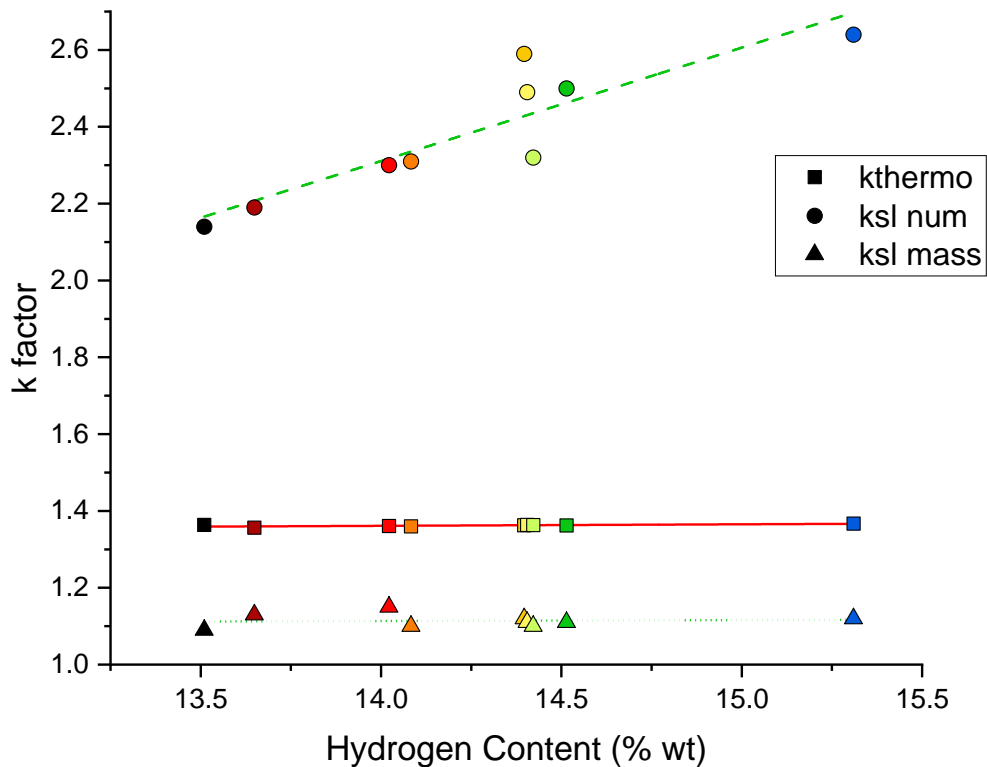


Figure 5-21 - k_{thermo} and k_{sl} factors across fuels determined for 1.9 bar, condition C

As expected El_{number} was most significantly affected by line loss correction, as to be expected given high loss of the smallest particles, which do not linearly impact the mass measurements which are dominated by the largest particles. Values of $k_{sl-number}$ are seen to typically be >2 , and increase with hydrogen content owing to the relatively smaller GMDs experienced. Values of k_{thermo} and $k_{sl-mass}$ were relatively consistent across fuels, conditions, and pressures, which would be expected owing to the modest changes in exhaust temperature and loss of the biggest particles. It is noted that $k_{sl-number}$ values were higher (often >4) at lower pressures, and for fuels of higher hydrogen content, where smaller GMD values were recorded. As a result, system loss corrected values of El_{number} were often an order of magnitude higher than uncorrected values. This increase in $k_{sl-number}$ towards fuels of higher hydrogen content, which are also found to exhibit smaller GMD values, demonstrates the size dependant nature of loss corrections, as discussed earlier (**Section 3.4.2**).

Because of higher losses for smaller particles, as are witnessed in the emissions data here, it was expected that the perceived improvements in El_{number} concentrations witnessed for the higher hydrogen content fuels prior to loss corrections would be over-predicted. **Figure 5-22** shows the predicted

overreporting of E_{number} emissions across fuels, between uncorrected and corrected nvPM data at 1.9 bar condition C.

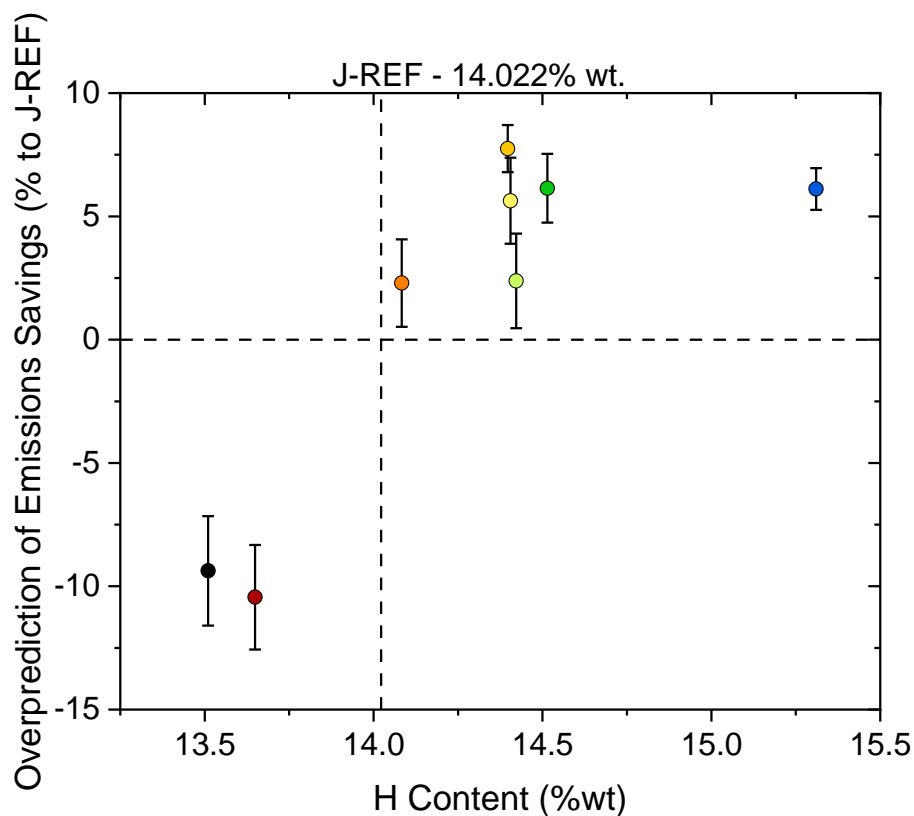


Figure 5-22 - Calculated overpredictions in E_{number} emissions savings (normalised to J-REF) by the exclusion of size-dependant system loss corrections.

Compared to J-REF, it is seen that reductions in E_{number} are overreported by up to ~8% for lower hydrogen fuels, with the overreporting greatest in the case of B-HE1. The opposite trend is observed with low hydrogen content fuels, whereby percentage increases of uncorrected E_{number} relative to J-REF are ~10% higher than corrected values. This is a particularly important consideration for the accurate reporting and prediction of the negative impacts to human health of nvPM from aircraft operating with high hydrogen content fuels.

5.5.2. Assessment of Specific Energy Corrections

During experimentation, combustor exhaust temperatures were monitored and subsequently analysed, so as to ensure flame stability and because flame temperatures are known to impact nvPM emissions. The results serve to indicate the kind of temperature differences which can occur across alternative fuels in comparison to conventional jet fuels, as well as at different operating conditions. Again, for the reference test condition (condition C), combustor exhaust

temperature is observed to vary by 20-25 K across fuels as a result of varying energy release across fuels, with higher hydrogen content fuels usually resulting in the higher temperatures, shown in *Figure 5-23*.

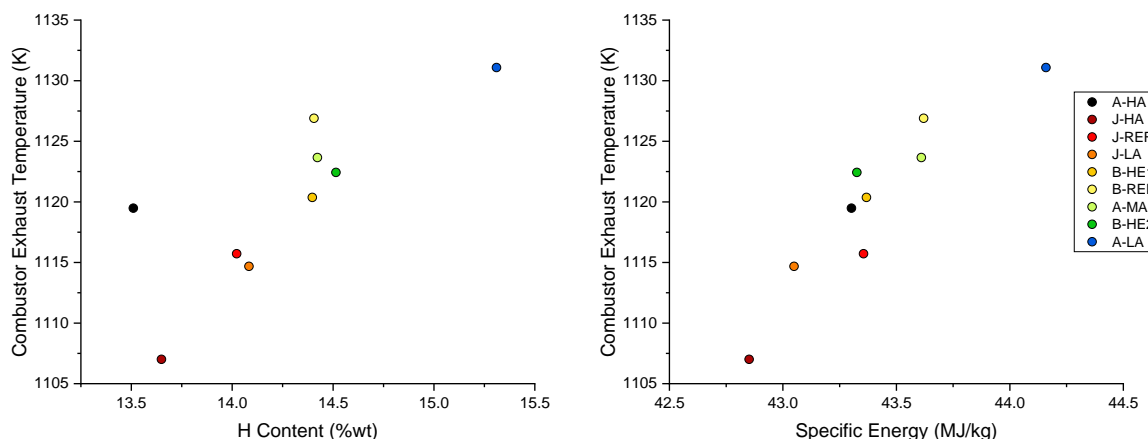


Figure 5-23 - Combustor exhaust temperature plotted against fuel hydrogen content (left) and specific energy (right)

Fuels with lower specific energies to J-REF would be expected to exhibit slightly higher energy corrected EI values compared to non-corrected values, and vice versa. This is to be expected, as lower specific energy fuels require higher mass flowrates to deliver the same energy release as fuels of higher specific energy. Additionally, fuels exhibiting higher specific energies would be expected to provide higher heat release during combustion, raising the flame temperature, which can encourage additional soot burnout. In an attempt to predict the effect specific energy may have had on emission formation, specific energy corrections were applied in the form of ENERGY-EI values (*See Equation 3-13*) normalised to J-REF, as are shown in *Figure 5-24*.

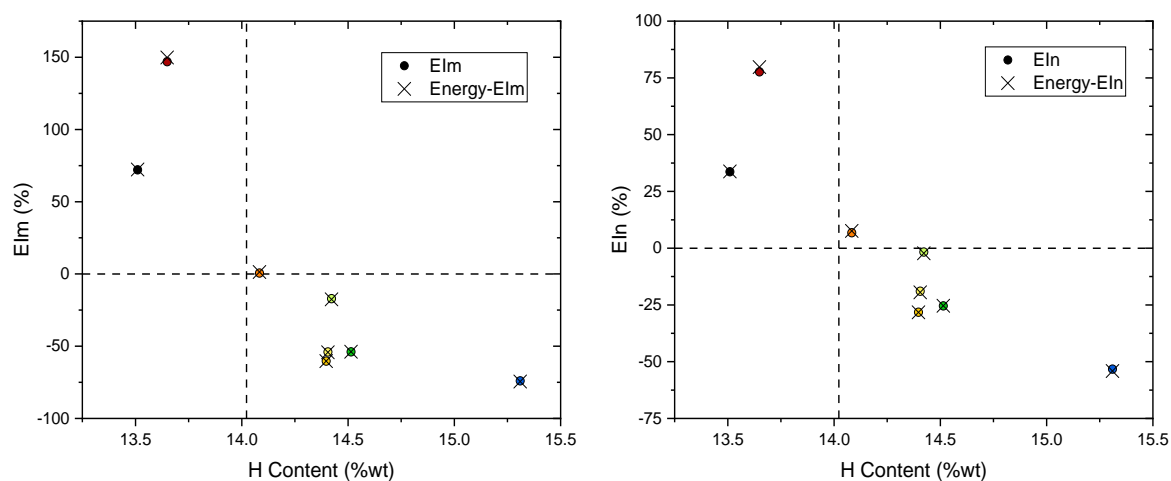


Figure 5-24 - Specific energy normalised nvPM emissions

The largest increases to non-energy corrected data were observed for J-HA, with the lowest specific energy of the fuels studied. Normalised ENERGY-EI values for this fuel were calculated to deviate from standard EI values by a maximum of +2.93% and +2.27% for EI_{mass} and EI_{number} , respectively. Conversely, the largest decreases to the same results were observed for A-LA, which exhibited the highest specific energy. The calculated deviations for this fuel were -0.59% and -1.21% for EI_{mass} and EI_{number} , respectively. The range of deviations for EI_{mass} and EI_{number} across all fuels were found to be 3.52% and 3.48%, respectively. Deviations were not large enough to affect the order of fuels with regard to nvPM emissions at any point in the study, but indicate that small additional improvements in emissions reductions are achievable when factoring in the energy release of high hydrogen content fuels, which typically exhibit higher specific energies.

Figure 5-25 shows the calculated equivalent fuel consumption (See **Equation 3-14**) for all fuels compared to J-REF for a matched power output by both a mass and volume basis. Reductions to equivalent fuel consumption when normalised to specific energy (gravimetric basis) may be considered as corresponding to CO₂ reductions. In general, the blended fuels allow for similar or slightly reduced (<1%) fuel consumption on a mass basis compared to J-REF. Fuel A-LA shows the greatest reductions, where consumption is reduced by ~2%, while fuel J-HA shows the highest consumption at over 1% increase. Data on a volume basis is taken as a measure of fuel consumption relative to fuel tank capacity. Here, fuels of higher hydrogen content exhibit higher rates of consumption for a consistent power output, leading to fuel tanks emptying faster when filled to a matched volume. B-HE2 shows the greatest increases in fuel consumption rates, approximately 2% higher than J-REF, while A-HA shows the greatest reductions at almost 4%.

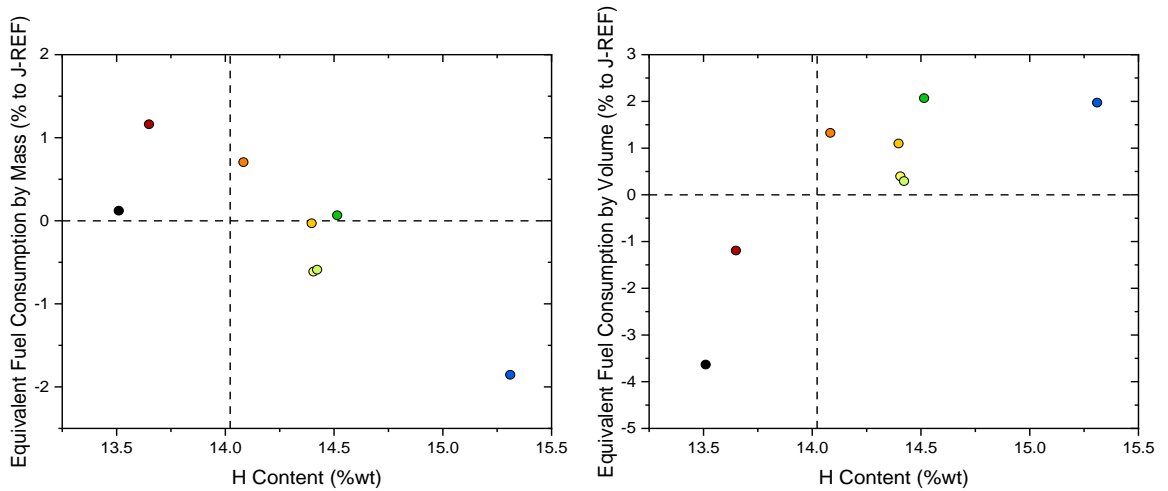


Figure 5-25 - Predicted equivalent fuel consumptions across fuels, relative to J-REF, normalised for fuel specific energy content (left) and volumetric energy content (right)

5.6. Assessment of the Effects of Combustor Conditions on nvPM

5.6.1. Power/Thrust

Because rig operating parameters (fuel flowrate, primary air, secondary air, and pressure) could be individually controlled for this rig, an analysis of the individual impacts of these conditions was undertaken. It was found that increasing combustor power, achieved through an increase in combustor pressure for which air and fuel flowrates were then scaled (representative of increasing engine thrust), generally exacerbated nvPM emissions for mass, number, and size, as shown in **Figure 5-26**. The increase in particle sizes with increasing power is consistent with the findings of Kumal *et al.* [94], who observed increasing particle sizes at higher thrust settings, with a higher dependence on power attributed to higher aromatic fuels. Increasing EEP GMD values are observed for this study as power increases, but no noticeable change in gradients is observed across fuels with the apparent variability.

Both EI_{mass} and EI_{number} are seen to increase with combustor power, with gradients appearing steeper at lower hydrogen/higher aromatic contents. The increase in EI_{number} values at lower pressures shows that emissions are worsened by factors other than the increasing fuel flow, since EI data is normalised to fuel flowrates. This could be due to an acceleration in nvPM formation chemistry by the higher pressures and temperatures. It is also observed however that EI_{number} shows a somewhat declining gradient as pressure increases, causing some fuels to exhibit lower EI_{number} values at the 2.4 bar condition than the 1.9 bar condition. It

is possible that this indicates a plateau value exists for EI_{number} , where the increase in particle number is solely a result of higher fuel flowrates at increased power, and this will be further considered in later sections in this thesis. Meanwhile, the fact that the declining gradient is not also observed for EI_{mass} is because particle mass is affected by both number and size, and so the increase in GMD values lead to overall higher EI_{mass} at 2.4 bar.

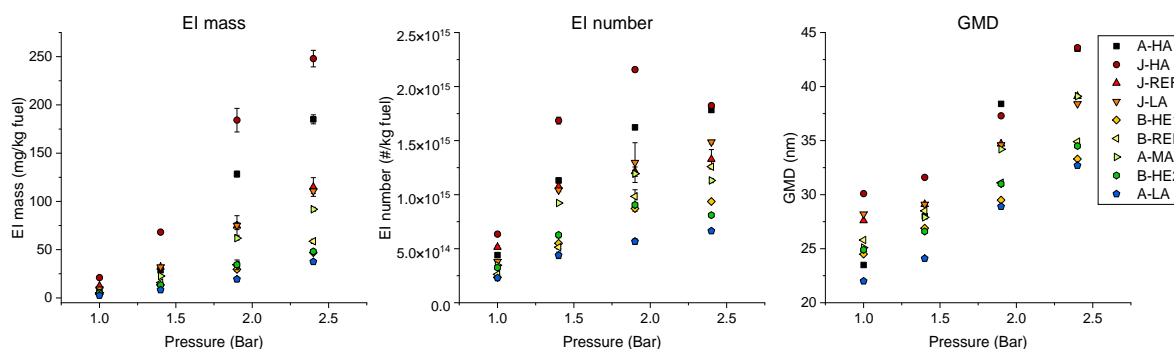


Figure 5-26 - Impact of pressure vs. loss corrected emissions

5.6.2. Primary Air

For analysis of the effects of fluid flowrates, data at 1.9 bar combustor pressure was used, since the most operating conditions were conducted at this pressure condition, and the data was also deemed more stable than at the lower pressures. The effects of increasing the primary air flowrate from 4.2 to 4.8 g/s between conditions A to B, and conditions C to D, are shown in **Figure 5-27** and **Figure 5-28**. In both cases, the primary AFR is increased by ~10% by the increase in atomisation air, which would also improve atomisation quality, both of which are expected to decrease overall nvPM formation. It is also possible that the increase in atomiser exit airspeed could worsen nvPM emissions as a result of a decrease in residence time for the flame in the secondary zone of the combustor, affording less time for soot oxidation and consumption, as suggested by Durdina *et al.* [189], but this effect is likely small compared to the others mentioned. Global AFR is slightly increased due to the additional air input, shifting the global equivalence ratio slightly further from stoichiometry and into leaner combustion.

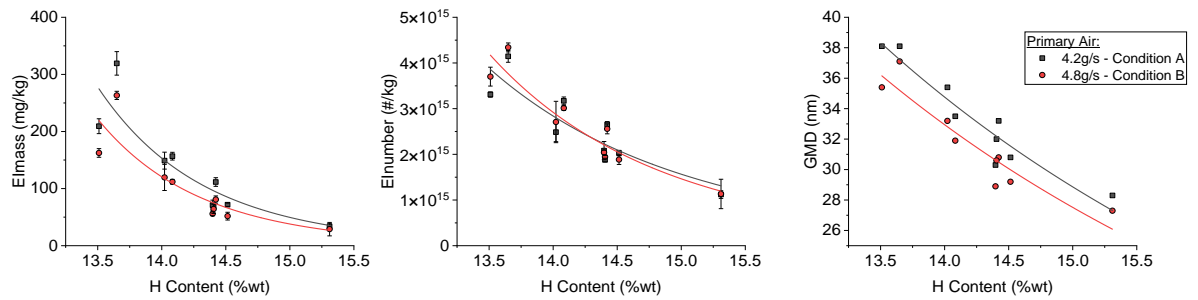


Figure 5-27: Impact of primary air flow rate on nvPM formation across different fuels tests

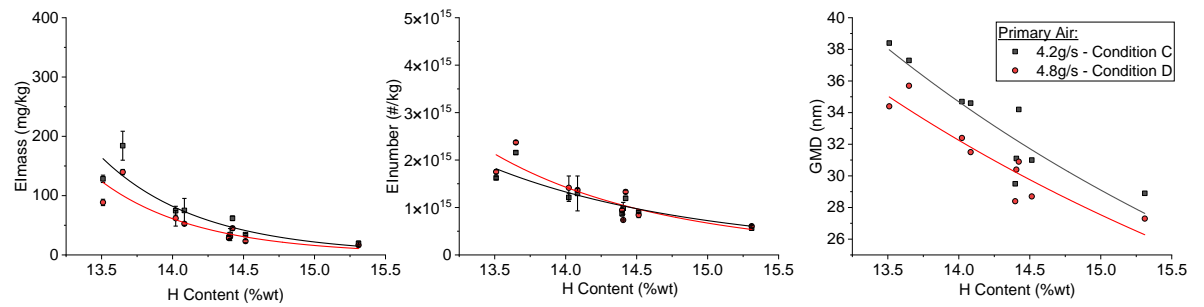


Figure 5-28: Effect of varying the primary air on combustor-exit nvPM El mass (a), number (b) and measured GMD (c)

The overall result was a decrease in GMD by ~4% and ~8% for each change in condition respectively, causing the nvPM PSDs to shift left towards smaller particles. Increases in average values of ~2% and ~5% are observed for El_{number} , although these changes are very small for the range of values across fuels, with plotted trendlines overlapping each other in both cases. The largest impact was to El_{mass} , which exhibited average reductions of ~21% and ~24%. It is important to note that increases in particle size will reflect as a much larger increases in particle mass, since, assuming spherical particles with a density of 1 g/cm^3 , mass scales proportionally with particle volume. The reduction in particle sizes with a small increase in El_{number} suggest either that nvPM agglomeration in the primary zone is slowed, resulting in more smaller particles in place of larger fractal structures, or that particle oxidation is increased due to the additional air available for combustion.

5.6.3. Fuel Flowrate

The increase in fuel flow rate by from conditions A to C, and B to D, is shown in **Figure 5-29** and **Figure 5-30**. At 1.9 bar, the 0.2 g/s increase results in a higher power output of ~9 kW, with no additional change to fluid flows. The overall result is a decrease to both the primary and global AFR, resulting in a richer

primary zone and bringing the global equivalence ratio closer to stoichiometry (0.31 to 0.36). Although increasing fuel flowrate has been shown to reduce atomisation quality, changes are expected to be small and atomisation behaviour is assumed to remain relatively constant across conditions, with variations in nvPM solely a result of flame chemistry. The additional heat release and shift in global equivalence ratio towards stoichiometry is accompanied by the aforementioned increase in exhaust temperature (**Section 5.3.3**), which is expected to promote nvPM burnout. However, the richer primary equivalence ratio may be expected to encourage nvPM formation in the primary zone.

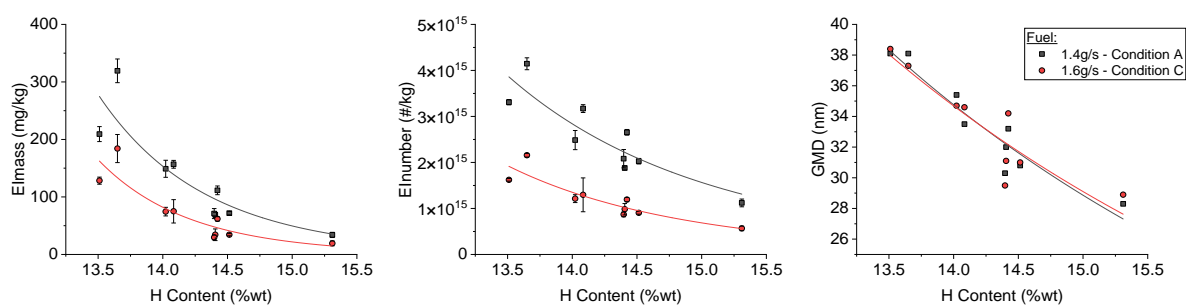


Figure 5-29 - Effect of varying the fuel flow rate on combustor-exit nvPM EI mass (a), number (b) and measured GMD (c), conditions A vs. C

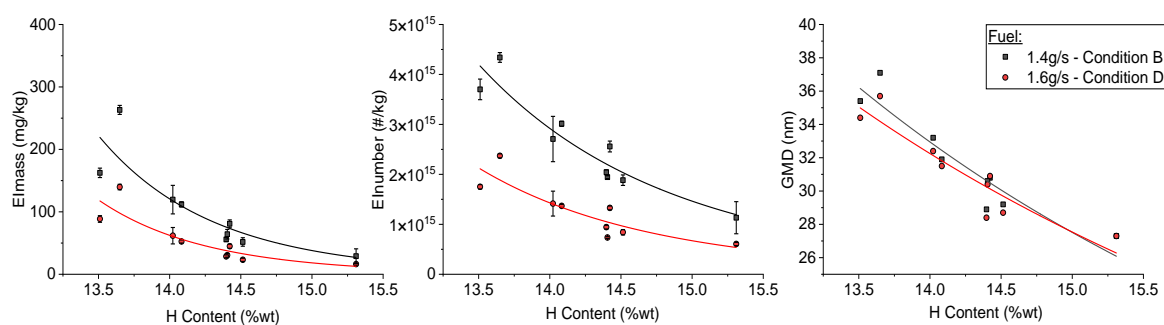


Figure 5-30 - Effect of varying the fuel flow rate on combustor-exit nvPM EI mass (a), number (b) and GMD (c), conditions B vs. D

The overall impact is a reduction to both EI_{number} and EI_{mass} at similar rates to each other (~50% average reductions for each case), while having little observable effect on GMD, which suggests that the observed impact is due to a change in nvPM formation rates. Increasing richness of the primary zone would be expected to lead to higher nvPM emissions, but the overall decrease in particle number with no change in GMD suggests that particle nucleation is being suppressed, resulting in fewer particles overall which form fractal structures at the same rate.

Figure 5-31 highlights that combustion efficiency is improved for all fuels by the increased fuel flow at conditions C and D, accompanied by reduced CO and UHC emissions, and increased NO_x emissions. CO₂ emissions are higher at this condition due to the additional carbon input at higher fuel flows.

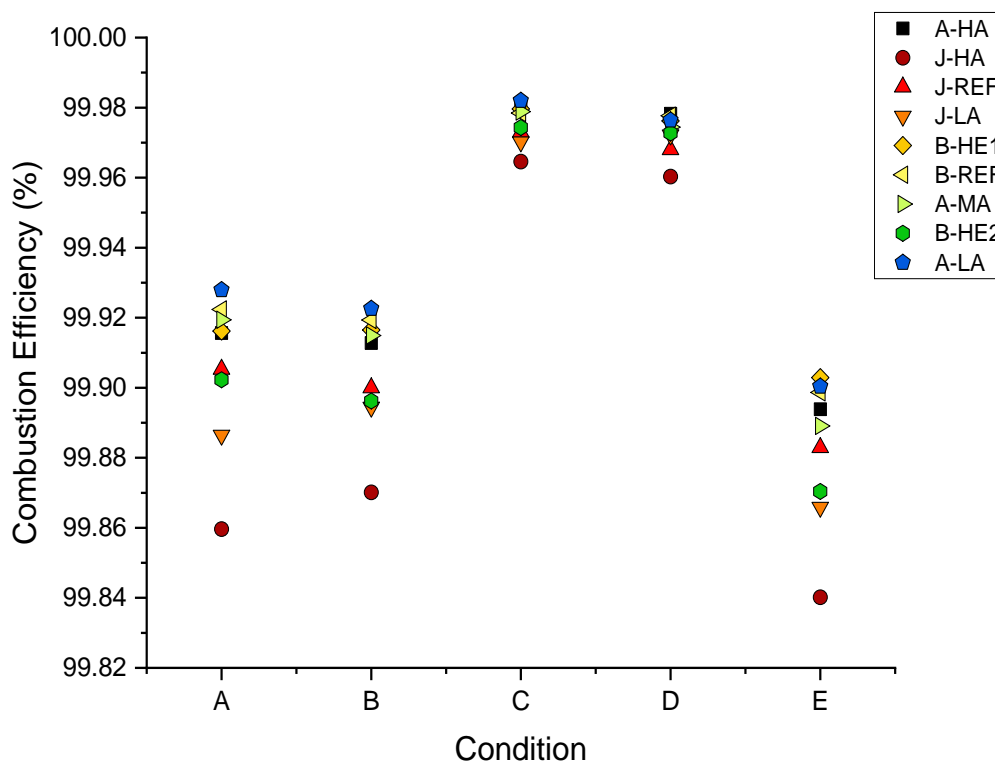


Figure 5-31 - Calculated combustion efficiency across operating conditions

Between conditions A and D, both primary air and fuel were scaled by the same degree. Primary AFR is slightly reduced for condition D, while reducing the global AFR from ~46 to ~40, again serving to bring the global equivalence ratio closer to stoichiometry (0.31 to 0.36). Atomisation quality is expected to improve for condition D due to the higher velocity of atomisation air. Across conditions, nvPM emissions are shown to be reduced for mass, number, and particle size by 50%, 59%, and 7% respectively. Because the reduction in GMD is approximately the same magnitude as observed in **Section 5.6.2**, it appears that GMD is reduced by the addition of higher quantities of primary air irrespective of the primary zone AFR.

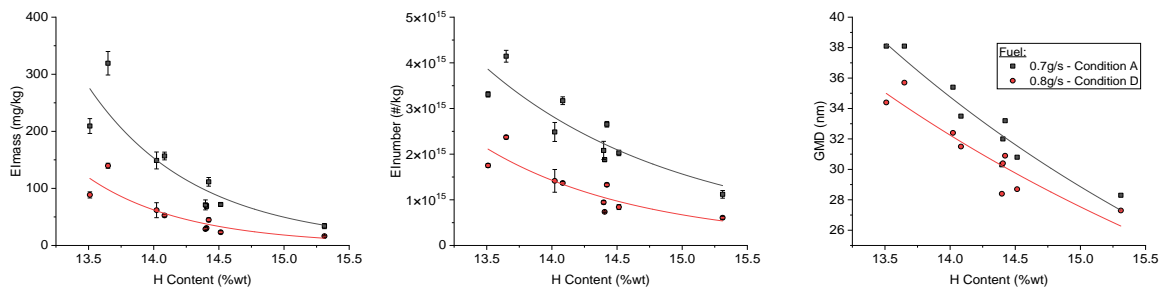


Figure 5-32 - Combustor-exit nvPM EI mass (a), number (b) and GMD (c), conditions A vs. D

5.6.4. Secondary Air

Increasing the secondary air flowrate from 60 to 70 g/s while maintaining constant primary air and fuel flow (conditions C to E) resulted in an increase in nvPM EI number along with a decrease in GMD, with an overall effect of increasing EI mass and worsening of nvPM emissions. The increase in secondary air would not be expected to interfere significantly with primary zone combustion, thereby affecting nvPM oxidation without significantly impacting formation, although a small influence on the primary zone is expected due to the slightly increased air flowrate through the primary cooling holes. However, it has been seen that if too much secondary air is used, soot “freezing” may occur, whereby high velocity air streams leading to higher rates of exhaust nvPM, CO or UHC [16].

The increased air is calculated to raise the global AFR from 40 to 46, resulting in leaner overall combustion. Primary AFR is expected to remain mostly constant, although realistically is slightly leaner for condition E due to the added cooling air entering the primary zone. This coincided with a drop in combustion temperature across all fuels by approximately 50-60 K, which may have been as a result of either the lower overall equivalence ratio or due to a cooling effect from the increased air flowrates. The overall effect of increased EI_{mass} and EI_{number} values appears to indicate that soot “freezing” significantly worsens nvPM emissions by reducing the burnout of smaller particles, resulting in a greater number of these small particles to remain in the exhaust composition and shifting GMD to smaller values.

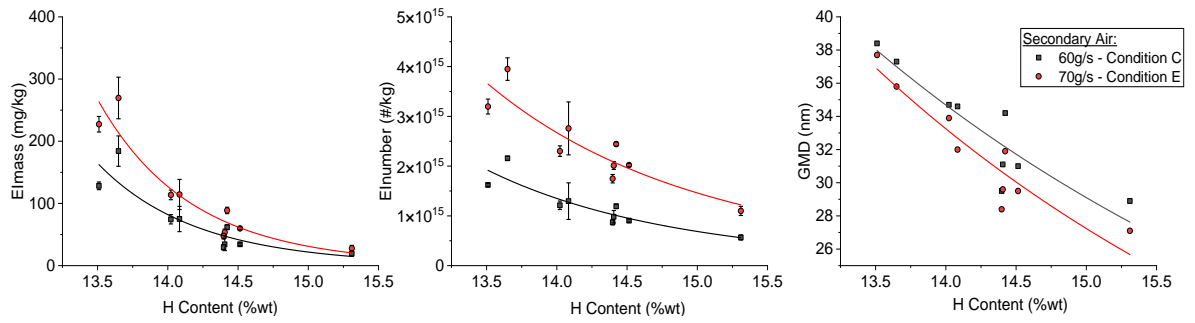


Figure 5-33: Effect of varying the secondary air on combustor-exit nvPM EImass (a), number (b) and measured GMD (c)

5.7. Chapter Summary

The Mk. I RQL burner was successfully operated using a range of conventional fuels, SAF, and blended fuels, yielding a full nvPM emissions dataset. Data was collected over a range of operating conditions and pressures, allowing for an analysis of their impacts on nvPM emissions. Data was subsequently corrected for system losses to give calculated concentrations at the combustor exit plane. In agreement with previous studies on full-scale engines, hydrogen content trends were shown to generally best describe nvPM emission reductions caused by fuel changes. It was found that a newly developed constrained power law hydrogen content trend offers a potential improvement over the previously proposed polynomial trend, able to slightly improve R^2 fitting values, whilst being more scientifically consistent. However, the measured R^2 values are lower than ideal, which is symptomatic of scatter around the fitted hydrogen content trendlines and highlights that there is significant day-to-day variability of rig conditions and AFR, which would need to be addressed if fuel physical properties and their impact on atomisation are to be fully understood.

Because of the generally systematic nature of the scatter, it was hypothesised to stem from additional influences such as variations in fuel compositions, molecular weights, and atomisation effectiveness, as well as day-to-day variability such as variations in AFR and fluctuations in combustor pressures. Compositional variability for fuels of similar hydrogen content was also examined. It was found that a modified hydrogen content power law provided the best correlation overall. The use of a published compound variable consisting of hydrogen content and di-aromatics was examined as a potential method of better describing nvPM emissions, but was not found to yield better data fits compared to hydrogen content alone. It is suggested that future work utilising the RQL rig

explores further whether di-aromatic content can be used alongside hydrogen content to better understand nvPM emissions. However, the current data suggests that the impact of di-aromatic content in the quantities present does not present a discernible trend, and as explained earlier rig variability would need to be improved to achieve this.

A simple estimate for the variability of spray quality across fuels was utilised. The trends indicate that predicted variations in atomisation across the tested fuels would likely be small (~5%). While some evidence suggests a larger impact of fuel physical properties, this could not be quantified with the current data due to the variability of the combustion rig appearing to be larger than the expected impacts, therefore this requires further investigation, should a more repeatable combustor source be developed.

An examination of the correction methods employed was undertaken, including system losses and specific energy corrections. Loss corrected emissions show a restricted range of variability for nvPM data when normalised to a reference fuel. It was found that reductions in EI_{number} through the use of low aromatic, high hydrogen content fuels were overpredicted by up to ~8%. This was as expected and as a direct result of greater losses of smaller particles via diffusion loss mechanisms in the sampling system. Specific energy corrections impacted results by ~3%, and it was shown that the use of high hydrogen content fuels could result in around 2% reductions to fuel consumption by mass, which ultimately translates to CO₂ reductions to the same degree. However, on a volume basis, around 2% less energy would be available from the same fuel for an equally sized fuel tank.

An analysis of the impacts of combustor operating conditions on nvPM emissions was undertaken. As expected, nvPM emissions were shown to generally worsen with increasing pressures, consistent with the literature. Consistent increases were observed in GMD and EI_{mass} , while EI_{number} values were generally exacerbated but showed a levelling off at increasing pressures for most fuels.

Increasing primary air was seen to reduce GMD values, which in turn allowed for reductions in EI_{mass} . However, EI_{number} did not appear to be significantly affected. Due to the non-decoupled nature of primary AFR and when atomisation air is increased, additional experimentation is deemed necessary to determine

whether atomisation effectiveness can be decoupled to provide a better understanding its effect on nvPM emissions.

Reductions in nvPM were most significant when increasing fuel flowrate, which were shown to reduce EI_{number} and EI_{mass} by ~50%. This was highlighted as a result of the global equivalence ratio shifting closer towards stoichiometry, reducing the effectiveness of the RQL concept (increased NOx) but improving the overall combustion efficiency and resulting in higher heat release, thereby promoting nvPM burnout.

Increasing secondary air served to reduce the flame temperature and combustor global equivalence ratio, resulting in significant increases in EI_{number} and EI_{mass} . This seemed to imply that nvPM burnout was reduced, either by dilution of the combustor with air, or through soot “freezing” mechanisms, or both. Meanwhile GMD was seen to reduce, showing that reductions can be achieved in average particle size by increased availability of air to the combustor.

Ultimately, while a good deal of control over combustion was achieved with the rig setup, the numerous influences on nvPM emissions, such as AFR, turbulent mixing, atomisation, and air entrainment, make attributing variations to physical phenomena difficult. However, it appears that a combustor global equivalence ratio closer to stoichiometry helps to reduce ICAO regulated nvPM emissions, with the greatest emissions reductions achieved when power output was increased along with atomisation air, allowing for reductions in mass, number, and size. This reduces the effectiveness of the RQL concept, but combustion efficiencies are also reduced. Because the combustion efficiencies were generally good (above 99%), this suggests that combustor is operating close to optimised combustion performance, and slight increases in both fuel along with atomisation air are recommended for future designs.

6. Refinement of the RQL Design (Mk. II Combustor)

6.1. Overview

The previous Mk I. combustor experimental campaign (*Chapter 5*) had demonstrated that the RQL combustion rig was capable of producing a full emissions dataset for the study of SAF, although scatter and instabilities were observed during operation. Refinement of the RQL combustor design was desirable so as to improve operational stability and optimise the combustor for future emissions testing. This chapter outlines the development of the Mk. II RQL rig towards achieving these outcomes, which was benchmarked through combustion experimentation as part of the H2020 Raptor test campaign, during which an additional emissions dataset was produced for a range of fuels, so as to first assess the performance of the Mk. II combustor and consolidate previously observed emissions trends.

The main purpose of developing the Mk II combustor was to increase understanding and control of the primary zone, so as to facilitate further exploration into the impact of primary zone characteristics on emissions. Particular emphasis was to be given to the sprays produced by the atomisers, of which the phase I atomisers had been manufactured at this time. As such, the main aim of this chapter was to develop a method of characterising the atomisation quality produced by the atomisers, as a means to estimate the impact of atomiser design features and fuel properties. This would help to improve understanding over the combustor performance, towards exploring the impact atomisation can have on nvPM emissions.

6.2. Laser Diffraction Experimentation

6.2.1. Ambient Temperature Atomiser Characterisation

To afford better characterisation of the atomisation performance across the phase I atomisers, empirical spray measurement was undertaken using a Malvern Spraytec97 (as previously discussed in *Section 3.6*), with unheated ambient primary air and water as a fuel. Initial assessment of the filming behaviour across atomisers was undertaken using water only, so as to assess the atomiser symmetry and determine if there were any blockages within the atomiser

fuels channels. As shown in **Figure 6-1**, all of the atomisers tested exhibited the expected stages of spray development across increasing water flow rates, as described in Lefebvre and McDonnell [112]. The flowrates used were higher than those used during spray characterisation and combustor operation, and were chosen to examine symmetry of the fluid channel which may have been a function of either manufacturing tolerances or metal powder blockages.

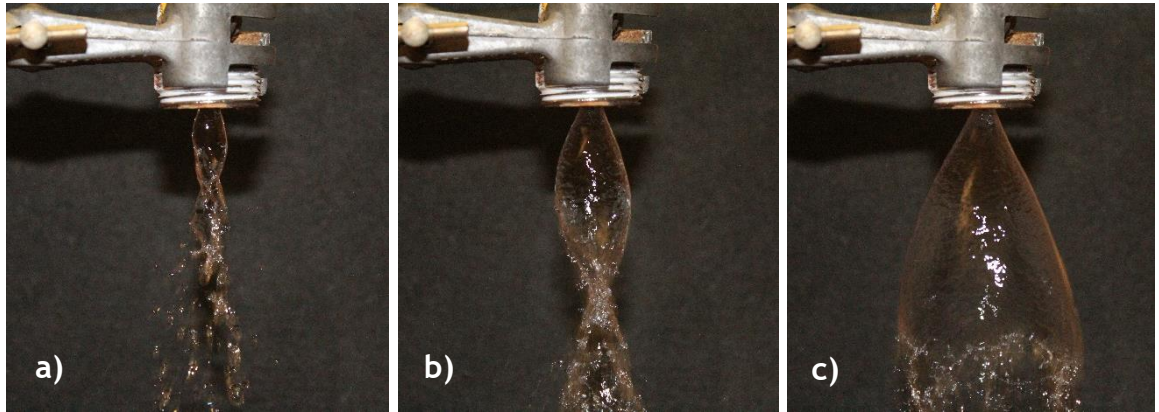


Figure 6-1 - Atomiser I-C operating with water flowrates of a) 10 g/s, b) 20 g/s, c) 30 g/s

Subsequent measurement of spray droplet sizes was undertaken following the recommended practice of the diffraction sizing instrument given by manufacturer in the user manual. Reference noise signals were taken once a day before all measurements, to correct for ambient anomalous signals caused by lighting or electrical signals from improper grounding. Across all tests, the high-speed flash mode setting was used for data acquisition, with measurements taken over a user-defined sample time of 2.0 seconds and a data acquisition rate of 2500 Hz. The resultant 5000 measurement points were automatically averaged every 5 scans, resulting in a total of 1000 data points per test point. Data rates below 1000, in the 2 second window, were taken as an indication of poor spray quality with a threshold of 950 used in this work to define a reliable measurement and operating condition.

Next, the reduction control parameters and process variables were set. The reduction control parameters allowed the user to define a sample size range based on the recommended values of the 450 mm lens used (2.5-1040 μm) and a calibration file containing medium refractive index values was chosen as suitable for water particles ($1.33 + 0.00i$) atomised in an air medium ($1.00 + 0.00i$). Across each series of tests, atomisers were operated across a range of air mass flowrates (2.0-10.0 g/s), at three corresponding water mass flowrates (0.8 g/s, 1.2 g/s and

1.6 g/s). Measurements were taken at a fixed location, 40 mm downstream of the atomiser exit plane. This location was selected as representative of the location of the quench holes during combustion tests, by which time atomisation should have been complete. Images of the operation of the atomiser and laser diffraction system are shown in **Figure 6-2**.

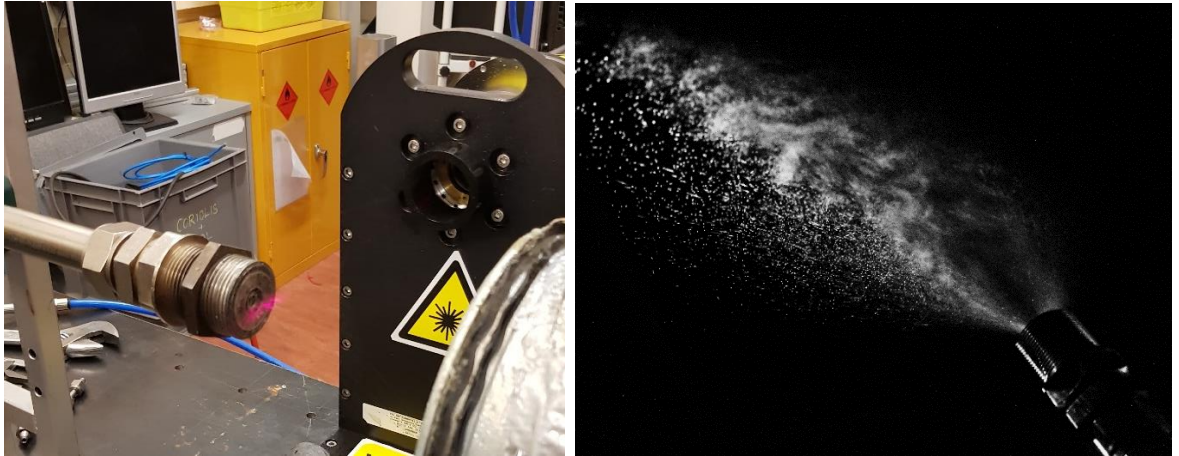


Figure 6-2 - Atomiser operation during laser diffraction experimentation

A plot of measured SMD values against air mass flowrate for atomisers I-A to I-D at 1.6 g/s water flowrate are shown in **Figure 6-3**, with allometric power trendlines fitted to highlight general trends. The error bars included are standard deviations outputted by the Malvern system, representing the standard deviation about the mean droplet size values.

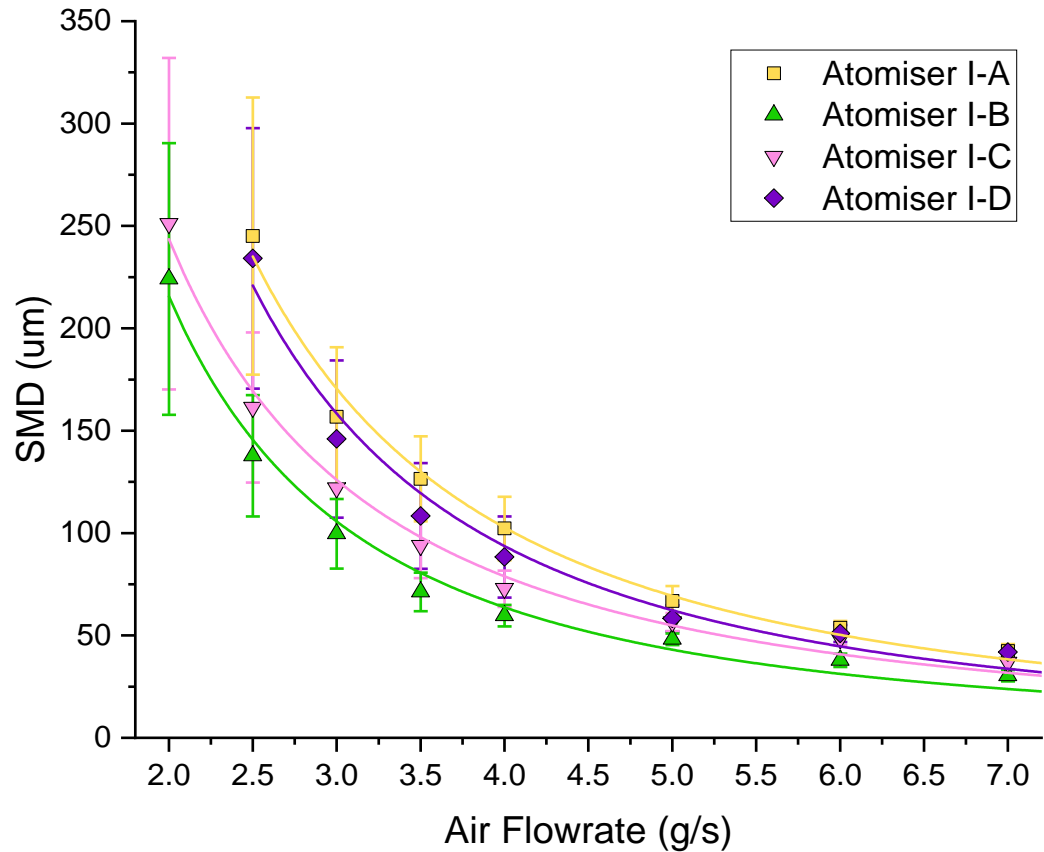


Figure 6-3 - Measured SMD values vs. air mass flowrate

Per mass flowrate of air, atomiser I-A is seen to produce the coarsest sprays, and would appear to be the worst performing atomiser. Atomiser I-B produces the finest atomisation quality, although this comes at the cost of the high pressure drop characteristics, as shown in **Section 4.3.2**, which restrict the operating range of the atomiser to low air flow rates. The SMD values produced by I-D are somewhat higher than I-C, despite the relative similarities in design. This was especially evident at low air flowrates, where atomisation quality is seen to break down sharply. A potential cause of the discrepancy in atomisation quality could be the dimensional offsets due to poor manufacturing tolerances observed in **Section 4.5**, which were seen to result in narrower flow channels in the case of atomiser I-C, supported by the slightly lower coefficient of discharge observed for this atomiser in **Section 4.3.2**. This likely would have increased the exit air velocity for this atomiser and resulted in slightly better atomisation over I-D.

Points at low air flowrates exhibit very large standard deviations during measurements, indicating a broad range of droplet sizes were present within the spray. Because of the wide measurement range of the Malvern Spraytec97 (2.5-1040 µm), and the fact that SMD values are calculated on a volume basis, a small

number of large droplets are capable of significantly impacting the SMD (due to the cubic nature of volume increase), skewing average droplet sizes towards larger values, and causing wider variability in measured values. As such, the worsening of atomisation quality at low flowrates, characteristic of airblast atomisers operating below optimal air flowrates (*Section 2.4.4*) is identified as the most likely cause of the large standard deviations observed. Measurement stability was seen to significantly improve as air flowrates increased.

Figure 6-4 shows the variability in measured SMD against predicted average air velocity (U_a), and measured pressure drop. Pressure drop was measured as mbar, but is presented in this work as a percentage of atmospheric pressure at STP (dp/P), with ambient pressure assumed as ~ 1.013 bar. When plotted against both U_a and measured pressure drop, SMD values across atomisers converge to a more comparable trend. A global allometric power trend fitted over all SMD values against U_a yields an adjusted (adj.) R^2 value of 0.952, indicating that the method proposed for predicting U_a using calculated swirl areas can be used as an empirical design tool for prediction of desired atomisation quality. The same trend fitted to SMD values against pressure drop yields an adj. R^2 value of 0.921, indicating a slightly worse correlation. However, this was suspected to be a result of the decreased C_d value across Atomiser I-A due to the aforementioned gaps in the outer air swirler assembly (*Section 4.3.2*), deviating from the global trendline. When this atomiser is discounted, the quality of fit is improved, yielding an adj. R^2 values of 0.963. It may be noted that atomiser I-A is seen to produce the lowest SMD values per unit pressure drop, but at the cost of reduced stability highlighted earlier (*Section 4.1*).

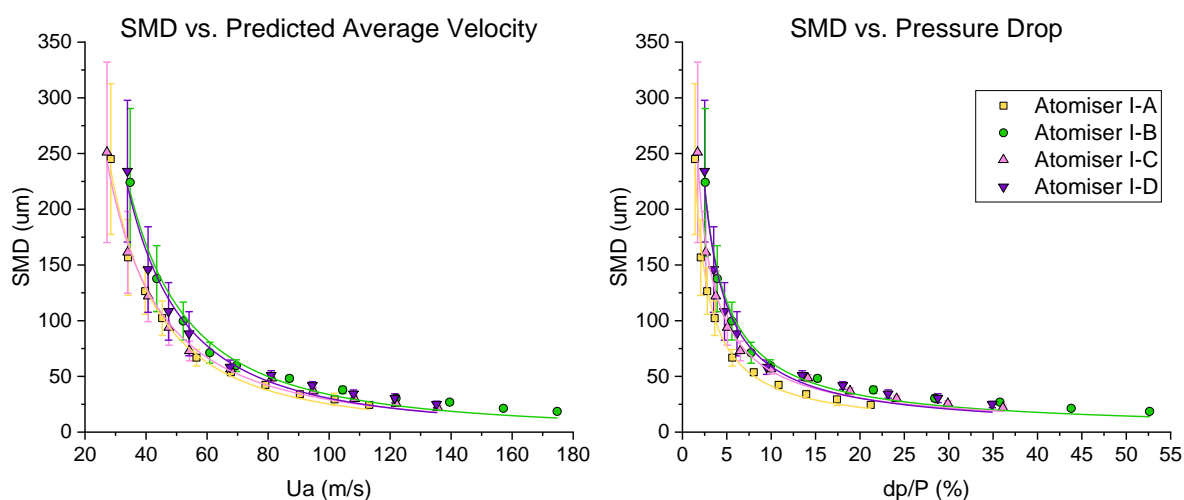


Figure 6-4 - Measured SMD values against U_a and measured dp/P

Figure 6-5 shows the impact of increasing liquid flowrate across the range of air flowrates studied. This is an important consideration, since the range of mass flowrates examined were comparable to those used across subsequent combustion testing. At the flowrates studied, SMD values appear to show the highest sensitivity to increasing liquid flowrate at lower air mass flowrates (<3.5 g/s), but become largely insensitive to changes as air flowrate increases.

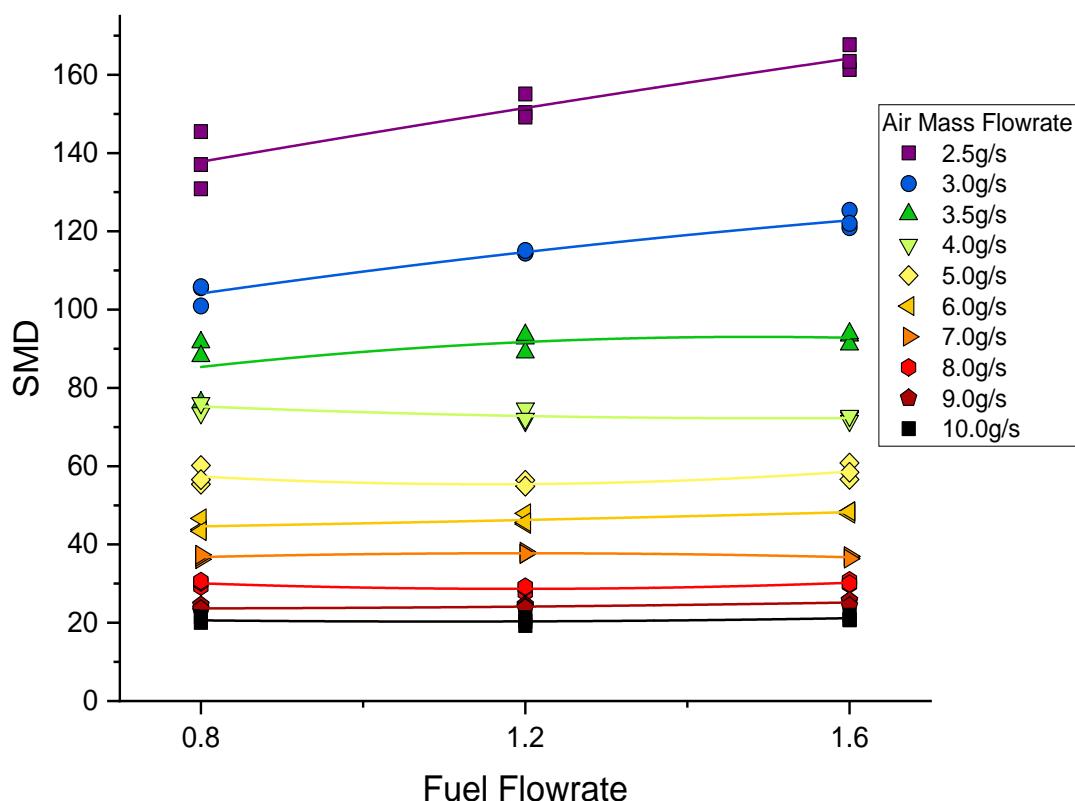


Figure 6-5 - Impact of increasing fuel flowrate on SMD

An analysis of the average PSDs indicates potential factors affecting the measurement accuracy. **Figure 6-6** shows the PSDs for atomiser I-C with increasing flowrates of atomisation air. At low flowrates, the spray appears to exhibit bimodality, as opposed to the expected normal distribution. The distribution is also relatively wide, indicating a large variability in droplet sizes. As air flowrates increase, the log normal shape becomes better defined. However, a consistent peak was apparent in the PSD towards larger particle sizes, which was seen to scale with increasing air flowrates. Because the peak becomes more evident at higher flowrates, it is possible that the cause may be the increased turbulence encountered at these conditions, affecting diffraction of the laser. Another suggested cause are vibrational uncertainties, in which the background signal is affected by large air flows utilised, as are described by Zaidi *et al.* [174]. It may

be noted that the flowrates in which the uncertainty is apparent lie outside of the expected ranges of combustion experimentation.

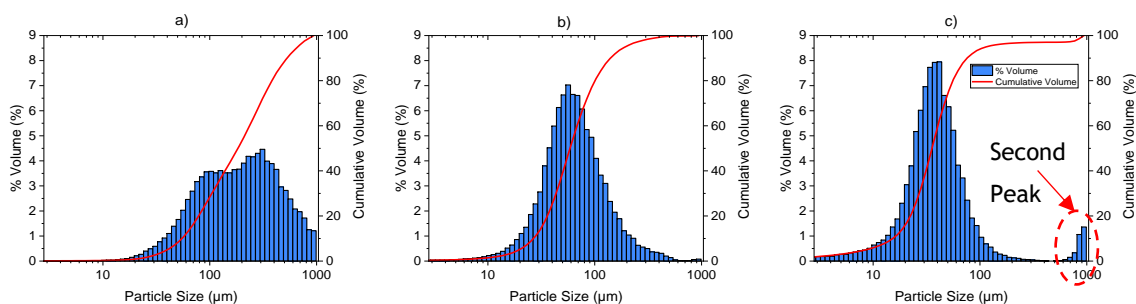


Figure 6-6 - PSD Profiles for atomiser I-C operating with 1.6 g/s water and a) 3.0 g/s of air b) 6.0 g/s of air c) 9.0 g/s of air

6.2.2. Elevated Temperature Atomisation Characterisation

Heated air testing was undertaken following unheated experimentation, so as to be more representative of real-world combustor conditions and to impose a velocity increase on the air for a given mass flow, using target primary air preheat temperatures of 20°C (ambient temperature), 80°C, and 130°C. The 80°C preheat temperature represented the preheat temperatures used during subsequent nvPM emissions testing. Measurements were undertaken at both 40 mm and 60 mm downstream of the atomiser exit for atomiser I-D. The 60 mm position was included to examine whether SMD values would be significantly different at points further downstream of the initial measurement distance. Primary air temperature was monitored using three temperature controllers at various points in the setup, one connected to the heater itself, one at the entrance to the fuel air lance, and one just before the atomiser. This was to account for temperature variations as a result of heat losses across the approx. 1.5 m of supply air piping. It is noted that at low air flowrates, heat loss meant the 130°C test case was slightly below the target temperature.

An observation during initial testing was that the airflow pattern produced by the atomiser would distort the scattering signal at higher air temperatures, significantly altering the diffraction pattern as shown in *Figure 6-7*, and this would subsequently impact reported SMD values. It is hypothesised that this was due to the subsequent change in the refractivity of the air at higher temperatures, causing a shimmering effect. Therefore, rather than using a single background measurement at the start of testing, individual background measurements were

taken at each air mass flowrate before the water flow was brought on. It is possible that the measurement protocol could be improved by altering the medium refractive index used in the Malvern software for each air temperature, but was not attempted for this project.

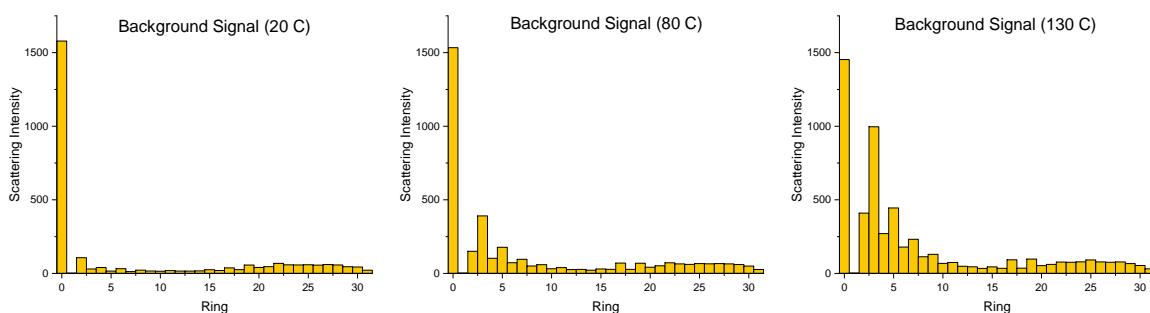


Figure 6-7 - Measured background signal across varying air temperatures

Figure 6-8 shows the effect of increasing primary air temperature on measured SMD for the two measurement locations used. It was found that the SMD values were not significantly affected by the change in measurement location. When the mass flow rate of primary air is held constant, it was found that increasing primary air temperature improved the atomisation quality. Mass continuity and the ideal gas law dictates that increasing temperature serves to linearly increase air velocity, helping to improve atomisation, but also linearly decreases air density which has the opposite effect. The overall improvement in atomisation is explained by the squared air velocity term used for the calculation of We number, which outweighs the impact of decreased air density and serves to improve atomisation. It is also possible that higher rates of evaporation caused by the higher preheat temperatures may have been a contributing factor to the observed trend, but it is suggested that the effect of air velocity was dominant given the proximity to the atomiser exit.

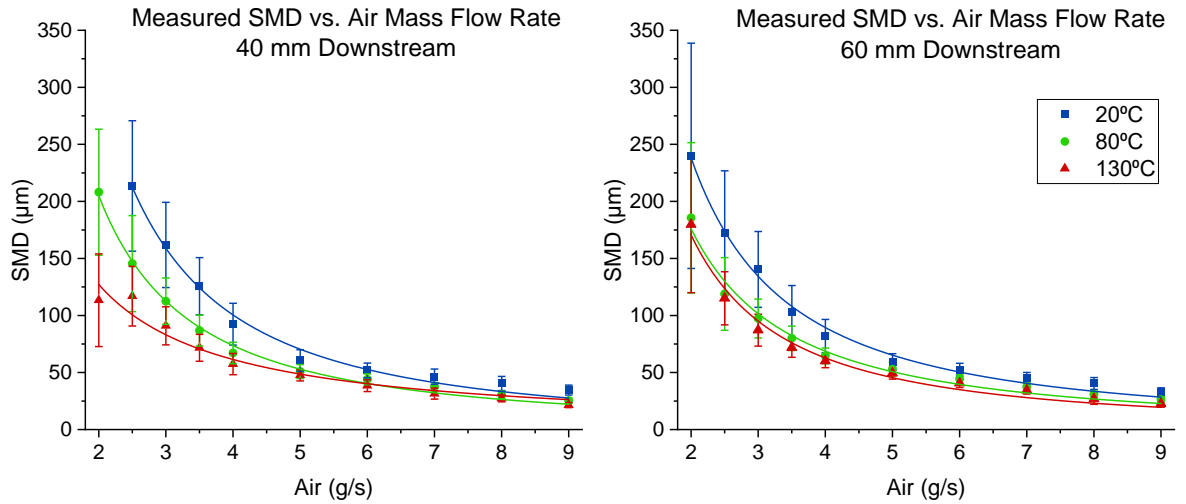


Figure 6-8 - Variation in measured SMD across different air preheat temperatures

When plotted against calculated average air velocity (U_a), SMD values again converge to a global trend, within the measurement error bars. This is shown in Figure 6-9.

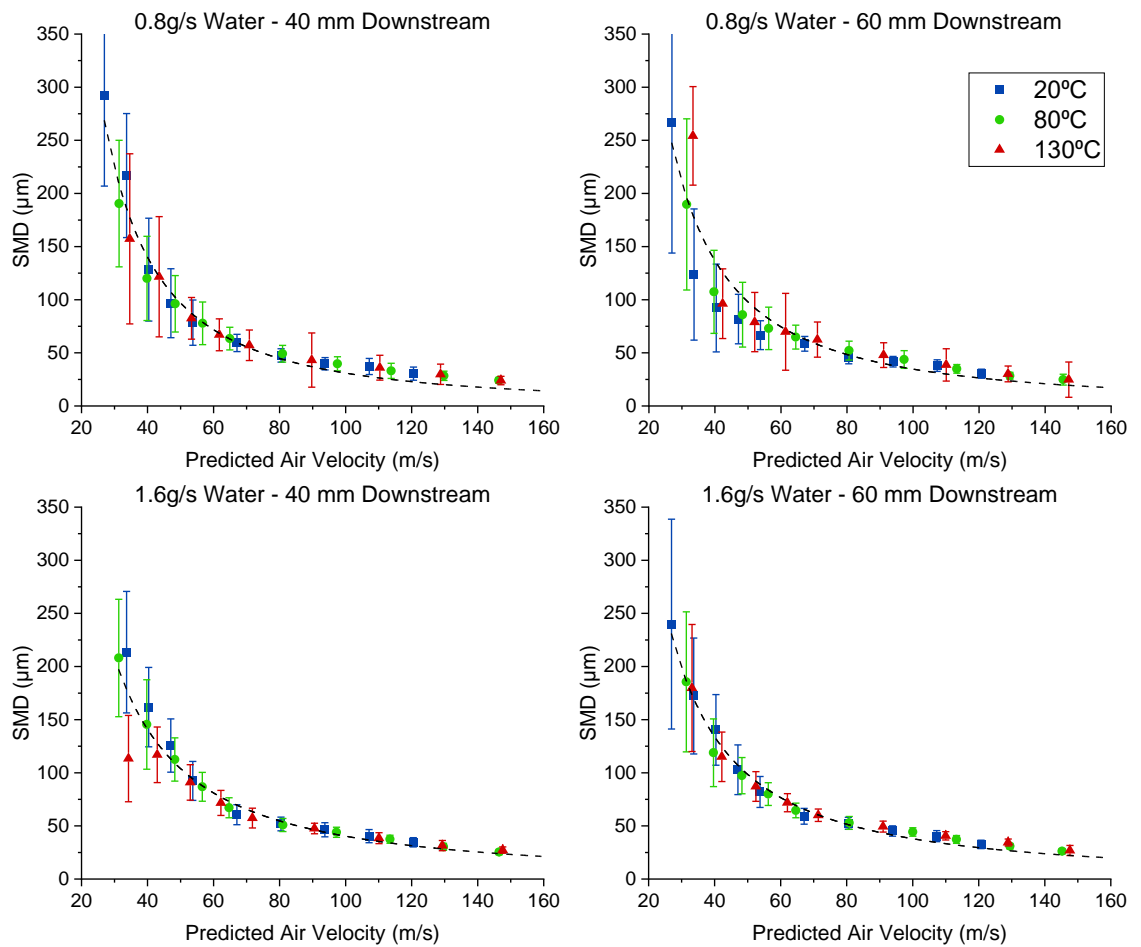


Figure 6-9 - SMD vs. air velocity across different air preheat temperatures

6.2.3. Sum Squared-Error Regression Analysis

As described in **Section 2.4.5**, a number of empirical correlations exist in the literature relating to the atomisation quality produced by airblast atomisers. These correlations were typically developed using a single atomiser design and multiple fluids with different liquid properties, although limited correlations derived from multiple atomisers are also described [129]. The relatively strong fit of global allometric power laws to droplet size data plotted against U_a , shown in previous section, suggests that U_a may be applicable in describing the changes in atomisation quality across different atomiser designs in this study. As a preliminary investigation, the suitability of the previously developed correlations from the literature outlined in **Section 2.4.5**, was assessed, and is shown in **Figure 6-10**.

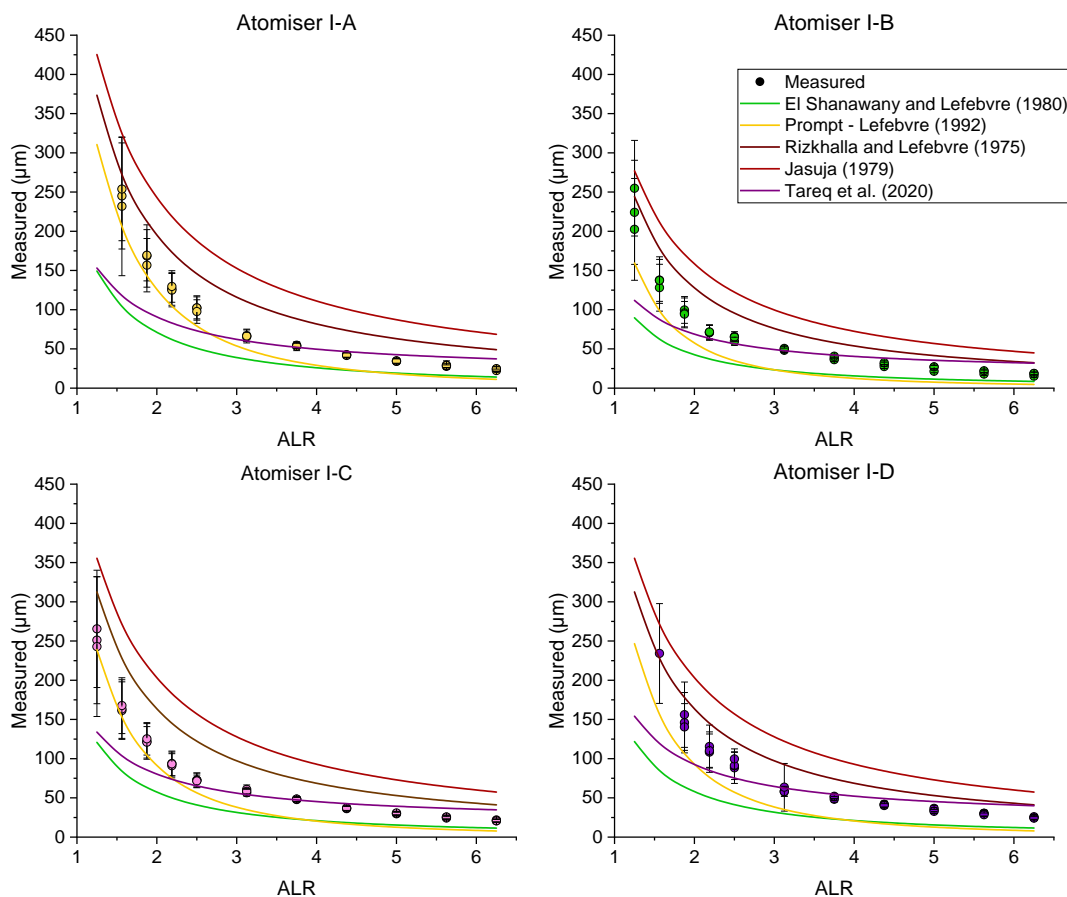


Figure 6-10 - Measured SMD values across atomisers vs. values predicted using correlations from the available literature

Previous studies [126] have shown that correlations from the literature often vary significantly to each other, most likely due to variations in atomiser

design and general repeatability across different experimental setups. In agreement with this, significant variations are observed between the empirical correlations, both to each other and to the measured data in this study. Therefore, the derivation of a new empirical correlation to describe the atomisers developed for this study was deemed necessary. This was achieved using a bespoke MATLAB code utilising a sum-squared error cost function and the *fmincon* feature, given in the appendix (**Section 10**). The function of the code was to iteratively determine optimised coefficients for the generic empirical SMD correlations outlined in **Section 2.4.5**, yielding the smallest possible deviations between predicted and measured data. Quality of fit was assessed by calculating R^2 values, determined following the standard statistical equations for regression analyses (**Equations 5-2 and 5-3**), as given in **Section 5.4.1**. The code used SMD value inputs from the unheated and heated laser diffraction experimentation outlined in the preceding sections. Atomiser I-A was not included due to the aforementioned concerns associated with gaps in the outer air swirler assemblies. **Figure 6-11** gives an example of the output of the code, where measured SMD values are compared to values predicted from an optimised correlation for the same operating parameters and fuel properties.

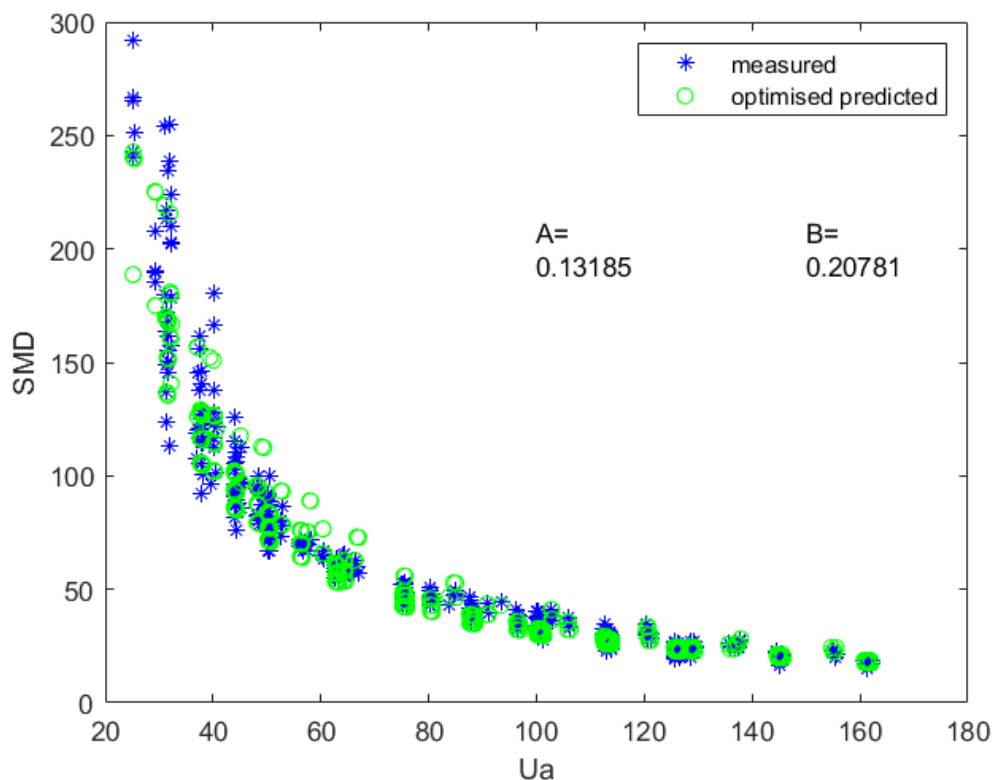


Figure 6-11 - MATLAB linear regression output

Table 6-1 shows the coefficients derived by the regression analysis for the empirical correlations chosen, against the original coefficients given in the literature, and the R² values.

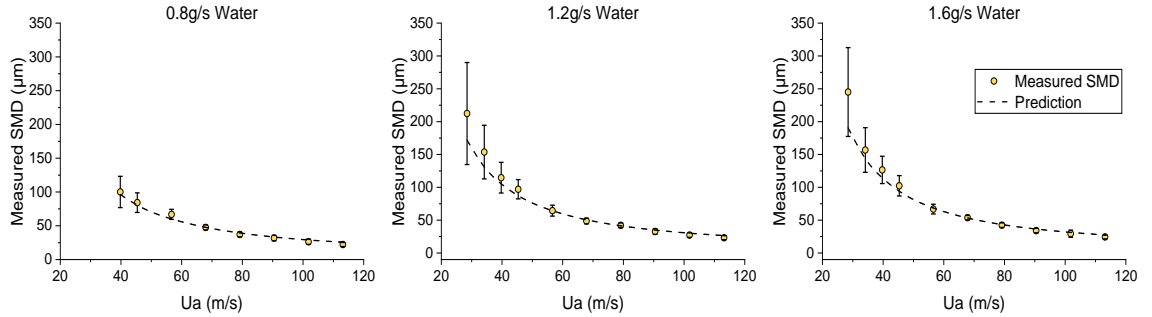
Table 6-1 - Linear Regression Derived Coefficients for Empirical Atomisation Equations

Correlation	Rizkhalla and Lefebvre [113], [120] (Equation 2-13)	El-Shanawany [129] (Equation 2-16)	Lefebvre - Prompt [190] (Equation 2-19)	Lefebvre/Tareq [16], [117] (Equation 2-11)	Lefebvre + Density Term [16] (Equation 2-12)
A (original)	n/a	0.073	-	1.299	n/a
A (derived)	1.9498 x 10 ⁻²	0.13185	-	2.3135	2.0075
B (original)	n/a	0.015	-	34.184	n/a
B (derived)	1.8387 x 10 ⁻⁶	0.20781	-	1.0684 x 10 ⁻⁶	4.9856
C (original)	-	-	1.75 x 10 ⁻³	-	-
C (derived)	-	-	1.1387 x 10 ⁻³	-	-
COD R ²	0.8316	0.9087	0.7085	0.8519	0.8875
Adj. R ²	0.8284	0.9067	0.7015	0.8488	0.8851

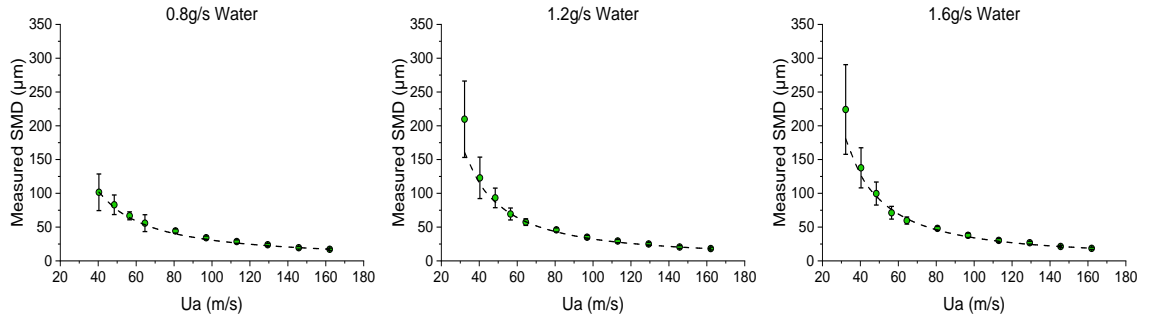
Of the correlations examined, the general form of the equation proposed by El-Shanawany *et al.* [129] with optimised coefficients provides the best fit with experimental data, as given by **Equation 6-1**. Derived coefficients are generally of a similar magnitude to those of the original correlations, although it is noted that the Oh term could range from very high to near zero. The Oh term tending towards zero is common for low viscosity liquids, and has been highlighted as indicative of the prompt atomisation mechanism becoming dominant, resulting in atomisation becoming insensitive to liquid viscosity. Overall however, the correlation appears to adequately capture the trends across different atomisers operating with water, as shown in **Figure 6-12**.

$$SMD = \left[0.13185 \left(\frac{\sigma}{\rho_a U_a^2} \right)^{0.6} \left(\frac{\rho_L}{\rho_a} \right)^{0.1} D_p^{0.4} \left(1 + \frac{1}{ALR} \right) \right] + \left[0.20781 \left(\frac{\mu_L^2 D_p}{\sigma \rho_L} \right)^{0.5} \left(1 + \frac{1}{ALR} \right) \right]$$

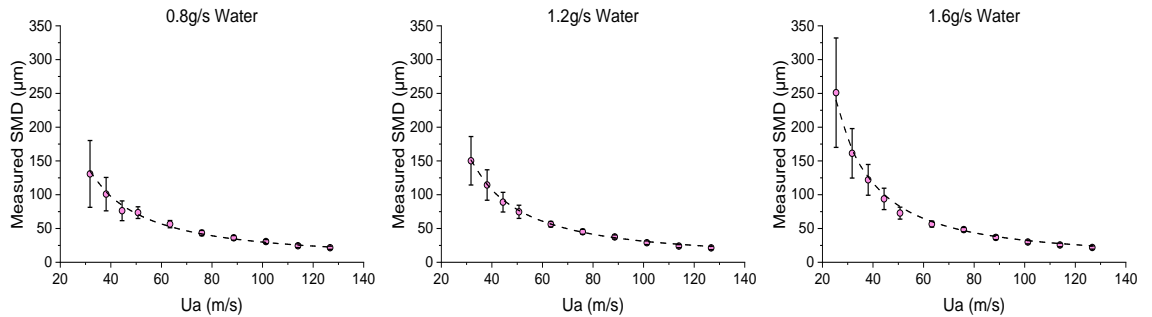
Atomiser I-A



Atomiser I-B



Atomiser I-C



Atomiser I-D

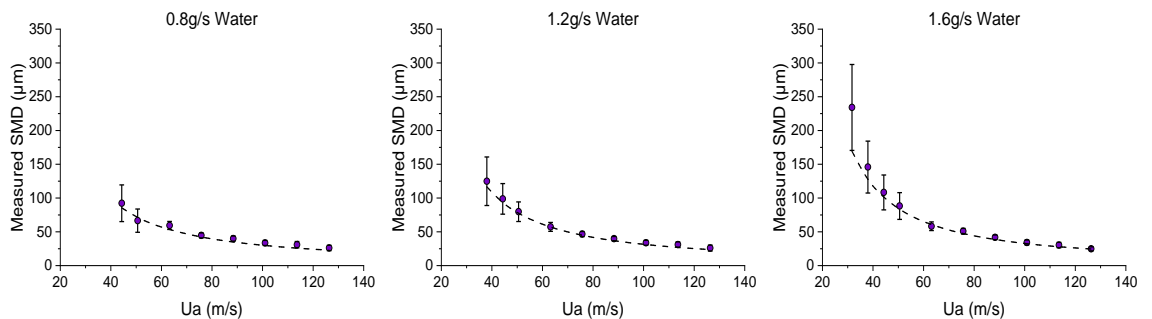


Figure 6-12 - Measured SMD values vs. derived correlation for all phase I atomisers

In **Figure 6-12**, the predicted SMD from developed correlation (**Equation 6-1**) is plotted against the empirically measured data from which it was derived.

As can be seen the prediction falls within experimental error bars across almost all points measured, including for atomiser I-A, which was not used in the optimisation of the correlation. R^2 values of 0.947, 0.954, 0.993 and 0.937 were determined for atomisers I-A, I-B, I-C, and I-D, respectively, yielding an average R^2 value across all atomisers of 0.958. Therefore, it can be surmised that atomisers of the same general family can be categorised using the developed correlation, assisting in an understanding of the impacts of different atomiser features, and hence informing the design process. It is noted that the derived correlation is less effective at predicting SMD values at lower flowrates, which is to be expected given the large standard deviations encountered for data at these conditions.

Given the demonstrated effectiveness of the derived correlation, it was subsequently used to estimate the atomisation quality at representative conditions used during operation of the Mk. I combustor (*Chapter 5*), with measured physical fuel properties. Predicted values are not expected to generate true values for the atomisers operating with aviation fuels under combustion conditions, but could offer some understanding as to the likely deviations across fuels and operating conditions. *Figure 6-13* shows the predicted SMD values across all fuels and pressures at condition C.

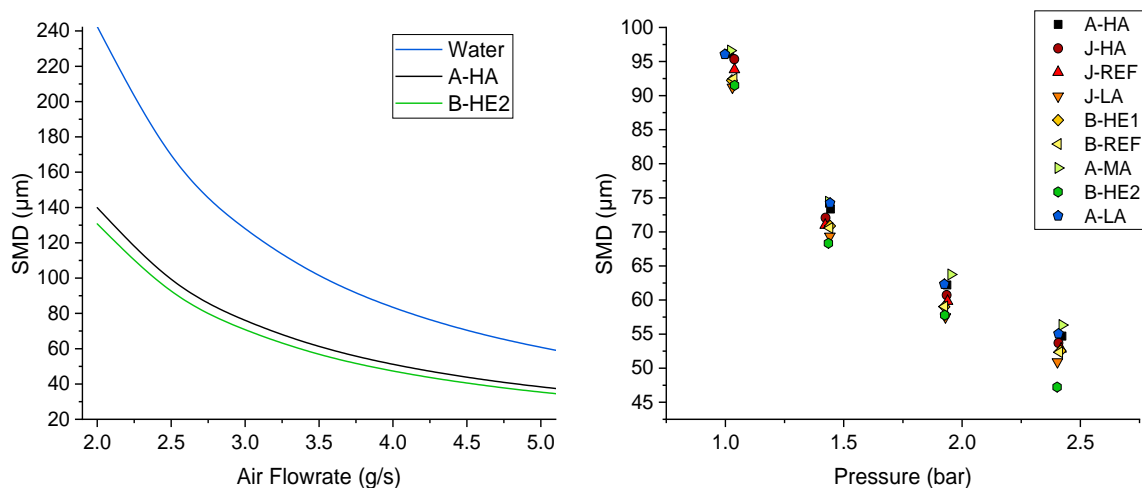


Figure 6-13 - (Left) variation in predicted SMD values across test fuels for 1.62 g/s liquid flowrate and unheated air using derived correlation. (Right) predicted SMD values across fuels at for the Mk. I combustor at condition C.

The correlation predicts that, within the expected range of flowrates comparable to emissions testing, a reduction in SMD values of ~40% may be expected for aviation fuels compared to water. As a result of fuel physical properties, it is predicted that A-HA and A-MA produce the poorest atomisation

quality, while B-HE2 would produce the finest, with expected variability across fuels estimated as ~7%. The observations for A-HA and B-HE2 agree with the simple correlation given in **Section 5.2.2**. However, the fact that fuel A-MA often exhibits the highest SMD values, indicates that the derived correlation attributes a larger weighting to fuel viscosity, for which this fuel exhibited the highest value out of the fuels used during Mk. I experimentation. The reliability of these predictions will be explored in subsequent experimentation.

When factoring in the known operating parameters used during the Mk. I experimentation at condition C, including air preheat temperatures, fuel properties, and subtle variations in flowrates recorded by the mass flow controllers, expected variability in SMD values derived using this correlation is in the range of 5-6 μm , which equates to a percentage variability of 5.7-10.3%. An exception is observed at the 2.4 bar ambient pressure case, which experienced a larger variation of ~9 μm (17.6%), found to be a result of a slightly higher average air mass flowrate witnessed during the B-HE2 testing, and demonstrating a known cause of day-to-day variability during experimentation. Across the Mk. I campaign, SMD values are predicted to have ranged between 40-90 μm , generally in agreement with recommended range of 40-80 μm for aviation combustors [117]. It is predicted that the three SAFs generally produced the highest SMD values, while the blended fuels generally produced the smallest values.

It is noted that SMD values are predicted to decrease with increasing combustor pressure, despite the fact that air velocities are anticipated to have remained constant across pressures due to the pressure scaling approach used in designing the experiment. The reduction comes as a result of the increased density of air at pressure, resulting in a higher We number and greater aerodynamic forces applied to the fuel during atomisation. As such it is predicted that atomisation improves with pressure provided all other variables are held constant, due to an increase in aerodynamic forces acting on the droplets. Therefore, it stands to reason that combustion at lower ambient pressures would be more susceptible to instabilities and potentially erratic emission formation resulting from poor spray quality.

6.3. Mk. II Combustion Liner

6.3.1. Design Considerations

From the above characterisation of the phase I atomisers, atomiser I-C was chosen as the most suitable for use in future emissions testing, since the atomiser had been shown to maintain similar pressure drop characteristics to atomiser I-D but exhibited slightly improved atomisation performance, especially at low air flowrates. The atomiser was accompanied by a second combustion liner design of similar scale to the Mk. I combustor (85 mm internal diameter) with modifications intended to improve performance. The most significant difference between the Mk. I and Mk. II combustors was the design of the frontal cooling holes, which were replaced for the Mk. II burner with a separate air supply being delivered via five ¼" diameter Swagelok unions set into the front section of the combustion liner. The five air streams fed a plenum before entering the main combustion region through a custom designed and manufactured transply dome. The independent control of both atomisation air and cooling air allowed for adjustments to atomisation quality and turbulence without impacting primary AFR, achieved by adjusting the ratio of cooling air to atomisation air while keeping the overall air supplied constant. The length of the transply dome used for the Mk. II burner was curved, extending 12.14 mm into the combustor and with an annular radius of 25.0 mm. The angle was estimated as $\sim 64^\circ$ from trigonometry.

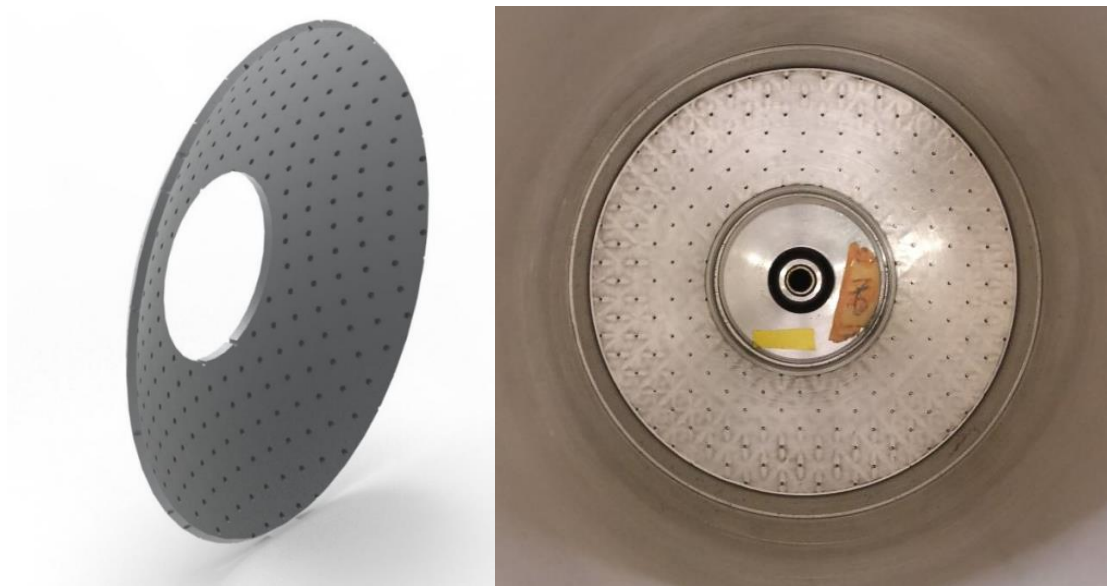


Figure 6-14 - Transply cooling dome

Additional modifications were based on the empirical equations for design of central recirculation zone in a combustor based on the “Magic Circles” concept [16], [49]. This assumes that the recirculation zone is encompassed by two vertically stacked circles placed within the combustion liner with diameters equal to half that of the combustion liner diameter, as shown in **Figure 6-15**. The recommended location for the ignitor downstream of the atomiser exit (L_{ig}) is at the centre of the magic circles. The quench holes are positioned further downstream at the end of the recirculation zone (L_{rc}). Calculation for L_{ig} and L_{rc} are given by **Equations 6-2** and **6-3**, respectively.

$$L_{ig} = \frac{D_{ft}}{4} \left[1 + \cot\left(\frac{180 - \theta_{dome}}{2}\right) \right] + L_{dome} - \frac{D_{ft}}{4} \quad 6-2$$

$$L_{rc} = L_{ig} + \frac{D_{ft}}{4} \quad 6-3$$

Using these calculations, the recommended value of L_{ig} was found to be 25.44 mm, and the expected value of the L_{rc} was 46.69 mm. As such, the ignitor and quench hole locations were positioned at 30 mm and 50 mm downstream respectively, approximately satisfying these values with a 5 mm allowance. The ignitor itself was held using a movable collar, held within a small circular chamber attached to the outside of the combustion liner, to allow for thermal expansion of the liner without adding a transverse load onto the ignitor, which was securely bolted to the liner wall. This was included due to observations in the prior test campaign that the ignitor hole warped over successive thermal cycles due to expansion of the liner. The chamber was sized so as to accommodate the anticipated thermal expansion of the collar, ensuring the part would not seize during operation.

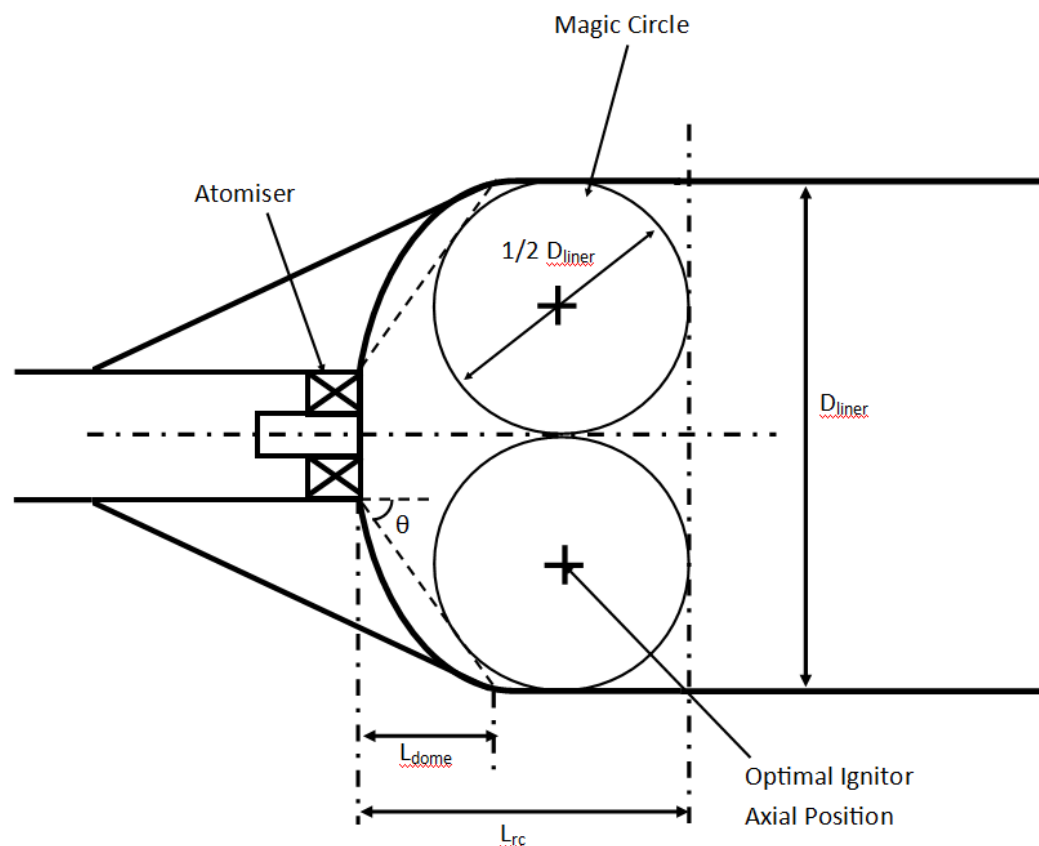


Figure 6-15 - The “magic circles” design concept [49]

Li *et al.* [52] explains that the lengths of the quench and lean zones in a combustor are sized for a compromise between high combustion efficiency and Nox reductions. Longer zone lengths result in higher residence times, which help to improve combustion efficiencies, but also typically result in higher NOx emissions. In conventional combustors, the secondary zone is recommended to be sized as a ratio of the liner diameter, given as 0.5-1. As such, the length of the quench zone was sized to 40 mm (~0.5 times the liner diameter), favouring NOx reductions, while the dilution zone was 80 mm, allowing sufficient residence time to promote complete combustion in the leaner (cooler) dilution regions.

6.3.2. Flow Partitioning

Successful application of the RQL concept relies on correct partitioning of air to the different sections of the combustor, so as to achieve the desired equivalence ratios highlighted in **Section 1.3.1**. Equivalence ratios were calculated by allocating air inputs to the three main combustion regions and assuming perfect mixing between fuel and air, and using a standard value of 14.7 as the stoichiometric AFR of a Jet A-1 fuel. The locations of the three combustion

zones are shown in **Figure 6-16**. The rich zone (RZ) was considered to extend from the atomiser exit plane to the quench air holes, with an equivalence ratio calculated using the primary air and cooling air supplies. Calculations for the Quench zone (QZ) included the area of the quench air holes (A_Q) and secondary cooling holes (A_{c2}). The remaining area (A_D , A_{c3} , A_{c4}) was used to calculate the equivalence ratio of the lean zone (LZ), equal to the global equivalence ratio. Partitioning of air through the combustion liner was estimated on the assumption that the ratio of secondary air passing through each hole would be equal to the ratio of the area of the hole relative to the total area of all air holes in the combustion liner. This is shown in **Equation 6-4**:

$$\dot{m}_i = \left(\frac{n_i A_i}{A_{total}} \right) \times \dot{m}_{total} \quad 6-4$$

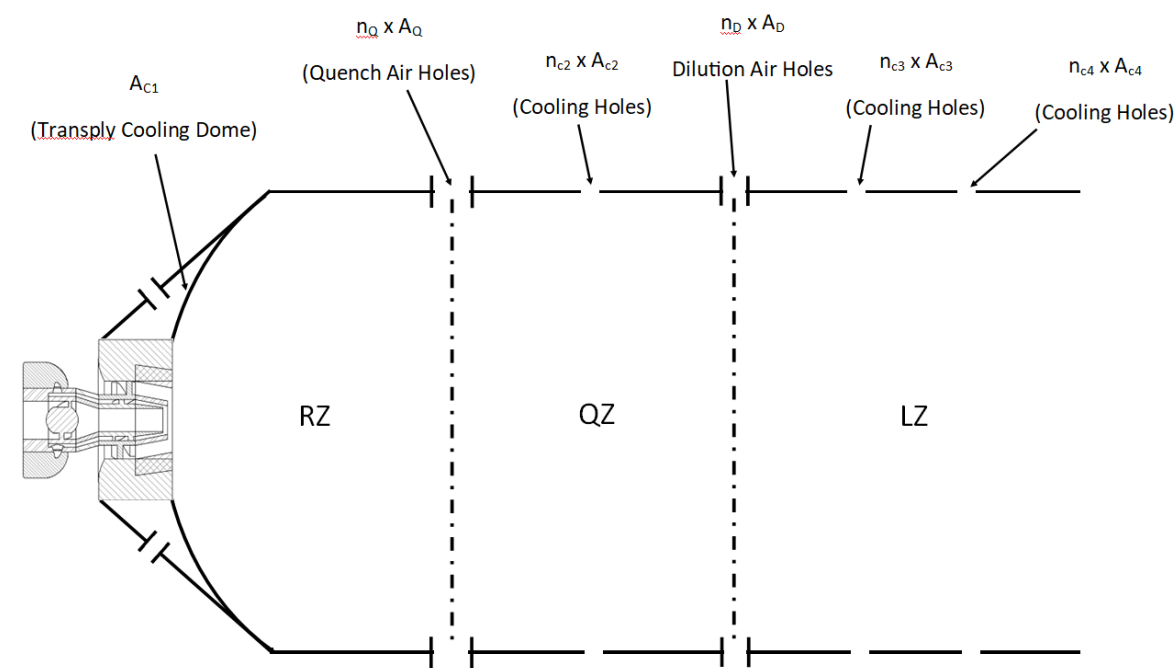


Figure 6-16 - RQL air partitioning

Using the flow partitioning equations outlined above, it was found that the primary zone of the combustor had been operating at equivalence ratios ranging from ~3.65 (condition C) to ~2.95 (condition B) during operation of the Mk. I combustor. This is considerably higher than recommended equivalence ratios for an RQL combustor outlined in **Section 1.3.2**, and likely to result in high nvPM formation. The quench zone equivalence ratio, which was calculated by considering the inputs of quench air and cooling air, was predicted to have operated at an equivalence ratio between 0.59-0.68, which was slightly leaner

than the recommended range for RQL combustors, and it was important to determine whether the quench flow was too strong so as to result in soot freezing. Overall, the decrease in equivalence ratio between the rich and quench zone was determined to be too high, and would need to be reduced to more suitable ranges.

The equivalence ratio of the primary zone could be easily controlled by the separate primary and cooling air flows. Li *et al.* [52] states that the conventional value for the sizing of the quench air holes is as a ratio to the main flow from the combustor dome, with a ratio of 2.5 typical of RQL combustors and 0.25 for conventional combustors. If the ratio is too high, then the product composition generated in the primary zone is likely to freeze, reducing overall combustion efficiency and worsening undesirable emissions. If the ratio is too low, then mixing at the quench zone will not be strong enough for successful implementation of the RQL concept. During operation of the Mk. I combustor, the predicted mass flowrate through the quench holes 2.10-2.51, with the highest value witnessed at condition E when secondary air was increased. These values suggest that the combustion holes were properly sized for the required combustion conditions, and that soot freezing would not have been significant. To prevent the quench zone from becoming too lean, the number of cooling at the quench zone was reduced from 36 to 24, while additional cooling holes were added further downstream at both locations in the lean zone, increasing from 24 to 32 in both cases. This would encourage more air to travel into the dilution zone as opposed to the quench zone, ensuring the quench zone equivalence ratio would not become too lean at the reduced primary zone equivalence ratio expected for subsequent experimentation, whilst also maintaining similar pressure drop characteristics to the Mk. I combustor at repeated secondary air flowrates, since summed flow area through the liners of each respective combustor would be approximately equal. A render of the Mk. II combustor, with the ignitor, atomiser, quench inserts, and cooling air inlets included, is shown in **Figure 6-17**.



Figure 6-17 - Render of the Mk. II combustor with atomiser placement

6.4. Mk. II Combustor Emissions Testing

6.4.1. Overview

The performance of the Mk. II combustor was subsequently explored during the H2020 Raptor experimental campaign. The flow partitioning correlations described above were used to determine operating conditions expected to give a leaner primary equivalence ratio. This was achieved by decreasing the baseline fuel flowrate at atmospheric conditions to 0.5 g/s, and tailoring the primary air and cooling air flows to maintain a primary equivalence ratio of $\sim 1.8-2.0$. This was still slightly richer than full-scale designs, ensuring sufficient nvPM was produced for measurements, but was much more comparable of typical RQL combustor operation. The ratio of primary air mass flowrates to cross flow is predicted as ranging between 1.4-1.6, which is below the value of 2.5 given by Li *et al.* [52], although well above the value of 0.25 given for conventional combustors. A wider range of operating pressures were chosen, so as to assess the performance of the combustor at power conditions more representative of real-world aircraft engines. Power conditions were then scaled at a constant 25 kW/bar, as was used for the Mk. I combustor. The final operating conditions used in the Mk. II testing are shown in **Table 6-2**.

Table 6-2 - Mk. II Combustor Operating Conditions

Condition	Pressure (bara)	Primary Air (g/s)	Cooling Air (g/s)	Secondary Air (g/s)	Fuel (g/s)	ϕ_{PZ}	ϕ_{QZ}	ϕ_{LZ} /Global
Rich	2.0	3.90	3.50	42.00	1.0	1.986	0.580	0.298
Lean	2.0	4.50	3.50	40.90	1.0	1.838	0.576	0.301
Rich	3.0	5.86	5.31	64.30	1.5	1.974	0.571	0.292
Lean	3.0	6.84	5.31	61.20	1.5	1.815	0.576	0.301
Rich	4.0	7.81	7.08	85.80	2.0	1.974	0.570	0.292
Lean	4.0	9.00	7.00	81.80	2.0	1.838	0.577	0.301
Rich	5.0	9.76	8.85	107.20	2.5	1.975	0.571	0.292
Lean	5.0	11.18	8.85	102.20	2.5	1.835	0.577	0.301

As before, a range of fuels of different manufacturing origins and fuel properties were used. Included in the test fuels was a different Jet A-1 fuel, previously used for the FLITES test campaign, and with a hydrogen content lower than that of J-REF. Also included was a near-zero aromatic FT-GTL fuel, and a blend of the two fuels, mixed as 75% vol. FT-GTL with 25% vol. FLITES Jet A-1. To provide a full range of hydrogen contents, these fuels were tested alongside A-HA, J-HA, and B-HE2. A-HA and J-HA were chosen to corroborate the unexpected nvPM emissions behaviour observed in **Section 5.3.1**. B-HE2 was chosen so as to include a higher hydrogen content fuel among repeated fuels, in addition to the fact that remaining supplies of this fuel were high. **Table 6-3** gives the fuel properties for the fuels used. Compositional data for the four new fuels was provided by Shell PLC, using data from GCxGC-FID measurements, as given in **Figure 6-18**. While the analysis method remains the same as was used for the previous fuel compositional data, some additional uncertainty is anticipated from the limits of reproducibility across laboratories.

Table 6-3 - General Fuel Properties of Mk. II Test Fuels

Fuel	Hydrogen Content (% wt.)	Total Aromatic Content (% wt.)	Di-Aromatic Content (% wt.)
Flites A1	13.427	24.24	1.07
A-HA	13.51	20.57	0.28
J-HA	13.649	22.75	2.18
B-HE2	14.514	12.82	0.14
75%GTL	14.895	6.71	0.38
100%GTL	15.47	0.06	0.00

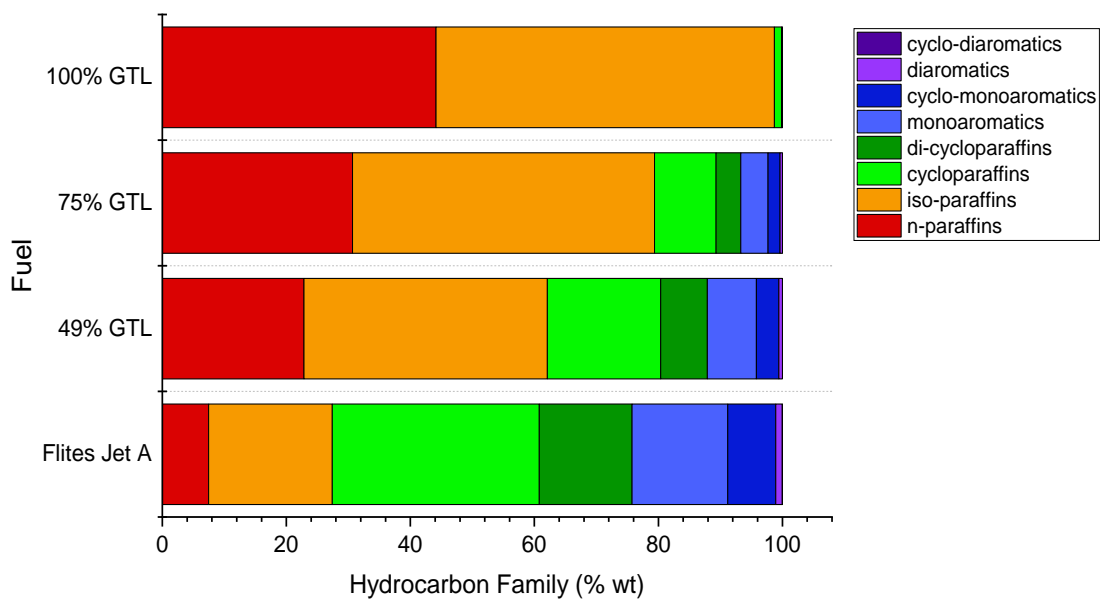


Figure 6-18 - GCxGC compositional data for additional test fuels

Using the correlation developed in **Section 6.2.3**, SMD values were estimated for the operating conditions used during this experiment. Data for fuel B-HE2 are provided in **Figure 6-19**. Other fuels are expected to yield similar values, with expected variability across fuels in the range calculated in **Section 6.2.3**. SMD values are predicted to range between 20-60 μm between the 2.0-5.0 bar pressure conditions, and so generally fall within the range of values recommended for RQL combustors. Values are predicted to fall below this range as pressure increases, but this is not anticipated to effect nvPM emissions, since large droplets are prevented.

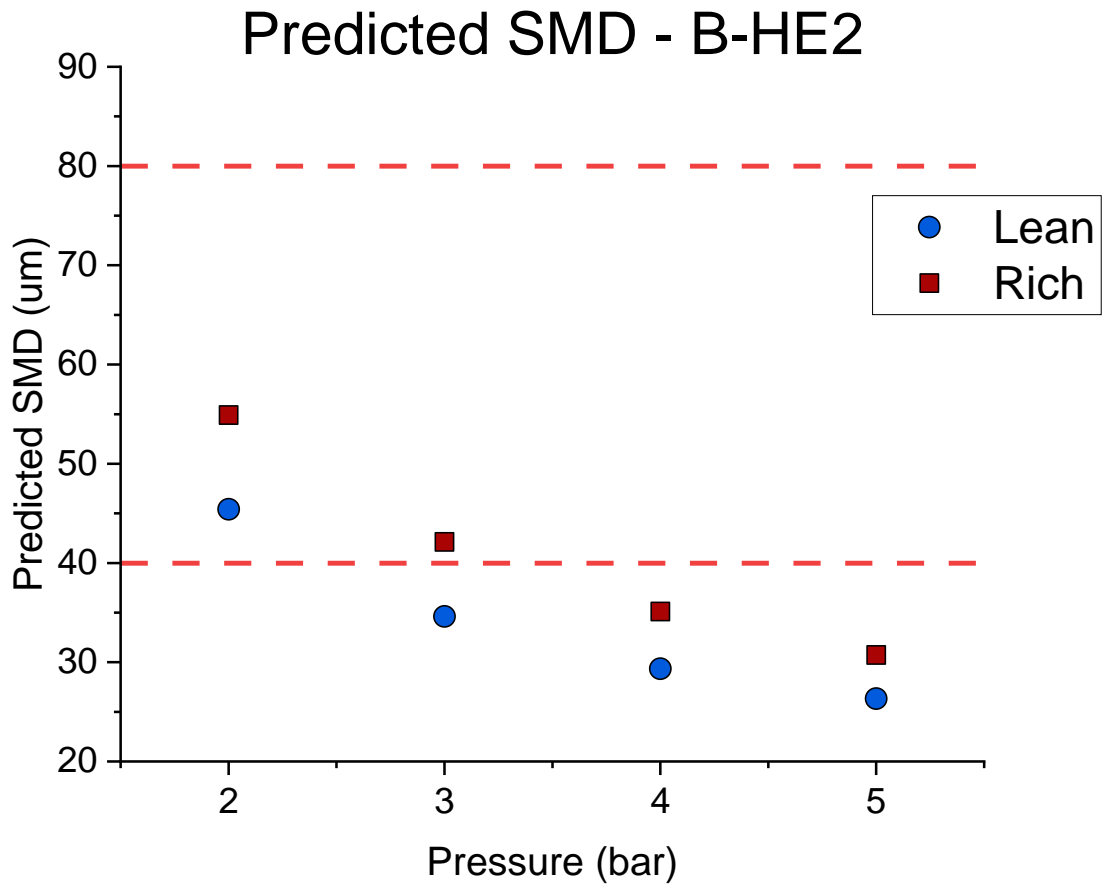


Figure 6-19 - Predicted SMD values for Mk. II combustor operating conditions (B-HE2)

6.4.2. Emissions Results

The Mk. II burner was successfully operated over the range of conditions specified, with the nvPM data shown in **Figure 6-20**. As before, the error bars included represent ± 2 standard deviations. The lean conditions typically produced lower E_{mass} and E_{number} values compared to the rich conditions, as expected from the global equivalence ratio being closer to stoichiometry. Increasing pressure generally increased nvPM E_{mass} emissions, until the operating pressure reached 5.0 bar, where reductions in E_{mass} compared to lower operating pressures were observed. E_{number} emissions appear relatively consistent across 2.0-4.0 bar pressures, but show significantly worsened scatter at the 5.0 bar for the GTL fuel.

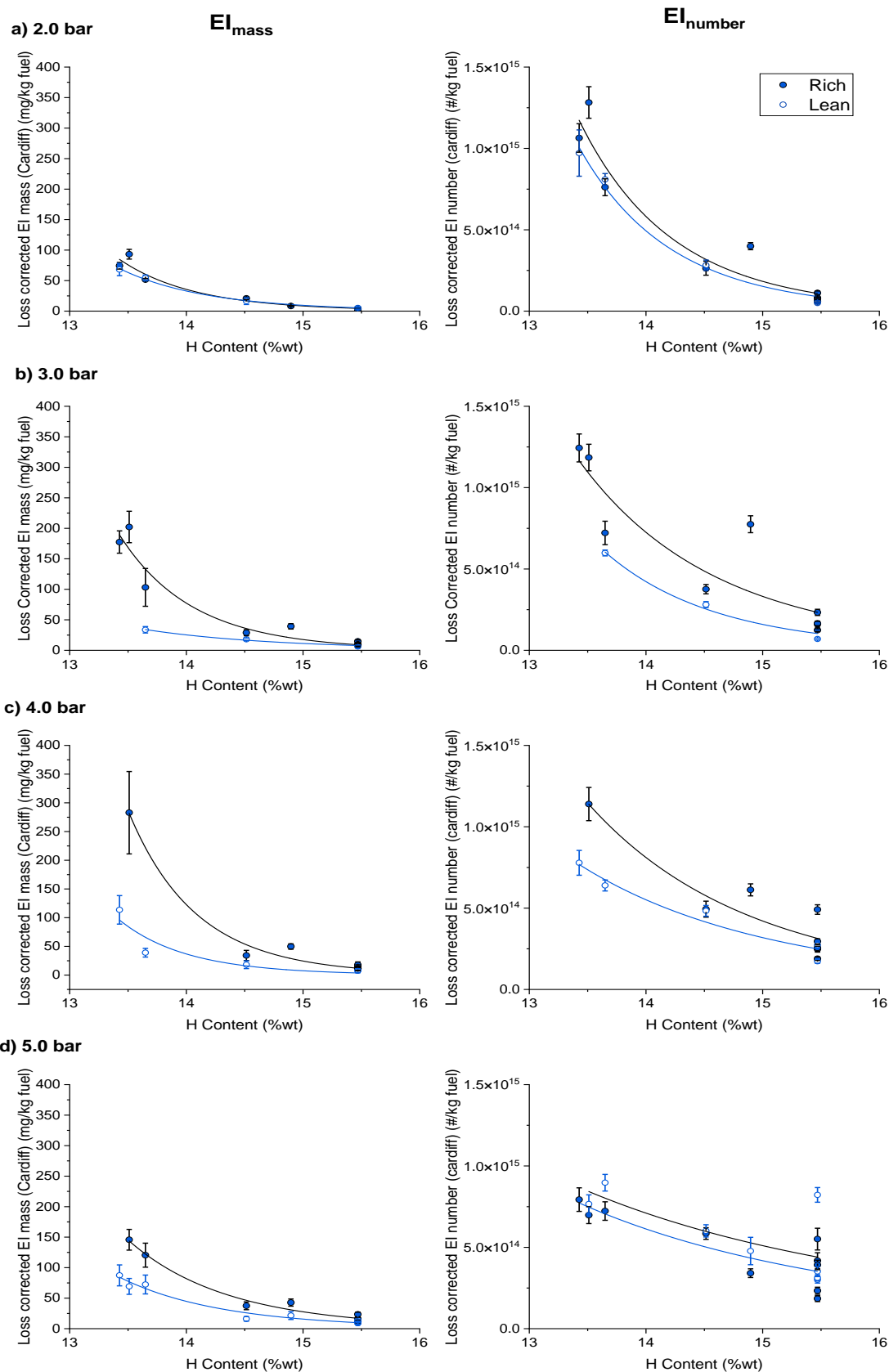


Figure 6-20 - Mk. II loss corrected nvPM emissions

This additional dataset provides further insight into the emission trends observed in *Chapter 5*. It was found that fuel A-HA generally produced higher quantities of nvPM across the study in comparison to J-HA, in contrast to

observations described in **Section 5.3.1**, with the two fuels now following the expected hydrogen content trendline. Therefore, the higher nvPM emissions witnessed for fuel J-HA during earlier testing are supported as a result of day-to-day variability. However, day-to-day variability was still observed for the current dataset, with several data points deviating from the hydrogen content trendline. At higher pressures, the GTL fuel demonstrates significant variability in EI_{number} , at times resulting in higher emissions than the lowest hydrogen content fuels. The 75% GTL fuel consistently produces higher nvPM emissions compared to fuel B-HE2, despite the former exhibiting the higher hydrogen content.

Gaseous data was again collected and processed using the SAE gas analysis tool. Calculated combustion efficiencies of the burner were comparable to those calculated for the Mk. I combustor, and were always above 99.8%. Slightly higher combustion efficiencies were determined during the lean condition, demonstrating that additional primary air over secondary air, resulting in a leaner primary zone, is beneficial to combustion. Small improvements in combustion efficiency (0.01-0.03%) are also observed for the higher hydrogen content fuels, attributed to the higher specific energies.

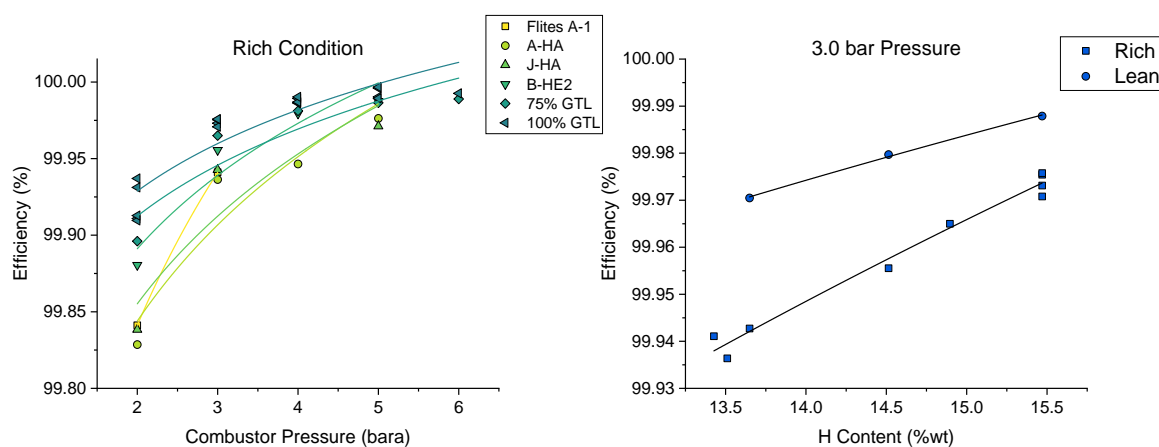


Figure 6-21 - Predicted combustion efficiency across fuels

An issue observed during experimentation was a bi-modal distribution in the measured nvPM PSD profile, as opposed to the expected mono-modal behaviour. This impacted a large number of datapoints across the study, but was also somewhat erratic. Because the behaviour impacted the accuracy of GMD values, particle sizes have not been included in the current dataset. It is possible that this behaviour was a feature of the atomiser, since a bi-modal behaviour had also been observed in the spray PSD for the atomiser used during laser diffraction

experiments (**Section 6.2.1**). However, it should be noted that the unheated water experiments are not representative of combustion conditions, and so it could not be concluded as to whether this behaviour was the cause of the observed PSD profiles.

A considerable deposit of nvPM was observed in the primary zone of the combustor, as shown in **Figure 6-22**. This is indicative of poor fuel and air distribution in the near atomiser region. Near the atomiser exit, it was consistently observed that deposits formed on one side of the combustor, while build ups further downstream tended to follow the direction of the outer air swirl (clockwise from the perspective of the image shown). It is suggested that the atomiser was operating below its optimum range of conditions, where low fuel flowrates prevented adequate prefilming behaviour in the atomiser, with the fuel instead pooling at the base of the fuel annulus due to the forces of gravity, before being entrained in the outer air flow.

Additionally, the higher operating pressures and powers compared to the previous JetSCREEN campaign were seen to impart significant thermal damage to the combustion liner. This caused a section of the liner to melt and ultimately lead to failure of the combustor at higher operating pressure conditions. A similar issue was observed by Mishra *et al.* [25], who attributed the thermal damage in the primary zone of a small representative aircraft engine liner to high spray cone angles produced by an airblast atomiser. Higher spray cone angles were associated with higher concentrations of soot in the primary zone, while also bringing the flame closer to the atomiser face and increasing thermal loading. It is possible that the cause of the aforementioned bi-modal PSD distribution was the presence of vaporised metal particles present in the exhaust due to the thermal damage, since metal particles are non-volatile, and would be able to pass through the catalytic stripper and to the detection modules in the EUR reference system. Since thermal loading would be greater at higher pressures, the reduction in nvPM observed at the 5.0 bar pressure may have been a result of additional air entering the liner through the damaged region of the liner, serving to increase the global AFR of the combustor and reduce nvPM measured.



Figure 6-22 - Primary zone nvPM buildup (left) and thermal damage to the liner (right)

6.5. Chapter Summary

The phase I atomisers were characterised through laser diffraction experimentation. It was found that SMD values plotted against predicted air velocity (U_a) converged to a global trend. Regression analysis was used to determine an optimised correlation for generated SMD values from data collected during experimentation, using several generic forms of empirical equations from the literature. It was found that a tuned correlation suggested by El-Shanawany *et al.* [129] resulted in the best quality of fit with the measured data, providing a correlation describing the atomisation trends across all of the phase I atomisers. This correlation was subsequently used to predict the expected variability in SMD values produced by fuel sprays used in the earlier testing of the Mk. I combustor as a result of fuel physical properties. The trend suggests that typical variation across the fuels tested previously would be ~7%.

A Mk. II RQL combustor was developed using empirical methods. Perceived operating issues with the Mk. I combustor were identified, helping to tune the operating conditions for a subsequent test campaign using the Mk. II combustor, which was operated at more representative local and global AFRs using a range of aviation fuels. An additional nvPM emissions dataset was produced, with several of the fuels used during earlier experimentation with the Mk. I combustor being retested, helping to validate the emissions results observed. Hydrogen content

trends again demonstrated strong correlations with measured emissions, although deviations in results were again observed throughout testing. It was proposed that these were likely caused by day-to-day variability, which resulted in repeated bias across test conditions and pressures, highlighting the subtlety of nvPM formation mechanisms (compared with other regulated gaseous species). Gaseous data was used to confirm that combustion efficiency was again representative of real-world combustors, and of a similar magnitude to that of the Mk. I burner. It was also noted that combustion efficiencies are improved by the use of high hydrogen content fuels as a result of higher specific energies. Issues with operation of the combustor believed to stem from atomisation/primary zone characteristics were highlighted, so as to inform future design and operation of the combustor.

7. Further Investigation of Airblast Atomiser Sprays (Mk. II-A Combustor)

7.1. Overview

During the previous chapter, a correlation was developed for the atomisers for the purposes of design refinement and predicting atomisation quality expected during combustion tests. However, given that the data was derived from benchmarking experiments using water, only modelled atomisation quality could be attained for the aviation fuels used during emissions experimentation. Additionally, it is known that spray properties other than droplet sizes may impact emissions, most notably spray cone angle, which acts as a measure of fuel and air distribution in the spray. In order to further examine the impacts of atomisation quality on the nvPM formed in the RQL combustor, it was decided that a more in-depth investigation of the atomiser spray characteristics should be undertaken. The high nvPM loading and asymmetrical deposit of nvPM observed in the primary zone of the Mk. II combustor were suggestive of atomisation characteristics affecting primary combustion. At this point in time the phase II atomisers had been developed, and so further experimentation could be used as validation of their suitability for use in the RQL combustor and impact on emissions.

To compliment the global atomisation trends established by laser diffraction experimentation, HSI and PDA experimentation were undertaken to explore the spatial variations in spray quality across atomiser designs using the experimental setups associated with the bespoke GTRC spray chamber described previously in **Sections 3.7** and **3.8**. Towards better understanding of fluid properties on droplet sizes, spray experimentation across the previously tested conventional fuels and SAF was undertaken. Results could be used to assess the earlier modelled impact of fuel composition on SMD. Finally, additional emissions experimentation was undertaken using the Mk. II combustor operating with a phase II atomiser, during which time the impact of predicted atomisation quality on nvPM emissions was assessed.

7.2. HSI Experimentation

7.2.1. Water Results

Examination of the spray profiles across atomisers was undertaken using the HSI setup outlined in **Section 3.7.1**. Initial water tests were undertaken for phase I and phase II atomisers, over a range of air mass flowrates (1.5-6.0 g/s), and fuel flowrates (1.1-2.2 g/s) covering the range of typical AFRs used during Mk. I and Mk. II testing. The aforementioned operating issues highlighted for atomisers I-A and I-C, resulted in these atomisers not being included in the test matrix. Similarly, imperfections in the AM process resulting in a partially blocked fuel channel, which could not be cleared, meant atomiser II-A was also not included. After extensive pre-test set-up and assessment, a frame rate of 3000 fps and a shutter speed of 1/30000 s was determined for the HSI camera, which was thought to offer sufficient data and image clarity, resulting in a collection time of 0.667 s for 2000 images. Throughout experimentation, pressure drop values were recorded in the same way as during laser diffraction experiments. The location of the pressure tap was moved between two different positions during initial trial runs: one in the same location as during laser diffraction experiments (**Section 3.6.3**), and one further upstream. Near identical readings were recorded with varying air mass flowrate, confirming that the location of the pressure tap did not impact reported pressure losses, as would be expected due to the minimal pressure drop expected between these two locations. Measured values of pressure drop are shown in **Figure 7-1**.

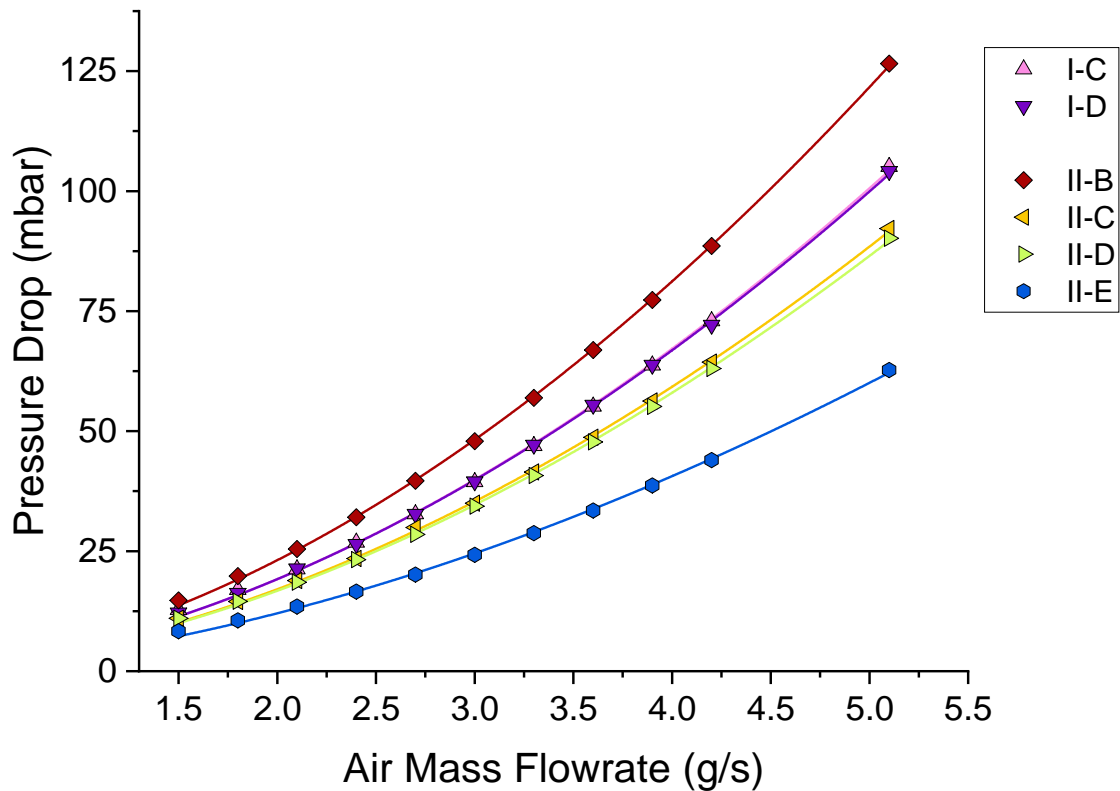

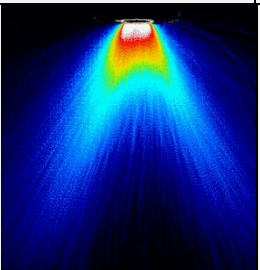
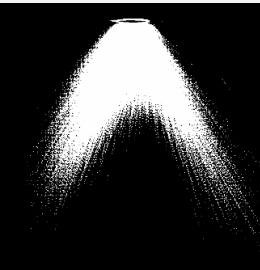
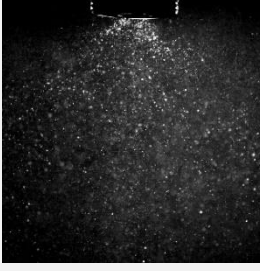
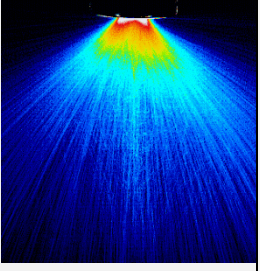
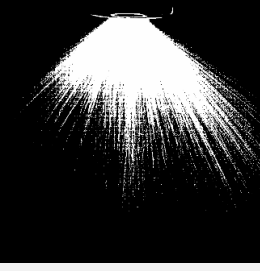

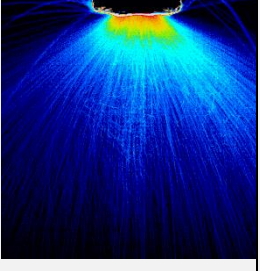


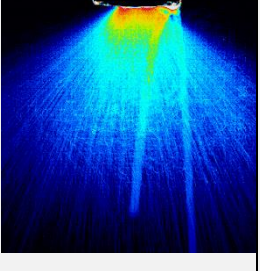
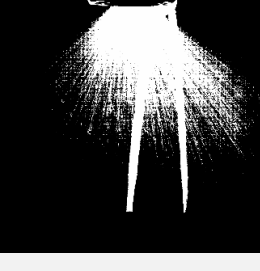
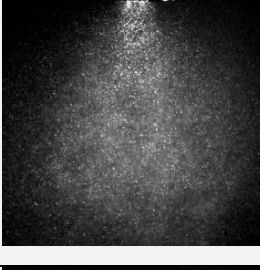
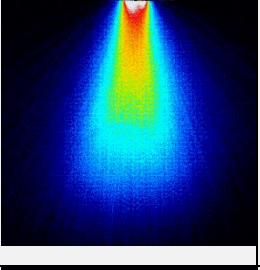
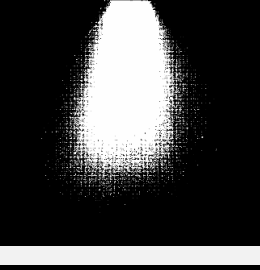
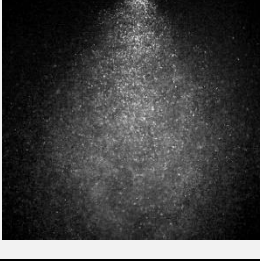
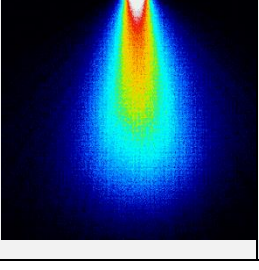
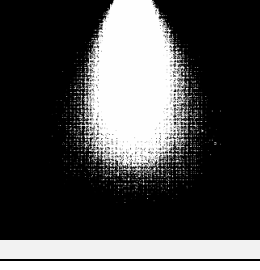


Figure 7-1 - Measured pressure drops for the phase II atomisers

Atomiser II-B exhibits a higher pressure drop trend compared to the phase I atomisers, which is attributed to the slightly thicker blades it incorporates, leading to increased blockage in the air paths. This was a design choice made to accommodate the new manufacturing orientation. It is also noted that the blade were longer, which may have contributed to increased losses due to additional surface area against which kinetic energy could dissipate from frictional forces. The perceived improvements in swirl geometry resulted in improvements in pressure drop values across the other atomiser designs tested. Atomiser II-E exhibits greatly reduced pressure losses in comparison to atomiser II-D, demonstrating the effectiveness of using curved blades over straight blades.

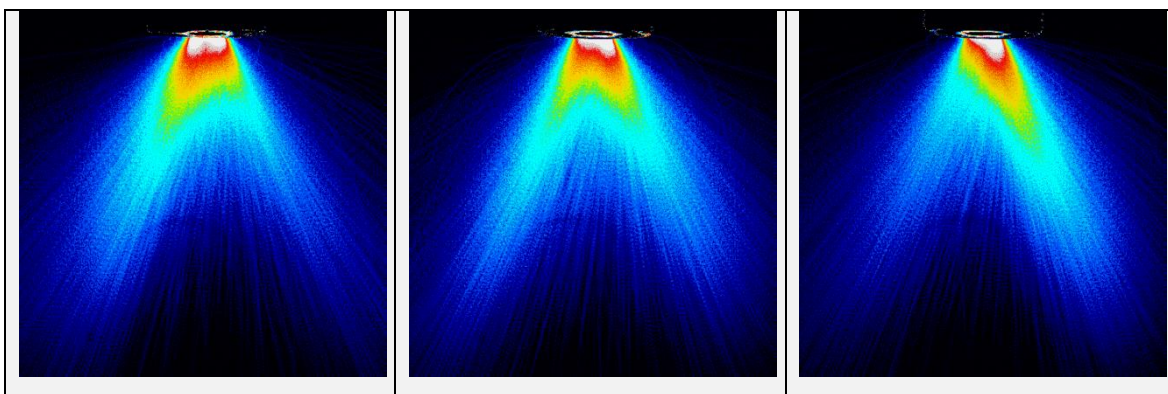
The recorded images were processed according to the method outlined in **Section 3.7.2**. A comparison between the atomisers operating with water is shown in **Table 7-1**. Atomisers are shown operating at a matched pressure drop of ~40 mbar (4% pressure ratio at atmospheric pressure), with a fuel flowrate of ~1.62 g/s, representative of Mk. I data at 1.9 bar and laser diffraction data taken at the same flowrate.

Table 7-1 - Variability in spray structure across atomisers (all atomisers operating with 1.62 g/s water flowrate)

Atomiser	Air (g/s)	dP (mbar)	Single Frame	Standard Deviation Plotted	Standard deviation + Thresholding
I-C	3.00	39.72			
I-D	3.00	40.34			
II-B	2.70	39.65			
II-C	3.30	41.48			
II-D	3.30	40.50			
II-E	3.90	38.73			

The spray structure is seen to vary significantly across atomisers. Atomiser I-C produces the expected hollow cone structure, with an increasingly low volume of droplets near the central axis with increasing distance from the atomiser exit. At the condition shown, this atomiser exhibits an asymmetrical cone structure in which a larger number of droplets were present in a narrow region to one side of the cone, observed as brighter regions in the collected images. This is undesirable, resulting in inconsistent fuel and air distribution and poorer mixing in combustion contexts, potentially leading to higher soot formation. To examine this asymmetry further, the atomiser was rotated in 45-degree increments, up to 90 degrees. **Table 7-2** shows the variation in atomisation behaviour for atomiser I-C at a fixed operating condition of 3.0 g/s of air and 1.37 g/s water.

Table 7-2 - Atomiser I-C (Mk. II Combustor) operating at A3.00 F1.37 rotated in 45-degree increments



As the atomiser is rotated, the region containing the higher quantity of droplets also appears to rotate to the opposite side of the spray. Visual analysis of the image stack did not indicate any large breakaway clusters of droplets causing this asymmetry. Instead, the asymmetry appears to have been as a result of either manufacturing defects caused by the tolerances involved in the AM process, or else poor interaction between the water and the air in the atomiser near region due to a the large prefilmer thickness. In combustion contexts, this asymmetry could be responsible in worsened distribution of fuel during operation, and higher incidences of localised rich regions, and was potentially responsible for the build-up of soot in the combustor observed during operation of the Mk. II combustor.

Atomisers I-D, II-B, and II-C exhibited much wider cone angles compared to the other atomisers tested. It was found that this was a shared instability across

atomisers, in which expanding inner air appeared to overpower the stabilising forces of the outer air, causing the spray cone to collapse outwards. In some cases, this caused a large portion of spray to collect on the atomiser face. The breakdown in conical structure appears to establish a narrow recirculation zone in the near vicinity of the atomiser, causing air flows to travel above the atomiser exit plane. A number of droplets were seen to become entrained in these air flows, and are subsequently carried upwards against the forces of gravity behind the atomiser exit plane, observed most clearly in the case of atomiser II-B, as shown in **Figure 7-2**. It is hypothesised that this behaviour was caused by the exit axial velocity of the outer air channel being too low, and exerting too weak an aerodynamic forces to effectively establish a conical spray. This was reasoned by the fact that modifications made to the point in which the instability was observed had served to reduce the outer air axial velocity, including increasing the outer air swirl and widening the outer air channel. It is also possible that blade stalling was associated with the behaviour, since the outer air channels utilised high blade angles, resulting in a high swirl number, but this cannot be confirmed at this time.

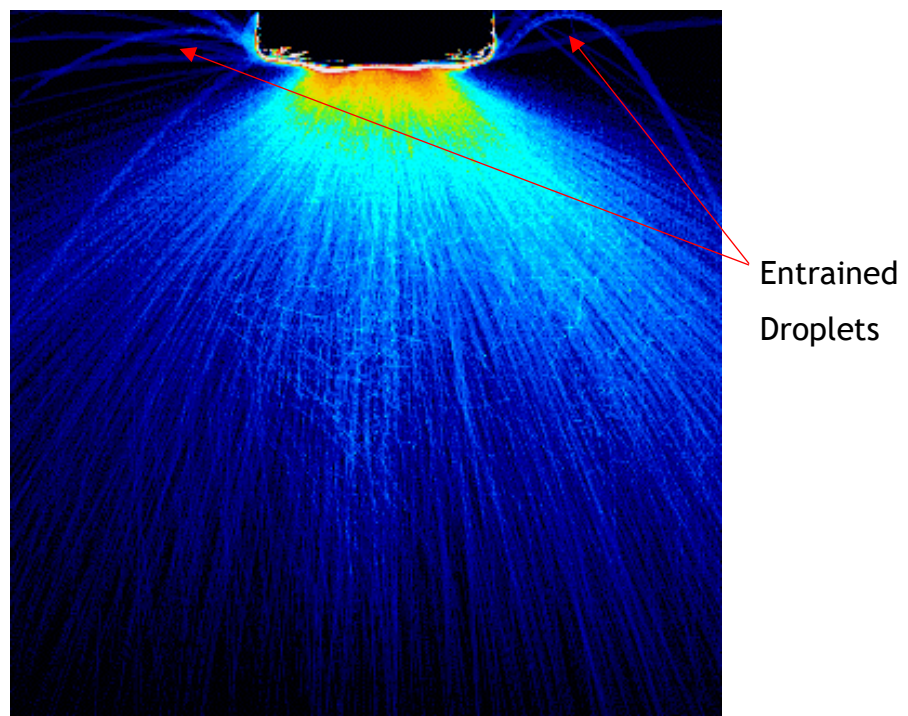


Figure 7-2 - Atomiser II-B exhibiting the collapse in spray cone

For the case of atomiser I-D, it is found that the breakdown in conical spray structure was not an inherent feature of the atomisers across all operating conditions. When operating with water at increasing flowrates, a point was reached where the spray appeared to “snap” forward, exhibiting the conical spray

structure produced by atomiser I-C. At higher flowrates of water, it was found that this transition was achieved at lower air flowrates. It was later found that the instability could also be resolved at lower flowrates by temporarily blocking the inner air channel, while application of a small amount of back pressure into the atomiser flow field would cause the spray to collapse again. **Figure 7-3** shows an example of the instability resolving for atomiser I-D across a relatively small increase in atomisation air.

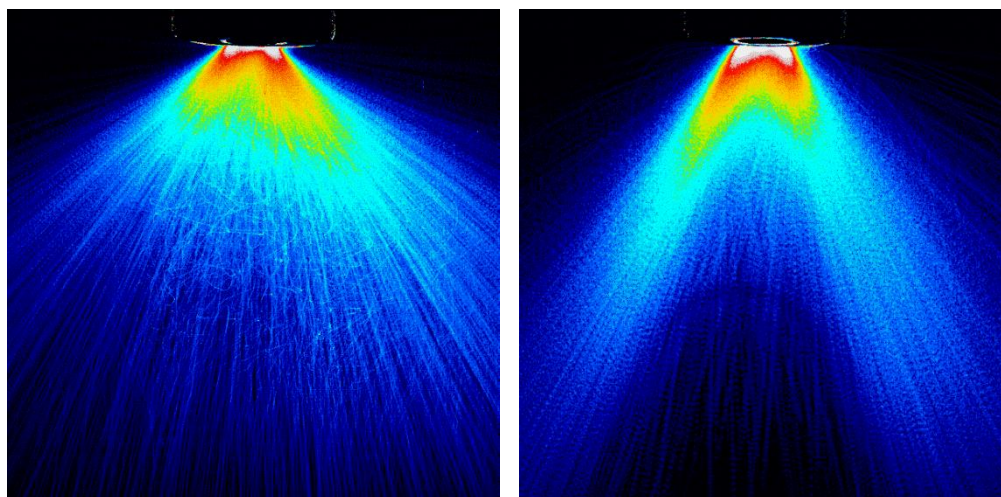


Figure 7-3 - Atomiser I-D operating at 1.6 g/s water with 3.30 g/s air (left) and 3.60 g/s air (right). The instability is resolved at 3.60 g/s air.

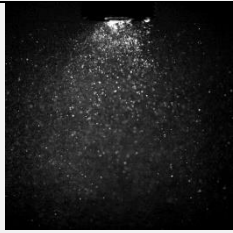
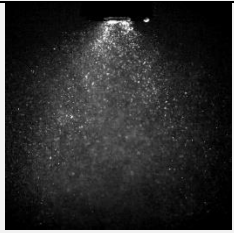
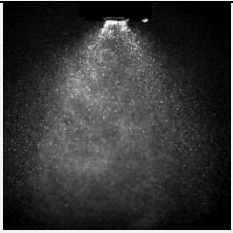
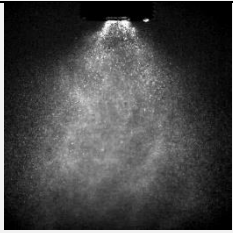
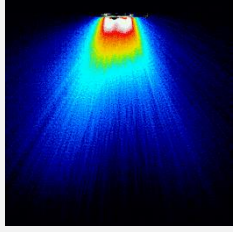
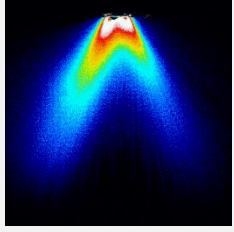
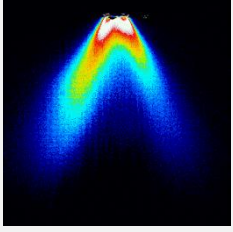
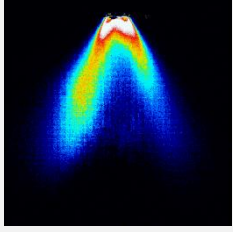

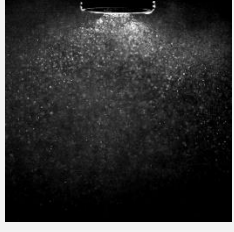

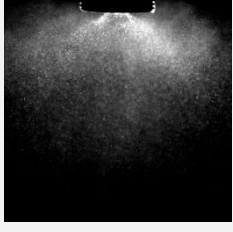
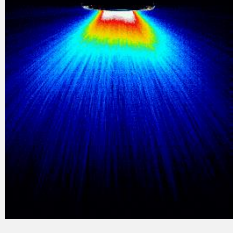
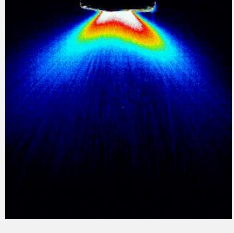
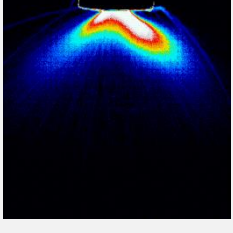
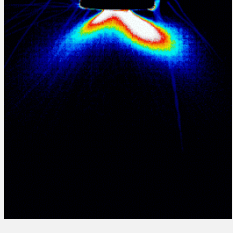
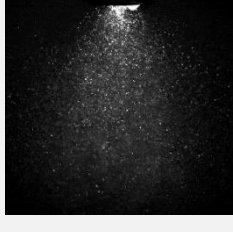
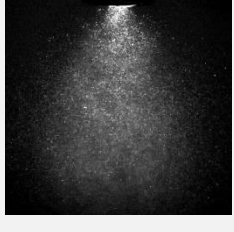
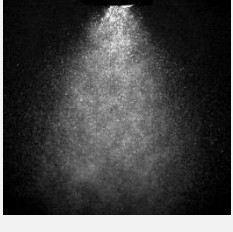
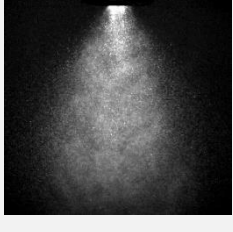
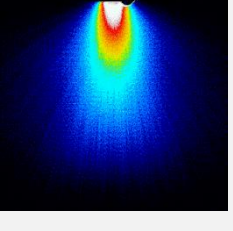
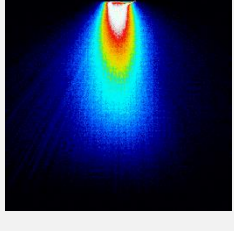
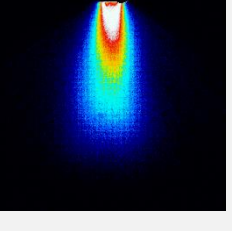
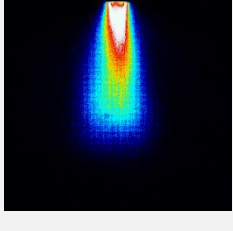
The instability was not present for Atomisers II-D and II-E, for which the inner air flow paths were widened, and the angle of inclination of the outer air orifice was increased, directing air towards the spray. These atomisers were instead observed to produce a narrow, ordered conical spray. The ordered structure of atomisers II-D and II-E is considered desirable over the chaotic structure observed for atomisers I-D, II-B, and II-C. However it is noted that the narrow cone would be expected to lead to a locally richer central region in comparison to atomisers producing wider spray cones, potentially leading to worsened emissions of CO, UHC, and nvPM. It is recommended that any future iterations of the atomiser look to slightly reduce the outer air swirler angles and angle of inclination to tailor the desired spray shape.

7.2.2. Jet A-1 Results

Subsequent imaging was undertaken using the Flites Jet A-1 fuel. For these tests, a frame rate of 1500 fps and a shutter speed of 1/40000 s were employed, extending the collection time to 1.333 s. The longer collection time was utilised

to reduce sample uncertainties due to random fluctuations in the spray affecting visualisation across the short sample time, which had been observed during water tests. Because of time constraints, Jet A-1 tests were not undertaken for the full range of atomisers, but only for the atomisers of most interest, namely, I-C, I-D, and II-E. **Table 7-3** shows the three atomisers operated across multiple air flowrates with Jet A-1.

Table 7-3 - Variability across atomisers operating with Flites Jet A-1 at 1.62 g/s fuel flowrate

Air (g/s)	1.80	2.40	3.00	3.60
Fuel (g/s)	1.62	1.62	1.62	1.62
ALR	1.11	1.48	1.85	2.22
Atomiser I-C (Mk. II Combustor)				
				
Atomiser I-D (Mk. I Combustor)				
				
Atomiser II-E				
				

As with water experiments, atomiser I-D exhibited the collapse in hollow cone shape, with the majority of droplets found in the upper half of the 100x100 mm measurement region. Unlike with water tests, the instability did not resolve

at higher flowrates and was observed across all air conditions tested. This indicates that the instability is likely a feature of the air flow pattern, but could also imply that the physical properties of water, namely the higher surface tension, served to resist atomisation and helped to stabilise the spray. It is unknown whether the instability propagated through to combustion testing, where additional flows and higher temperatures imparted additional aerodynamic forces on the atomiser flow field. Although atomiser I-D was successfully operated in combustion tests (*Chapter 5*), the instability is viewed as highly undesirable, and expected to result in high soot loading in the primary zone. In addition to concerns that the propagation of fuel droplets behind the atomiser exit plane could result in soot build-ups in the upstream regions of the combustor, leading to blockages around the cooling air inlets. The unstable nature of the instability would also introduce uncertainty into the RQL rig, potentially causing some of the day-to-day variability encountered. As such, it was concluded that the atomisers exhibiting this behaviour should not be used for further experimentation.

Atomisers I-C and I-E produced better defined cone shapes. Atomiser I-C maintains the wide hollow cone shape observed in the previous water tests, with the asymmetry previously observed again visible. Atomiser II-E produces a narrower but more uniform cone shape, with a higher number of droplets observed in the central region of the spray. *Table 7-4* shows the measured cone angles (θ_c) across the atomisers.

Table 7-4 - Measured Spray Cone Angles

	Air Flowrate (g/s)	Atomiser I-C			Atomiser I-D			Atomiser II-E		
		Left Half Angle (°)	Right Half Angle (°)	Cone Angle (θ_c , °)	Left Half Angle (°)	Right Half Angle (°)	Cone Angle (θ_c , °)	Left Half Angle (°)	Right Half Angle (°)	Cone Angle (θ_c , °)
Water	1.8	45.00	41.38	86.38	55.96	57.4	113.36	27.12	30.34	57.46
	2.4	32.98	30.96	63.94	49.23	52.2	101.43	29.13	29.74	58.87
	3.0	33.45	31.53	64.98	47.76	48.78	96.54	21.96	22.52	44.48
	3.6	34.6	30.43	65.03	36.31	34.09	70.40	22.98	28.22	51.20
Jet A-1	1.8	52.37	53.00	105.37	60.95	59.42	120.37	34.36	35.86	70.22
	2.4	43.36	33.26	76.62	58.92	59.3	118.22	33.47	39.73	73.20
	3.0	40.56	32.62	73.18	57.51	62	119.51	31.79	33.96	65.75
	3.6	39.31	33.58	72.89	59.28	57.8	117.08	28.97	27.81	56.78

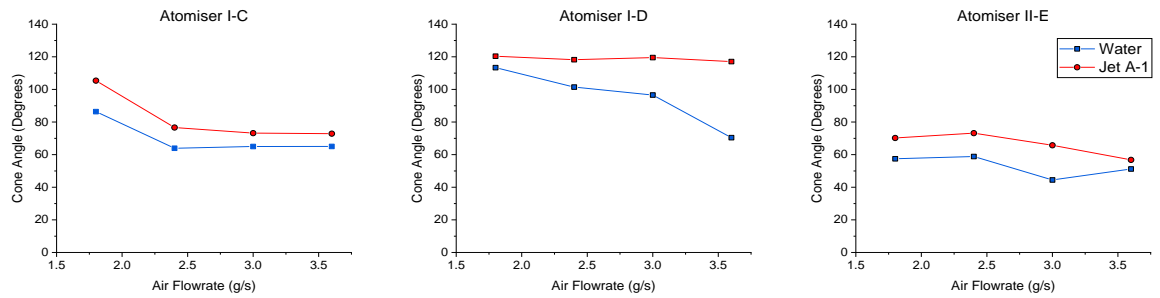


Figure 7-4 - Measured spray cone angles

For atomisers I-C and II-E, it is seen that cone angles tend to decrease with increasing air mass flowrate, in agreement with past studies [117], [131]. Wider cone angles are observed for Jet A-1 sprays compared to water sprays, as was also observed by Tareq *et al.* [117]. For atomiser I-C, the cone angle rapidly decreases between the 1.8 g/s and 2.4 g/s conditions, indicative of the very poor atomisation observed at low flowrates. For atomiser I-D, the transition to an ordered spray structure at higher flowrates was not achieved when using Jet A-1 as the test fuel within the operating conditions studied. It is suggested that the reason for which this transition was observed for water, but not Jet A-1, was as a result of the narrower cone angles produced by water sprays. Increasing air flowrate caused an additional narrowing of the cone, eventually resulting in a point where the aerodynamic stabilising forces acting on the spray were enough to encourage a more structured cone shape. Atomiser II-E exhibits slightly reduced cone angles compared to atomiser I-C, and maintains similar cone angles across operation. The atomiser therefore appears to be better suited for lower operating conditions. It was decided that the narrower cone angle may allow for a reduction of nvPM build up in the combustor primary zone. Because of this and the favourable pressure drop characteristics, this atomiser was chosen for subsequent experimentation.

Initial impressions of the sprays were that water sprays were wider than the Jet A-1 sprays, and it was only after thresholding that the wider cone angles were obtained for Jet A-1 sprays. The reason for this appears to be that water sprays are more prone to larger droplets propagating to the outer regions of the spray, causing a looser spray appearing to be wider in the downstream regions. The thresholding step helped to remove the majority of loose droplets and isolate the edges of the spray, yielding the result given. It is concluded that Jet A-1 produces more well-defined sprays with overall wider cone angles, particularly in the near atomiser (primary atomisation) region where measurements were made.

Meanwhile, water sprays are typically narrower in the near atomiser region but become wider into the secondary atomisation regions due to the presence of relatively large, loose droplets. This is most likely caused by the higher momentum held by the droplets due to the higher density of water and larger droplets sizes, allowing large droplets to propagate further outwards radially rather than becoming entrained in atomisation air flows. Because higher hydrogen content fuels typically exhibit lower densities (*Section 5.2.2*), this could imply that SAF would produce subtly different spray structures to Jet A-1, but it can only be speculated at this time as to the effect this may have on combustion and emissions.

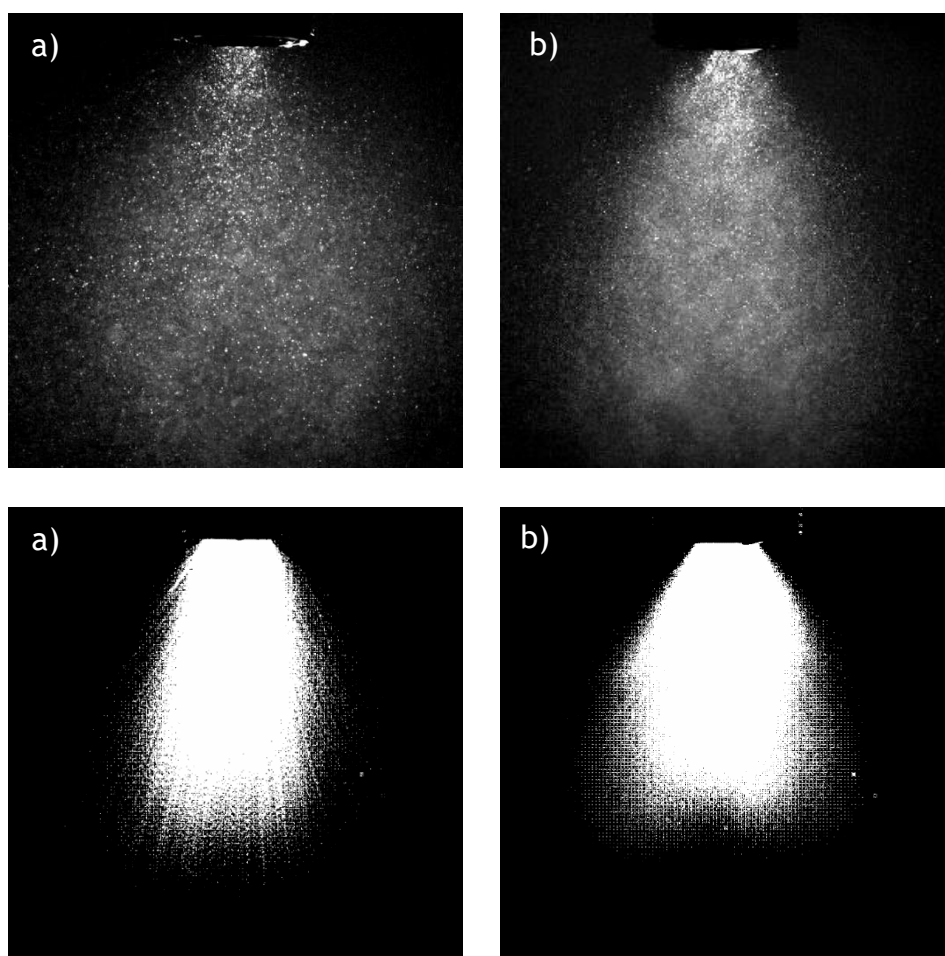


Figure 7-5 - Single frame (above) and thresholded images (below) of atomiser II-E operating with a) water and b) Jet A-1

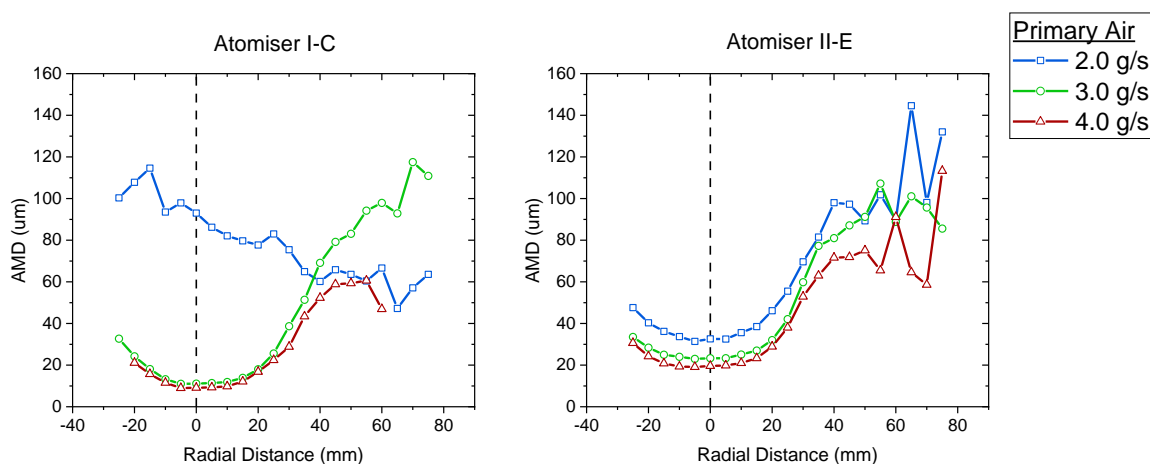
7.3. PDA Atomiser Characterisation

7.3.1. Comparison of Droplet Sizes across Atomisers

PDA experimentation was undertaken for the atomisers highlighted as the most likely candidates for future combustion experimentation based on

experimentation thus far: Atomiser I-C and II-E. Atomiser I-C was chosen to consolidate previous laser diffraction and emissions tests, and due to the hollow cone shape produced. II-E was chosen due to the ordered cone structure and favourable operating performance at low mass flowrates, as well as the low pressure differential. It had been decided that any atomiser exhibiting the aforementioned breakdown in cone angle should not be tested, not only because the behaviour was undesirable in future combustion contexts, but also because the wide spray cone angles observed during HSI tests would cause droplets to impinge onto the lenses of the PDA optics and receiver modules, affecting measurement accuracy and presenting a safety concern. The main objective of the experimentation was to characterise the atomisers' performance relative to each other, and temporally examine the spray characteristics using both water and aviation fuels of varying fluid properties.

During experimentation, the atomiser was operated over a range of air mass flow rates (2-4 g/s) at a fixed liquid flow rate of 1.6 g/s, resulting in a range of ALR values between 1.25-2.5. Results were recorded at a fixed 40 mm distance from the atomiser exit planes, replicating the downstream location used during earlier laser diffraction experimentation, and the laser focal point was traversed radially across the 40 mm plane from -25 mm to +75 mm based on the atomiser central line. **Figure 7-6** provides water case data of AMD and SMD for the two atomisers operating across the range of conditions studied.



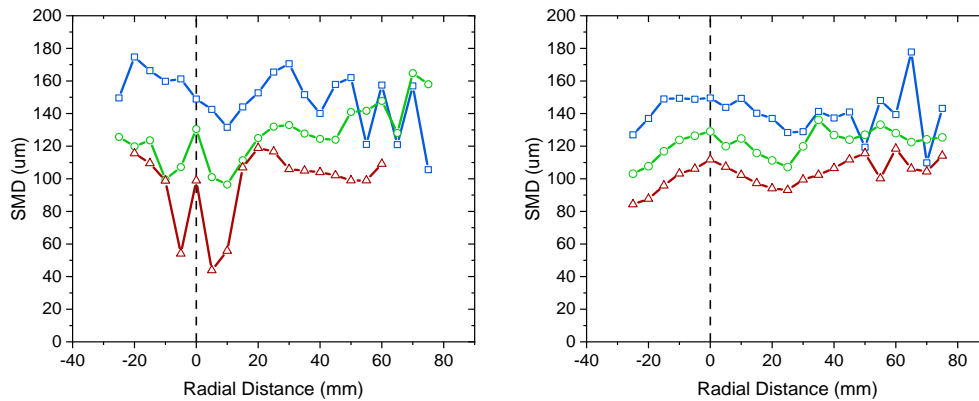


Figure 7-6 - Measured AMD (above) and SMD (below) for water sprays

It is seen that (with the exception of atomiser I-C at 2.0 g/s air) both atomisers produce approximately similar AMD profiles when operating under the same conditions. The general spray profile exhibits a large number of small droplets located in the central region of the spray, which shift towards larger droplet sizes as the radial distance from the centre line increases, and eventually decline towards the edge of the measurement region, indicative of the edge of the spray cone. It is noted that slightly higher AMD values are found in the central region of the spray in the case of II-E. The profile recorded for atomiser I-C at 2.0 g/s air is a result of the atomisation being too poor resulting in data rates deemed too low for accurate sizing, since particularly poor atomisation quality had been observed at this condition during HSI tests (*Section 7.2.1*)

Chong and Hochgreb [169] explain that larger droplet sizes with increasing radial distance from the centreline is typical of swirling hollow cone structures, in which large droplets are entrained to the outer regions of the cone structure by centrifugal forces. However, the PDA data supports the observation in *Section 7.2* in which atomiser II-E appears to produce a solid cone shape. It is seen that the SMD profile for atomiser I-C exhibits a narrow region to either side of the centre line (± 10 mm) in which SMD values drop sharply, with the exception of a consistent peak on the centre line. This may have been a result of the chosen downstream distance of 40 mm, which is seen to intersect the central region of low droplet quantity expected of a hollow cone shape. Additionally, the asymmetry towards the left region of the spray is reflected in a higher data rate, as shown in *Figure 7-7*, most evident at the 4.0 g/s air condition. Meanwhile, atomiser II-E displays a gentle upwards incline in values in the central region, indicative of larger droplet sizes. This is similarly reflected in the measured data

rates. A drop in rates towards the centre line of atomiser I-C, is again indicative of a hollow cone region, while atomiser II-E shows a normal distribution indicative of a greater number of droplets towards the centre line, representing a solid cone structure.

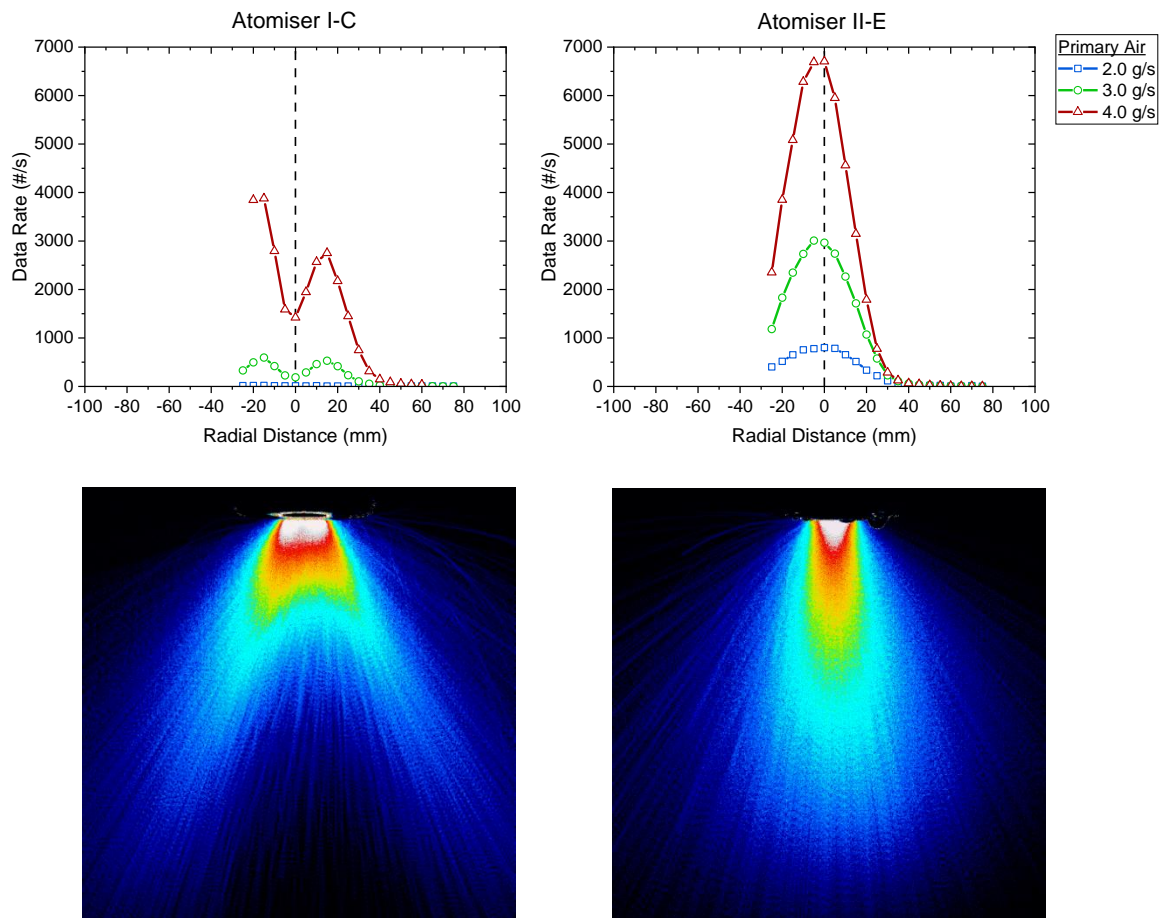


Figure 7-7 - Measured data rates (above) across water spray profiles for atomiser I-C (left) and II-E (right), compared to HSI images from Section 7.2.1

For comparison of the atomisation quality across the two atomisers, data was converted into WMSMD values using *Equation 3-24 (Section 3.8)*. The average of the WMSMD values is taken as a global measured of atomisation quality. The WMSMD values for atomisers I-C and II-E operating with water are shown in *Figure 7-8*. Across the two atomisers, values appear to be approximately comparable for a given mass flowrate of air. In a combustion context where local AFRs were replicated, overall atomisation quality would therefore not be expected to vary significantly across the two atomisers, and variations in emissions would more likely be attributable to local variations in atomisation. However, when presented against predicted air velocity or pressure drop, atomiser II-E exhibits improved atomisation in comparison to I-D, as is shown in *Figure 7-9*:

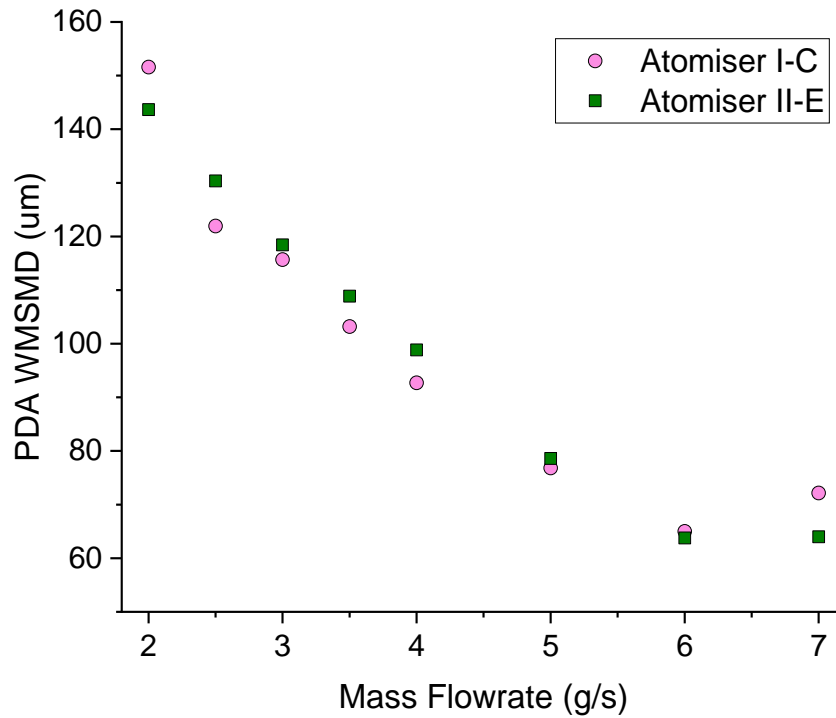


Figure 7-8 - WMSMD values vs. mass flowrate across the atomisers

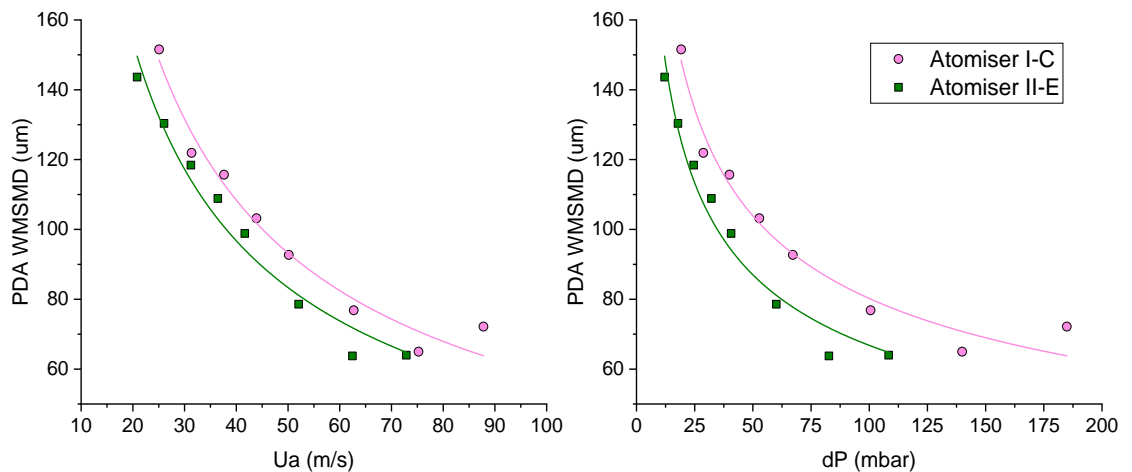


Figure 7-9 - WMSMD values across atomisers vs. predicted U_a (left) and dP/P (right)

Figure 7-10 shows a comparison between measured SMD values collected using the Malvern Spraytec97 laser diffraction data (Section 6.2.1) and PDA data. Significant discrepancies are observed between the measurement techniques, as was expected due to the aforementioned factors impacting the separate test methods Section 3.8. At low flowrates, data collected through laser diffraction exhibit significantly higher average SMD values compared to PDA data. It is expected that the reason for this is the higher maximum droplet size (1040 µm) measurable by the Malvern system compared to PDA, serving to skew SMD values towards larger particle sizes. At higher flowrates, values measured using PDA

begin to exhibit higher values in comparison to laser diffraction experimentation. This is perhaps the more expected result, in agreement with Zaidi *et al.* [174], who observed that SMD data taken for an air-water spray operating at using a PDA system consistently produced higher values compared to laser diffraction results for atomisers operating at atomisation air velocities above 30 m/s.

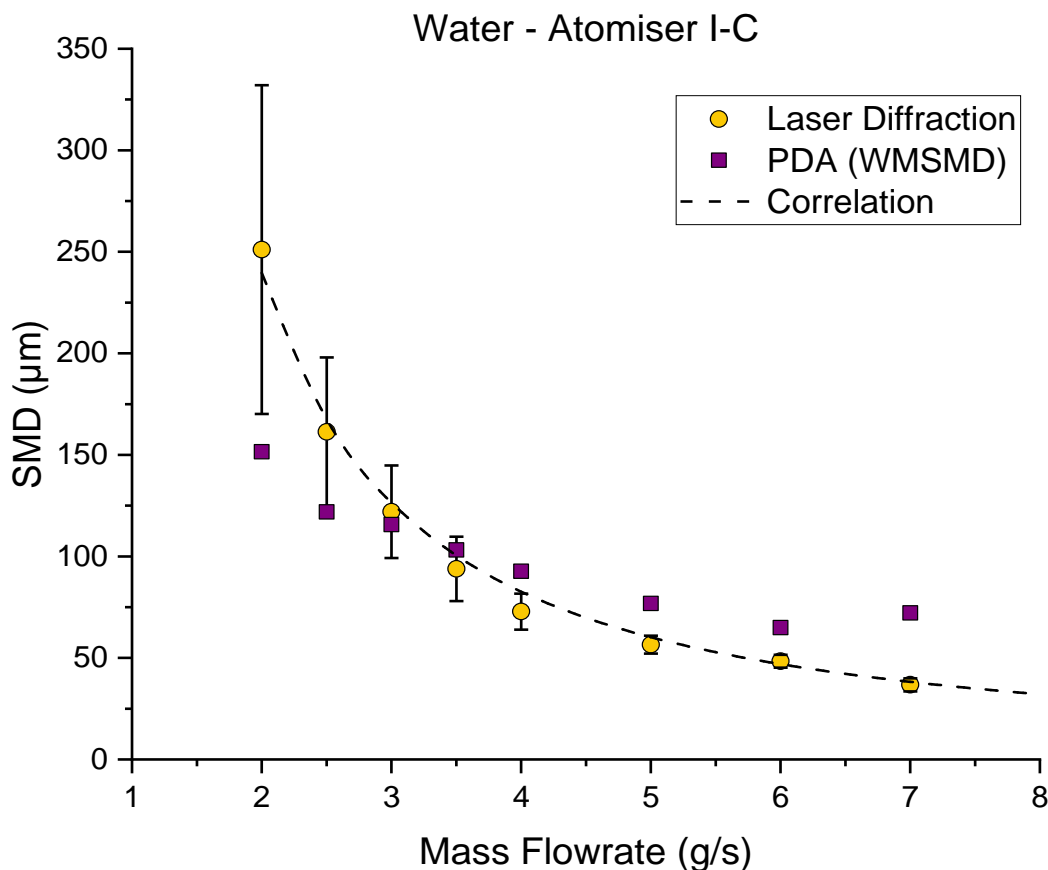


Figure 7-10 - Comparison between average SMD values for atomiser I-C measured using laser diffraction and PDA

7.3.2. Investigation of Spray Variability across Drop-in Fuels

Subsequent droplet sizing experimentation aimed to examine variations in atomisation quality and spray profile across drop-in fuels, which may subsequently impact emissions behaviour. The aviation fuels chosen for experimentation were Flites A-1, A-HA, B-REF, and B-HE2. Not only did this encompass a range of conventional fuels, SAF and blends, but was also expected to offer a relatively wide range of physical property variations, and give the best chance of detecting any impacts on spray quality. Variations across measured SMD profiles for the fuels, across both atomisers tested, are shown in **Figure 7-11**.

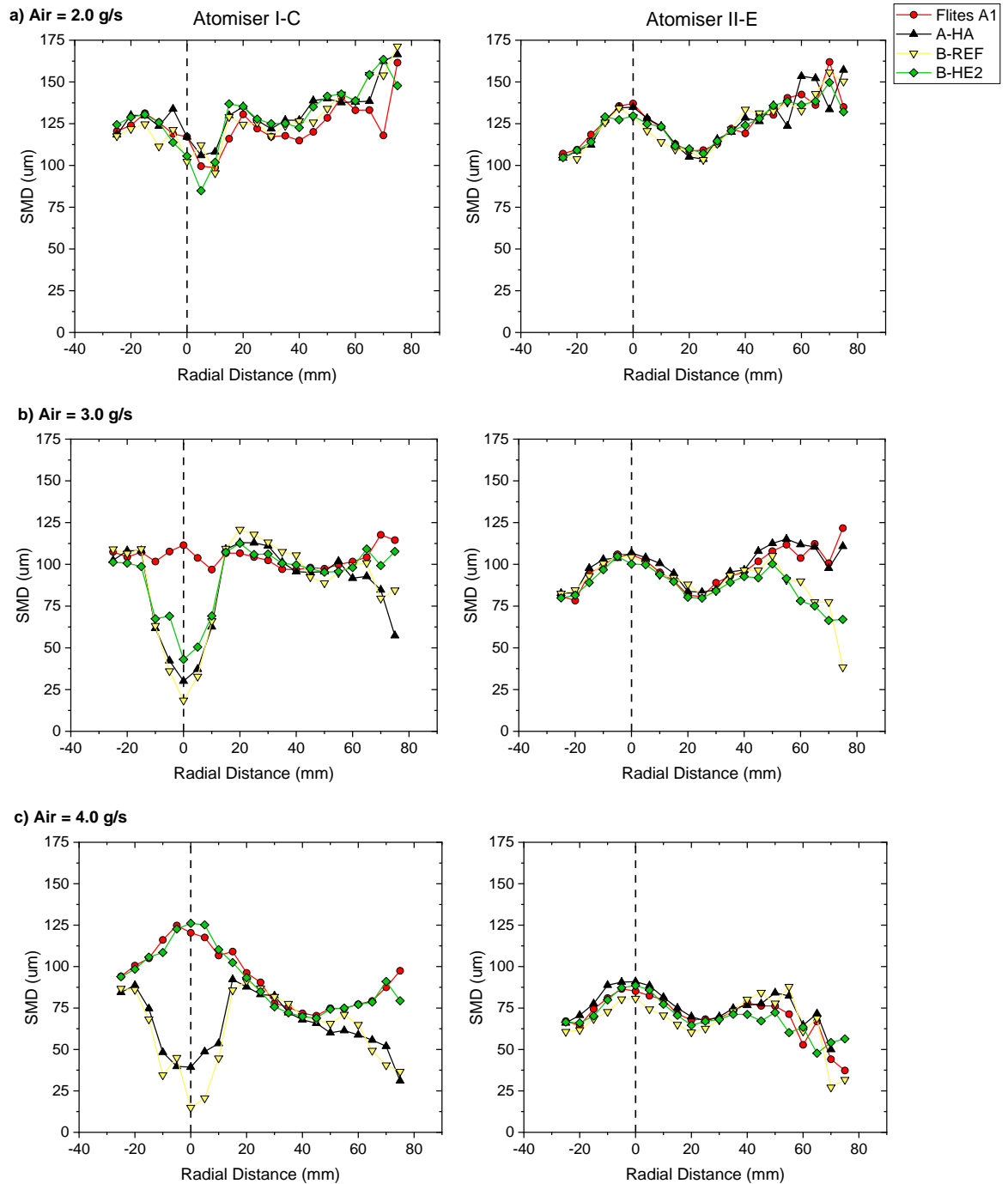


Figure 7-11 - SMD profiles across both atomisers operating with different aviation fuels

It is seen that differences across the atomisers are primarily observed in the central regions of the spray. A drop in SMD values in the central region for atomiser I-C is typically observed, indicative a large number of small droplets, and typical of a hollow cone structure [169]. However, this was not observed for all test points, with Flites Jet A-1 and B-HE2 exhibiting an increase in SMD values towards the centre line. Analysis of these points shows that a larger number of measured droplets are rejected by the PDA system, evident as lower outputted validation rates, while concentration rates remain high. For atomiser I-C, these

are observed in in the central region, and towards the edges of the measurement region. The rejection of small droplets would skew measured SMD values towards larger droplet sizes, which are scaled by volume as previously described in **Section 2.4.2**. Atomiser II-E also displays this behaviour across all fuels tested. However, although the validation rates are lower compared to atomiser I-C, the measured data rates for this atomiser remain high, suggesting that the profile was a result of a solid cone shape. **Figure 7-12** demonstrates the differences across measured data acquisition for atomiser I-C at 4.0 g/s air, with the Flites A-1 fuel exhibiting reduced validation rates, and A-HA believed to be operating normally.

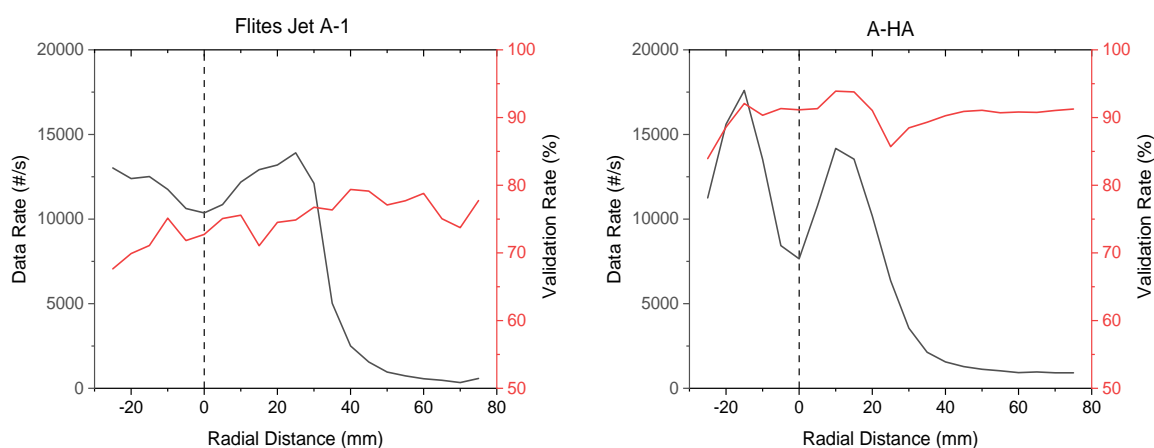


Figure 7-12 - Measured data rates and validation rates for atomiser I-C operating with Flites Jet A-1 (left) vs. A-HA

Figure 7-13 shows the shape of measured SMD values for the four fuels at the 4.0 g/s of air condition, with regions affected by poor data rates highlighted.

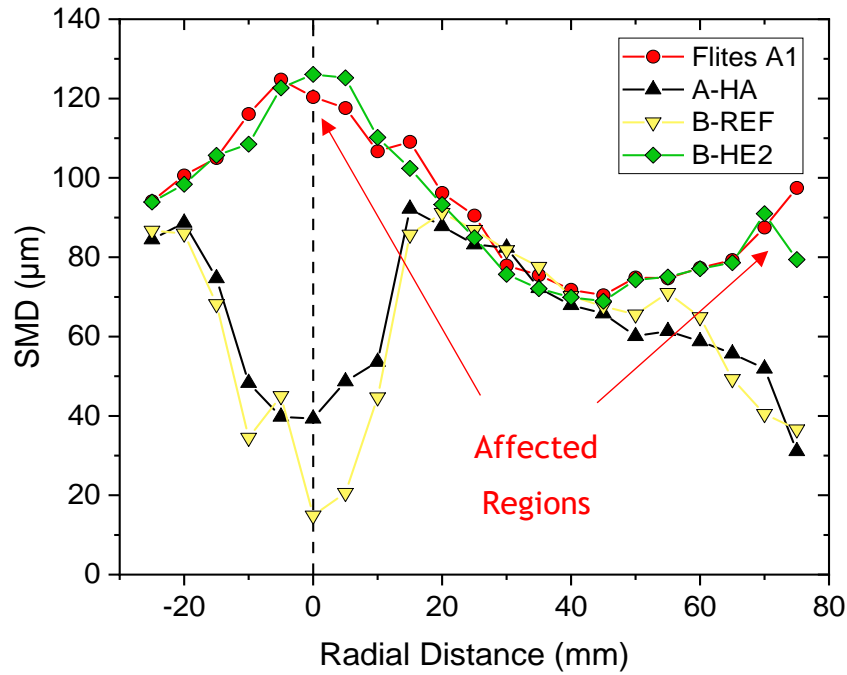


Figure 7-13 - SMD plot across aviation fuels with regions affected by low validation rates

Peaks in SMD values at both the central region and outward regions are observed for the Flites Jet A-1 fuel and B-HE2. This serves to increase the calculated WMSMD values, which are shown for the two atomisers across the range of flowrates with all fuels tested during experimentation in **Figure 7-14**. It is seen that points experiencing lowered data rates deviate away from the points for other fuels, to the point of overlapping with water data. Allometric power laws are fitted over measured points for visual aid.

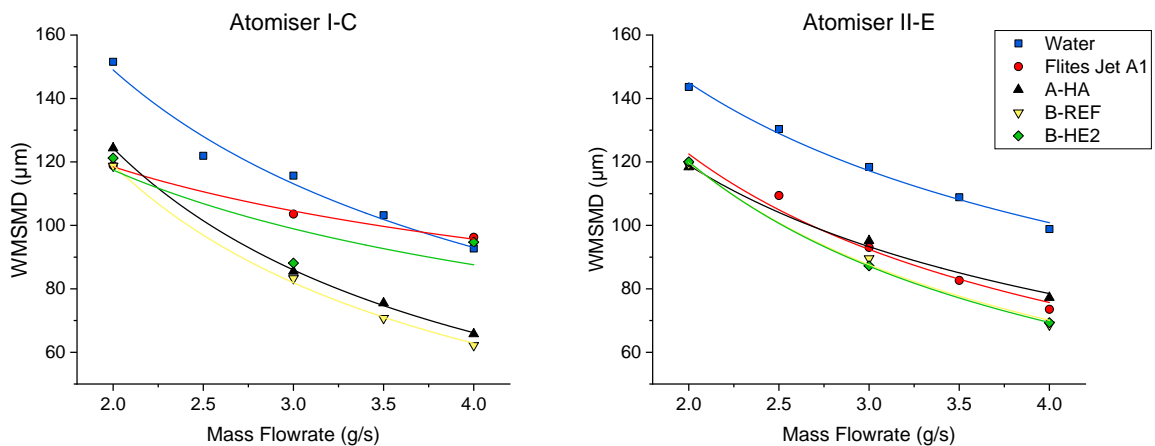


Figure 7-14 - Averaged WMSMD plots for atomiser I-C (left) and II-E (right) operating with water and aviation fuels

For the case of A-HA, reductions in WMSMD values of 18-29% compared to water are measured, with the greater reductions found at higher air flowrates. In general, it is observed that variations in SMD across the aviation fuels tested were

minimal. However, there is some evidence to suggest that small variations in WMSMD were found as a result of fuel physical properties. Fuel A-HA is seen to typically generate higher SMD values in comparison to B-REF, as may be expected due to the worsened atomisation properties demonstrated in *Section 5.2.2*. However, scatter is observed across the data points, preventing a consistent order of fuels from being established. Discounting datapoints believed to be affected by low validation rates, the maximum variability across fuels was found to be ~7% and ~12% for atomisers I-C and II-E, respectively.

An initial assessment of the data was made using the correlation derived from laser diffraction data in *Section 6.2.3*. Measured data points taken for atomiser I-C using the PDA system for fuels which were not affected by low validation rates are shown plotted against predicted points for the same fuels using the correlation in **Figure 7-15**.

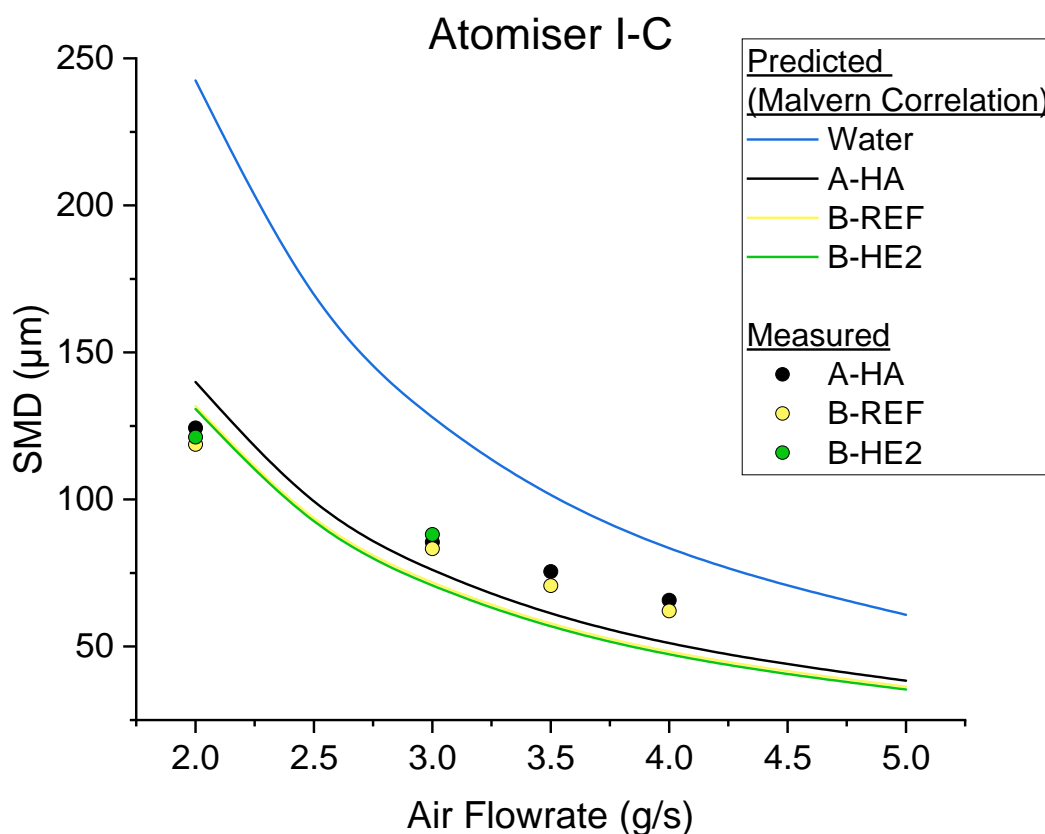


Figure 7-15 - Malvern correlation predictions vs. measured PDA values

Because of the aforementioned discrepancies between droplet size data obtained from laser diffraction experiments and PDA, it was not expected that agreement would be achieved between measured data and predictions. However, a similar general trend is observed between PDA and Malvern results as for the

water data given earlier in **Section 7.3.1**, in which predicted values are larger than those measured by PDA experimentation, before crossing the data points at a relatively low mass flowrate. Agreement between predicted and measured values is within ~25% variability. The relative spread across fuels from laser diffraction predictions is 7%, in agreement with measured PDA values, although the order of fuels is not consistent for measured data. This may imply that trends predicted from laser diffraction experimentation using water as a fuel can be used to somewhat capture the trends across fuels. However, the dataset is ultimately limited by a lack of data points, and the limited experimental validation. It is suggested that future studies explore the impact of fuel properties across alternative fuels using both measurement techniques.

Further assessment was undertaken using the PDA data for both water and jet fuels. In a similar study, Tareq *et al.* [117] states that water and Jet A-1 data are not comparable due to significant differences in fuel properties, and so individual correlations should be determined for each. Because the impact of fuel properties (as opposed to the impact of atomiser features) is the primary focus, correlations have been derived for atomisers I-C and II-E individually, using water and aviation fuels separately.

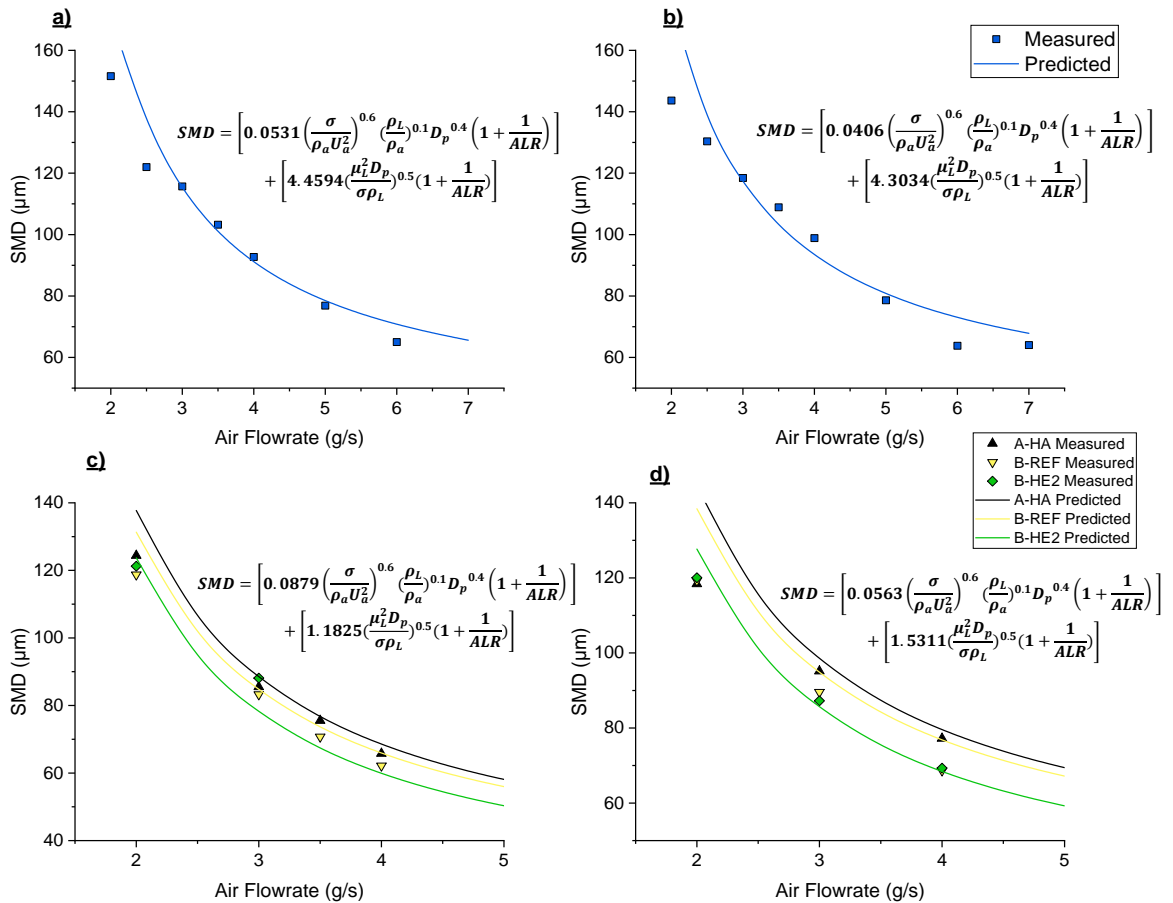


Figure 7-16 - Measured PDA data and correlations derived from linear regression using Equation 2-16. a) atomiser I-C with water, b) atomiser II-E with water, c) atomiser I-C with aviation fuels, d) atomiser II-E with aviation fuels

For SMD correlations derived using PDA data, both that of Lefebvre and Balal [16] (Equation 2-11) and that of El-Shanawany *et al.* [129] (Equation 2-16) result in lower derived A coefficients in comparison to the earlier correlation derived from laser diffraction data, implying a lower dependence on We number, and a reduced sensitivity to the aerodynamic forces applied on the fuel during atomisation. By comparison, derived values of B are higher when derived using PDA experimentation, resulting in a higher sensitivity to viscous effects encompassed by the Oh term. When correlations derived using water data are used to estimate SMD values for Jet A-1, the values are higher than water, which disagrees with experimental data. When derived from fuel PDA data, the high value of B results in predicted variations across the fuels tested in the range of 11-13% and 12-15% for atomisers I-C and II-E, respectively, across the range of flowrates used during experimentation.

The same overprediction of the B term in empirical correlations was observed by Tareq *et al.* [117] who also used PDA experimentation to derive

empirical trends. However, this was observed for the correlation suggested by Lefebvre (*Equation 2-11*) rather than that of El-Shanawany *et al.* [129] (*Equation 2-16*) although both correlations share similar dependencies on the We number and Oh number. For comparison, the regression code was used again to derive constants for the same equation proposed by Lefebvre and Balal [16] and used by Tareq *et al.* [117], yielding the coefficients give in *Table 7-5*.

Table 7-5 - Regression Coefficients derived for Equation 2-11

	Water		Jet-A1	
Experimental Constants	A	B	A	B
Regression Code (<i>Equation 2-11</i>)	1.2725	64.4882	1.9189	15.088
Constants derived by Tareq <i>et al.</i> [117]	1.299	34.184	5.243	22.995

This suggests that laser diffraction experimentation is more applicable when developing global trends across fuels compared to PDA data, which is logical given that most of the correlations available in the literature have been derived using laser diffraction experiments. The fact that the same general relationship between measured PDA data values for an atomiser operating with aviation fuels, and values estimated using a correlation derived from water data only, suggests that the impact of fuel properties is relatively well captured when derived from laser diffraction data. By comparison, correlations derived from PDA data have been shown to exhibit higher dependencies on viscous terms and a lower dependence on We number, leading to an overprediction of expected variability across alternative fuels due to physical properties, and limiting applicability of the correlation across fuels of significantly different fuel properties. As such, caution is recommended when attempting to derive these empirical correlations from PDA in future studies.

7.4. Emissions Experimentation

7.4.1. Overview

As mentioned in **Section 6.3.1**, the use of separately controlled front cooling air inputs was a unique feature of the Mk. II RQL burner, allowing for variation in atomisation quality without affecting the primary AFR. While it is known that atomisation quality impacts nvPM emissions, to the authors' knowledge no experimental study has previously been able to decouple atomisation quality from AFR and quantify the subsequent impact on nvPM emissions. To specifically address the impact of atomisation on emissions formation, it was decided that an additional test would be undertaken using the Mk. II combustor operating with atomiser II-E, henceforth referred to as the Mk. II-A combustor. This atomiser was chosen, because of its more symmetrical nature and relatively narrower cone angle, which was expected to lead to a more consistent pre-flame mixture, reducing the soot build ups and thermal damage witnessed previously. Additionally, as shown in **Section 7.3**, measured PDA data suggested that this atomiser would generate similar SMD values to atomiser I-C per unit mass flowrates, and so witnessed impacts on nvPM would be expected to result in changes to the spray other than SMD. The atomiser had also performed well in spray tests, demonstrating a stable spray at lower air flowrates compared to I-C, and improved pressure drop characteristics.

Figure 7-17 shows the spray produced by the two atomisers within the dimensions of the Mk. II combustion liner. The spray produced by the new atomiser appears to fit within the outlined dimensions without impinging significantly onto the combustion liner before the 40 mm mark. The lower spray cone angle measured in **Section 7.2.2** was expected to decrease thermal loading on the liner by pushing the flame further downstream, in line with the work of Mishra *et al.* [25]. This is not representative of the spray under pressurised conditions with combustion occurring, during which the cone angle would be expected to narrow as a result of increased pressure and the higher velocity brought about by the preheated air.

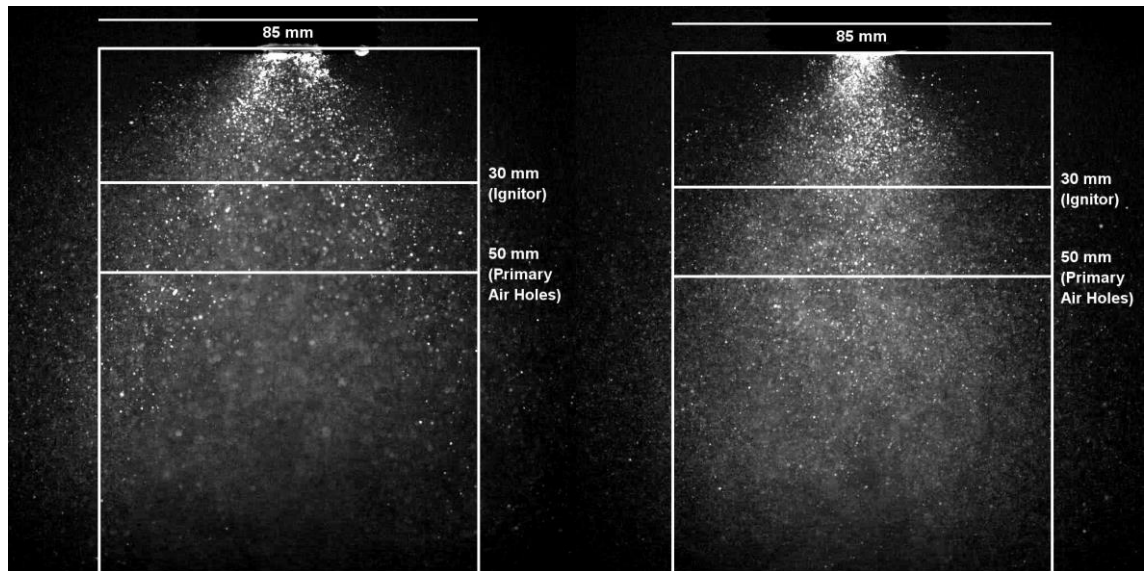


Figure 7-17 - Comparisons of sprays across atomiser I-C (left) and II-E (right) within the combustor confinement space

Fuels used for Mk. II-A experimentation were chosen from those already tested in earlier experimentation, so as to reproduce the wide range of hydrogen contents. These were A-HA, B-REF, B-HE2, and the Flites Jet A-1 fuels. The operating conditions were repeats of the 3.0 bar conditions used for experimentation with the Mk. II combustor (**Section 6.4**), selected in mind of thermal power output and previously observed stability. Two additional operating conditions were chosen to explore the impacts of atomisation quality independent of primary zone equivalence ratio. This involved reducing a portion of the primary air supplied to the atomiser, which was substituted in as cooling air, thereby reducing atomisation quality while maintaining primary zone and global AFR values. This was not a feature of the Mk. I combustor, for which increases in primary air were always accompanied by a reduction in primary zone equivalence ratio and SMD. The full set of operating conditions are shown in **Table 7-6**.

Table 7-6 -Operating Conditions during Mk II-A Testing

Condition	Pressure (bara)	Primary Air (g/s)	Cooling Air (g/s)	Secondary Air (g/s)	Fuel (g/s)	ϕ_{PZ}	ϕ_{QZ}	ϕ_{LZ}
Rich	3.0	5.9	5.3	64.6	1.5	1.969	0.568	0.291
Lean	3.0	6.9	5.3	61.4	1.5	1.807	0.574	0.300
Rich - Reduced Atomisation	3.0	5.4	5.9	64.9	1.5	1.951	0.565	0.289
Lean - Reduced Atomisation	3.0	6.3	5.9	61.5	1.5	1.807	0.573	0.299

7.4.2. Emissions Results

The processed emissions data for the four conditions is given in **Figure 7-18**, with error bars representative of ± 2 standard deviations of the scatter across a 30 second average. Unlike with the previous emissions dataset, nvPM data no longer displayed the bi-modal PSD trend, allowing for GMD values to be included. For the rich and lean conditions, switching to the reduced atomisation conditions reduces the mass flowrate of air through the atomiser by 8.5% and 8.7%, respectively. From mass continuity, it is predicted that this would induce an equal percentage change to air velocity, and would decrease the We number by ~16 - 17%. Using the equation derived from PDA experimentation with jet fuels for this atomiser, decreases in SMD are estimated to be ~5%, although the true value may be higher since the low A term derived makes the correlation less sensitive to changes in We number.

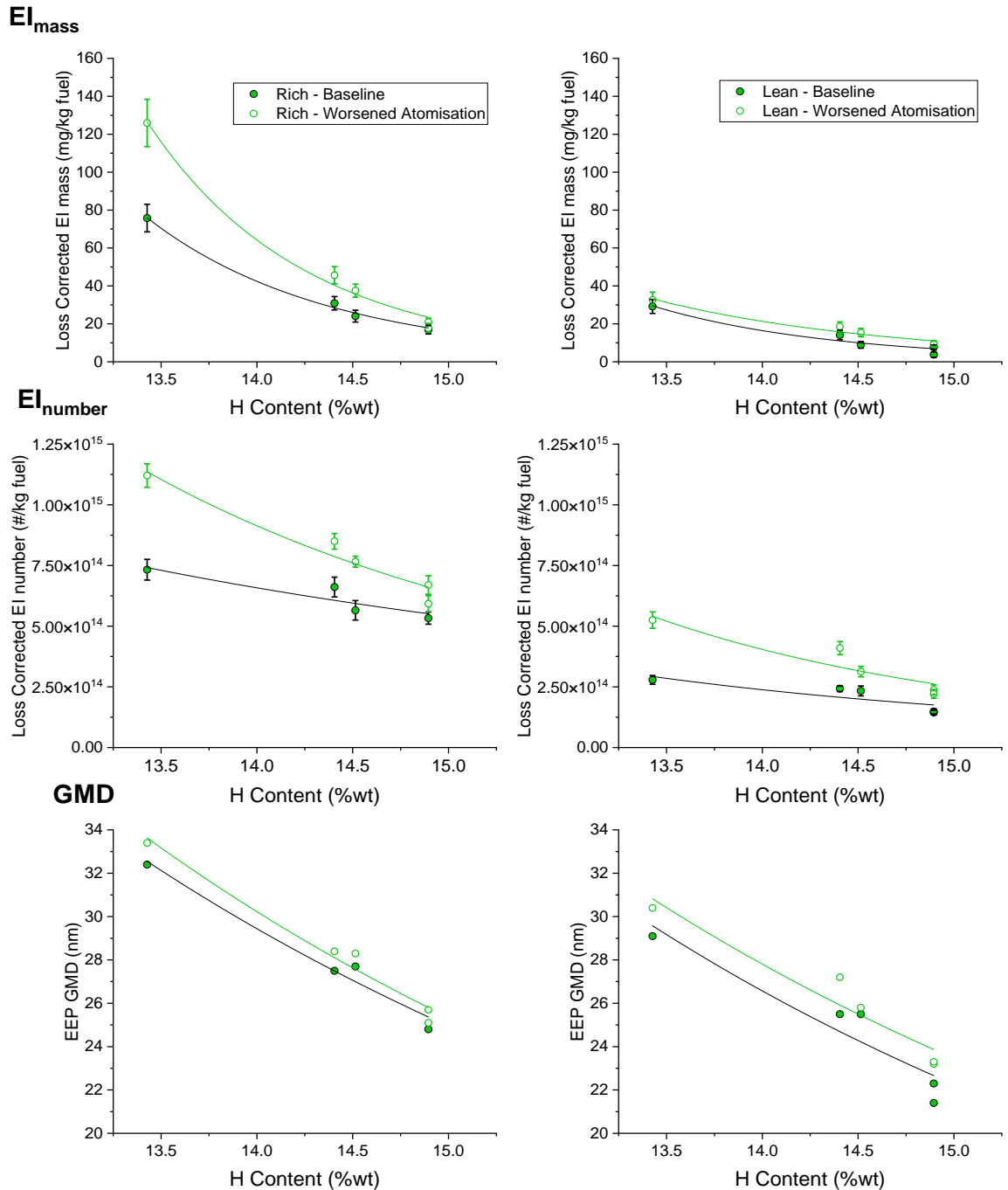


Figure 7-18 - Variations in nvPM emissions for reduced atomisation conditions

It is observed that the reduced atomisation conditions experience increased nvPM emissions by mass, number, and size, across all fuels studied and at both the rich and lean conditions. This is in agreement with the computational study undertaken by Zhamatkesh [118], previously described in **Section 2.4.3**, who concluded that improvements to atomisation quality led to higher numbers of smaller particles in the primary zone, which were more easily consumed in the secondary lean zone, leading to overall reduced mass emissions. A large range in the relative increases of nvPM emissions across fuels is encountered, from 5-72%

for EI_{mass} , 11-89% for EI_{number} , and 1-7% for GMD. This, along with the lack of repeated data points, makes determining average nvPM changes as a result of atomisation quality difficult at this time. However, analysis of the gradients of the plotted trendlines across the range of hydrogen contents studied suggests that higher increases in nvPM due to worsened atomisation are expected for fuels of lower hydrogen contents, implying that high aromatic conventional fuels could be more sensitive to changes in atomisation quality. The results also serve to experimentally demonstrate how small changes to atomisation quality can significantly impact nvPM number and mass, at least under the relatively low power conditions used for experimentation in this project, as well as the design of the combustor.

A comparison of loss corrected EI values obtained using the Mk. II and Mk. II-A combustors is shown in *Figure 7-19*, with the data showing rich and lean conditions at 3.0 bar, which were repeated across both studies.

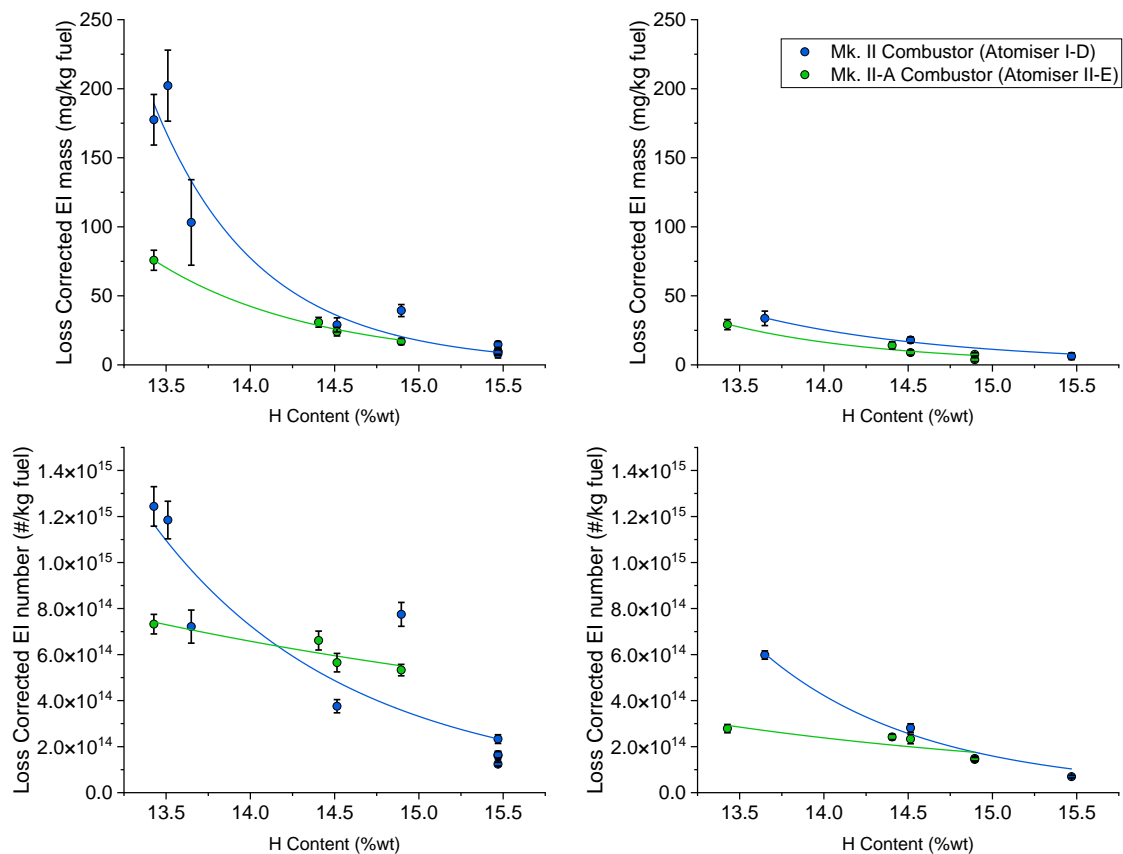


Figure 7-19 - Comparison of nvPM emissions across Mk. II and Mk. II-A experimentation

Reduced nvPM mass is observed across both conditions when the combustor was operated with atomiser II-E compared to I-D. Additionally, the combustion stability appears to have improved, as evidenced by the narrower error bars. The

results presented here may demonstrate the impact of varying combustor designs on emissions, especially regarding atomisation, but it is important to be aware that the probe was moved to the downstream location between Mk. II and Mk II-A tests, and the results may have been a result of increased oxidation of nvPM prior to collection by the probe due to the increased distance and residence time between the combustor exit and probe. However, while improvements in the stability of data and reductions in nvPM emissions are observed for the Mk. II-A combustor, significantly higher quantities of CO and UHC were observed across testing, indicative of poorer combustion efficiency. This is likely a result of the solid cone structure, and reduced distribution of fuel in the combustor primary zone, since PDA results had indicated that SMD values should remain relatively consistent for the atomiser compared to I-C. Combustion efficiencies were determined across experimentation using the same method used previously (*Section 3.5.2*), and are shown in *Figure 7-20*.

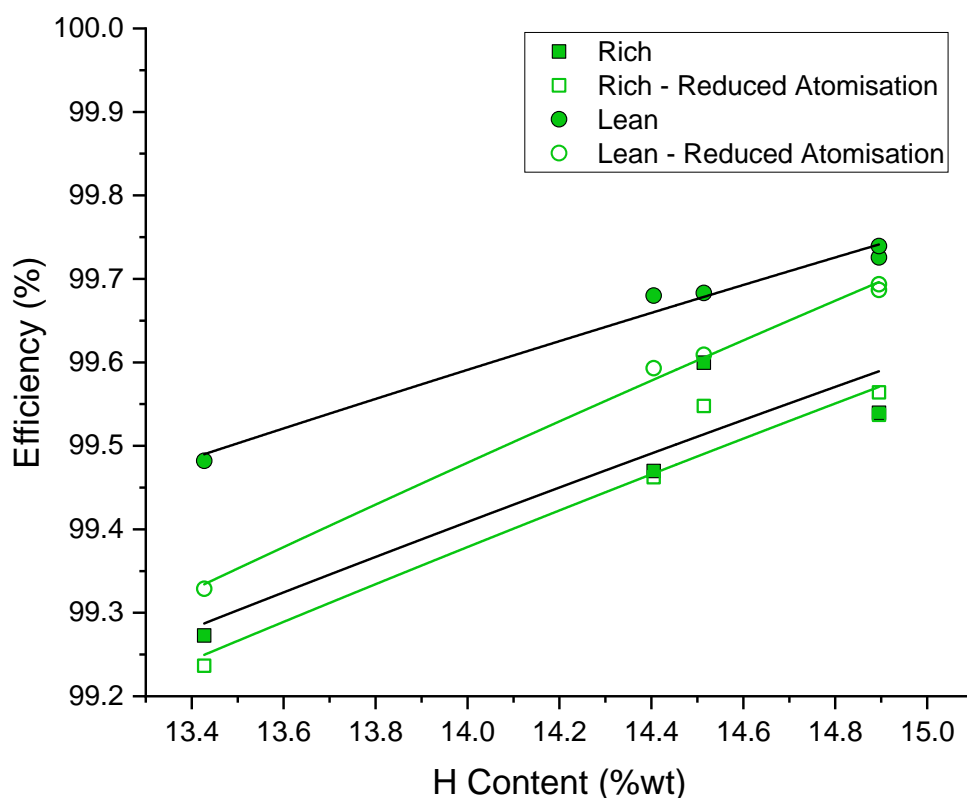


Figure 7-20 - Calculated combustion efficiencies for the Mk. II-A combustor

As before, it is witnessed that increasing hydrogen content again serves to improve combustion efficiency. However the combustion efficiency is seen to have reduced in comparison the Mk. I and Mk. II combustor, falling to a minimum of approximately 99.2%. Improving atomisation quality is seen to slightly improve

combustion efficiencies, with a more pronounced impact across the lean conditions. This suggests that increasing primary air would be beneficial for the operation of the Mk. II-A combustor. Build-up of nvPM in the combustor was again witnessed, although appears to have been reduced compared to the Mk. II combustor. The deposit was located in the same region as the Mk. II combustor, which implies that the asymmetry for atomiser I-C highlighted in *Section 7.2*, was not the sole cause. Therefore, it is suggested that the cause was a pooling of fuel due to insufficient flowrates, which was then carried in the direction of the swirling air exiting the outer air channel (clockwise in *Figure 6-22* and *Figure 7-21*), and deposited onto the liner walls. Additionally, thermal damage is again witnessed for the Mk. II-A combustor.

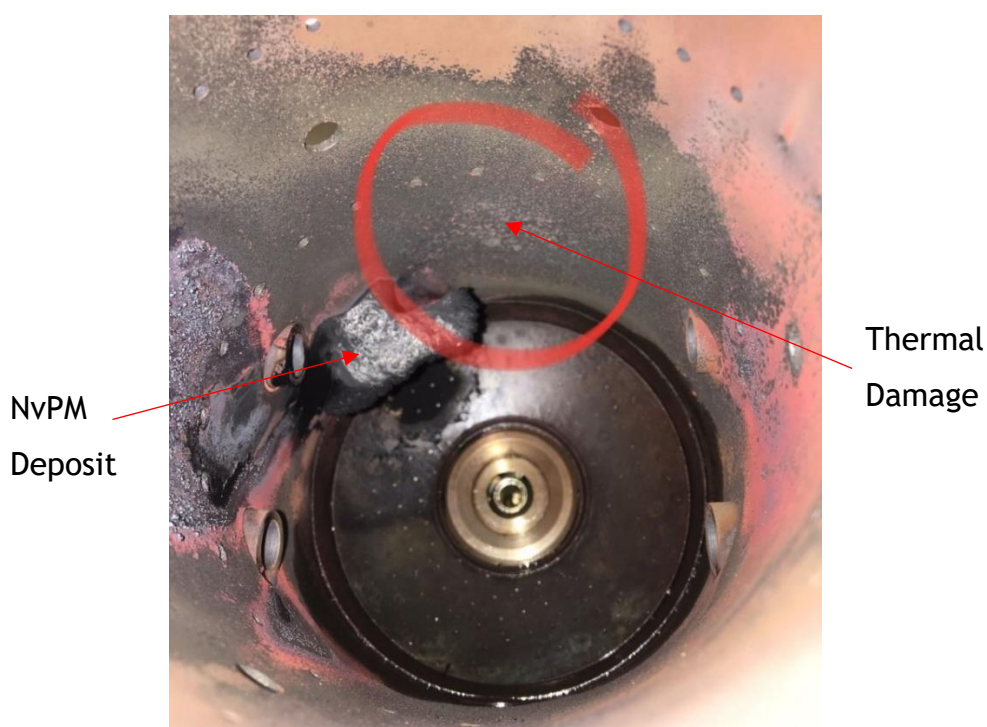


Figure 7-21 - NvPM deposit and thermal damage observed for the Mk. II-A combustor

Overall, it appears that the operating conditions used for both the Mk. II and Mk. II-A combustor are currently too low for successful operation of the combustor, particularly with regards to those affecting the primary zone. In *Section 5.6*, it was shown that EI values (especially EI_{mass}) were reduced by increasing primary air and fuel flow. Therefore, it is suggested that future operation of the combustor should increase both primary air and fuel flow at the same rate, so as to maintain the current primary equivalence ratio, until combustion efficiencies are comparable to those of the previous experimental campaigns. In order to prevent excessive NO_x emissions, secondary air flowrates

should only be subtly altered so as to maintain the current local equivalence ratios in each respective combustion zone, and thus, the effectiveness of the RQL concept. To prevent soot freezing, changes to secondary air should be kept to as low as possible, with the suggested ratio between quench air and flow to the primary zone maintained below 2.5. It is hoped that this would allow for minimisation of emissions, and determination of the optimal conditions for combustor operation.

7.4.3. Comparisons Across Datasets

As mentioned in *Section 2.3.3*, Durand *et al.* [106] demonstrated that values of nvPM EI_{mass} and EI_{number} produced by an APU across separate test campaigns and varying operating conditions could be described by a global trend when normalised to a reference fuel, but this was undertaken using the same APU across all experimentation. In order to determine whether hydrogen content trends could be applied across the different versions of the RQL combustor, EI_{mass} and EI_{number} values were normalised to a common fuel across the three test campaigns (B-HE2), shown in *Figure 7-22*. A trend was produced using constrained power law, with adj. R^2 values shown. Here, it was decided that data points should be presented as individual measurement points rather than averaged values with error bars representing variability across test conditions, as this allowed for a better observation the impact of scatter on nvPM data.

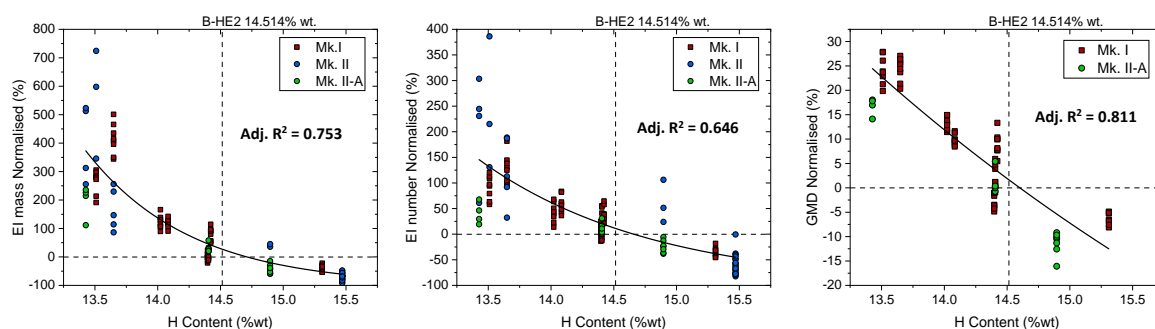


Figure 7-22 - Normalised emissions datasets across the Mk. I, Mk. II and Mk. II-A experimentation

It is witnessed that normalised trends are able to provide a fit between the three datasets, highlighting that a normalised trend can be used to loosely describe emissions trends irrespective of operating conditions and combustor designs. The scatter observed across testing is seen to limit the quality of fit, with the highest quality of fit observed for GMD values, followed by EI_{mass} , and then

EI_{number} . Data collected using the Mk. II combustor exhibits the most scatter in normalised trends, especially for EI_{number} . Additionally, scatter across EI_{mass} is seen to be particularly prominent for fuels of lower hydrogen contents, implying that combustion stability can be improved by the use of high hydrogen content fuels, through a combination of improved atomisation quality, higher specific energy, and improved combustion efficiencies, although as previously mentioned, this trend does not apply to all fuels in this study.

As was undertaken in *Section 5.5.1*, the offsets between emissions reductions relative to a Jet A-1 fuel between uncorrected (ICAO) and system loss corrected EI_{number} values was assessed. *Figure 7-23* demonstrates the overprediction of EI_{number} reductions relative to the Flites Jet A-1 fuel across the fuels in the Mk. II and Mk. II-A combustor. It may be noted that the Flites Jet A-1 fuel exhibited a lower hydrogen content than that of J-REF, and effectively acted as the reference Jet A-1 fuel across tests undertaken using the Mk. II and Mk. II-A combustors. Although scatter is observed across the data, especially for the Mk. II combustor dataset, the general trend appears similar to the trend observed for the Mk. I combustor, with a larger overprediction in emissions reductions observed as hydrogen content increases. Overpredictions for fuels in the typical range of near-zero aromatic fuels (>15%) appear to converge on an EI_{number} overprediction of ~9%. However, it should be noted that the high hydrogen content GTL shows an average value closer to 6%. The slightly higher overestimate in comparison is explained by the lower hydrogen content of the reference Jet A-1 fuel used here.

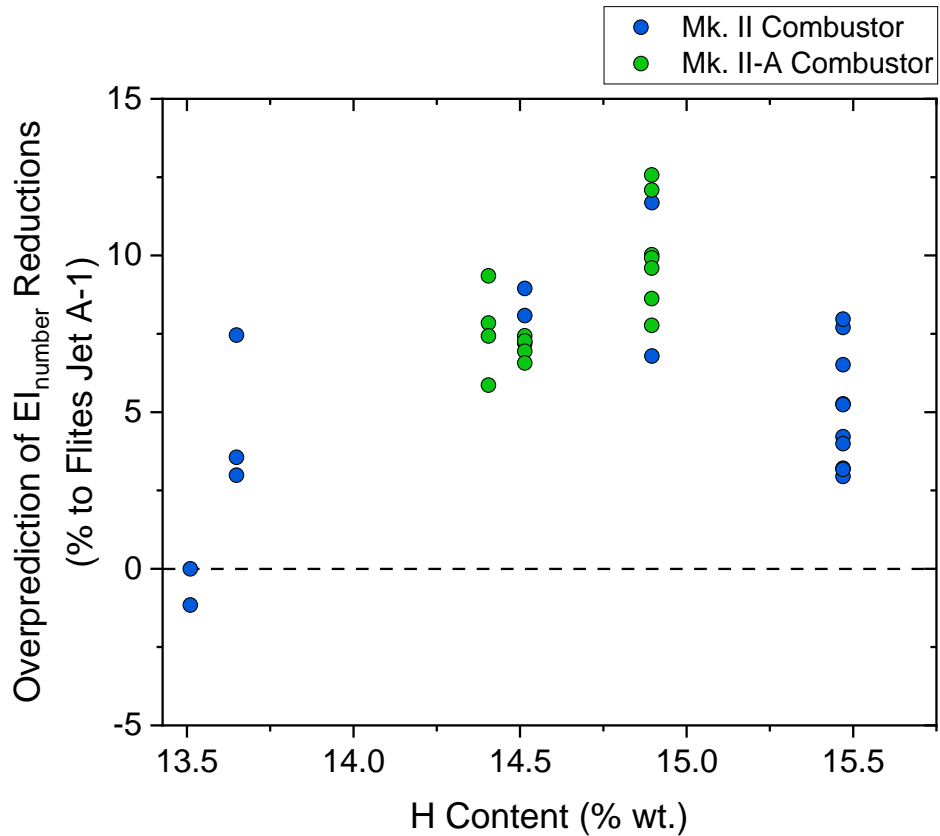


Figure 7-23 - Overprediction of achievable nvPM number reductions for non-loss corrected emissions data vs. fuel hydrogen content

7.5. Chapter Summary

Assessment of the spray quality across the Phase II atomisers was undertaken using HSI and PDA experimentation. HSI results highlighted a characteristic breakdown in spray cone angle for several atomisers, including the design used in conjunction with the Mk. I combustor. The behaviour was seen to be inconstant across operating conditions, and is therefore highlighted as a sources of uncertainty and instability in emissions data. It is believed that this behaviour was caused by the ratio of axial air velocities between the inner to outer air channels being too high, preventing stabilising effect of the outer air on the spray cone, and changes to the atomiser designs made with the intention of reducing the aerodynamic forces applied through the inner air channel prevented the cone breakdown. Atomiser I-C was observed to produce a hollow cone spray, with a somewhat asymmetrical distribution of fuel droplets. The design changes made to atomiser II-D and II-E reduced the spray cone angle and improved uniformity, although the sprays exhibited solid cone structures. The inclusion of curved blades for atomiser II-E significantly reduced the atomiser pressure drop

without sacrificing atomisation performance at lower air flowrates, improving the operating range of the atomiser. As such, this atomiser was selected as the most suitable for the Mk. II-A combustor.

PDA experimentation was used to characterise the droplet sizes produced by the Mk. II and Mk. II-A atomisers, which were found to produce approximately similar SMD values across operating conditions. The main differences were observed across spray profiles, which served to consolidate the spray structures witnessed during HSI testing. The spray profiles across multiple drop-in fuels were tested, and variability of ~7% and ~12% was observed for atomisers I-C and II-E, respectively, as a result of fuel physical properties. Low validation rates were witnessed as a source of uncertainty during experimentation for atomiser I-C, producing much larger WMSMD values than expected.

Droplet size data collected using laser diffraction and PDA experimentation show deviations to each other. Laser diffraction SMD values were higher than PDA values at lower flowrates, attributed to the larger droplet size measurement range associated with the Malvern Spraytec97, and the larger scaling effect of large droplets when measurements are taken on a volume basis. Empirical trends derived from laser diffraction experimentation appear to better capture the impact of fuel properties on SMD data, to the point that trends derived from water data alone may allow for a valid estimate of the SMD values produced by aviation fuels. Meanwhile, correlations derived from PDA were found to underestimate the impact of aerodynamic forces and overestimate the impact of viscous effects on atomisation quality, supported by the findings of Tareq *et al* [117]. This ultimately leads to an overprediction of atomisation quality variability across drop-in fuels, and restricts derived correlations from being applied across fuels of differing fuel properties.

Following development of the Mk. II RQL combustor, additional emissions experimentation was undertaken using conventional and alternative fuels. The newly developed atomiser was shown to reduce nvPM emissions from the Mk. II-A combustor compared to the Mk. II combustor, but also worsened emissions of CO and UHC, and reduced combustion efficiency. This demonstrated the significant impact on emissions due to differences in spray structure, for atomisers expected to produce approximately similar SMD values. Changes to the combustor operating conditions have been suggested for future experimentation. A novel combustor

design feature allowed for the reduction of atomisation quality without impacting primary zone equivalence ratio. It was found that small decreases in atomisation air (~0.5 g/s) at 3 bar could increase nvPM emissions by as much as 72% for particle mass, 89% for particle number, and 7% for particle sizes.

The new nvPM datasets helped to consolidate the constrained hydrogen content trend outlined in *Section 5.4.1*, and examine some of the deviations to the trend observed in previous experimentation. Ultimately, hydrogen content provides a good fit with measured nvPM mass emissions, but is limited by repeated bias attributed to day-to-day variability, as opposed to fuel physiochemical properties.

8. Discussion and Conclusions

8.1. Discussion

This work was undertaken towards improved understanding of the link between aviation fuel properties, combustor operating conditions, and nvPM emissions. This is a crucial area of study for the civil aviation sector given the increase in SAF usage anticipated in upcoming years. A better understanding of the causes of nvPM emission from RQL combustors can help to inform decisions made towards optimising SAF properties or aircraft designs, so as to reduce nvPM from aircraft and the overall impact on LAQ and the global environment. The relevance of the findings provided in this work is in building the body of knowledge concerning the performance and benefits achievable when using SAF in existing aircraft engines.

Breakthroughs in alternative combustor technologies, most notably lean burn combustors, suggest that nvPM emissions could be dramatically reduced by combustor technologies in the future. However, it appears that these technologies still require a period of time for development and implementation before their potential for emissions reductions can be realised. Given the urgency of replacing fossil fuels with low-carbon alternatives to achieve emissions targets, increased use of high hydrogen content SAF into existing RQL combustor engines in the nearer term will allow the benefits of operational stability and NO_x reductions associated with these combustors to be preserved, while also reducing nvPM and lifecycle CO₂ emissions. In particular, nvPM emissions, which RQL combustors are known to be especially prone to, can be dramatically reduced by the use of SAF, which could be particularly important if it is concluded that contrails are as detrimental to the global environment as current research suggests.

The RQL combustor developed for this project acts as a testbed for the characterisation of nvPM emissions from SAF. The use of the bin-by-bin method for system loss corrections was chosen because of the improved accuracy the method provides for nvPM concentrations consisting of very small particles. Continued utilisation of the system loss correction procedure in emissions studies could help to establish it as a standard practice, which is recommended to avoid the overreporting of nvPM number observed during emissions testing in this thesis.

Although the greatest achievable reductions to nvPM emissions on the whole will be as a result of increased fuel hydrogen content, particularly at high thrust conditions where nvPM formation rates are highest, the conditions targeted during this project are more applicable to aircraft operating at low power conditions, such as at idle on a runway. As such, the information provided will be most applicable towards improving the LAQ around airports and other high traffic areas. At low power conditions, atomisation quality appears to become a more significant factor in nvPM production, where small reductions in atomisation quality can result in worsened nvPM emissions which become more erratic and less stable. Although variability in SMD values across conventional aviation fuels and SAF appears to be small, it is possible that this would be enough to significantly impact nvPM emissions under these conditions. Measured values of fuel density and surface tension were seen to typically reduce across fuels as hydrogen content increased, suggesting that better atomisation may be achieved for higher hydrogen content SAF compared to current Jet A-1 fuels (although this trend was not always the case, as seen for the pure ATJ fuels studied). Nevertheless, the generally improved atomisation properties associated with higher hydrogen content fuels may account for a small portion of the associated nvPM emissions reductions observed, and a better understanding of these effects can dictate the suitability of different SAF in the commercial aviation towards the greatest emission reductions possible.

The observations concerning deriving SMD correlations from benchmarking experiments highlights issues apparent with the method. At first glance, it might be thought that PDA experimentation is unsuitable for the characterisation of atomiser sprays, given the tendency for the coefficient of the Oh term to be overpredicted when using PDA data. However, this is believed to be unlikely, given that PDA experimentation is a more modern technique compared to laser diffraction experiments, and has a proven track record in spray categorisation studies. It is important to be aware that most of the widely used correlations in the literature, which are seen to still be used in studies to this day, were developed several decades ago using laser diffraction experimentation, and are empirical in nature. Additionally, global correlations do not account for the complex nature of the spray flow field in 3D space, which is of importance due to the impact of fuel and air distribution in emissions formation in addition to droplet sizes. As such, caution is advised when attempting to predict the impacts of fuel

properties from derived correlations, and it is the authors belief that it is worth the added complexity and effort of undertaking extensive experimentation to better understand the variability across sprays of different aviation fuel. Despite the uncertainties, the spray data provided in this project does act as a step towards better understanding the impact of sprays produced by SAF in aero engine settings, towards quantifying the impact they may have on nvPM emissions, and the suitability of different SAF as alternatives to current Jet A1 fuels.

8.2. Conclusions

Towards improving the understanding between airblast sprays, SAF properties and nvPM, the key outcomes and findings of this work are as follows:

- An RQL combustor was developed for fuel combustion testing using a combination of AM and traditional manufacturing, and was successfully operated using conventional aviation fuels, SAF, and fuel blends, providing a set of emissions datasets.
- In agreement with previous studies, hydrogen content was found as the fuel property correlating most strongly with nvPM emissions.
- A constrained power law is suggested as a more scientifically robust method of correlating hydrogen content to nvPM emissions compared to the polynomial trend suggested by previous authors, and could be used to describe the trends across nvPM data sets taken from different combustor designs when normalised to a reference fuel.
- The achievable nvPM EI_{number} reductions through the use of low aromatic, high hydrogen content fuels compared to reference Jet A-1 fuels may be overreported in the range of 6-9% without system loss corrections, due to higher system losses affecting nvPM concentrations with smaller particle sizes, as are typically generated by high hydrogen content fuels.
- It was found that linear regression could be used to determine a global correlation applicable to multiple atomiser designs, but the correlations available in the literature appear to be specialised for laser diffraction data. Correlations derived using PDA data tended to

underestimate the impact of aerodynamic forces and overestimate viscous fuel effects.

- Measured variability in SMD values across different SAF and blended fuels tested using PDA experimentation was found to be small, at around 7-12% at the conditions tested.
- Reductions to the atomisation air mass flowrate of ~9%, predicted to result in We number reductions ~16-17% and reductions in SMD of ~5%, were found to reduce combustion stability and consistently exacerbate nvPM emissions, leading to relative increases of 5-72% for EI_{mass} , 11-89% for EI_{number} , and 1-7% for GMD.

8.3. Future work

This work has mainly been an applied study, relying on experimental data and empirical correlations to identify trends. Measurements of nvPM emissions were taken using an ICAO compliant measurement system and included corrections for system losses following the combustor exit, ensuring that data is better representative of emissions at the combustor exit plane. This data is intended to facilitate future modelling studies, and so the next logical step would be a computational modelling study, using either CFD or chemical kinetic software to consolidate the collected emissions data for the combustors. The datasets produced over the course of this work are recommended in the facilitation of this, with the dataset produced in *Chapter 5* now published [1].

Further refinement of the RQL combustor design may be undertaken if desired. Day-to-day variability was seen to impact all nvPM datasets in this work, and an effort to identify and reduced sources of variability could be undertaken more closely to see if they can be reduced. It is also believed that the ideal operating conditions for the combustor have not yet been found, and should be examined during future experimentation. Manufacturing newer iterations of the combustor with more heat resistant materials may help to prevent the thermal damage witnessed to the combustors developed in this work. While thermal damage was not observed for the Mk. I combustor, this is likely because a higher primary zone equivalence ratio was used during its operation, which was much higher than is recommended for RQL designs and is not recommended for use in further experimentation. The RQL combustor may also be upgraded to an optical

combustor, allowing for further insight into the flame shape and regions of soot formation in the combustor. This could then be paired with computational CFD analysis, as described in the previous paragraph, for validation of the flows.

AM has proven to be a useful tool for the rapid prototyping of prefilming aircraft atomisers designed using empirical methods, which were able to markedly improve the operability and combustion stability of the combustor. The face up printing orientation is recommended for future atomiser designs. Future development of the atomisers may wish to explore methods of reducing the observed drawbacks associated with AM, including dimensional offsets between CAD files and printed parts of as much as -0.8 mm (6%), higher surface roughness, and part failures due to powder blockage or failure of manufacturing supports. Additionally, the empirical methods employed were shown to lack fidelity, and a more robust method is recommended for future design, such as CFD analysis.

The methods used to determine atomisation quality relied on predictions from benchmarking experiments, which were not representative of operating conditions during combustion. As such, it is recommended that additional spray experimentation using the aviation fuels under pressurised/preheated conditions are undertaken. Atomisation air velocities should be characterised using particle seeding and velocity measurements, or CFD simulations. Results from both of these experiments would help to more accurately determine the variability in SMD values across aviation fuels and operating conditions during combustion tests, towards more accurately determining the subsequent impact this may have on nvPM formation rates.

9. References

- [1] J. Harper, E. Durand, P. Bowen, D. Pugh, M. Johnson, and A. Crayford, "Influence of alternative fuel properties and combustor operating conditions on the nvPM and gaseous emissions produced by a small-scale RQL combustor," 2022.
- [2] A. P. Crayford *et al.*, "Manufacture, Characterization and Stability Limits of an AM Prefilming Air-Blast Atomizer," in *Proceedings of the ASME Turbo Expo 2019: Turbomachinery Technical Conference and Exposition. Volume 4B: Combustion, Fuels, and Emissions*, 2019.
- [3] EASA, "European Aviation Environmental Report 2019," 2019.
- [4] IATA, "Aircraft Technology Roadmap to 2050," 2019.
- [5] S. Blakey, L. Rye, and C. W. Wilson, "Aviation gas turbine alternative fuels: A review," *Proc. Combust. Inst.*, vol. 33, no. 2, pp. 2863-2885, Jan. 2011.
- [6] M. Masiol and R. M. Harrison, "Aircraft engine exhaust emissions and other airport-related contributions to ambient air pollution: A review," *Atmos. Environ.*, vol. 95, pp. 409-455, 2014.
- [7] V. Grewe *et al.*, "Evaluating the climate impact of aviation emission scenarios towards the Paris agreement including COVID-19 effects," *Nat. Commun.*, vol. 12, no. 1, Dec. 2021.
- [8] E. Commercial-fuel and U. States, "ExxonMobil Jet Fuel," pp. 1-3, 2020.
- [9] ASTM, "D1655-18 Standard Specification for Aviation Turbine Fuels," 2018.
- [10] C. Zhang, X. Hui, Y. Lin, and C.-J. Sung, "Recent development in studies of alternative jet fuel combustion: Progress, challenges, and opportunities," *Renew. Sustain. Energy Rev.*, vol. 54, pp. 120-138, Feb. 2016.
- [11] ICAO, "2019 Environmental Report - The Next Chapter," 2019.
- [12] World Energy Council, "World Energy Trilemma Index," 2021. [Online]. Available: <https://www.worldenergy.org/transition-toolkit/world-energy-trilemma-index>. [Accessed: 25-Nov-2021].
- [13] "Aviation - Analysis - IEA." [Online]. Available: <https://www.iea.org/reports/aviation>. [Accessed: 16-Aug-2022].
- [14] "Reducing emissions from aviation." [Online]. Available: https://ec.europa.eu/clima/eu-action/transport-emissions/reducing-emissions-aviation_en#aviation-emissions. [Accessed: 17-Aug-2022].
- [15] ICAO, "Aircraft Engine Emissions," 2021. [Online]. Available: <https://www.icao.int/environmental-protection/pages/aircraft-engine-emissions.aspx>. [Accessed: 20-Sep-2021].
- [16] A. H. Lefebvre and D. R. Balal, *Gas turbine combustion: alternative fuels and emissions*, 3rd ed. CRC press, 2010.
- [17] S. Farokhi, *Aircraft Propulsion*, 2nd ed. Chichester, England: Wiley, 2014.
- [18] T. C. Lieuwen and V. Yang, *Gas Turbine Emissions*, vol. 38. 2013.
- [19] K. K. Rink and A. H. Lefebvre, "Influence of fuel drop size and combustor operating conditions on pollutant emissions," *SAE Tech. Pap.*, 1986.
- [20] ICAO, "NEW PARTICULATE MATTER STANDARD FOR AIRCRAFT GAS TURBINE ENGINES," 2016. [Online]. Available: <https://www.icao.int/environmental->

protection/Documents/EnvironmentalReports/2016/ENVReport2016_pg85-88.pdf.
[Accessed: 27-Sep-2021].

- [21] P. Lobo *et al.*, “Measurement of Aircraft Engine Non-Volatile PM Emissions: Results of the Aviation-Particle Regulatory Instrumentation Demonstration Experiment (A-PRIDE) 4 Campaign,” *Aerosol Sci. Technol.*, vol. 49, no. 7, pp. 472-484, 2015.
- [22] A. M. Boies *et al.*, “Particle Emission Characteristics of a Gas Turbine with a Double Annular Combustor,” *Aerosol Sci. Technol.*, vol. 49, no. 9, pp. 842-855, Sep. 2015.
- [23] B. Cary and D. Smith, “What is Elemental Carbon and How Do Definitions Differ for Different Applications?,” 2003.
- [24] ICAO, “Annex 16 - Environmental Protection,” 2018.
- [25] R. K. Mishra and S. Chandel, “Soot formation and its effect in an aero gas turbine combustor,” *Int. J. Turbo Jet Engines*, vol. 36, no. 1, pp. 61-73, 2019.
- [26] World Health Organization, “Health effects of particulate matter,” 2013.
- [27] H. Richter and J. . Howard, *Formation of polycyclic aromatic hydrocarbons and their growth to soot - a review of chemical reaction pathways*, vol. 26, no. 4-6. 2000.
- [28] C. I. Davidson, R. F. Phalen, and P. A. Solomon, “Aerosol Science and Technology Airborne Particulate Matter and Human Health: A Review Airborne Particulate Matter and Human Health: A Review,” *Aerosol Sci. Technol.*, vol. 39, pp. 737-749, 2005.
- [29] D. D. Das *et al.*, “Sooting Tendencies of Diesel Fuels, Jet Fuels, and Their Surrogates in Diffusion Flames,” *Fuel*, vol. 197, no. 9, pp. 445-458, 2017.
- [30] S. H. L. Yim *et al.*, “Global, regional and local health impacts of civil aviation emissions,” *Environ. Res. Lett.*, vol. 10, no. 3, 2015.
- [31] Institute for Advanced Sustainability Studies, “IASS Policy Brief Black Carbon in Europe,” 2017.
- [32] Center for Climate and Energy Solutions, “SCIENCE WHAT IS BLACK CARBON?,” 2010.
- [33] T. C. Bond *et al.*, “Bounding the role of black carbon in the climate system: A scientific assessment,” *J. Geophys. Res. Atmos.*, vol. 118, no. 11, pp. 5380-5552, Jun. 2013.
- [34] C. Voigt *et al.*, “Cleaner burning aviation fuels can reduce contrail cloudiness,” *Commun. Earth Environ.*, vol. 2, no. 1, Dec. 2021.
- [35] D. S. Lee *et al.*, “The contribution of global aviation to anthropogenic climate forcing for 2000 to 2018,” *Atmos. Environ.*, vol. 244, Jan. 2021.
- [36] O. B. Popovitcheva *et al.*, “Experimental characterization of aircraft combustor soot: Microstructure, surface area, porosity and water adsorption,” *Phys. Chem. Chem. Phys.*, vol. 2, no. 19, pp. 4421-4426, 2000.
- [37] J. S. Kinsey, M. D. Hays, Y. Dong, D. C. Williams, and R. Logan, “Chemical Characterization of the Fine Particle Emissions from Commercial Aircraft Engines during the Aircraft Particle Emissions eXperiment (APEX) 1 to 3,” *Environ. Sci. Technol.*, vol. 45, no. 8, pp. 3415-3421, Apr. 2011.
- [38] UK Government, “COP26 THE GLASGOW CLIMATE PACT.”
- [39] European Commission, “Flightpath 2050 Europe’s Vision for Aviation.”
- [40] ICAO, “Home.” [Online]. Available: <https://www.icao.int/Pages/default.aspx>.

[Accessed: 26-Mar-2022].

- [41] UK Government, “Jet Zero Consultation A consultation on our strategy for net zero aviationdepartment-for-transport,” 2021.
- [42] SAE Aerospace, “ARP1179D Aerospace Recommended Practice,” 2011.
- [43] S. Christie, P. Lobo, D. Lee, and D. Raper, “Gas Turbine Engine Nonvolatile Particulate Matter Mass Emissions: Correlation with Smoke Number for Conventional and Alternative Fuel Blends,” 2016.
- [44] ICAO, “Local Air Quality Technology Standards,” 2019. [Online]. Available: https://www.icao.int/environmental-protection/Pages/LAQ_TechnologyStandards.aspx. [Accessed: 31-Jul-2021].
- [45] ICAO, “ICAO Council adopts important environmental standard,” 2021. [Online]. Available: <https://www.icao.int/Newsroom/Pages/ICAO-Council-adopts-important-environmental-standard.aspx>. [Accessed: 22-Sep-2021].
- [46] SAE Aerospace, “ARP6320 - Procedure for the Continuous Sampling and Measurement of Non-Volatile Particulate Matter Emissions from Aircraft Turbine Engines,” 2017.
- [47] Rolls-Royce, “Trent 1000,” 2021. [Online]. Available: <https://www.rolls-royce.com/products-and-services/civil-aerospace/airlines/trent-1000.aspx#section-overview>. [Accessed: 17-Sep-2021].
- [48] Rolls-Royce, “Advance and UltraFan.” [Online]. Available: <https://www.rolls-royce.com/media/our-stories/innovation/2016/advance-and-ultrafan.aspx#challenge>. [Accessed: 06-Jun-2021].
- [49] Z. Saboohi, F. Ommi, and A. Fakhrtabatabaei, “Development of an Augmented Conceptual Design Tool for Aircraft Gas Turbine Combustors,” *Int. J. Multiphys.*, vol. 10, no. 1, pp. 53-74, 2016.
- [50] R. Tacina, C. Wey, and P. Laing, “A Low NO_x Lean-Direct Injection, Multipoint Integrated Module Combustor Concept for Advanced Aircraft Gas Turbines,” 2002.
- [51] M. Khosravy eL_Hossaini, “Review of the New Combustion Technologies in Modern Gas Turbines,” *Prog. Gas Turbine Perform.*, p. 13, Jun. 2013.
- [52] Y. Liu, X. Sun, V. Sethi, D. Nalianda, Y.-G. Li, and L. Wang, “Review of modern low emissions combustion technologies for aero gas turbine engines,” *Prog. Aerosp. Sci.*, vol. 94, pp. 12-45, Oct. 2017.
- [53] S. Samuelsen, “Rich Burn, Quick-Mix, Lean Burn (RQL) Combustor Introduction.”
- [54] “ICAO Aircraft Engine Emissions Databank | EASA.” [Online]. Available: <https://www.easa.europa.eu/domains/environment/icao-aircraft-engine-emissions-databank>. [Accessed: 04-Nov-2021].
- [55] Airbus, “Electric flight - Zero emission.” [Online]. Available: <https://www.airbus.com/innovation/zero-emission/electric-flight.html#projects>. [Accessed: 27-Sep-2021].
- [56] A. Valera-Medina *et al.*, “Ammonia, Methane and Hydrogen for Gas Turbines,” *Energy Procedia*, vol. 75, pp. 118-123, Aug. 2015.
- [57] O. Kurata *et al.*, “Performances and emission characteristics of NH₃-air and NH₃CH₄-air combustion gas-turbine power generations,” *Proc. Combust. Inst.*, vol. 36, no. 3, pp. 3351-3359, Jan. 2017.
- [58] H. Kobayashi, A. Hayakawa, K. D. K. A. Somarathne, and E. C. Okafor, “Science and technology of ammonia combustion,” *Proc. Combust. Inst.*, vol. 37, no. 1, pp.

109-133, Jan. 2019.

- [59] D. Daggett, O. Hadaller, R. Hendricks, and R. Walther, "Alternative Fuels and Their Potential Impact on Aviation," in *CAS-Secretariat - 25th Congress of the International Council of the Aeronautical Sciences*, 2006, no. 5, pp. 2888-2897.
- [60] M. J. Dewitt, E. Corporan, J. Graham, and D. Minus, "Effects of Aromatic Type and Concentration in Fischer-Tropsch Fuel on Emissions Production and Material Compatibility," *Energy & Fuels*, vol. 22, pp. 2411-2418, 2008.
- [61] ASTM, "D4054 – 20a Evaluation of New Aviation Turbine Fuels and Fuel Additives," 2020.
- [62] L. Rye, S. Blakey, and C. W. Wilson, "Sustainability of supply or the planet: a review of potential drop-in alternative aviation fuels," *Energy Environ. Sci.*, vol. 3, pp. 17-27, 2010.
- [63] W.-C. Wang and L. Tao, "Bio-jet fuel conversion technologies," *Renew. Sustain. Energy Rev.*, vol. 53, pp. 801-822, Jan. 2016.
- [64] ICAO, "Conversion processes," 2021. [Online]. Available: <https://www.icao.int/environmental-protection/GFAAF/Pages/Conversion-processes.aspx>. [Accessed: 28-Sep-2021].
- [65] ICAO, "Sustainable Aviation Fuels Guide," 2017.
- [66] EU, "Directive (EU) 2018/2001 of the European Parliament and of the Council of 11 December 2018 on the promotion of the use of energy from renewable sources (recast)," *Off. J. Eur. Union*, vol. 2018, no. L 328, pp. 82-209, 2018.
- [67] "Renewable Energy - Recast to 2030 (RED II)." [Online]. Available: https://joint-research-centre.ec.europa.eu/welcome-jec-website/reference-regulatory-framework/renewable-energy-recast-2030-red-ii_en. [Accessed: 19-Aug-2022].
- [68] D. R. Shonnard, L. Williams, and T. N. Kalnes, "Camelina-Derived Jet Fuel and Diesel: Sustainable Advanced Biofuels," *Environ. Prog. Sustain. Energy*, vol. 29, no. 3, pp. 382-392, 2010.
- [69] ICAO, "CORSIA Sustainability Criteria for CORSIA Eligible Fuels," 2019.
- [70] Sustainable Aviation, "SUSTAINABLE AVIATION FUELS ROAD-MAP Fueling the future of UK aviation Sustainable Aviation wishes to thank the following organisations for leading the work in producing this Road-Map: Sustainable Aviation Fuels Road-Map 2 CONTENTS," 2019.
- [71] B. E. Anderson *et al.*, "Alternative Aviation Fuel Experiment (AAFEX)," 2011.
- [72] R. H. Moore *et al.*, "Influence of jet fuel composition on aircraft engine emissions: A synthesis of aerosol emissions data from the NASA APEX, AAFEX, and ACCESS missions," *Energy and Fuels*, vol. 29, no. 4, pp. 2591-2600, 2015.
- [73] ASTM, "D7566 – 20b Standard Specification for Aviation Turbine Fuel Containing Synthesized Hydrocarbons," 2020.
- [74] E. Corporan *et al.*, "Emissions characteristics of a turbine engine and research combustor burning a Fischer-Tropsch jet fuel," *Energy and Fuels*, vol. 21, no. 5, pp. 2615-2626, 2007.
- [75] X. Xue, X. Hui, P. Singh, and C. J. Sung, "Soot formation in non-premixed counterflow flames of conventional and alternative jet fuels," *Fuel*, vol. 210, no. May, pp. 343-351, 2017.
- [76] L. Zheng *et al.*, "Effects of Alternative Fuel Properties on Particulate Matter Produced in a Gas Turbine Combustor," *Energy & Fuels*, vol. 32, no. 9, pp. 9883-

9897, Sep. 2018.

- [77] S. Sharma, P. Singh, A. Gupta, A. Chowdhury, B. Khandelwal, and S. Kumar, "Distributed combustion mode in a can-type gas turbine combustor - A numerical and experimental study," *Appl. Energy*, vol. 277, Nov. 2020.
- [78] Chevron, "Aviation Fuels Technical Review," 2007.
- [79] G. Liu, B. Yan, and G. Chen, "Technical review on jet fuel production," 2013.
- [80] P. Schmidt, V. Batteiger, A. Roth, W. Weindorf, and T. Raksha, "Power-to-Liquids as Renewable Fuel Option for Aviation: A Review," *Chemie Ing. Tech.*, vol. 90, no. 1-2, pp. 127-140, Jan. 2018.
- [81] S. H. Won *et al.*, "Predicting the global combustion behaviors of petroleum-derived and alternative jet fuels by simple fuel property measurements," *Fuel*, vol. 168, pp. 34-46, Mar. 2016.
- [82] D. Kang, D. Kim, V. Kalaskar, A. Violi, and A. L. Boehman, "Experimental characterization of jet fuels under engine relevant conditions - Part 1: Effect of chemical composition on autoignition of conventional and alternative jet fuels," *Fuel*, vol. 239, pp. 1388-1404, Mar. 2019.
- [83] Applied Research Associates (ARA), "ReadiJet," 2021. [Online]. Available: <https://www.ara.com/products/readijet/>. [Accessed: 05-Oct-2021].
- [84] L. Li, E. Coppola, J. Rine, J. L. Miller, and D. Walker, "Catalytic Hydrothermal Conversion of Triglycerides to Non-ester Biofuels," *Energy & Fuels*, vol. 24, pp. 1305-1315, 2010.
- [85] D. J. Luning Prak *et al.*, "Analysis of Catalytic Hydrothermal Conversion Jet Fuel and Surrogate Mixture Formulation: Components, Properties, and Combustion," *Energy & Fuels*, vol. 31, pp. 13802-13814, 2017.
- [86] D. Castello, T. H. Pedersen, and L. A. Rosendahl, "Continuous hydrothermal liquefaction of biomass: A critical review," *Energies*, vol. 11, no. 11, 2018.
- [87] T. Schripp *et al.*, "Particle emissions of two unblended alternative jet fuels in a full scale jet engine," *Fuel*, vol. 256, 2019.
- [88] M. O. P. Fortier, G. W. Roberts, S. M. Stagg-Williams, and B. S. M. Sturm, "Life cycle assessment of bio-jet fuel from hydrothermal liquefaction of microalgae," *Appl. Energy*, vol. 122, no. July 2011, pp. 73-82, 2014.
- [89] M. Frenklach, "Reaction mechanism of soot formation in flames," *Phys. Chem. Chem. Phys.*, vol. 4, no. 11, pp. 2028-2037, May 2002.
- [90] M. Frenklach and H. Wang, "Detailed modeling of soot particle nucleation and growth," *Symp. Combust.*, vol. 23, no. 1, pp. 1559-1566, Jan. 1991.
- [91] H. Bockhorn, *Soot Formation in Combustion*, vol. 59. Berlin, Heidelberg: Springer Berlin Heidelberg, 1994.
- [92] J. Appel, H. Bockhorn, and M. Frenklach, "Kinetic modeling of soot formation with detailed chemistry and physics: laminar premixed flames of C2 hydrocarbons," *Combust. Flame*, vol. 121, no. 1-2, pp. 122-136, Apr. 2000.
- [93] I. M. Kennedy, "Models of soot formation and oxidation," *Prog. Energy Combust. Sci.*, vol. 23, no. 2, pp. 95-132, 1997.
- [94] R. R. Kumal *et al.*, "Impact of Biofuel Blends on Black Carbon Emissions from a Gas Turbine Engine," *Energy & Fuels*, vol. 34, no. 4, pp. 4958-4966, Apr. 2020.
- [95] H. Ghiassi, D. Lignell, and J. S. Lighty, "Soot Oxidation by OH: Theory

- Development, Model, and Experimental Validation,” *Energy & Fuels*, vol. 31, p. 2236–2245, 2016.
- [96] K. K. Rink and A. H. Lefebvre, “Pollutant formation in heterogeneous mixtures of fuel drops and air,” *Journal of Propulsion and Power*, vol. 3, no. 1, pp. 5-10, 1986.
- [97] P. Lobo *et al.*, “Impact of Alternative Fuels on Emissions Characteristics of a Gas Turbine Engine - Part 1: Gaseous and Particulate Matter Emissions,” *Environ. Sci. Technol.*, vol. 46, no. 19, pp. 10805-10811, 2012.
- [98] A. J. Beyersdorf *et al.*, “Reductions in aircraft particulate emissions due to the use of Fischer-Tropsch fuels,” *Atmos. Chem. Phys.*, vol. 14, no. 1, pp. 11-23, Jan. 2014.
- [99] P. Lobo, D. E. Hagen, and P. D. Whitefield, “Comparison of PM emissions from a commercial jet engine burning conventional, biomass, and fischer-tropsch fuels,” *Environ. Sci. Technol.*, vol. 45, no. 24, pp. 10744-10749, 2011.
- [100] T. Schripp *et al.*, “Impact of Alternative Jet Fuels on Engine Exhaust Composition During the 2015 ECLIF Ground-Based Measurements Campaign,” *Environ. Sci. Technol.*, vol. 52, no. 8, pp. 4969-4978, Apr. 2018.
- [101] P. Lobo *et al.*, “Comparison of standardized sampling and measurement reference systems for aircraft engine non-volatile particulate matter emissions,” *J. Aerosol Sci.*, vol. 145, 2020.
- [102] M. T. Timko *et al.*, “Combustion products of petroleum jet fuel, a fischer-tropsch synthetic fuel, and a biomass fatty acid methyl ester fuel for a gas turbine engine,” *Combust. Sci. Technol.*, vol. 183, no. 10, pp. 1039-1068, 2011.
- [103] B. T. Brem *et al.*, “Effects of Fuel Aromatic Content on Nonvolatile Particulate Emissions of an In-Production Aircraft Gas Turbine,” *Environ. Sci. Technol.*, vol. 49, no. 22, pp. 13149-13157, Nov. 2015.
- [104] H. F. Calcote and D. M. Manos, “Effect of molecular structure on incipient soot formation,” *Combust. Flame*, vol. 49, no. 1-3, pp. 289-304, Jan. 1983.
- [105] P. Lobo, S. Christie, B. Khandelwal, S. G. Blakey, and D. W. Raper, “Evaluation of Non-volatile Particulate Matter Emission Characteristics of an Aircraft Auxiliary Power Unit with Varying Alternative Jet Fuel Blend Ratios,” *Energy & Fuels*, vol. 29, no. 11, pp. 7705-7711, Nov. 2015.
- [106] E. Durand, P. Lobo, A. Crayford, Y. Sevcenco, and S. Christie, “Impact of fuel hydrogen content on non-volatile particulate matter emitted from an aircraft auxiliary power unit measured with standardised reference systems,” *Fuel*, vol. 287, Mar. 2021.
- [107] R. L. Schalla and G. E. McDonald, “Variation in Smoking Tendency Among Hydrocarbons of Low Molecular Weight,” *Ind. Eng. Chem.*, vol. 45, no. 7, pp. 1497-1500, 1953.
- [108] Y. Yang, A. L. Boehman, and R. J. Santoro, “A study of jet fuel sooting tendency using the threshold sooting index (TSI) model,” *Combust. Flame*, vol. 149, no. 1-2, pp. 191-205, 2007.
- [109] D. W. Naegeli and C. A. Moses, “Effect of Fuel Molecular Structure on Soot Formation in Gas Turbine Engines,” 1980.
- [110] T. J. ROSFJORD, “Role of fuel chemical properties on combustor radiative heat load,” *J. Propuls. Power*, vol. 3, no. 6, pp. 494-501, Nov. 1987.
- [111] M. L. Botero, S. Mosbach, and M. Kraft, “Sooting tendency of paraffin components of diesel and gasoline in diffusion flames,” *Fuel*, vol. 126, pp. 8-15, Jun. 2014.

- [112] A. H. Lefebvre and V. G. McDonell, *Atomization and Sprays*, 2nd ed. Boca Raton: CRC Press, 2017.
- [113] A. A. Rizkalla and A. H. Lefebvre, "The Influence of Air and Liquid Properties on Airblast Atomization," *J. Fluids Eng.*, vol. 97, no. 3, pp. 316-320, Sep. 1975.
- [114] Lord Rayleigh, "On the instability of jets," *Proc. London Math. Soc.*, vol. s1-10, no. 1, pp. 4-13, 1878.
- [115] A. H. Lefebvre, "Energy Considerations in Twin-Fluid Atomization," *J. Eng. Gas Turbines Power*, vol. 114, no. 1, p. 89, Jan. 1992.
- [116] A. Williams, *Combustion of Liquid Fuel Sprays*, 1st ed. Elsevier, 1990.
- [117] M. M. Tareq, R. A. Dafsari, S. Jung, and J. Lee, "Effect of the physical properties of liquid and ALR on the spray characteristics of a pre-filming airblast nozzle," *Int. J. Multiph. Flow*, vol. 126, p. 103240, 2020.
- [118] I. Zahmatkesh and M. Moghiman, "Effect of liquid fuel droplet size on soot emission from turbulent spray flames," *Iran. J. Sci. Technol. Trans. B Eng.*, vol. 30, no. 3, pp. 339-351, 2006.
- [119] I. S. Carvalho and M. V Heitor, "Liquid film break-up in a model of a prefilming airblast nozzle," *Exp. Fluids*, vol. 24, no. 5-6, pp. 408-415, 1998.
- [120] A. A. Rizkalla and A. H. Lefebvre, "Influence of Liquid Properties on Airblast Atomizer Spray Characteristics," *J. Eng. Power*, vol. 97, no. 2, p. 173, Apr. 1975.
- [121] G. Charalampous and Y. Hardalupas, "How do liquid fuel physical properties affect liquid jet development in atomisers?," *Phys. Fluids*, vol. 28, no. 10, Oct. 2016.
- [122] A. P. Vouros, A. P. Vouros, and T. Panidis, "Spray Characteristics of Alternative Aviation Fuel Blends," *Aerosp. 2017, Vol. 4, Page 18*, vol. 4, no. 2, p. 18, Mar. 2017.
- [123] R. A. Dafsari, H. J. Lee, J. Han, D.-C. Park, and J. Lee, "Viscosity effect on the pressure swirl atomization of an alternative aviation fuel," *Fuel*, vol. 240, pp. 179-191, Mar. 2019.
- [124] C. M. Reeves and A. H. Lefebvre, "Fuel Effects on Aircraft Combustor Emissions," in *Proceedings of the ASME 1986 International Gas Turbine Conference and Exhibit. Volume 3: Coal, Biomass and Alternative Fuels; Combustion and Fuels; Oil and Gas Applications; Cycle Innovations*, 1986.
- [125] Y. Levy, V. Erenburg, V. Sherbaum, V. Ovcharenko, and D. Kutikov, "Experimental CFD study of miniature air-blast atomizers," *Int. J. Turbo Jet Engines*, vol. 26, no. 3, pp. 169-185, 2009.
- [126] S. Gepperth, R. Koch, and H. J. Bauer, "Analysis and comparison of primary droplet characteristics in the near field of a prefilming airblast atomizer," *Proc. ASME Turbo Expo*, vol. 1 A, pp. 1-14, 2013.
- [127] H. C. Simmons, R. R. Conrad, and M. Orav, "AIR-ATOMIZING FUEL NOZZLE," 3,980,233, 1975.
- [128] A. K. Jasuja, "Atomization of Crude and Residual Fuel Oils," 1979.
- [129] M. S. El-Shanawany and A. H. Lefebvre, "Airblast Atomization: The Effect of Linear Scale on Mean Drop Size," in *Proceedings of the ASME Turbo Expo*, 1980, vol. 1A-1980.
- [130] R. K. Mishra, S. K. Kumar, and S. Chandel, "Effect of spray cone angle on flame stability in an annular gas turbine combustor," *Int. J. Turbo Jet Engines*, vol. 33, no. 1, pp. 35-44, Apr. 2016.

- [131] Q. P. Zheng, A. K. Jasuja, and A. H. Lefebvre, "INFLUENCE OF AIR AND FUEL FLOWS ON GAS TURBINE SPRAYS AT HIGH PRESSURES," 1996.
- [132] Z. Zhang, Y. Liu, and H. Hu, "Effects of chamber pressure on the kinematic characteristics of spray flows exhausted from an airblast atomizer," *Exp. Therm. Fluid Sci.*, vol. 130, 2022.
- [133] J. Keeler, *Understanding NMR Spectroscopy*. 2002.
- [134] H. Z. Carreras, "NMR Spectroscopy Principles, Interpreting an NMR Spectrum and Common Problems," *Technology Networks*, 2021. [Online]. Available: <https://www.technologynetworks.com/analysis/articles/nmr-spectroscopy-principles-interpreting-an-nmr-spectrum-and-common-problems-355891#D2>. [Accessed: 21-Feb-2022].
- [135] J. L. Burger, J. A. Widgren, T. M. Lovestead, and T. J. Bruno, "1 H and 13 C NMR Analysis of Gas Turbine Fuels As Applied to the Advanced Distillation Curve Method," *Energy & Fuels*, vol. 29, no. 8, pp. 4874-4885, 2015.
- [136] ASTM, "D3701-17 Standard Test Method for Hydrogen Content of Aviation Turbine Fuels by Low Resolution Nuclear Magnetic Resonance Spectrometry," 2017.
- [137] ASTM, "D4808 - Standard Test Methods for Hydrogen Content of Light Distillates, Middle Distillates, Gas Oils, and Residua by Low-Resolution Nuclear Magnetic Resonance Spectroscopy," ASTM International, 100 Barr Harbor Drive, PO Box C700, West Conshohocken, PA 19428-2959, 2017.
- [138] ASTM, "D7171-16 Standard Test Method for Hydrogen Content of Middle Distillate Petroleum Products by Low-Resolution Pulsed Nuclear Magnetic Resonance," 2016.
- [139] ASTM, "D1319 - 20a Standard Test Method for Hydrocarbon Types in Liquid Petroleum Products by Fluorescent Indicator Adsorption," 2020.
- [140] ASTM, "D6379 - Standard Test Method for Determination of Aromatic Hydrocarbon Types in Aviation Fuels and Petroleum Distillates-High Performance Liquid Chromatography Method with Refractive Index Detection," 2011.
- [141] ASTM, "D8267 - 19a Standard Test Method for Determination of Total Aromatic, Monoaromatic and Diaromatic Content of Aviation Turbine Fuels Using Gas Chromatography with Vacuum Ultraviolet Absorption Spectroscopy Detection (GC-VUV)," 2019.
- [142] Z. Liu and J. B. Phillips, "Comprehensive Two-Dimensional Gas Chromatography using an On-Column Thermal Modulator Interface," *J. Chromatogr. Sci.*, vol. 29, no. 6, pp. 227-231, Jun. 1991.
- [143] L. Mondello, P. Q. Tranchida, P. Dugo, and G. Dugo, "COMPREHENSIVE TWO-DIMENSIONAL GAS CHROMATOGRAPHY-MASS SPECTROMETRY: A REVIEW," 2008.
- [144] J. B. Phillips and J. Beens, "Comprehensive two-dimensional gas chromatography: a hyphenated method with strong coupling between the two dimensions," 1999.
- [145] R. C. Y. Ong and P. J. Marriott, "A review of basic concepts in comprehensive two-dimensional gas chromatography," *J. Chromatogr. Sci.*, vol. 40, no. 5, pp. 276-291, 2002.
- [146] P. Vozka, H. Mo, P. Šimáček, and G. Kilaz, "Middle distillates hydrogen content via GC×GC-FID," *Talanta*, vol. 186, pp. 140-146, Aug. 2018.
- [147] M. Makida, H. Yamada, Y. Kurosawa, T. Yamamoto, K. Matsuura, and S. Hayashi, "PRELIMINARY EXPERIMENTAL RESEARCH TO DEVELOP A COMBUSTOR FOR SMALL CLASS AIRCRAFT ENGINE UTILIZING PRIMARY RICH COMBUSTION APPROACH," *ASME Turbo Expo 2006*, pp. 1-8, 2006.

- [148] S. Singamneni, Y. LV, A. Hewitt, R. Chalk, W. Thomas, and D. Jordison, "Additive Manufacturing for the Aircraft Industry: A Review," *J. Aeronaut. Aerosp. Eng.*, vol. 08, no. 01, 2019.
- [149] B. Blakey-Milner *et al.*, "Metal additive manufacturing in aerospace: A review," *Mater. Des.*, vol. 209, p. 110008, Nov. 2021.
- [150] General Electric, "New manufacturing milestone: 30,000 additive fuel nozzles | GE Additive," 2018. [Online]. Available: <https://www.ge.com/additive/stories/new-manufacturing-milestone-30000-additive-fuel-nozzles>. [Accessed: 03-May-2021].
- [151] Rolls-Royce, "Additive Manufacturing of Front Bearing Housing Aerofoils for Rolls-Royce Test Bed Engines," 2015. [Online]. Available: <https://ncam.themtc.org/case-studies/additive-manufacturing-of-front-bearing-housing-aerofoils-for-rolls-royce-test-bed-engines/>. [Accessed: 07-Mar-2022].
- [152] S. Sun, M. Brandt, and M. Easton, "Powder bed fusion processes," in *Laser Additive Manufacturing*, Elsevier, 2017, pp. 55-77.
- [153] ASTM International, "The 5 Most Important Standards in Additive Manufacturing | ASTM Standardization News." [Online]. Available: <https://sn.astm.org/?q=features/5-most-important-standards-additive-manufacturing-.html>. [Accessed: 22-Feb-2022].
- [154] D. G. Pugh *et al.*, "Dissociative influence of H₂O vapour/spray on lean blowoff and NO_x reduction for heavily carbonaceous syngas swirling flames," *Combust. Flame*, vol. 177, pp. 37-48, Mar. 2017.
- [155] A. Crayford *et al.*, "SAMPLE III: Contribution to aircraft engine PM certification requirement and standard Third Specific Contract-Final Report," 2013.
- [156] A. P. Crayford *et al.*, "SAMPLE III: Contribution to aircraft engine PM certification requirement and standard Fifth Specific Contract-Final Report," 2014.
- [157] SAE Aerospace, "AIR6241 Procedure for the Continuous Sampling and Measurement of Non-Volatile Particle Emissions from Aircraft Turbine Engines," 2013.
- [158] NIOSH, "Diesel particulate matter (as Elemental Carbon): Method 5040," *NIOSH Man. Occup. Saf. Heal.*, vol. 4, no. 3, pp. 1-5, 2003.
- [159] A. Bergmann, "Sampling of Non-Volatile Vehicle Exhaust Particles: A Simplified Guide Development of In-Situ, Full Stream, Laser Induced Incandescence Technique for Measurement of Transient Soot Emissions for Diesel Engine View project Fiber Optical Current Measurement | FORESEEN View project Barouch Giechaskiel European Commission," *Artic. SAE Int. J. Engines*, 2012.
- [160] E. F. Durand, "Towards improved correction methodology for regulatory aircraft engine nvPM measurement," p. 276, 2019.
- [161] E. F. Durand, A. P. Crayford, and M. Johnson, "Experimental validation of thermophoretic and bend nanoparticle loss for a regulatory prescribed aircraft nvPM sampling system," *Aerosol Sci. Technol.*, vol. 54, no. 9, pp. 1019-1033, Sep. 2020.
- [162] SAE Aerospace, "Aerospace Recommended Practice ARP6481," 2019.
- [163] SAE Aerospace, "AIR6504 Procedure for the Calculation of non-volatile Particulate Matter Sampling and Measurement System Penetration Functions and System Loss Correction Factors," 2016.
- [164] ASTM, "D3338 - 20a - Standard Test Method for Estimation of Net Heat of Combustion (Specific Energy) of Aviation Fuels," 2020.

- [165] SAE International, "ARP1533C," 2016.
- [166] R. P. Benedict, *Fundamentals of Temperature, Pressure, and Flow Measurements*, 3rd ed. Hoboken, NJ, USA: John Wiley & Sons, Inc., 1984.
- [167] B. G. Liptak, *Instrument Engineers' Handbook Vol 1: Process Measurement and Analysis*, 4th ed. 2003.
- [168] "ImageJ." [Online]. Available: <https://imagej.nih.gov/ij/index.html>. [Accessed: 29-Mar-2022].
- [169] C. Tung Chong and S. Hochgreb, "Effect of Atomizing Air Flow on Spray Atomization of an Internal Mix Twin-fluid Atomizer Studying properties of ashes produced in power stations View project DUST FLAME View project EFFECT OF ATOMIZING AIR FLOW ON SPRAY ATOMIZATION OF AN INTERNAL-MIX TWIN-FLUID ATOMIZER," *At. Sprays*, vol. 25, no. 8, pp. 657-673, 2015.
- [170] L. Durdina, J. Jedelsky, and M. Jicha, "Experimental Investigation on Spray Characteristics of Pressure-Swirl Atomizers for a Small-Sized Jet Engine," 2012.
- [171] R. Ma, B. Dong, Z. Yu, T. Zhang, Y. Wang, and W. Li, "An experimental study on the spray characteristics of the air-blast atomizer," 2014.
- [172] W. D. Bachalo and M. J. Houser, "Phase/Doppler Spray Analyzer For Simultaneous Measurements Of Drop Size And Velocity Distributions," *Opt. Eng.*, vol. 23, no. 5, pp. 583-590, 1984.
- [173] "Measurement Principles of PDA - Dantec Dynamics | Precision Measurement Systems & Sensors." [Online]. Available: <https://www.dantecdynamics.com/solutions-applications/solutions/spray-and-particle/phase-doppler-anemometry-pda/measurement-principles-of-pda/>. [Accessed: 29-Mar-2022].
- [174] S. H. Zaidi, A. Altunbas, and B. J. Azzopardi, "A comparative study of phase Doppler and laser diffraction techniques to investigate drop sizes in annular two-phase flow," *Chem. Eng. J.*, vol. 71, no. 2, pp. 135-143, Dec. 1998.
- [175] M. Aigner and S. Wittig, "Swirl and Counterswirl Effects in Prefilming Airblast Atomizers," *J. Eng. Gas Turbines Power*, vol. 110, no. 1, pp. 105-110, 1988.
- [176] A. K. Gupta, D. G. Lilley, N. Syred, A. K. Gupta, D. G. Lilley, and N. Syred, *Swirl flows*. Abacus Press, Tunbridge Wells, Kent, England, 1984.
- [177] J. S. Chin, N. K. Rizk, and M. K. Razdan, "Effect of Inner and Outer Airflow Characteristics on High Liquid Pressure Prefilming Airblast Atomization," *J. Propuls. Power*, vol. 16, no. 2, pp. 297-301, 2000.
- [178] S. Sharma, S. Sahu, and T. Sundararajan, "Effect of Air Swirler Profile on Spray Characteristics," in *International Conference on Fluid Flow, Heat and Mass Transfer*, 2019.
- [179] T. Parra-Santos, J. R. R. Pérez-Domínguez, R. Z. Z. Szasz, and F. Castro-Ruiz, "An isothermal analysis of curved-vane and flat-vane swirlers for burners," *Eng. Comput. (Swansea, Wales)*, vol. 32, no. 3, pp. 668-686, May 2015.
- [180] H. C. Simmons, "The Prediction of Sauter Mean Diameter for Gas Turbine Fuel Nozzles of Different Types," 1980.
- [181] T. Inamura, N. Katagata, H. Nishikawa, T. Okabe, and K. Fumoto, "Effects of prefilmer edge thickness on spray characteristics in prefilming airblast atomization," *Int. J. Multiph. Flow*, vol. 121, p. 103117, Dec. 2019.
- [182] N. K. Rizk and A. H. Lefebvre, "The Influence of Liquid Film Thickness on Airblast

Atomization,” 1980.

- [183] H. A. Knight and R. B. Walker, “The Component Pressure Losses in Combustion Chambers,” 1957.
- [184] A. S. Morris, *Measurement and Instrumentation Principles*. 2001.
- [185] Y. Nakayama and R. F. Boucher, *Introduction to Fluid Mechanics*. 1999.
- [186] J. Runyon *et al.*, “CHARACTERIZATION OF ALM SWIRL BURNER SURFACE ROUGHNESS AND ITS EFFECTS ON FLAME STABILITY USING HIGH-SPEED DIAGNOSTICS,” 2019.
- [187] F. Giuliani, N. Paulitsch, D. Cozzi, M. Görtler, and L. Andracher, “An assessment on the benefits of additive manufacturing regarding new swirler geometries for gas turbine burners,” *Proc. ASME Turbo Expo*, vol. 4A-2018, pp. 1-12, 2018.
- [188] P. Lobo, D. E. Hagen, P. D. Whitefield, and D. Raper, “PM emissions measurements of in-service commercial aircraft engines during the Delta-Atlanta Hartsfield Study,” *Atmos. Environ.*, vol. 104, pp. 237-245, 2015.
- [189] L. Durdina *et al.*, “Determination of PM mass emissions from an aircraft turbine engine using particle effective density,” 2014.
- [190] T. Sattelmayer and S. Wittig, “Internal Flow Effects in Prefilming Airblast Atomizers: Mechanisms of Atomization and Droplet Spectra,” *J. Eng. Gas Turbines Power*, vol. 108, no. 3, p. 465, Jul. 1986.
- [191] J. Li, X. Sun, Y. Liu, and V. Sethi xsun, “Preliminary Aerodynamic Design Methodology for Aero Engine Lean Direct Injection Combustors,” *Aeronaut. J.*, vol. 121, pp. 1087-1108, 2017.
- [192] J. Li, J. Chen, L. Yuan, G. Hu, and J. Feng, “Flow Characteristics of a Rich-Quench-Lean Combustor-Combined Low-Emission and High-Temperature Rise Combustion,” *Int. J. Aerosp. Eng.*, pp. 1-22, Feb. 2019.

10. Appendices

10.1. HSI Image Processing Macros

“Background Correction”

//This Macro corrects for uneven backlighting illumination across a stack of images

```
//First Pass (last 100 images)
```

```
setSlice(1);
```

```
run("Clear Results");
```

```
run("Make Substack...", "slices=1901-2000");
```

```
run("Z Project...", "projection=[Average Intensity]");
```

```
run("Measure");
```

```
var lavg = getResult("Mean",0)
```

```
close();
```

```
close();
```

```
for (i=1; i<= nSlices; i++) {
```

```
//showProgress(i, nSlices);
```

```
run("Measure");
```

```
var lx = getResult("Mean",getSliceNumber);
```

```
var d = lavg - lx;
```

```
setResult("lavg",getSliceNumber,lavg); // sets the value in the last line of  
the results table
```

```
setResult("lx",getSliceNumber,lx); // sets the value in the last line of the  
results table
```

```
    setResult("d",getSliceNumber,d); // sets the value in the last line of the
results table
```

```
    updateResults(); // updates the results table to show the new value
```

```
    //Correct for difference
```

```
    setMinAndMax(-d, (255-d));
```

```
    run("Apply LUT", "slice");
```

```
    run("Next Slice [>]");
```

```
    }
```

```
“Background Residual”
```

```
makeRectangle(750, 30, 250, 30);
```

```
run("Measure");
```

```
var o = getResult("Mean");
```

```
run("Select None");
```

```
setMinAndMax(o, (255+o));
```

```
run("Apply LUT", "slice");
```

10.2. Linear Regression MATLAB Code (El-Shanawany et al. Example)

```
clear all; close all; clc;
```

```
% get data
```

```
dataset = xlsread('FILE NAME HERE');
```

```
Y = dataset(:,1);
```

```
ALR = dataset(:,2);
```

```
Ua = dataset(:,3);
```

```
Dp = dataset(:,4);
```

```
p1 = dataset(:,5);
```

```
s1 = dataset(:,6);
```

```
v1 = dataset(:,7);
```

```
pa = dataset(:,8);
```

```

Lc = dataset(:,9);
t = dataset(:,10);

% % SMD Equation (example provided is El-Shanawany et al.
[])
%
SMD=1000000*Lc*(1+1/ALR)*[Aval*(((sl/(pa*Ua*dp))^0.6*(pl
/pa)^0.1)]+[Bval*(((v1^2)/(sl*pl*dp))^0.5)
% VARIABLE MAPPING: v(:,1) = Y, v(:,2) = ALR, v(:,3) =
Ua, v(:,4) = Dp, v(:,5) = pl, v(:,6) = sl, v(:,7) = v1
v(:,8) = pa
% PARAMETER MAPPING: p(1) = Aval, p(2) = Bval
p0 = [0.0; 0.0];
v = [Y(:) ALR(:) Ua(:) Dp(:) pl(:) sl(:) v1(:)
pa(:) Lc(:)];
[n,j] = size(v); %Computes number of rows in A
k = j-1;
Yp = @(p,v) 1000000.*v(:,4).*(1+(v(:,2).^(-
1))).*((p(1).*((v(:,6)./(v(:,8).*(v(:,3).^2).*(v(:,4))).^
0.6).*(v(:,5)./v(:,8)).^0.1)) +
(p(2).*((v(:,7).^2)./(v(:,6).*(v(:,5).*(v(:,4))).^0.5))));

%Sum-Squared-Error Cost Function
objective = @(p) sum(((Yp(p,v)-(v(:,1)))./(v(:,1))).^2);

disp(['Initial Objective: ' num2str(objective(p0))])

% % Optimise parameters using fmincon
% linear constraints
A = []; b = [];
Aeq = []; beq = [];
% bounds
lb = ones(2)*0.000001 ; ub = [];
popt = fmincon(objective, p0, A, b, Aeq, beq, lb, ub);
disp(['Final Objective: ' num2str(objective(popt))])
disp('Optimal Parameters: ')
Aval = popt(1)
Bval = popt(2)

% plots for comparison
plot(Ua,Y,'b*')
hold on
%plot(Ua,Yp(p0,v),'ro')
plot(Ua,Yp(popt,v),'go')
legend('measured', 'optimised predicted')
xlabel('Ua')
ylabel('SMD')

```

```
R_squared      =      1 - ((sum((Y - Yp(popt, v)).^2)) ./ (sum((Y -
mean(Y)).^2)))
R_squared_adj  =  1 - (((1 - R_squared) .* (n - 1)) ./ (n - k - 1))

txt3 = {'A=', num2str(Aval)};
text(100, 200, txt3);
txt4 = {'B=', num2str(Bval)};
text(150, 200, txt4);
```